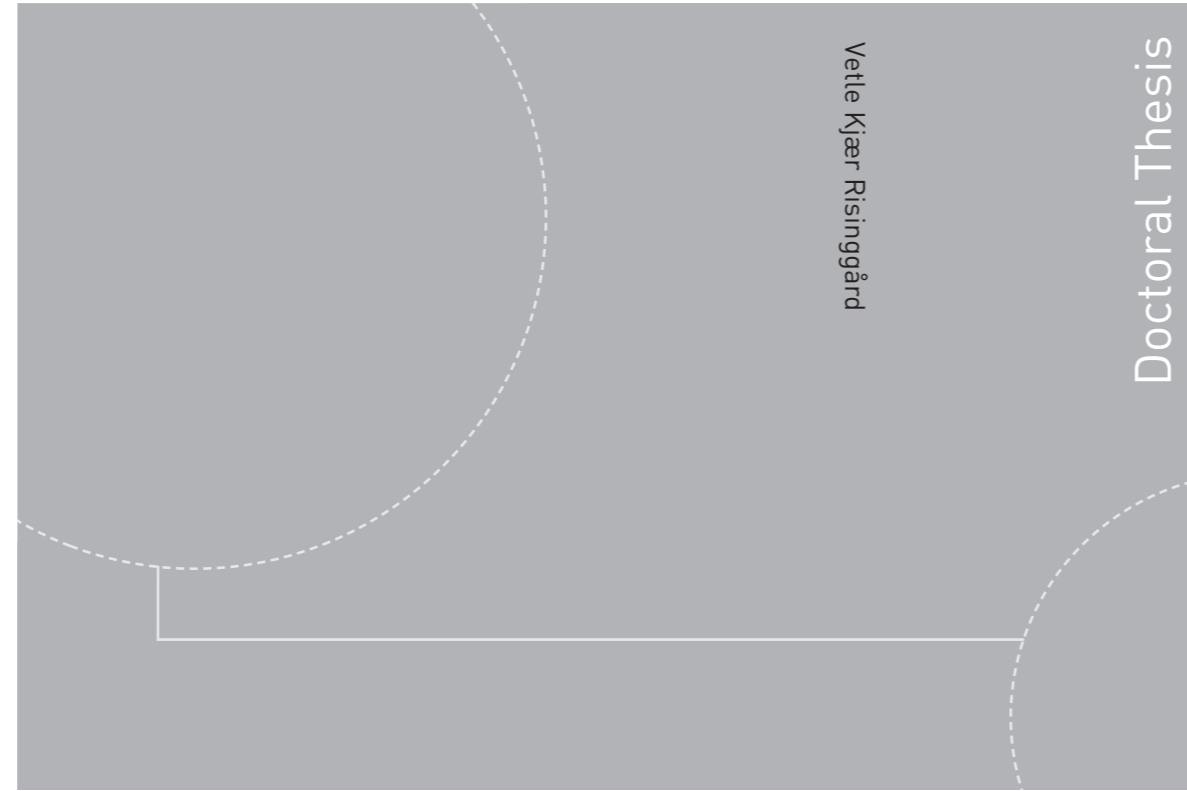


ISBN 978-82-326-4044-7 (printed version)
ISBN 978-82-326-4045-4 (electronic version)
ISSN 1503-8181



Doctoral theses at NTNU, 2019:224

NTNU
Norwegian University of
Science and Technology
Faculty of Natural Sciences
Department of Physics

 NTNU

Doctoral theses at NTNU, 2019:224

Vetle Kjær Risinggård
**Spin currents and torques
via magnons, electrons,
and Cooper pairs**

 **NTNU**
Norwegian University of
Science and Technology

 **NTNU**
Norwegian University of
Science and Technology

Vetle Kjær Risinggård

Spin currents and torques via magnons, electrons, and Cooper pairs

Thesis for the degree of Philosophiae Doctor

Trondheim, August 2019

Norwegian University of Science and Technology
Faculty of Natural Sciences
Department of Physics



Norwegian University of
Science and Technology

NTNU

Norwegian University of Science and Technology

Thesis for the degree of Philosophiae Doctor

Faculty of Natural Sciences
Department of Physics

© Vetle Kjær Risinggård

ISBN 978-82-326-4044-7 (printed version)

ISBN 978-82-326-4045-4 (electronic version)

ISSN 1503-8181



Doctoral theses at NTNU, 2019:224

Printed by Skipnes Kommunikasjon as

Abstract

Spin-based electronics—spintronics—is a candidate technology for complementing or replacing traditional semiconductor electronics at the end of Moore’s law. We consider different spin carriers—electrons, magnons, and Cooper pairs—and their potential for providing energy-efficient spin currents and spin torques.

In two papers we consider spin–orbit torques in synthetic antiferromagnets and van der Waals magnets. Using a collective coordinate model, we are able to explain a switching anomaly in synthetic antiferromagnets which may mitigate the dependence on an in-plane field to switch reliably using spin-Hall torques. We also find that spin–orbit torques in van der Waals magnets with trigonal prismatic symmetry may provide an accessible platform for studying the Berezinskii–Kosterlitz–Thouless transition.

Joule heating is inherent to all resistive spin currents, but can be circumvented using magnons. In two further papers we consider magnonic spin-transfer in ferromagnets and multiferroics. By deriving collective coordinate equations, we clear up some of the confusion over the frequency-dependence of the domain wall velocity. In a multiferroic, we show that the domain wall velocity can be controlled using an applied electric field.

Joule heating can also be avoided by spin polarizing a supercurrent. In the two final papers we consider a superconducting spin Hall effect: the *superspin Hall effect*. We demonstrate and explain the occurrence of a transverse spin current in a ferromagnetic Josephson junction with Rashba interlayers, and consider experimental signatures of the effect. We find that the inverse superspin Hall effect can give rise to an anomalous Josephson current, and suggest that the resulting ϕ_0 junction can be used to directly detect the spin-polarization of a supercurrent.

Contents

Abstract	i
Preface	v
Acknowledgements	vii
Publications	ix
Errata	xi
1 Introduction	1
1.1 The computer and the human genome	1
1.2 Exaflops, zetabytes, and Moore's law	2
1.3 Spintronics	4
1.4 Superconducting spintronics	5
1.5 Two-dimensional materials	6
2 Magnetism	9
2.1 Classifying magnetic materials	9
2.2 Magnetism is quantum	11
2.3 Exchange interactions	12
2.4 Spin-wave theory	16
2.5 Magnetic anisotropy	19
2.6 Magnetostatics	23
2.7 Magnetization dynamics	29
3 Current-induced spin torques	33
3.1 Metallic ferromagnets	33
3.2 Spin-transfer torques	34
3.3* Spin-Hall torques	39
3.4 The Rashba spin-orbit torque	43
3.5 Phenomenology of current-induced spin torques	45
3.6* Spin-orbit torques in Fe_3GeTe_2	49

4	Magnon-induced spin torques	53
4.1	Magnons as spin waves	53
4.2*	Spin-wave spin current and spin transfer	55
4.3	Classifying multiferroic materials	57
4.4*	Magnetization dynamics in type-II multiferroics	61
5	Superconductivity	63
5.1	The Cooper problem	63
5.2	Fermi-liquid theory	65
5.3	Phonon-mediated attractive interactions	66
5.4	The effective Hamiltonian	68
5.5	The BCS gap equation	72
5.6	Pairing symmetries	74
6	Superconducting spintronics	77
6.1	Andreev reflection and the proximity effect	77
6.2	Josephson junctions	80
6.3	Spin mixing and π junctions	82
6.4	Spin rotation and spin supercurrents	83
6.5	φ_0 junctions	85
6.6*	The superspin Hall effect	89
7	Outlook	93
	Bibliography	95
	Enclosed papers	167

* Entries marked with an asterisk denote sections that describe the main results of this thesis.

Preface

This thesis is submitted in partial fulfillment of the requirements for the degree philosophiae doctor at the Norwegian University of Science and Technology (NTNU), Trondheim, Norway. The research presented in the introductory chapters and the enclosed papers was conducted as part of the 3-year graduate program in physics, and was supervised by Profs. Jacob Linder and Arne Brataas. It was funded by the Research Council of Norway under grants 240806 and 262633.

In addition to the thesis, the graduate program includes 30 ECTS credits of coursework and an option for a 1-year extension under obligation of teaching duties at the Department of Physics. I have mainly taught in the undergraduate physics laboratory, where I have developed laboratory exercises and supervised students from the engineering programs.

Acknowledgements

I am indebted to many for their assistance and advice during my PhD.

For gentle supervision and interesting research problems, my supervisors Jacob Linder and Arne Brataas.

For good discussions, fun, and invaluable help, Jabir Ali Ouassou and Morten Amundsen, with whom I have shared an office.

For enjoyable travels and help navigating my first conferences, fellow group member Sol H. Jacobsen.

For a great place to work, everyone at the Center for Quantum Spintronics, with special mention to Atousa Ghanbari Birgani, Christoph Brüne, Jeroen Danon, Therese Frostad, Sverre A. Gulbrandsen, Henning G. Hugdal, Martin Fonnum Jakobsen, Øyvind Johansen, Lina G. Johnsen, Akashdeep Kamra, Fredrik Nicolai Krohg, Alireza Qaiumzadeh, Arnau Sala, Karen-Elisabeth Sødahl, and Roberto Troncoso.

For good collaborations and interesting ideas, my collaborators Mario Amado, Annica Black-Schaffer, Paramita Dutta, Timo Hyart, Graham Kimbell, Iryna Kulagina, Yang Li, Grzegorz Mazur, Lauren McKenzie-Sell, Jason W.A. Robinson, Asle Sudbø, Erlend G. Tveten, Thomas Wagner, and Jörg Wunderlich.

For a successful partnership during my teaching duties, Jon Andreas Støvneng and Randi Holmestad

For love, support, for everything, my wife Helene. I know that my working hours and our stay in Trondheim have strained your patience.



Publications

- I **V. Risinggård, J. Linder.**
Universal absence of Walker breakdown and linear current–velocity relation via spin–orbit torques in coupled and single domain wall motion.
Physical Review B **95**, 134423 (2017).
10/c2q9.
- II **Ø. Johansen*, V. Risinggård*, A. Sudbø, et al.**
Current control of magnetism in two-dimensional Fe₃GeTe₂.
Physical Review Letters **122**, 217203 (2019).
10/c6nz.
- III **V. Risinggård, E.G. Tveten, A. Brataas, J. Linder.**
Equations of motion and frequency dependence of magnon-induced domain wall motion.
Physical Review B **96**, 174441 (2017).
10/c2q8.
- IV **V. Risinggård*, I. Kulagina*, J. Linder.**
Electric field control of magnon-induced magnetization dynamics in multiferroics.
Scientific Reports **6**, 31800 (2016).
10/f8zhsc.
- v **Y. Li*, M. Amado*, T. Hyart, G.P. Mazur, V. Risinggård, et al.**
Competition between canted antiferromagnetic and spin-polarized quantum Hall states at $\nu = 0$ in graphene on a ferrimagnetic insulator.
arXiv: 1905.06866.

- VI J. Linder, M. Amundsen, V. Risinggård.**
Intrinsic superspin Hall current.
Physical Review B **96**, 094512 (2017).
10/gc5rm.
- VII V. Risinggård, J. Linder.**
Direct and inverse superspin Hall effect in two-dimensional systems: Electrical detection of spin supercurrents.
Physical Review B **99**, 174505 (2019).
10/c5qh.

* Authors marked with an asterisk contributed equally.

Errata

After the publication of paper VI on September 13, 2017, small but significant errors were discovered in the text and equations. Although the scientific conclusions remain unchanged, these errors affected the readability of the paper. The errors were announced in a Publisher's Note on May 3, 2018 (*Phys. Rev. B* **97**, 179901(E); 2018), and are corrected in the online version.

- The transpose has been removed in Eq. (4) as B_{ik}^\dagger is a row vector.
- A sentence has been inserted after Eq. (5), indicating that the matrices $\hat{\tau}_i$ that appear in Eq. (5) are the usual Pauli matrices ($i = 0, 1, 2, 3$, where $\hat{\tau}_0$ refers to the identity).
- A sentence has been inserted after Eq. (10), indicating that β is $\beta = 1/T$, where T is temperature.
- References to Fig. 1(a) in the captions of Fig. 2 and 4 have been changed to Fig. 1.
- In the discussion following Eq. (25) on page 5, the word “imaginary” has been changed to “real”.
- In the last paragraph of the same column, the word “real” has been changed to “imaginary”.
- On page 6, “band structure to” has been changed to “band structure due to”.

Introduction

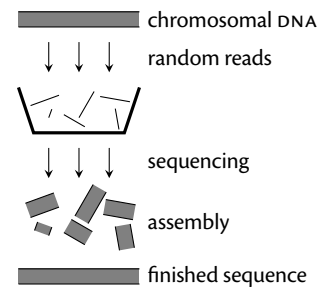
1.1 The computer and the human genome

The availability of large amounts of computing power is an *enabling technology* in the sense that it permits radical advances in unrelated derivative technologies. One example is the large amount of genetic information that has become available over the last two decades due to advances in DNA sequencing.

The joint announcement by the Human Genome Project and Celera Genomics in June 2000 of the first working draft of the entire sequence of the human genome [1–3] is undoubtedly one of the great achievements of modern biotechnology. Although the methods of the two partners differed in several aspects, they both relied at the most basic level on a sequencing technique known as *shotgun sequencing* [4]. Because sequencing long stretches of DNA remains a difficult task, shotgun sequencing proceeds by copying many short random fragments from the original string of DNA. Each of the fragments is then sequenced. By identifying overlaps between the fragments, they can be lined up to reveal the sequence of the original piece of, say, chromosomal DNA [5].

Each of these steps could in principle be performed by a human. However, in practice whole-genome sequencing is impossible without assistance from computers. In this and countless other ways the rapid increase in computing power over the last half century has a daily impact on our lives.

Shotgun sequencing:



1.2 Exaflops, zetabytes, and Moore's law

Unlike previous enabling technologies such as the printing press or the steam engine, electronic computers based on integrated circuits have pulled off an exponential increase in performance. Consequently, they have spawned several waves of derivative technologies based on, for instance, the personal computer, internet, and big data.

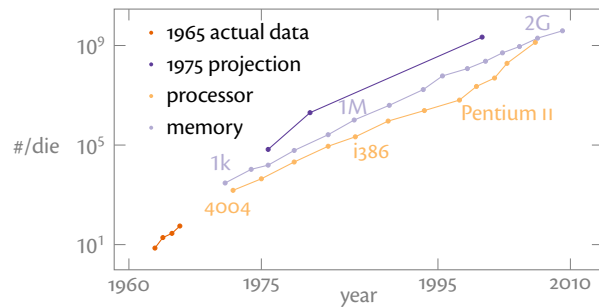
The exponential increase in computing power that we have seen over the last five decades comes down to larger and larger numbers of transistors working at a faster and faster pace. Gordon Moore, then director of research and development at Fairchild Semiconductor, predicted in 1965 that the number of components in an integrated circuit would double every year for the next decade [6]. In 1975, he revised his estimate, forecasting a doubling of components every two years [7]. This trend became known as *Moore's law*, see Fig. 1.1.

The reduction in transistor size has also allowed for an increase in operation frequency at the same power density because of the reduced capacitance and reduction in threshold voltage. So-called *Denard scaling* [8, 9] thus gave an effective doubling of computing power every 18 months. At the same time, it provided an opportunity to avoid the *heat problem*—that

Transistors are the basic building blocks of modern electronics. They function as amplifiers and switches.

Simply put, the reduction in gate capacitance reduces the time it takes to charge the gate and switch the transistor.

Figure 1.1 Moore's law predicts an exponential increase in components per die. Over the last five decades both processors and memory chips have roughly upheld Moore's 1975 prediction. Redrawn after Ref. 7.



is, the problem of removing from the chip all the heat dissipated by its integrated components.

Dennard scaling broke down in the early 2000s [10], bringing an end to increasing clock frequencies. The heat problem—initially dismissed by Moore—is now putting an end to Moore’s law itself [11, 12]. This gives reason to be concerned, not only because it heralds the end of a golden age for the semiconductor industry, but more importantly because a stagnation in computing power spells the end of the unlimited growth of derivative technologies.

Not only does the breakdown of Moore’s law challenge a continued increase in computing power. All that heat that threatens to melt the chips also represents energy that must be supplied. To reach the next step in computing power, so-called exascale computing, would require a power consumption of hundreds of megawatts. This is 10–30 times more than the worlds fastest supercomputers consume today [13]. The world’s information and communication technology already accounts for an appreciable amount of the global electricity demand [14]. Hence, developing energy-efficient computing technologies is not only a matter of technological development, but also an economical and environmental issue.

To keep up the increase in computing power, chip manufacturers today try to circumvent the heat problem by keeping part of the chip ‘dark’ at any time—with an obvious cost in CPU performance—and by dividing the load over multiple parallel cores. Yet these tricks can only take us so far. Although computer performance can still be improved by a factor of 10^5 before we reach the Landauer limit [17–19], it is becoming increasingly clear that traditional semiconductor technology cannot take us all the way there. Several candidate technologies have been proposed to replace or complement traditional CMOS technology [15, 16]. In this thesis, we will focus mainly on spin-based technologies, so-called *spintronics* [20–22].

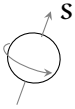
China’s Sunway TaihuLight clocks in at 93 pflops and 15 MW [13].

	%
Consumer devices	4.4
Networks	2.3
Production of ICT	2.2
Data centers	1.6
% of global demand	10.5

Other well-known candidate technologies include optical interconnects, integration with III–IV semiconductors, three-dimensional integration, beyond-Boltzmann transistors, memory-in-logic architectures, superconducting computers, carbon electronics, and memristors [15, 16].

1.3 Spintronics

A useful classical analogy to the electron spin is a spinning charged sphere. A circulating charge gives rise



to a magnetic moment, which explains the connection

between spin and magnetism. However, this analogy should not be taken literally. To achieve an angular momentum of $\hbar/2$ the equatorial velocity of a “classical electron” would have to be larger than the speed of light! (See Ref. 23.)

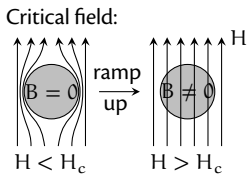
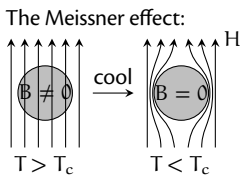
Spin is a fundamental property of the electron, just like mass or charge. The charge e of the electron gives rise to electrical phenomena, like lightning or household electricity. The spin $\hbar/2$, on the other hand, gives rise to magnetism, such as in fridge magnets or compass needles.

A magnet that points either ‘up’ or ‘down’ can be used to store a bit of information (‘0’ or ‘1’). Examples of such magnetic memories include magnetic tape recorders, hard drives, and magnetic random-access memories (MRAM) [24, 25]. To read and write the magnetic memory the direction of the magnetization must be addressed electrically. *Magnetoresistance*, whereby changing the magnetization changes the material’s electrical resistivity [26], has long been used as an efficient way to read magnetic memories [24].

The memory is written using magnetic fields [24]. The magnetic field is created by passing a current through a wire or coil in, say, the write head of the hard disk. However, because of the resistance in the wires, passing a large current implies a large energy expenditure. Magnetic-field-based solutions are also poorly scalable [27].

Better scalability and energy efficiency can be obtained by sending the current through the magnetic bit itself [28]. As we will see in Chap. 3, spin transferred from the current can act with a torque on the magnetization, thereby rotating the magnetization from ‘up’ (‘0’) to ‘down’ (‘1’) or *vice versa*. Several manufacturers have already commercialized MRAMs based on such *spin-transfer torques* (STT-MRAM) [29–31].

An inherent limitation of this technology is that each conduction electron can transfer no more than \hbar angular momentum to the magnetization. This limit can be circumvented using so-called *spin-orbit torques* [32]. As we will see in Chap. 3, the properties of heavy metals such as platinum makes it possible for each electron to transfer its angular momentum multiple times, thereby achieving the same torque with a smaller applied cur-



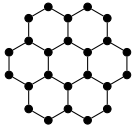
to be mutually incompatible phenomena [52, 53]. Not only do superconductors expel magnetic fields (known as the *Meissner effect* [44]), but large magnetic fields destroy superconductivity and push the superconductor over the phase boundary into the normal state [45–48].

At the microscopic scale, the story is different. Superconductivity is an intrinsically quantum-mechanical phenomenon. On a phenomenological level, the superconducting material can be described by a wave function [54]. When the superconductor is placed next to another material, the evanescent tail of this wave function will reach into the other material and endow it with superconducting properties. As we will see in Chap. 6, this *proximity effect* [55–60] can give rise to new forms of superconductivity at the interface with properties that are different from those of either bulk material [61–63]. *Superconducting spintronics* aims to harness such exotic forms of superconductivity to obtain new device functionality [64]. In papers VI and VII we consider one such effect, namely the *superspin Hall effect*.

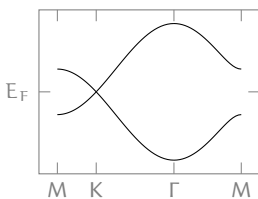
1.5 Two-dimensional materials

Graphene:

A honeycomb of carbon atoms.



Dispersion of the graphene π electrons:



Graphene is a sheet of graphite, only one atomic layer thick. The isolation of graphene in 2004 [65–67] marked the start of the exploration of two-dimensional crystalline materials. By exfoliation from bulk crystals, or otherwise by chemical vapor deposition (CVD) or similar techniques, dozens of two-dimensional crystals have been produced [68].

Graphene has a linear dispersion close to the Fermi level [69, 70]. Consequently, low-energy quasiparticles behave similarly to massless electrons or holes (also known as *massless Dirac fermions*). Other two-dimensional crystals exhibit similarly exciting properties, such as superconductivity, semiconductivity, insulating behavior, large spin–orbit coupling, ferroelectricity, and magnetism [68, 71, 72]. A unique feature of the two-dimensional crystals is that their Fermi level can be shifted a rel-

atively large amount by gating, which makes their properties electrically tunable. This makes it interesting to incorporate these materials in devices by combining them with three-dimensional materials or by stacking two-dimensional crystals to form a so-called van der Waals heterostructure [68, 71].

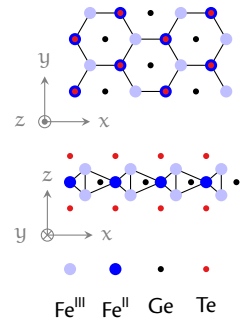
Two-dimensional magnetic materials were discovered only in 2016 [72]. In paper II we consider spin-orbit torques in one such material, Fe_3GeTe_2 . Before the discovery of two-dimensional magnets, attempts were made at making magnetic graphene [74]. These efforts include vacancies, adatoms, and nanoribbon edges. In paper V we consider a fourth approach, namely the *magnetic proximity effect* [75]. A disadvantage of introducing vacancies or adatoms to graphene is that it degrades the interesting electronic properties. Proximitizing graphene to a magnetic insulator has the advantage that most of the transport properties of graphene remain unchanged.

The discovery of other two-dimensional magnets has made magnetic graphene less technologically relevant. Magnetic graphene is, however, still an interesting material. As a magnet it is unusual because it has no d or f electrons. An applied magnetic field can induce dissipationless, spin-polarized edge states (paper V), and it could possibly realize the quantum anomalous Hall effect, the quantum spin Hall effect, and the quantum valley Hall effect [76].



In the following chapters I will present some of the most important concepts for understanding papers I–VII. The main results of the papers are described in the sections marked with an asterisk in the table of contents.

Crystal structure of Fe_3GeTe_2 :



Redrawn after Ref. 73.

Magnetism

2.1 Classifying magnetic materials

The susceptibility χ of a material to be magnetized by an applied magnetic field \mathbf{H} can be defined as

$$\chi = \left(\frac{\partial M}{\partial H} \right)_T, \quad (2.1)$$

where M is the magnetization, H is the magnitude of the applied field, and the parentheses indicate that the derivative is taken at constant temperature. This simplified expression assumes that the magnetization \mathbf{M} is parallel to the applied magnetic field \mathbf{H} . As we will see later in this chapter, this is not always the case for finite-sized or crystalline samples.

The susceptibility is a dimensionless material parameter. For magnetic applications, it has proven useful to classify materials according to the sign and magnitude of their magnetic susceptibility.

A negative magnetic susceptibility ($\chi < 0$) means that the induced magnetization points in the opposite direction of the applied magnetic field. Consequently, the magnetic flux density $\mathbf{B} = \mu_0(\mathbf{H} + \mathbf{M})$ inside the material is smaller than its vacuum value $\mathbf{B} = \mu_0\mathbf{H}$. (Here, μ_0 is the magnetic permeability of vacuum $\mu_0 = 4\pi \cdot 10^{-7} \text{ T}/(\text{A/m})$.) Materials with a negative susceptibility are known as *diamagnets*. Although many common materials exhibit a diamagnetic response, the response is typically quite weak. The exceptions to this rule are superconducting materials. Because of the Meissner effect, superconductors are perfect diamagnets ($\chi = -1$).

Some common diamagnets include [77]:

silver	$\chi = -2 \cdot 10^{-6}$
α -quartz	$-1 \cdot 10^{-6}$
graphite	$-1 \cdot 10^{-6}$
copper	$-8 \cdot 10^{-7}$
water	$-7 \cdot 10^{-7}$

Some common paramagnets include [77]:

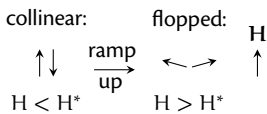
manganese	$\chi = 7 \cdot 10^{-5}$
platinum	$2 \cdot 10^{-5}$
aluminum	$2 \cdot 10^{-6}$
sodium	$7 \cdot 10^{-7}$

The formation of *flux-closure domains* may produce a ferromagnet with zero net magnetization:



Yet another type of order is *ferrimagnetism*. Ferrimagnets are antiferromagnets in which magnetic dipoles of different magnitude partially cancel.

Spin-flop transition:



A small and positive magnetic susceptibility ($\chi \gtrsim 0$) means that the induced magnetization adds to the applied magnetic field, producing a larger magnetic flux density inside than outside the material. Materials with small positive susceptibilities are known as *paramagnets*. A paramagnetic response indicates that the applied field aligns thermally disordered magnetic dipoles in the material.

A large and positive magnetic susceptibility indicates that the material is *ferromagnetic*. Ferromagnetic materials exhibit a spontaneous magnetization M due to the alignment of magnetic dipoles in the material. Even so, the net magnetization of a ferromagnetic sample may be zero due to domain formation. Ferromagnetic materials are the subject of this chapter, and we will consider domain formation in Sect. 2.6.

The spontaneous alignment of magnetic dipoles in a ferromagnetic material is not the only possible magnetically ordered phase. In *antiferromagnetic* materials the magnetic moments of the material dipoles cancel each other on the level of the unit cell. Still, neutron scattering experiments show that these materials exhibit a high degree of order [78]. Evidence of a phase transition can also be seen in the specific heat and in the temperature dependence of the magnetic susceptibility. Yet, under the simple classification scheme we considered above, these materials would be classified as paramagnets.

However, whereas the induced magnetization of a paramagnet saturates smoothly at large applied magnetic fields, antiferromagnets are prone to exhibit discontinuous magnetization curves. One particular example is the *spin-flop transition* of a collinear antiferromagnet [26]. In a collinear antiferromagnet the microscopic magnetic dipoles are oriented antiparallel to each other. If a magnetic field is applied parallel to this axis, the induced magnetization will initially be very small. However, at some critical field H^* the antiferromagnet will *flop*, orienting the microscopic dipoles almost perpendicular to the applied field. In this way the material can satisfy its preference for an almost antiparallel arrangement of dipoles *and* lower its energy by partially aligning the dipoles with the magnetic field.

2.2 Magnetism is quantum

The magnetic susceptibility is a well-defined quantity in classical electromagnetism. However, catastrophe strikes when we attempt to calculate the magnetization of a classical system microscopically [79]. Consider a collection of charged particles. This could be the conduction electrons of a metal, say, or a gas of ionized atoms. We apply a magnetic field $\mathbf{H} = \nabla \times \mathbf{A}/\mu_0$ to this system and calculate the resulting magnetization. (\mathbf{A} is the magnetic vector potential.)

Biot–Savart’s law gives the magnetic field from a collection of charges as

$$\mathbf{B}(\mathbf{r}) = \sum_i \frac{\mu_0}{4\pi} \frac{q_i \mathbf{v}_i \times \mathbf{r}'}{r'^3}, \quad (2.2)$$

where $\mathbf{r}' = \mathbf{r} - \mathbf{r}_i$, \mathbf{r}_i is the position of charge i , \mathbf{v}_i is the velocity of charge i , and q_i is the charge of charge i . The velocities of the particles are distributed according to the Maxwell–Boltzmann thermal distribution. It gives the probability of finding particle n at position \mathbf{r}_n with momentum \mathbf{p}_n as

$$dP = \exp[-\beta \mathcal{H}(\mathbf{p}_1, \dots, \mathbf{p}_N, \mathbf{r}_1, \dots, \mathbf{r}_N)] d\mathbf{p}_1 \cdots d\mathbf{p}_N d\mathbf{r}_1 \cdots d\mathbf{r}_N, \quad (2.3)$$

where $\beta = 1/k_B T$, k_B is Boltzmann’s constant, and T is temperature. \mathcal{H} is the Hamiltonian of the system,

$$\mathcal{H} = \sum_i \frac{(\mathbf{p}_i - q_i \mathbf{A})^2}{2m_i} + q_i \varphi + V, \quad (2.4)$$

where φ is the scalar potential and V is, say, the crystal potential.

If we now attempt to calculate the thermally averaged magnetic field,

$$\langle \mathbf{B} \rangle = \frac{1}{Z} \int dP \mathbf{B}, \quad Z = \int dP, \quad (2.5)$$

we discover that, because $\mathbf{B}_i(\mathbf{r})$ from Eq. (2.2) is odd in momentum, the net field is zero. Classical systems are not magnetized by an applied field—their magnetic susceptibility is identically zero, $\chi = 0$.

This important theorem in classical statistical mechanics is called the *Bohr–van Leeuwen theorem* [79, 80]. Independently discovered by N. Bohr and J. H. van Leeuwen in 1911 and 1919, it became widely known only after J. H. Van Vleck promoted it [81].

Consequently, we must turn to quantum mechanics to explain diamagnetism, paramagnetism, ferromagnetism, and all the other magnetic orders. Our classical calculation fails at two counts in explaining ferromagnetism in particular. First, it fails to account for the quantum-mechanical spin of electrons and other fundamental particles. The spin contributes with a magnetic dipole moment that is independent of the orbital moment. Second, it fails to account for the interaction that allows the spins in a ferromagnet to spontaneously align. Magnetostatic dipole–dipole interactions are much too weak ($\sim 10^{-2}$ meV) to provide the experimentally observed transition temperatures ($\sim 10^1$ meV).

2.3 Exchange interactions

To illustrate how quantum mechanics can give rise to spin interactions, we consider the hydrogen molecule, H_2 . The hydrogen molecule consists of two electrons and two protons. The Hamiltonian of the electrons is

$$\mathcal{H} = \mathcal{H}_a + \mathcal{H}_b + V_{ab}, \quad (2.6)$$

with

$$\mathcal{H}_i = -\frac{\hbar^2}{2m} \nabla_i^2 - \frac{e^2}{4\pi\epsilon_0} \left(\frac{1}{|\mathbf{r}_i - \mathbf{R}_1|} + \frac{1}{|\mathbf{r}_i - \mathbf{R}_2|} \right),$$

$$V_{ab} = \frac{e^2}{4\pi\epsilon_0} \frac{1}{|\mathbf{r}_a - \mathbf{r}_b|}.$$

Here, e is the electron charge, m is the electron mass, ϵ_0 is the permittivity of vacuum, \mathbf{r}_i is the position of electron i , and \mathbf{R}_j is the position of proton j .

To find the exact solution of this Hamiltonian is very hard, but the properties of the exact solution can be captured using the variational method [87]. As a trial wave function we choose a linear combination of the $1s$ states of the hydrogen atom,

$$\psi(\mathbf{r}_a, \mathbf{r}_b) = \alpha\varphi_1(\mathbf{r}_a)\varphi_2(\mathbf{r}_b) + \beta\varphi_2(\mathbf{r}_a)\varphi_1(\mathbf{r}_b), \quad (2.7)$$

The hydrogen molecule was first treated by Refs. 82 and 83. It is also treated in many books. Two particularly readable treatments are those by Refs. 84 and 85. A nontechnical treatment can be found in Ref. 86.

Quantum chemists call this *linear combination of atomic orbitals*, or LCAO for short [88].

where, φ_1 is the 1s state of proton 1 and φ_2 is the 1s state of proton 2. By combining states where the electrons reside at different atoms, we avoid the large on-site repulsion that comes with having two electrons in the same orbital. The energy E of this state is

$$E = \frac{\int d\mathbf{r}_a d\mathbf{r}_b \psi^* \mathcal{H} \psi}{\int d\mathbf{r}_a d\mathbf{r}_b \psi^* \psi}. \quad (2.8)$$

We calculate the normalization integral first,

$$\int d\mathbf{r}_a d\mathbf{r}_b \psi^* \psi = \alpha^2 + \beta^2 + 2\alpha\beta\lambda^2,$$

where λ is the overlap integral, $\lambda = \int d\mathbf{r} \varphi_1^*(\mathbf{r}) \varphi_2(\mathbf{r}) = \lambda^*$. Second, the energy expectation value is

$$\int d\mathbf{r}_a d\mathbf{r}_b \psi^* \mathcal{H} \psi = (E_1 + E_2) \int d\mathbf{r}_a d\mathbf{r}_b \psi^* \psi + \int d\mathbf{r}_a d\mathbf{r}_b \psi^* V_{ab} \psi.$$

Here, we assumed that $|\mathbf{r}_i - \mathbf{R}_2| \gg |\mathbf{r}_i - \mathbf{R}_1|$ for $\varphi_1(\mathbf{r}_i)$ and *vice versa*, which gives $\mathcal{H}_i \psi_j = E_j \psi_j$. Since φ_1 and φ_2 are both 1s states, $E_1 = E_2 = \epsilon$. The expectation value of the Coulomb interaction is

$$\int d\mathbf{r}_a d\mathbf{r}_b \psi^* V_{ab} \psi = (\alpha^2 + \beta^2)U + 2\alpha\beta W$$

with

$$U = \int d\mathbf{r}_a d\mathbf{r}_b V_{ab} |\psi_1(\mathbf{r}_a)|^2 |\psi_2(\mathbf{r}_b)|^2, \\ W = \int d\mathbf{r}_a d\mathbf{r}_b V_{ab} \psi_1^*(\mathbf{r}_a) \psi_2(\mathbf{r}_a) \psi_2^*(\mathbf{r}_b) \psi_1(\mathbf{r}_b). \quad (2.9)$$

U and W are both real. W is known as the *exchange term* because it exchanges electron a and b . Assembling all this we have

$$(E - 2\epsilon)(\alpha^2 + \beta^2 + 2\alpha\beta\lambda^2) = (\alpha^2 + \beta^2)U + 2\alpha\beta W. \quad (2.10)$$

To find the values of α and β which makes E minimal, we differentiate with respect to α and β , and set the derivatives equal to zero. The result is a set of two linear equations. Writing them on matrix form we find

$$\left[\begin{pmatrix} U & W \\ W & U \end{pmatrix} + (2\epsilon - E) \begin{pmatrix} 1 & \lambda^2 \\ \lambda^2 & 1 \end{pmatrix} \right] \begin{pmatrix} \alpha \\ \beta \end{pmatrix} = 0$$

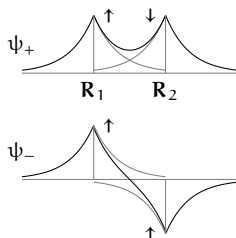
This homogeneous set of equations has a solution only if the determinant vanishes. That condition gives us an equation for E , which has the solutions

$$E_{\pm} = 2\epsilon + \frac{U \pm W}{1 \pm \lambda^2}. \quad (2.11)$$

Substituting each of these energies back into the matrix, we find the solutions $(\alpha_{\pm}, \beta_{\pm}) = (1, \pm 1)/\sqrt{2}$, which correspond to the wave functions

$$\psi_{\pm} = \sqrt{\frac{1}{2}} [\varphi_1(\mathbf{r}_a)\varphi_2(\mathbf{r}_b) \pm \varphi_2(\mathbf{r}_a)\varphi_1(\mathbf{r}_b)]. \quad (2.12)$$

The spatially symmetric and antisymmetric wave functions of the H_2 molecule:



The wave function ψ_+ is symmetric under particle interchange and the wave function ψ_- is antisymmetric under particle interchange. However, the Pauli principle requires the total wave function to be antisymmetric. Consequently, the spin part of ψ_+ must be the singlet state, and the spin part of ψ_- must be one of the triplet states. The integrals U and W have been evaluated and W is negative, $W < 0$ [84]. The energy is therefore minimized by the spatially symmetric wave function, ψ_+ . Hence, the spins are in the singlet state.

This effective spin interaction originates ultimately in the Pauli exclusion principle and the Coulomb interaction. The electrostatic repulsion between the electrons connects the two $1s$ states—they are no longer stationary states. The electrons can gain *kinetic* energy by hopping between the states, but due to the Pauli principle that is only possible as long as they do not have the same spin. This favors an ‘antiferromagnetic’ state [89].

We can see this more clearly by writing out the exchange interaction in creation and annihilation operators. The ‘exchange operator’ is

$$\begin{aligned}
 V &= \frac{1}{2} \sum_{\mu \neq \nu} \sum_{\sigma_1, \sigma_2} \int d\mathbf{r}_a d\mathbf{r}_b \varphi_{\mu}^*(\mathbf{r}_a) \varphi_{\nu}^*(\mathbf{r}_b) V_{ab} \varphi_{\mu}(\mathbf{r}_b) \varphi_{\nu}(\mathbf{r}_a) \\
 &\quad \times c_{\mu, \sigma_1}^{\dagger} c_{\nu, \sigma_2}^{\dagger} c_{\mu, \sigma_2} c_{\nu, \sigma_1} \\
 &= -W \sum_{\substack{\sigma_1, \sigma_2 \\ \mu \neq \nu}} c_{\mu, \sigma_1}^{\dagger} c_{\mu, \sigma_2} c_{\nu, \sigma_2}^{\dagger} c_{\nu, \sigma_1},
 \end{aligned}$$

where μ and ν run over $\mu, \nu = 1, 2$ and σ_i runs over $\sigma_i = \uparrow, \downarrow$. Performing the sum over spins we obtain

$$V = -W \sum_{\mu \neq \nu} \left(\frac{1}{2} n_{\mu} n_{\nu} + 2 \mathbf{S}_{\mu} \cdot \mathbf{S}_{\nu} \right), \quad (2.13)$$

using $\mathbf{S}_{\mu} = \frac{1}{2} \sum_{\gamma, \eta} \sigma_{\gamma \eta} c_{\mu, \gamma}^{\dagger} c_{\mu, \eta}$ and $\mathbf{S}_{\mu} \cdot \mathbf{S}_{\nu} = S_{\mu}^z S_{\nu}^z + \frac{1}{2} (S_{\mu}^+ S_{\nu}^- + S_{\mu}^- S_{\nu}^+)$, where $S_{\mu}^{\pm} = S_{\mu}^x \pm i S_{\mu}^y$ and σ is the vector of Pauli matrices. Since $W < 0$, the classical state that minimizes the expectation value of this operator is that the spins point in opposite direction—that is, an ‘antiferromagnetic’ spin coupling.

There is no such simple two-electron model that illustrates a ground-state ‘ferromagnetic’ coupling between the electrons. In fact, it can be proven that the ground state of a two-electron system is *always* the spin singlet state [79]. However, ferromagnetic exchange is possible in the ground state of systems with three or more electrons. As a rule of thumb, ferromagnetism is usually the result of many-particle physics. When ferromagnetic exchange does occur, the resulting symmetric spin state is accompanied by an antisymmetric orbital state. That maximizes the average distance between the electrons, thus minimizing their Coulomb repulsion. Ferromagnetism is therefore often the result of minimizing the system’s potential energy [89].

Heisenberg was the first to suggest that ferromagnetism could be understood in terms of minimizing the electrons’ electrostatic repulsion [90, 91]. Whereas Heisenberg’s intuition was—in this case—guided by his earlier studies of the *ortho* and *para* states of helium, this explanation also makes sense in light of our discussion of H_2 . In the spin-triplet state, the spatial part of the two-electron wave function is ψ_{-} . This wave function has a node at $|\mathbf{r}_a - \mathbf{r}_b| = 0$, where the electrostatic repulsion is maximal.

2.4 Spin-wave theory

In Eq. (2.13) we saw that the exchange interaction can be expressed as a dot product of spins. We can use this as a phenomenological model for exchange in many-electron systems. This is known as the *Heisenberg model* [89, 90]. On a lattice with only nearest-neighbor interactions, the Heisenberg model takes the form

$$\mathcal{H} = J \sum_{\langle i,j \rangle} \mathbf{S}_i \cdot \mathbf{S}_j, \quad (2.14)$$

where the angle brackets indicate that we sum over each nearest-neighbor pair once. For $J < 0$ the spin–spin interaction is ferromagnetic.

In the classical ground state of this model, all spins are aligned in the same direction. This is also the quantum-mechanical ground state. To see this, we rewrite the Heisenberg Hamiltonian as

$$\mathcal{H} = J \sum_{\langle i,j \rangle} \left[\frac{1}{2} (S_i^+ S_j^- + S_i^- S_j^+) + S_i^z S_j^z \right]. \quad (2.15)$$

Applying this Hamiltonian to a state where all spins are aligned, the first two terms give zero because the z components of spins i and j are already maximal and cannot be increased further by S_i^+ and S_j^+ . The last term gives $E = JS^2 N n / 2$, where S is the spin at each site, N is the total number of lattice sites, and n is the number of nearest neighbors at each site. Consequently, the classical ground state is a quantum-mechanical eigenstate. Since $E = JS^2 N n / 2$ is the smallest energy possible, it is also the ground state.

To study the eigenexcitations and the spectrum of the Heisenberg Hamiltonian, we need to diagonalize it. For that we use the Holstein–Primakoff representation [92],

$$S_i^+ = \sqrt{2S - a_i^\dagger a_i} a_i, \quad S_i^- = a_i^\dagger \sqrt{2S - a_i^\dagger a_i}, \quad S_i^z = S - a_i^\dagger a_i, \quad (2.16)$$

where the a -operators fulfill bosonic commutation relations. In the ground state, $\langle a_i^\dagger a_i \rangle = 0$, and all the spins point in the z direction. Thus the

Holstein–Primakoff representation singles out the z direction as the orientation of the magnet in the ground state. However, the Heisenberg Hamiltonian itself has global spin-rotation symmetry (the generator of global spin rotations, $\mathbf{S}_{\text{tot}} \cdot \mathbf{n}$, commutes with the Hamiltonian). Hence, the ground state breaks the symmetry of the Hamiltonian. This is known as *spontaneous symmetry breaking* [89].

For large spins S we can expand the square roots in the Holstein–Primakoff representation in $1/S$. Truncating the expansion at zeroth order gives the approximate relations

$$S_i^+ \approx \sqrt{2S} a_i, \quad S_i^- \approx \sqrt{2S} a_i^\dagger, \quad S_i^z = S - a_i^\dagger a_i. \quad (2.17)$$

Substituting these relations into the Hamiltonian and keeping only bilinear terms we obtain

$$\mathcal{H} = JS^2 N n + JS \sum_{\langle i,j \rangle} (a_j^\dagger a_i + a_i^\dagger a_j - a_i^\dagger a_i - a_j^\dagger a_j).$$

This Hamiltonian is still not diagonal, but it can be diagonalized by a Fourier transformation,

$$a_i = \sqrt{\frac{1}{N}} \sum_{\mathbf{k}} a_{\mathbf{k}} e^{+i\mathbf{k} \cdot \mathbf{r}_i}, \quad a_i^\dagger = \sqrt{\frac{1}{N}} \sum_{\mathbf{k}} a_{\mathbf{k}}^\dagger e^{-i\mathbf{k} \cdot \mathbf{r}_i}. \quad (2.18)$$

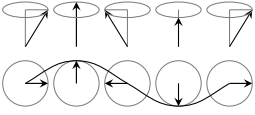
The resulting Hamiltonian is

$$\begin{aligned} \mathcal{H} &= E_0 + \sum_{\mathbf{k}} \omega_{\mathbf{k}} a_{\mathbf{k}}^\dagger a_{\mathbf{k}}, & (2.19) \\ \omega_{\mathbf{k}} &= -JS \sum_{\delta} (1 - \cos \mathbf{k} \cdot \delta), & E_0 = JS^2 N n, \end{aligned}$$

where δ is the nearest-neighbor vectors. (Thus for a square lattice we have $\delta = \pm \mathbf{e}_x, \pm \mathbf{e}_y$.)

The eigenexcitations of the Heisenberg Hamiltonian are known as *magnons*. As we will see in Chap. 4, their classical interpretation is spin

Spin waves:



waves— wave solutions to the magnetization's classical equation of motion. For small wave vectors, their spectrum is quadratic,

$$\omega_{\mathbf{k}} = -JSk^2. \quad (2.20)$$

The magnetization can be calculated as the thermal expectation value of the spin,

$$M = \frac{1}{N} \sum_i \langle S_i^z \rangle = \frac{1}{N} \sum_{\mathbf{k}} \langle S - a_{\mathbf{k}}^\dagger a_{\mathbf{k}} \rangle = S - \Delta M. \quad (2.21)$$

Since the magnons are noninteracting bosons, at least to bilinear order, the thermal expectation value of the number operator is the Bose–Einstein distribution function [93]

$$\langle a_{\mathbf{k}}^\dagger a_{\mathbf{k}} \rangle = \frac{1}{\exp(\beta\omega_{\mathbf{k}}) - 1}. \quad (2.22)$$

If we consider temperatures for which $|J|Sk^2 \gg k_B T$, we can use the $k \rightarrow 0$ limit of the magnon dispersion. That gives the thermal correction

$$\Delta M = \frac{1}{N} \left(\frac{L}{2\pi} \right)^3 \int d\mathbf{k} \frac{1}{\exp(\beta|J|Sk^2) - 1}$$

in the continuum limit. This integral diverges as $1/k$ for $k \rightarrow 0$ in one dimension and as $-\log k$ for $k \rightarrow 0$ in two dimensions [89]. Consequently, in one and two dimensions the Heisenberg ferromagnet is not ordered at finite temperatures. However, in three dimensions we can use the substitution $x = \beta|J|Sk^2$ to evaluate the integral as [94, 95]

$$\begin{aligned} \Delta M &= \frac{1}{2N} \left(\frac{L}{2\pi} \right)^3 \left(\frac{k_B T}{|J|S} \right)^{3/2} \int_0^{2\pi} d\varphi \int_0^\pi d\vartheta \sin \vartheta \int_0^\infty dx \frac{\sqrt{x}}{e^x - 1} \\ &= \frac{1}{4\pi^2} \frac{L^3}{N} \left(\frac{k_B T}{|J|S} \right)^{3/2} \Gamma\left(\frac{3}{2}\right) \zeta\left(\frac{3}{2}\right), \end{aligned} \quad (2.23)$$

This result is known as *Bloch's three-halves power law* [96].

where L^3 is the sample volume, Γ is the gamma function, $\Gamma(3/2) = \sqrt{\pi}/2$, and ζ is Riemann's zeta function, $\zeta(3/2) \approx 2.61$.

The divergence of ΔM in one and two dimensions is not incidental. In fact, the Hohenberg–Mermin–Wagner theorem states, under quite general conditions, that no continuous symmetry can be spontaneously broken in one or two dimensions at finite temperature [89, 97, 98]. Since the Heisenberg Hamiltonian has continuous $O(3)$ symmetry, this theorem prevents it from ordering at finite temperature in $d \leq 2$.

Nonetheless, truly two-dimensional magnetic materials exist [72]. Their existence depends on anisotropic terms in the magnetic Hamiltonian, such as

$$\mathcal{H} = J \sum_{\langle i,j \rangle} \mathbf{S}_i \cdot \mathbf{S}_j + D \sum_i (S_i^z)^2.$$

This Hamiltonian has only discrete $z \rightarrow -z$ symmetry, so the Hohenberg–Mermin–Wagner theorem does not apply.

2.5 Magnetic anisotropy

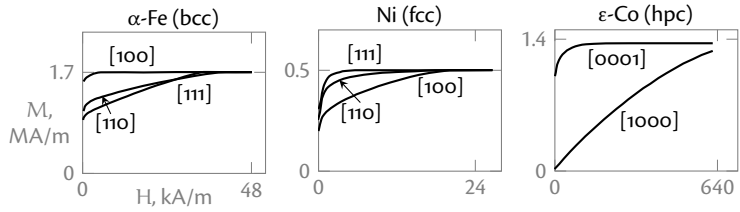
Whereas two-dimensional materials *require* anisotropic terms in the Hamiltonian to order magnetically, three-dimensional materials can do without them. Even so, most magnetic materials have an anisotropic magnetic susceptibility. As we will see in Sect. 2.6, magnetostatic dipole–dipole interactions can give rise to *shape anisotropies*, which depend on the shape of the magnetic sample. In this section, we consider *magnetocrystalline anisotropies*, which are due to the crystal lattice.

The magnetization curves of iron, nickel, and cobalt in Fig. 2.1 demonstrate that the magnetic susceptibility of these materials depends on the direction of the applied magnetic field with respect to the crystal lattice. The shapes of these curves can be understood by analyzing the symmetry of the crystal lattices.

The perhaps most famous model that orders magnetically in two-dimensions is the Ising model [99]. Onsager's exact solution of the two-dimensional Ising model has a phase transition at [100]

$$T_c = \frac{2J|S^2}{k_B \ln(1 + \sqrt{2})}.$$

Figure 2.1 Magnetization curves for single crystals of α -iron, nickel, and ϵ -cobalt. The easy axis of α -iron is $[100]$ and the hard axis is $[111]$. Redrawn after Refs. 101–103.



Although named for F. Neumann [104], this principle has perhaps been stated most eloquently by P. Curie [105]: *c'est la dissymétrie, qui crée le phénomène*. In terms of asymmetry Neumann's principle states that a property tensor cannot exhibit an asymmetry that is not present in the crystal. The lower the symmetry of the crystal, the more independent elements exist in the property tensors.

Any type of symmetry which is exhibited by the point group of the crystal is possessed by every physical property of the crystal. This is known as *Neumann's principle* [106]. Thus, to identify the magnetocrystalline anisotropies, we expand the magnetic energy density in the normalized magnetization components $m_i = M_i/M$, and identify the terms of the expansion that are invariant under the symmetries of the lattice. Because the energy must be time-reversal invariant, only even orders of the magnetization components can appear in the series expansion,

$$u = u_0 + \Lambda_{ij} m_i m_j + \Gamma_{ijkl} m_i m_j m_k m_l + \dots \quad (2.24)$$

(Summation over repeated indices is implied.) The magnetic energy density u is a scalar and is invariant under coordinate transformations. The magnetization m_i is an axial vector, and consequently Λ_{ij} and Γ_{ijkl} are polar tensors.

We consider α -iron as an example. The bcc lattice has point-group symmetry $m\bar{3}m$ (O_h). Any polar second-rank tensor that is invariant under the symmetry operations of $m\bar{3}m$ is proportional to the identity [106]:

$$\Lambda_{ii} = \Lambda_0; \quad \Lambda_{ij} = 0 \quad \forall i \neq j.$$

Consequently, the second-order term does not contribute to the magnetocrystalline anisotropy: $\Lambda_0(m_x^2 + m_y^2 + m_z^2) = \Lambda_0$. A polar fourth-rank tensor that is invariant under the symmetry operations of $m\bar{3}m$ has

21 nonzero components, but depends on only two independent parameters [106]:

$$\begin{aligned}\Gamma_{iiii} &= \Gamma_1, \\ \Gamma_{xxyy(6)} &= \Gamma_{xxzz(6)} = \Gamma_{yyzz(6)} = \Gamma_2, \\ \Gamma_{ijkl} &= 0 \text{ for all other } ijkl\end{aligned}$$

($xxyy(6)$ indicates the six tensor elements that are obtained by unrestricted permutation of the indices $xxyy$). Thus, the fourth-order terms evaluate to

$$\Gamma_1(m_x^4 + m_y^4 + m_z^4) + 6\Gamma_2(m_x^2 m_y^2 + m_x^2 m_z^2 + m_y^2 m_z^2).$$

Because we have normalized the magnetization vector to 1,

$$1 = (m_x^2 + m_y^2 + m_z^2)^2 = m_x^4 + m_y^4 + m_z^4 + 2(m_x^2 m_y^2 + m_x^2 m_z^2 + m_y^2 m_z^2),$$

these terms describe the same magnetocrystalline anisotropies,

$$\Gamma_1 + (6\Gamma_2 - 2\Gamma_1)(m_x^2 m_y^2 + m_x^2 m_z^2 + m_y^2 m_z^2).$$

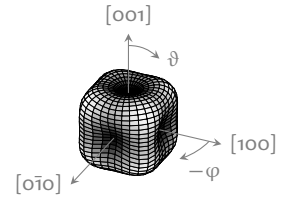
We conclude that the magnetic energy density can be written as

$$u = K_0 + K_1(m_x^2 m_y^2 + m_x^2 m_z^2 + m_y^2 m_z^2) + K_2 m_x^2 m_y^2 m_z^2 + \dots, \quad (2.25)$$

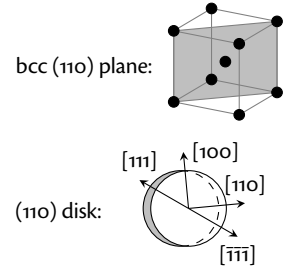
where $K_0 = u_0 + \Lambda_0 + \Gamma_1$, $K_1 = 6\Gamma_2 - 2\Gamma_1$, and the sixth-order term has been obtained in the same fashion as the fourth-order terms.

The coefficients K_1 and K_2 can be obtained by comparing this expression to experimental data. The plane of a circular disk with a (110) orientation contains all the three major symmetry directions of the bcc lattice ($[100]$, $[110]$, and $[1\bar{1}1]$). By applying a magnetic field of constant magnitude in the plane of this disk, we can map out a cut through the magnetization energy density at $\varphi = \pi/4$. The magnetization curve we

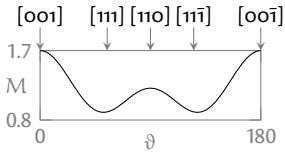
The magnetic energy density as a function of magnetization direction:



Redrawn after Ref. 85.



In-plane magnetization curve:



Redrawn after Ref. 85.

obtain is a representation of the negative of the magnetic energy density of the system: $u = -\mathbf{M} \cdot \mathbf{B}$. Its two minima correspond to the corners of the cube at $[111]$ and $[1\bar{1}\bar{1}]$, and its three maxima correspond to $[001]$, $[110]$, and $[00\bar{1}]$, respectively. Careful comparison of the experimental data and the theoretical prediction shows that the values of K_1 and K_2 are $K_1 = 48 \text{ kJ/m}^3$ and $K_2 = -10 \text{ kJ/m}^3$ [85].

The magnetization of a solid is (mostly) due to the spin magnetic moments. The presence of magnetocrystalline anisotropies must therefore be a result of a coupling between the spin-space and real-space properties. Such a coupling is known as *spin-orbit coupling*.

From the point of view of an atomic electron, the *nucleus* orbits around *it*. This circulating charge (the nucleus) generates a magnetic field. The electron will tend to align its spin along the field, thus coupling its spin to its orbital moment. We consider for simplicity the hydrogen atom. Using the Biot-Savart law, the magnetic field of the proton is

$$B = \frac{\mu_0 I}{2r},$$

where $I = e/T$ is the effective current and T is the period of the orbit. The field points along the angular momentum L of the electron, $L = r m v = 2\pi m r^2 / T$, so

$$\mathbf{B} = \frac{1}{4\pi\epsilon_0} \frac{e}{m c^2 r^3} \mathbf{L}, \quad (2.26)$$

The rest frame of the electron is not an inertial system—it accelerates. In Eq. (2.28) we have made the appropriate kinematic correction, known as the *Thomas precession*, which gives rise to an extra factor of $\frac{1}{2}$ [107, 108]

where $c = 1/\sqrt{(\epsilon_0 \mu_0)}$ is the velocity of light. The magnetic moment of the electron is

$$\boldsymbol{\mu}_e = -\frac{e}{m} \mathbf{S}. \quad (2.27)$$

Consequently, the spin-orbit interaction of the hydrogen atom is [87]

$$\mathcal{H} = \frac{e^2}{8\pi\epsilon_0} \frac{\mathbf{S} \cdot \mathbf{L}}{m^2 c^2 r^3}. \quad (2.28)$$

The atomic spin–orbit interaction couples the electron’s spin to its orbital moment—or, if you like, to the orientation of the atom. If, in addition, there is a preferred orientation of the atomic orbitals because of a low-symmetry crystal-field environment, the result is a magnetocrystalline anisotropy. As an example of this rule, we consider gadolinium (Gd) and terbium (Tb). Both crystallize in the hexagonal close-packed structure. The magnetic state of gadolinium, $4f^7$, is $\langle L_z \rangle = 0$, whereas that of terbium, $4f^8$, is $\langle L_z \rangle = 3$. This is reflected in their uniaxial anisotropy coefficients, which differ by two orders of magnitude at liquid helium temperatures, $K_{u1}(\text{Gd}) = -0.12 \text{ MJ/m}^3$ and $K_{u1}(\text{Tb}) = -57 \text{ MJ/m}^3$ [85].

2.6 Magnetostatics

As mentioned at the beginning of the previous section, the magnetostatic dipole–dipole interactions can also contribute to the anisotropy of a sample’s magnetic susceptibility. A magnetic dipole moment μ gives rise to a magnetic field \mathbf{B} . Far away from the magnetic dipole, this field can be written as [26]

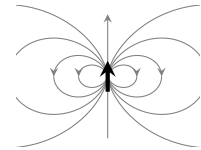
$$\mathbf{B}(\mathbf{r}) = \frac{\mu_0}{4\pi} \left(\frac{3(\boldsymbol{\mu} \cdot \mathbf{r})\mathbf{r}}{r^5} - \frac{\boldsymbol{\mu}}{r^3} \right). \quad (2.29)$$

The interaction energy of two magnetic dipoles that interact solely via their magnetic fields is thus

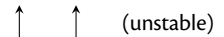
$$U = -\boldsymbol{\mu}_1 \cdot \mathbf{B}_2 - \boldsymbol{\mu}_2 \cdot \mathbf{B}_1 = \frac{\mu_0}{2\pi} \left(\frac{\boldsymbol{\mu}_1 \cdot \boldsymbol{\mu}_2}{r^3} - \frac{3(\boldsymbol{\mu}_1 \cdot \mathbf{r})(\boldsymbol{\mu}_2 \cdot \mathbf{r})}{r^5} \right).$$

Depending on the dipoles’ relative position and orientation, the interaction energy varies between $+(\mu_0/2\pi)(\mu_1\mu_2/r^3)$ in the unstable *up–up* state and $-(\mu_0/\pi)(\mu_1\mu_2/r^3)$ in the stable *head-to-tail* state. As we will see below, it is exactly this anisotropy that gives rise to the anisotropy of the dipole–dipole interactions’ contribution to the sample’s magnetic susceptibility.

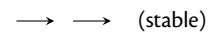
The dipole \mathbf{B} field:



up–up:



head-to-tail:



The dipole–dipole interactions in a ferromagnet—that is, an ensemble of magnetic dipoles—can be found by generalizing from the two-dipole case. The interaction energy is given by

$$\begin{aligned} U &= -\frac{1}{2} \sum_i \sum_{j \neq i} \boldsymbol{\mu}_i \cdot \mathbf{B}_{ij} \\ &= -\frac{1}{2} \sum_i \boldsymbol{\mu}_i \cdot \sum_{j \neq i} \frac{\mu_0}{4\pi} \left(\frac{3(\boldsymbol{\mu}_j \cdot \mathbf{r}_{ij})\mathbf{r}_{ij}}{r_{ij}^5} - \frac{\boldsymbol{\mu}_j}{r_{ij}^3} \right), \end{aligned} \quad (2.30)$$

where \mathbf{r}_{ij} is the vector from $\boldsymbol{\mu}_j$ to $\boldsymbol{\mu}_i$. In principle, we can evaluate this sum directly. This has in fact been done analytically for some particular lattices for arrays of equal and parallel dipoles [109]. However, for most practical purposes, evaluating the sum directly is impractical, even using numerical methods. As the size of the sample increases, the number of terms in the sum grows as r_{ij}^3 , but the summand falls off only as $1/r_{ij}^3$. Consequently, the contributions of distant dipoles never cease to be important. Since the interaction of each dipole with every other dipole must be taken into account, the computational complexity grows as N^2 , where N is the number of dipoles.

We can avoid evaluating the sum directly by considering the corresponding integral instead. In the continuum limit, we replace each dipole $\boldsymbol{\mu}_i$ with the dipole $\mathbf{M}(\mathbf{r}) d\mathbf{r}$, where $d\mathbf{r}$ is a volume element. The resulting dipole–dipole interaction reads

$$U = -\frac{1}{2} \int d\mathbf{r} \mathbf{M}(\mathbf{r}) \cdot \int d\mathbf{r}' \mathbf{B}(\mathbf{r}, \mathbf{r}'),$$

with

$$\mathbf{B}(\mathbf{r}, \mathbf{r}') = \frac{\mu_0}{4\pi} \left(\frac{3[\mathbf{M}(\mathbf{r}') \cdot (\mathbf{r} - \mathbf{r}')](\mathbf{r} - \mathbf{r}')}{|\mathbf{r} - \mathbf{r}'|^5} - \frac{\mathbf{M}(\mathbf{r}')}{|\mathbf{r} - \mathbf{r}'|^3} \right).$$

The integrals run over the sample volume. However, *we* run into trouble as soon as we try to evaluate them. The integral over $d\mathbf{r}'$ of the magnetic field

$\mathbf{B}(\mathbf{r}, \mathbf{r}')$ is well-defined only as long as we evaluate it at positions \mathbf{r} *outside* the magnet, but the integral of $\mathbf{M} \cdot \mathbf{B}$ runs over the magnet *itself*. Provided that none of the dipoles μ_j overlap with the dipole μ_i , this divergence is absent in Eq. (2.30). We introduced it upon taking the continuum limit.

Lorentz gave an argument to remove this divergence [110]. Since the divergence is absent in the sum, we separate the dipoles μ_j into two groups. For the dipoles inside a sphere of radius R around the dipole μ_i we evaluate the sum over $j \neq i$ directly, and for the dipoles outside the sphere we evaluate the integral over $d\mathbf{r}'$ instead,

$$\mathbf{B}_L(\mathbf{r}) = \int_{\Omega} d\mathbf{r}' \mathbf{B}(\mathbf{r}, \mathbf{r}') + \sum_{j \in \omega} \mathbf{B}_{ij}, \quad (2.31)$$

where ω is the volume of the Lorentz cavity and Ω is the volume of the sample minus ω . The radius R must be large compared to the lattice spacing, but small enough for the dipoles inside the sphere to be almost parallel.

We start by considering an equivalent form of the integral over $d\mathbf{r}'$. The \mathbf{B} field, the \mathbf{H} field, and the magnetization \mathbf{M} are related by the constitutive relation $\mathbf{B} = \mu_0(\mathbf{H} + \mathbf{M})$. Since \mathbf{B} is solenoidal, the divergence of \mathbf{H} is entirely due to \mathbf{M} :

$$\nabla \cdot \mathbf{H} = -\nabla \cdot \mathbf{M}.$$

Comparing this equation to Coulomb's law,

$$\nabla \cdot \mathbf{D} = \rho,$$

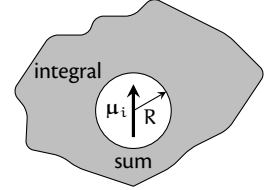
it is apparent that the divergence of the magnetization,

$$\rho_M = -\nabla \cdot \mathbf{M}, \quad (2.32)$$

can be interpreted as a magnetic charge ρ_M for \mathbf{H} . Furthermore, in the static limit and in the absence of currents \mathbf{H} is irrotational,

$$\nabla \times \mathbf{H} = \mathbf{J} + \frac{\partial \mathbf{D}}{\partial t} = 0. \quad (2.33)$$

The Lorentz cavity:



Redrawn after Ref. 26.

The characteristic length scale of magnetization variations due to dipolar interactions is the exchange length, $\ell = \sqrt{(A/\mu_0 M_s^2)}$. Here, A is the exchange stiffness and M_s is the saturation magnetization. Typical exchange lengths are $\ell = 3-9$ nm. Since typical lattice spacings a are on the order of ångströms, finding a radius $a \ll R < \ell$ is physically feasible.

Finding \mathbf{H} given the magnetic charge $\rho_M = -\nabla \cdot \mathbf{M}$ is therefore formally equivalent to the electrostatic problem of finding \mathbf{D} given the electric charge ρ . Using the existing formal solution for \mathbf{D} , we can thus write down \mathbf{H} as [111]

$$\mathbf{H}(\mathbf{r}) = -\frac{1}{4\pi} \int_{\Omega} d\mathbf{r}' \frac{[\nabla' \cdot \mathbf{M}(\mathbf{r}')](\mathbf{r} - \mathbf{r}')}{|\mathbf{r} - \mathbf{r}'|^3}. \quad (2.34)$$

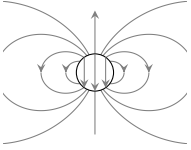
The \mathbf{H} and \mathbf{B} fields inside a uniformly magnetized sphere are

$$\mathbf{H} = -\frac{1}{3}\mathbf{M}, \quad \mathbf{B} = \frac{2}{3}\mathbf{M},$$

respectively [111]. The fields outside the sphere are those of a dipole of dipole moment

$$\boldsymbol{\mu} = \frac{4\pi R^3}{3}\mathbf{M}.$$

\mathbf{H} field:



The \mathbf{H} field is generated by the free surface poles, where

$$\nabla \cdot \mathbf{M} = \mathbf{M} \cdot \mathbf{e}_n \neq 0.$$

Consequently, the field inside a spherical hole in a uniformly magnetized body is

$$\mathbf{H} = \mathbf{M}/3.$$

This integral depends on the shape and the size of the sample. However, by dividing the integration volume into two pieces we can separate out a contribution that is independent of these particularities, namely that from a thin spherical shell around the Lorentz cavity. Since we assumed that the magnetization close to the Lorentz cavity is almost uniform, the contribution from this shell is $\mathbf{M}/3$. Hence, the integral over $d\mathbf{r}'$ evaluates to

$$\mathbf{H}(\mathbf{r}) = -\frac{1}{4\pi} \int_{\Omega'} d\mathbf{r}' \frac{[\nabla' \cdot \mathbf{M}(\mathbf{r}')](\mathbf{r} - \mathbf{r}')}{|\mathbf{r} - \mathbf{r}'|^3} + \frac{\mathbf{M}(\mathbf{r})}{3} = \mathbf{H}' + \frac{1}{3}\mathbf{M} \quad (2.35)$$

inside the Lorentz cavity. Here, Ω' denotes the volume remaining after separating out the thin spherical shell.

Next, we consider the sum over $j \neq i$ inside the Lorentz cavity. As it turns out, the sum vanishes for a cubic lattice [112]. This can be seen by noting that the x component of \mathbf{B}_{ij} is

$$\frac{\mu_0}{4\pi} \frac{3(\mu_x x_{ij}^2 + \mu_y y_{ij} x_{ij} + \mu_z z_{ij} x_{ij}) - \mu_x r_{ij}^2}{r_{ij}^5}.$$

In the sum over dipoles at a given distance r_{ij} from dipole i

$$\sum_j x_{ij} y_{ij} = \sum_j x_{ij} z_{ij} = \sum_j y_{ij} z_{ij} = 0$$

and

$$\sum_j x_{ij}^2 = \sum_j y_{ij}^2 = \sum_j z_{ij}^2 = \frac{1}{3} \sum_j r_{ij}^2$$

if the lattice is cubic. Consequently, the contribution from each such group of dipoles to B_{ij} vanishes. If the crystal is not cubic, B_{ij} does not vanish, however the resulting contribution to the dipole–dipole interaction is local and proportional to $\Lambda_{ij}m_i m_j$ and can be incorporated in the magnetocrystalline anisotropy [112].

We conclude that the dipole–dipole interaction energy for a cubic crystal is

$$U = -\frac{\mu_0}{2} \int d\mathbf{r} \mathbf{M} \cdot (\mathbf{H}' + \frac{1}{3}\mathbf{M}),$$

where the integral is taken over the magnet. The term $-(\mu_0/6)M^2(\Omega + \omega)$ is simply a constant, and is customarily ignored, giving

$$U = -\frac{\mu_0}{2} \int d\mathbf{r} \mathbf{M} \cdot \mathbf{H}'. \quad (2.36)$$

Using the constitutive relation $\mathbf{M} = \mathbf{B}/\mu_0 - \mathbf{H}$, and the fact that the integral of $\mathbf{B} \cdot \mathbf{H}$ over all of space vanishes [26, 112], this integral over the magnet can also be written on the form

$$U = \frac{\mu_0}{2} \int d\mathbf{r} H'^2, \quad (2.37)$$

where the integral is taken over all of space.

Written on this form, we observe that the dipole–dipole interaction energy is always positive, and attains its minimum value if $\nabla \cdot \mathbf{M} = 0$ so that \mathbf{H}' is zero. Left to its own devices, a ferromagnet with negligible magnetocrystalline anisotropy will therefore tend to divide into domains that reduce the net magnetization. The most favorable form of domains are so-called *flux-closure domains*, as pointed out at the beginning of this chapter.

We saw on the facing page that the magnetic field inside a uniformly magnetized sphere is $\mathbf{H} = -\mathbf{M}/3$. Since the magnetic field opposes the

Using $\mathbf{B} = \nabla \times \mathbf{A}$ the integral of $\mathbf{B} \cdot \mathbf{H}$ over space is

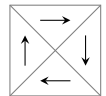
$$\int d\mathbf{r} \mathbf{B} \cdot \mathbf{H} = \int d\mathbf{r} [\nabla \cdot (\mathbf{A} \times \mathbf{H}) + \mathbf{A} \cdot (\nabla \times \mathbf{H})].$$

The second term is zero by Eq. (2.33), and by the divergence theorem the first term is

$$\int d^2r \mathbf{e}_n \cdot (\mathbf{A} \times \mathbf{H}).$$

The volume integral was taken over all of space, so the surface integral is over a sphere of infinite radius. Since \mathbf{A} and \mathbf{H} vanish as $A \sim r^{-2}$ and $H \sim r^{-3}$ far from the magnet, this term is also zero.

The formation of *flux-closure domains* may produce a ferromagnet with zero net magnetization:

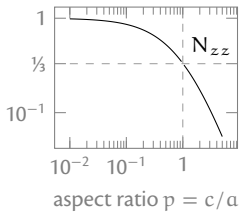


magnetization that creates it, it is often called the *demagnetization field*. It is true in general for all ellipsoids that are magnetized along one of their principal axes that the magnetic field inside the ellipsoid can be written as

$$H_i = -N_{ij}M_j,$$

where the demagnetization tensor N_{ij} is diagonal [85]. (Summation over repeated indices is implied.) The trace of the demagnetization tensor is equal to one, $N_{ii} = 1$. For ellipsoids of revolution, $N_{xx} = N_{yy}$, and [85]

Demagnetization factor N_{zz} :

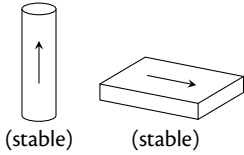


Redrawn after Ref. 26.

$$N_{zz} = \begin{cases} \frac{1}{1-p^2} \left(1 - \frac{p \arccos p}{\sqrt{1-p^2}} \right), & p < 1 \quad (\text{oblate}), \\ \frac{1}{p^2-1} \left(\frac{p \operatorname{arccosh} p}{\sqrt{p^2-1}} - 1 \right), & p > 1 \quad (\text{prolate}), \end{cases} \quad (2.38)$$

where $p = c/a$ is the aspect ratio of the semimajor axis c to the semiminor axis a . For a sphere, $p = 1$, we recover $N_{xx} = N_{yy} = N_{zz} = 1/3$.

Given a direction of the applied field with respect to the ellipsoid, the smaller the demagnetization factor (N_{xx} , N_{yy} , or N_{zz}), the smaller the demagnetization field. The smaller the demagnetization field, the easier it is to magnetize the ellipsoid. For instance, it is easier to magnetize a cylinder along its axis than perpendicular to it, or to magnetize a thin film in the plane than out of it. In other words, the dipole–dipole interaction gives rise to an anisotropic magnetic susceptibility that depends on the sample’s shape.



Samples that have shapes other than ellipsoids, and that have magnetizations that are not solenoidal ($\nabla \cdot \mathbf{M} \neq 0$) will in general have internal magnetic fields that are nonuniform. Still, it is common to define approximate demagnetization factors for such samples to get a rough idea of the demagnetization field. Such approximate demagnetization factors for right rectangular prisms are extensively used by codes such as OOMMF [113] and

MuMax3 [114] because it gives an analytical expression for the demagnetization field of each cell. Combined with FFT acceleration of the volume integral, this makes it possible for these codes to reduce the computational complexity of the dipole–dipole interaction from N^2 to $N \log N$ [115].

The dipole–dipole interactions do not only affect the static magnetization, but also its dynamics properties. For instance, Refs. 117 and 118 have shown that in the thin-film geometry, dipole–dipole interactions significantly alter the long-wavelength spin-wave dispersion relation. For large wave numbers (small wavelengths) the dispersion relation is still parabolic as in Eq. (2.20), however, for small wave numbers (large wavelengths) the dipole–dipole interactions introduce a minimum at $k \neq 0$. Exploiting this property of the thin-film dispersion and the boson nature of magnons, Refs. 119–121 have realized Bose–Einstein condensates of magnons.

2.7 Magnetization dynamics

The equation of motion for a free magnetic dipole can be obtained from Newton’s second law for rotation,

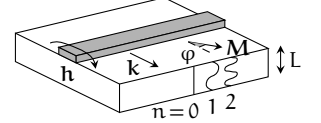
$$\frac{\partial \mathbf{J}}{\partial t} = \boldsymbol{\tau}, \quad (2.39)$$

where \mathbf{J} is the angular momentum and $\boldsymbol{\tau}$ is the torque. Substituting $\boldsymbol{\mu} = \gamma \mathbf{J}$ (where γ is the gyromagnetic ratio) and $\boldsymbol{\tau} = \boldsymbol{\mu} \times \mathbf{B}$ we obtain

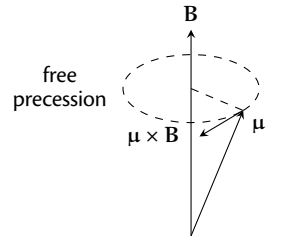
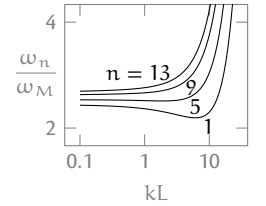
$$\frac{\partial \boldsymbol{\mu}}{\partial t} = \gamma \boldsymbol{\mu} \times \mathbf{B}. \quad (2.40)$$

Like a spinning top in a gravitational field, the magnetic dipole precesses about the magnetic field. If any form of dissipation is present, the free dipole will eventually align with the applied magnetic field to minimize its energy.

Magnetostatic spin waves are classified based on the angle φ between \mathbf{k} and \mathbf{M} [116]. Backward-volume waves have $\varphi = 0$ and Damon–Eshbach waves have $\varphi = \pi/2$.



Dispersion relation of backward-volume waves:



Magnetic dipoles in solids are not free, but are constrained by, for instance, exchange interactions, magnetocrystalline anisotropies, and dipole-dipole interactions. However, just as the free dipole, magnetic dipoles in a solid ($\mathbf{M} = \mu/V$) will minimize their energy $U = \int d\mathbf{r} u$ in equilibrium [122],

$$\int d\mathbf{r} \left(-\frac{\partial u}{\partial M_i} + \nabla \cdot \frac{\partial u}{\partial (\nabla M_i)} \right) \cdot \delta M_i = 0. \quad (2.41)$$

In SI units, the effective field has units of tesla. Nonetheless, it is customarily assigned to the symbol \mathbf{H} .

They do this by aligning with the *effective* field

$$\mathbf{H}_i = -\frac{\delta U}{\delta M_i} = -\frac{\partial u}{\partial M_i} + \nabla \cdot \frac{\partial u}{\partial (\nabla M_i)}. \quad (2.42)$$

Outside equilibrium (nonsteady state), the effective field will exert a torque $\boldsymbol{\tau} = \mathbf{M} \times \mathbf{H}$ on the magnetization. Using again $\mathbf{M} = \gamma \mathbf{J}/V$, this gives the equation of motion

$$\frac{\partial \mathbf{M}}{\partial t} = \gamma \mathbf{M} \times \mathbf{H}. \quad (2.43)$$

This equation of motion for the magnetization was first derived by Landau and Lifshitz [122].

Since the magnetization is usually dominated by the electron spins, the gyromagnetic ratio is usually negative, $\gamma < 0$.

The macroscopic dynamics of the magnetization is directly coupled to the microscopic thermal motion of spin waves (magnon–magnon scattering), and also to the conduction electrons (eddy currents, magnon–electron scattering) and phonons (magnetostriction, magnon–phonon scattering). By ways of coupling to these thermal baths, the macroscopic dynamics of the magnetization will be damped out and loose kinetic energy to random thermal motion. To derive the appropriate damping term in the magnetization’s equation of motion from first principles is generally quite challenging, although theories for magnetic damping [123, 124] have improved to the point where they have predictive power [125–127]

There exist damping mechanisms that are not captured by local Gilbert damping, such as radiative damping [129], exchange-mediated damping [130–133], and texture-induced damping [134, 135].

We can circumvent the problem of identifying the exact mechanism of energy loss by constructing a phenomenological damping term. The

most commonly used model is *Gilbert damping* [128]. Gilbert damping is *viscous damping*, in which the damping force is proportional to the rate of change of the magnetization, $\eta \partial \mathbf{M} / \partial t$. Here, η is an unknown, positive parameter. Such a damping force can be derived from the functional

$$R = \frac{1}{2} \eta \int dt \dot{\mathbf{M}} \cdot \dot{\mathbf{M}}, \quad (2.44)$$

The functional R is known as Rayleigh's dissipation function [136].

where the dot denotes a time derivative. This gives the Lagrange equations

$$\frac{d}{dt} \frac{\delta L}{\delta \dot{M}_i} - \frac{\delta L}{\delta M_i} + \frac{\delta R}{\delta \dot{M}_i} = 0. \quad (2.45)$$

The Lagrangian L is in general $L = T - U$. Since $\delta U / \delta \mathbf{M} = -\mathbf{H}$ and $\delta U / \delta \dot{\mathbf{M}} = 0$, the Lagrange equations can be written

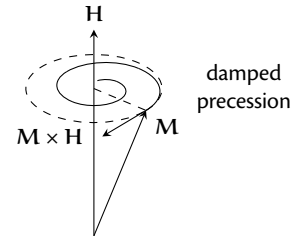
$$\frac{d}{dt} \frac{\delta T}{\delta \dot{\mathbf{M}}} - \frac{\delta T}{\delta \mathbf{M}} - [\mathbf{H} - \eta \dot{\mathbf{M}}] = 0.$$

The kinetic term $T = (M/\gamma)(1 \pm \cos \vartheta) \partial \varphi / \partial t$ in the Lagrangian of a ferromagnet originates from the spin Berry phase. A rigorous discussion of this term is rather involved, but can be avoided by the following observation: When there is no damping, $\eta = 0$, the Lagrange equations must be equivalent to Eq. (2.43). Consequently, the effect of introducing damping is to reduce the effective field, $\mathbf{H} \rightarrow \mathbf{H} - \eta \dot{\mathbf{M}}$. In the presence of damping, the equation of motion of the magnetization must therefore be

The kinetic term is considered in more detail by Refs. 137–139.

$$\frac{\partial \mathbf{M}}{\partial t} = \gamma \mathbf{M} \times \left(\mathbf{H} - \eta \frac{\partial \mathbf{M}}{\partial t} \right) = \gamma \mathbf{M} \times \mathbf{H} - \frac{\alpha}{M} \mathbf{M} \times \frac{\partial \mathbf{M}}{\partial t}. \quad (2.46)$$

This equation is known as the *Landau–Lifshitz–Gilbert (LLG) equation*, and the parameter $\alpha = \gamma M \eta < 0$ is known as the *Gilbert damping parameter*.



Current-induced spin torques

3.1 Metallic ferromagnets

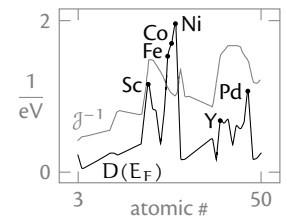
The Heisenberg model we considered in Chap. 2 is not a realistic description of magnetism in the transition metals [26, 85]. In solids, the atomic states hybridize to form bands. Band formation is in general detrimental to the spin polarization of a solid because of the kinetic-energy cost related to moving electrons from lower-energy filled states to higher-energy unoccupied states. Iron, cobalt, and nickel are exceptions to this rule. These metals have both strong hybridization and strong exchange splitting.

The *Stoner model* is a simple model for magnetism in the conduction band [26]. In materials that fulfill the *Stoner criterion*,

$$\mathcal{J}D(E_F) > 1, \quad (3.1)$$

the conduction bands are spontaneously spin polarized. Here, $D(E_F)$ is the density of states at the Fermi level and \mathcal{J} is the exchange. Among the elemental metals, only iron, cobalt, and nickel satisfy the Stoner criterion.

However, the fact that magnetism in iron, cobalt, and nickel and their alloys depends strongly on the position of the Fermi level in the 3d band (Slater–Pauling curve) [85], and that the magnetic moments in these metals retains features of the 3d electrons [85], are indications that the Stoner model is too simple to fully capture their magnetic properties. The so-called *s–d exchange* is frequently used to model the interaction between



$D(E_F)$ v. \mathcal{J}^{-1} for elements in periods 2–5. Pd comes close to fulfilling the Stoner criterion. Redrawn after Ref. 26.

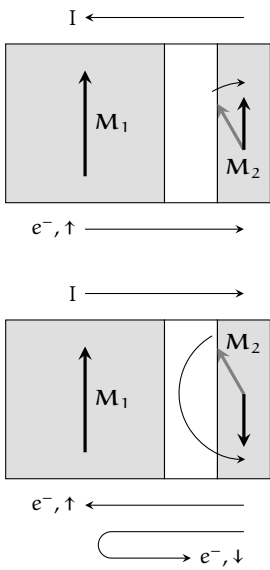
the partially localized 3d electrons and the itinerant 4s electrons [26],

$$\mathcal{H} = D \sum_{i,j} \mathbf{S}_i \cdot \mathbf{s}_j. \quad (3.2)$$

Here, $D < 0$ is the s - d exchange integral, \mathbf{S}_i is the spin operator of a localized d electron, and \mathbf{s}_j is the spin operator of an itinerant s electron. The s electrons can mediate an indirect exchange interaction between the d electrons, but the localized magnetic moments will also spin polarize the itinerant electrons.

3.2 Spin-transfer torques

Spin-transfer torques:



The spin polarization of the conduction electrons is not only important for explaining the origin of magnetism in the transition metals, but can also be exploited to manipulate the magnetic state. Consider a spin-polarized current flowing perpendicular to a stack consisting of two ferromagnets separated by a nonmagnetic (normal) metal. If there is a misalignment between the two magnetizations M_1 (polarizer) and M_2 (free layer), some of the electrons traversing the stack will have their spins flipped. Assuming that spin angular momentum is separately conserved, this process transfers spin from the conduction electrons to the magnetization of the free layer. The transferred spin will eventually reorient M_2 to point in the same direction as M_1 .

The process can be reversed by reversing the direction of the current. We assume that the free layer is too small to impart any appreciable spin polarization on the unpolarized current that enters it from the right reservoir. Upon reaching the fixed layer, the spin-down electrons are more likely to be backscattered than the spin-up electrons. The spin transfer from the resulting accumulation of spin-down electrons will eventually reorient M_2 in the direction opposite to M_1 .

Looking at the numbers, one electron can transfer a maximum of \hbar of

angular momentum to the magnetization. The magnetic moment corresponding to this amount of spin is $2\mu_B = e\hbar/m$, where e is the electron charge and m is the electron mass. Since $2\mu_B = 2 \cdot 10^{-23} \text{ A m}^2$ is such a small number, and the magnetic moment per area of a thin film is so large (typically $M \cdot t = 6 \cdot 10^5 \text{ A/m} \cdot 2 \text{ nm} = 1 \text{ mA}$, where M is the magnetization and t is the film thickness), the number of electrons required to deposit the right amount of angular momentum is about $5 \cdot 10^{19}/\text{m}^2$. Given that the magnetization dynamics in a ferromagnet is typically on the gigahertz time scale, this corresponds to a current density of roughly 10^{10} A/m^2 . The sheer magnitude of this current density was one of the principal reasons why spin-transfer-induced magnetization dynamics did not receive widespread attention until the advent of magnetic nanostructures.

In symmetric F/N/F stacks the torque on the free-layer magnetization \mathbf{M}_2 due to spin transfer is [152]

$$\boldsymbol{\tau}_S = \frac{\gamma\hbar P I}{2eMV M^2} \mathbf{M}_2 \times (\mathbf{M}_2 \times \mathbf{M}_1), \quad (3.3)$$

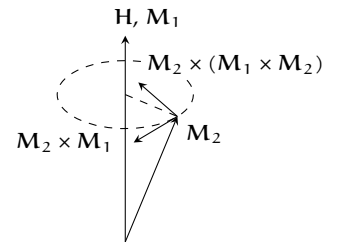
where I is the applied charge current, P is the current's spin polarization, and V is the volume of the free layer. To accurately describe the dynamics of the free-layer magnetization, this torque must be added to the right-hand side of the LLG equation. The torque in Eq. (3.3) is known as the *Slonczewski torque* or the *antidamping torque* because—depending on the direction of the current—it acts in the opposite (same) direction of (as) the Gilbert-damping torque. The Slonczewski torque is usually accompanied by a small correction

$$\boldsymbol{\tau}_\beta = \frac{\gamma\hbar P I}{2eMV M} \beta \mathbf{M}_2 \times \mathbf{M}_1, \quad (3.4)$$

where β is a small number on the order of 0.1. This torque is known as the *field-like torque* because it acts in the same (opposite) direction as (of) the torque from the effective field.

Berger was the first to consider the possibility of spin transfer in 1978 [140–143]. However, because of the large current densities required, the phenomenon did not receive widespread attention until the discovery of interlayer exchange coupling (1986) [144–146] and giant magnetoresistance (1988) [147, 148] had attracted attention to magnetic nanostructures. In 1996, Berger [149] and Slonczewski [150] independently predicted that an electric current could excite dynamics in a magnetic multilayer system, which was experimentally confirmed shortly thereafter [151].

Orientation of $\boldsymbol{\tau}_S$ and $\boldsymbol{\tau}_\beta$:



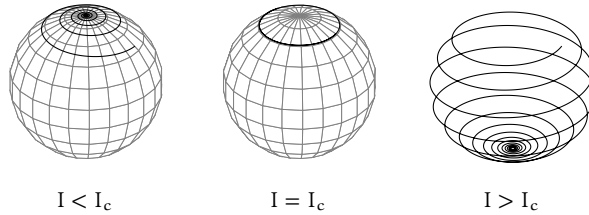
The qualitative types of dynamics that can be excited by the spin-transfer torques can be understood using linear stability analysis [153, 154]. The three panels in Fig. 3.1 show solutions for \mathbf{M}_2 of the *Landau–Lifshitz–Gilbert–Slonczewski (LLGS) equation* [28],

$$\frac{\partial \mathbf{M}}{\partial t} = \gamma \mathbf{M} \times \mathbf{H} - \frac{\alpha}{M} \mathbf{M} \times \frac{\partial \mathbf{M}}{\partial t} + \boldsymbol{\tau}_S + \boldsymbol{\tau}_\beta, \quad (3.5)$$

with $\mathbf{H} = H_k m_z \mathbf{e}_z$ and $\mathbf{M}_1 = M \mathbf{e}_z$, for different values of the current I . In all three cases, \mathbf{M}_2 is displaced from the fixed point at $\vartheta = 0$ to $\vartheta = \pi/4$. For currents below the threshold value, $I < I_c$, the damping is stronger than the Slonczewski torque, and the magnetization spirals back to the fixed point at $\vartheta = 0$. For currents above the threshold value, $I > I_c$, the Slonczewski torque is stronger than the damping, and the fixed point at $\vartheta = 0$ is no longer stable. Instead of spiralling back to $\vartheta = 0$, the magnetization switches, spiralling all the way down to $\vartheta = \pi$. If the current is exactly equal to the threshold value, $I = I_c$, the damping and the Slonczewski torques are equally strong, resulting in stable precession.

The case of $I < I_c$ (net damping) corresponds to the first case we considered on page 34, in which spin transfer from the polarizer to the free layer aligns the free layer with the polarizer. The case of $I > I_c$ (net antidamping) corresponds to the second case we considered on page 34, in which spin transfer to the free layer from electrons reflected by the polarizer aligns the free layer antiparallel to the polarizer. This kind of current-

Figure 3.1 Solutions of the LLGS equation for different currents, $I < I_c$, $I = I_c$, and $I > I_c$. Redrawn after Ref. 154.



induced magnetization switching has been implemented in commercially available MRAM chips, known as STT-MRAM [29–31]. In addition to these two cases, $I = I_c$ affords the possibility to achieve stable precession, which can be used to make a spin-torque oscillator [155–157].

Thus far we have only considered spin transfer between two uniformly magnetized layers, which is known as the *macrospin approximation*. However, spin transfer will also take place as the current traverses a slowly varying magnetization texture in a single ferromagnet. In the long-wavelength limit, the spin-transfer torques in Eqs. (3.3) and (3.4) can be written as [158–160]

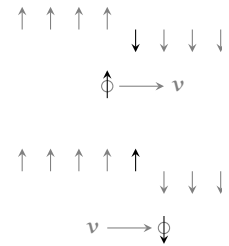
$$\boldsymbol{\tau} = \mathbf{u}(\mathbf{J} \cdot \nabla)\mathbf{M} - \frac{\beta\mathbf{u}}{M}\mathbf{M} \times (\mathbf{J} \cdot \nabla)\mathbf{M}, \quad (3.6)$$

where $\mathbf{u} = \mu_B P/eM(1 + \beta^2)$ and \mathbf{J} is the current density. The first term is known as the *adiabatic torque* because it is a result of the spin-current divergence that arises when the conduction-electron spin polarization follows the magnetization adiabatically [160]. The second term is known as the *nonadiabatic torque* or the β *torque*. Its physical origin is spin relaxation processes due to spin-orbit coupling or impurities that leads the conduction-electron spin polarization to locally deviate from the magnetization [158]. This is similar to the antidamping and field-like torques: If the spin current is completely absorbed by the free layer, only the antidamping torque is expected to be significant, but if the spin current is not completely absorbed, the field-like torque can also be strong [161].

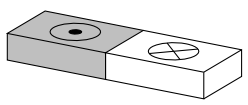
One particular example of a slowly varying magnetization texture is a domain wall. The result of the transfer of spin from the itinerant electrons to the magnetization is *domain wall motion*: the spin-polarized current will drag the domain wall along with it. In the limit of an atomically sharp domain wall, domain wall motion by spin transfer can be understood as a null-sum process whereby the flipping of an electron spin results in the flipping of an atomic spin.



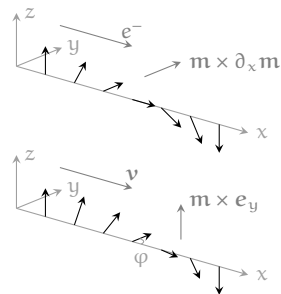
Current-induced dw motion:



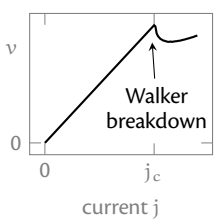
Using this simple picture of domain wall motion, we expect the domain wall velocity to scale linearly with the amount of spin that can be transferred from the current. Since the spin carriers and the charge carriers are one and the same, that implies that the domain wall velocity scales linearly with the current.



Current-induced DW motion:



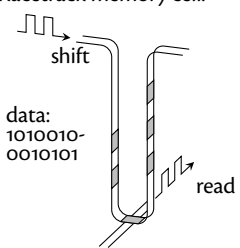
DW velocity v. current:



Domain-wall-motion experiments are usually carried out in rectangular strips [162, 163]. In a strip with an out-of-plane easy axis it is harder to magnetize the strip in the in-plane transverse direction than in the in-plane longitudinal direction because of the shape anisotropy. Consequently, the spins of an up-down domain wall lie in the xz plane. A detailed calculation reveals that it is the β torque that is most important for domain wall motion [164]. The β torque tilts the spins out of the xz plane. This gives rise to a torque in the z direction due to the hard y axis, which drives the domain wall. However, increasing the current density tilts the wall farther and farther out of the xz plane. When the tilt φ increases beyond $\pi/4$ the wall slips past the hard axis and begins to rotate. This event is known as *Walker breakdown* [165], and results in a reduction of the domain wall velocity.

The *racetrack memory* is a proposal for a memory cell in which information is encoded in a train of magnetic domains [166–168]. As opposed to MRAM based on magnetic bilayers, each memory cell can hold several bits. The bits are read and written by shifting the train of domains back and forth using current-induced domain wall motion [167]. Although the racetrack memory has not seen commercialization, it has inspired a lot of research on domain wall dynamics.

Racetrack memory cell:



Even though racetrack memories are not yet for sale, current-driven domain wall motion is more than an academic curiosity. Injection of a large spin current into a uniform magnet can destabilize the uniformly magnetized state [160, 169, 170], and break the magnet into domains [171]. Thus, even switching of a uniform magnet may proceed by domain wall motion. In particular, this is often the case for spin-Hall torques [172–174], which we consider next.

Redrawn after Ref. 166.

3.3* Spin-Hall torques

In the previous section we saw that one way to spin polarize a current is to use a conducting ferromagnet as a polarizer or spin filter. Another way to obtain a spin current is the spin Hall effect [175–178].

The ordinary Hall effect is the deflection of a charge current in a magnetic field due to the Lorentz force. The Hall effect is usually studied in nonmagnetic materials such as copper or various doped semiconductors. Consider what would happen if the material was magnetic: experiments show that in addition to the usual contribution to the transverse resistivity ρ_{xy} due to the applied magnetic field H_z , there is an *anomalous* term that is proportional to the z component of the magnetization [180],

$$\rho_{xy} = R_0 H_z + R_1 M_z. \quad (3.7)$$

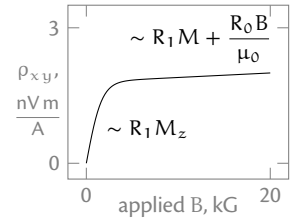
The increase in transverse resistivity cannot simply be explained as the Lorentz force due to the additional contribution to the magnetic field B_z from M_z because $R_1 \gg R_0$. Furthermore, whereas R_0 depends chiefly on the density of charge carriers, R_1 depends subtly on a variety of material parameters.

The origin of the anomalous term is spin–orbit coupling [180]. Itinerant electrons that scatter off spin–orbit-coupled impurities will experience spin-dependent *skew scattering* and *side jumps* (extrinsic mechanisms). Moreover, a spin–orbit-coupled band structure can give rise to an *intrinsic* spin-dependent deflection of the itinerant electrons,

$$\frac{d\mathbf{r}}{dt} = \frac{1}{\hbar} \frac{\partial E}{\partial \mathbf{k}} - \frac{e}{\hbar} \mathbf{E} \times \boldsymbol{\Omega}(\mathbf{k}). \quad (3.8)$$

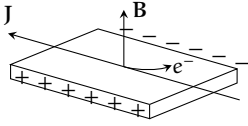
Here, the first term is the ordinary semiclassical velocity of the electron (energy E and wave vector \mathbf{k}), and the second term is the so-called *anomalous velocity* [181–183]. It is perpendicular both to the applied electric field \mathbf{E} and to the Berry curvature $\boldsymbol{\Omega}(\mathbf{k}) = i\langle \nabla_{\mathbf{k}} u_{\mathbf{k}} | \times | \nabla_{\mathbf{k}} u_{\mathbf{k}} \rangle$ of the band ($u_{\mathbf{k}}$

The Hall effect in nickel at room temperature:

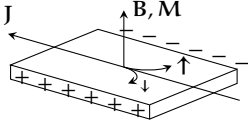


Redrawn after Ref. 179.

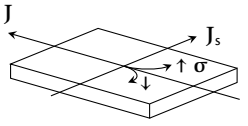
ordinary Hall effect:



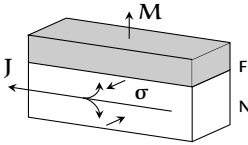
anomalous Hall effect:



spin Hall effect:



Spin injection via the spin Hall effect:



are the Bloch functions). The Berry curvature is often proportional to the electron spin σ . Combined with the spin polarization of the itinerant electrons in a ferromagnet, the spin-dependent skew scattering, side jumps, and the anomalous velocity give rise to a transverse charge current that adds to the ordinary Hall effect.

The anomalous Hall effect is relatively easy to detect because it gives rise to a charge current. However, if the bands have a finite Berry curvature, the itinerant electrons will be deflected in a spin-dependent manner even if they are not spin polarized. The result is a transverse *spin* current, but no *net* transverse charge current.

This *spin Hall effect* [175] is now routinely detected in heavy metals such as platinum and tantalum. Since the anomalous velocity is perpendicular both to the electron spin σ and the applied electric field $E = \rho J$, the resulting spin current J_s , its spin polarization σ , and the applied charge current J are all at right angles to each other.

Just as a current that is spin-polarized by a ferromagnet, a spin current injected into a ferromagnet from a heavy metal due to the spin Hall effect will relax by transferring spin to the magnetization. The result is a spin-transfer torque [184]

$$\tau = \frac{\gamma \hbar \vartheta J}{2eMt} \frac{1}{M} \mathbf{M} \times (\mathbf{M} \times \boldsymbol{\sigma}) + \frac{\gamma \hbar \vartheta J}{2eMt} \beta \mathbf{M} \times \boldsymbol{\sigma}, \quad (3.9)$$

where J is the applied charge-current density, ϑ is the so-called spin-Hall angle, $\vartheta = (2e/\hbar)(J_s/J)$, and t is the thickness of the ferromagnetic layer.

The spin-Hall spin-transfer torque can induce both switching and uniform precession in a uniformly magnetized sample just as the ordinary spin-transfer torque [25, 157]. However, there are significant differences between the domain wall dynamics induced by the spin-Hall torque and the spin-transfer torques. For instance, there is no Walker breakdown when a domain wall is driven by a pure spin-Hall torque [1], because the spin-Hall torque $\mathbf{M} \times \boldsymbol{\sigma}$ vanishes when the wall reaches a tilt angle of

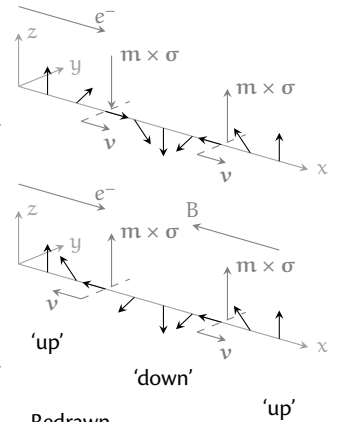
$\varphi = \pi/2$ ($\mathbf{M} \parallel \boldsymbol{\sigma}$). In paper I we consider the different types of domain wall dynamics that can be induced by spin-Hall torques and so-called Rashba spin-orbit torques. (Rashba spin-orbit torques will be discussed in the next section.) In particular, we consider the range of different current-velocity characteristics that are possible.

The sign of the velocity of a domain wall driven by spin-Hall torques depends on the chirality of the wall. Homochiral walls move in the same direction whereas heterochiral walls move in different directions. We mentioned on page 38 that even switching of uniform magnets by spin-Hall torques usually proceeds by domain wall motion [172–174]. However, due to the Dzyaloshinskii–Moriya interaction (DMI) [186–189] that is usually present in these systems, the domains that nucleate are separated by walls of the same chirality. Since homochiral walls move in the same direction there is no domain expansion or contraction, and consequently no deterministic switching.

Application of an in-plane field that is stronger than the Dzyaloshinskii–Moriya interaction leads to the formation of heterochiral walls. If the magnetic field is applied parallel to the applied current, ‘down’ domains expand and ‘up’ domains contract, and if the magnetic field is antiparallel to the applied current, ‘up’ domains are favored over ‘down’ domains.

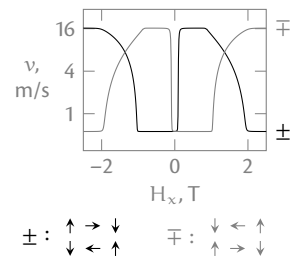
The dependence on an applied magnetic field to switch the magnet deterministically is an obstacle to the adoption of devices using spin-Hall torques. In paper I we point out that in a synthetic antiferromagnet (two ferromagnets coupled by an antiferromagnetic interlayer exchange) deterministic switching can be achieved both by toggling the polarity of the applied field, and by toggling the magnitude of the field between two judiciously chosen large and small values. This explained an observed switching anomaly [190] and might, depending on the device geometry, be more favorable than changing the polarity of an applied field. However, several field-free approaches have also been suggested, such as structural engineering [191, 192], tilted anisotropy [193], exchange bias [194–196],

Homo- and heterochiral SHE-driven DW motion:



Redrawn after Ref. 185.

DW velocity in a SAF
v. in-plane field H_x :



ferromagnetic/ferroelectric hybrids [197], and combining spin-Hall and spin-transfer torques [198].

The reason for the prominence spin-Hall torques have achieved in the field of spintronics is the very high *efficiencies* of these torques [161]. By efficiencies in this context we mean the amount of torque that can be obtained for a given current. In the spin-transfer-torque geometry we considered on page 34, the current flows perpendicular to the layers. The efficiency of the torque is

$$\eta = \frac{\gamma \hbar P I}{2eV} \frac{1}{I} = \frac{\gamma \hbar P}{2etA},$$

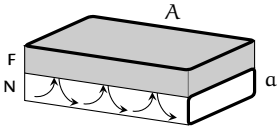
where t is the thickness of the free layer and A is the cross-sectional area of the stack. Each electron in the spin-polarized current can only transfer \hbar of angular momentum to the free layer. In the spin-Hall geometry we considered on page 40, the current flows parallel to the layers. The efficiency of the torque is

$$\eta' = \frac{\gamma \hbar \vartheta J}{2et} \frac{1}{Ja} = \frac{\gamma \hbar \vartheta}{2eta},$$

where t is the thickness of the magnet and a is the cross-sectional area of the normal metal. The ratio A/a can be 30 or more for a typical geometry, giving the spin-Hall torques a vastly improved efficiency over spin-transfer torques. Microscopically, this can be understood by considering a particular electron in the normal metal that is deflected towards the N/F interface. The electron may be scattered off the ferromagnet multiple times, each time transferring \hbar of angular momentum to the magnetization [161].

The spin Hall effect has also found applications in spintronics besides spin torques. In the direct spin Hall effect, injection of a charge current gives rise to a transverse spin current. In the Onsager reciprocal process [199–201], injection of a spin current gives rise to a transverse charge current. This effect is known as the *inverse spin Hall effect* [175, 202–204],

Geometrical efficiency of STT v. SHE:



Redrawn after Ref. 161.

and has turned out to be an indispensable tool for measuring spin currents due to phenomena such as spin pumping [205, 206] or the spin Seebeck effect [207]. Through an ingenious combination of the direct and inverse effects, the spin Hall effect can also be used to detect the magnetization direction of a ferromagnet using the *spin-Hall magnetoresistance* [208, 209].

3.4 The Rashba spin–orbit torque

A two-dimensional free electron gas in the xy plane with broken symmetry in the z direction will exhibit Rashba spin–orbit coupling [210–213]. The Hamiltonian of these electrons is

$$\mathcal{H} = \frac{\mathbf{p}^2}{2m} + \frac{\lambda}{\hbar} (\mathbf{p} \times \mathbf{e}_z) \cdot \boldsymbol{\sigma}, \quad (3.10)$$

where λ is the Rashba parameter. In equilibrium the Rashba term couples the electron's momentum and spin so that an electron with momentum $\mathbf{p} = p\mathbf{e}_x$ will minimize its energy by aligning its spin with the y axis. However, the net spin polarization of the electron gas is zero. On the other hand, if a current $\mathbf{J} = ne\langle\mathbf{p}\rangle/m$ runs through the system (n is the electron density), the electrons will experience an effective magnetic field $\mathbf{B} = (\lambda m^2/n\hbar e^2)(\mathbf{J} \times \mathbf{e}_z)$, which will spin polarize the electron gas. This effect is known as the *Edelstein effect* [175, 214–216].

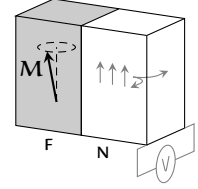
If the two-dimensional electron gas lies at the interface between a normal metal and a ferromagnet, the electrons will also experience the s – d exchange,

$$\mathcal{H} = \frac{\mathbf{p}^2}{2m} + \frac{\lambda}{\hbar} (\mathbf{p} \times \mathbf{e}_z) \cdot \boldsymbol{\sigma} + D\mathbf{M} \cdot \boldsymbol{\sigma}. \quad (3.11)$$

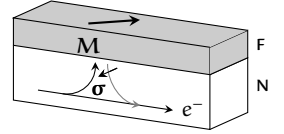
Through the s – d exchange, the current-induced spin polarization will then exert a torque [217, 218]

$$\boldsymbol{\tau} = \frac{\gamma\lambda P}{2\mu_B M} \mathbf{M} \times (\mathbf{J} \times \mathbf{e}_z) \quad (3.12)$$

Detection of spin pumping:

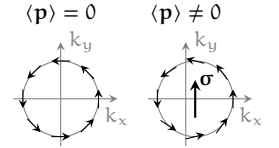


Spin-Hall magnetoresistance:



$$\rho_{\text{SMR}} = \rho_0 [\mathbf{m} \cdot (\mathbf{J} \times \mathbf{e}_z)] / J^2$$

The Edelstein effect:

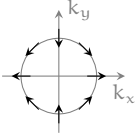


The Edelstein effect is also known as the *inverse spin galvanic effect*.

on the magnetization of the ferromagnet. This torque is a pure interface effect—that is, the torque from the two-dimensional electron gas acts exclusively on the surface spins of the ferromagnet. However, if the ferromagnet is very thin we can define an average torque that can be thought of as acting throughout the magnet. The efficiency of the Rashba spin–orbit torque is

$$\eta'' = \frac{\gamma\lambda P J}{2\mu_B} \frac{1}{Ja} = \frac{\gamma\lambda P}{2\mu_B a'}$$

Linear Dresselhaus SOC:



Dresselhaus noted that close to the Γ point [223–225], the zinc-blende structure of the III–V semiconductors permits a cubic spin–orbit coupling

$$\mathcal{H} = \frac{\lambda}{\hbar} [(p_y^2 - p_z^2)p_x \sigma_x + (p_z^2 - p_x^2)p_y \sigma_y + (p_x^2 - p_y^2)p_z \sigma_z].$$

In the presence of strain along the [001] direction the cubic Dresselhaus coupling reduces to linear Dresselhaus coupling [213, 226],

$$\mathcal{H} = \frac{\beta}{\hbar} (p_x \sigma_x - p_y \sigma_y).$$

and can be as high as the efficiency η' of the spin–Hall torque, $\lambda/\mu_B \approx 10^5 \text{ T m} \approx \hbar/et$.

Since the spin–Hall and Rashba spin–orbit torques can be of similar magnitude in F/N bilayer systems, the effects of the two torques can be difficult to disentangle [161]. This difficulty is compounded by the fact that the Rashba spin–orbit torque can be accompanied by an antidamping-like correction [219, 220].

Pure spin–orbit torques generated by the Edelstein mechanism can however be observed in high-quality bulk crystals with spin–orbit coupling [221, 222]. Experiments show that these torques are sufficiently strong to switch the magnetization. Whereas the spin–orbit coupling at a F/N interface is predominantly of the Rashba type, the spin–orbit coupling in the $\text{Ga}_{1-x}\text{Mn}_x\text{As}$ and NiMnSb crystals employed in these experiments is predominantly of the Dresselhaus type [227, 228].

Just like for the spin Hall effect, there is also an Onsager reciprocal of the Edelstein effect [229]. This reciprocal process is known as the *inverse Edelstein effect* or the *spin-galvanic effect*. Whereas the Edelstein effect gives rise to a spin polarization as a response to an applied current, the spin-galvanic effect gives rise to a current as a response to an induced spin polarization. The spin-galvanic effect was first demonstrated in GaAs by an optically induced spin polarization [230, 231].

In a ferromagnetic material the Edelstein effect and the s–d exchange

together produce spin–orbit torques. Similarly, the spin-galvanic effect and the s – d exchange together produce *magnonic charge pumping* [232], which is thereby the Onsager reciprocal process of spin–orbit torques. For a generic spin–orbit coupling, the Hamiltonian in Eq. (3.11) can be written as

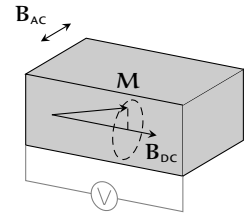
$$\mathcal{H} = \frac{\mathbf{p}^2}{2m} + \mathbf{g}(\mathbf{p}) \cdot \boldsymbol{\sigma} + D\mathbf{M} \cdot \boldsymbol{\sigma}. \quad (3.13)$$

The velocity operator corresponding to this Hamiltonian is

$$\mathbf{v} = \frac{\partial \mathcal{H}}{\partial \mathbf{p}} = \frac{\mathbf{p}}{m} + \mathbf{g}'(\mathbf{p}) \cdot \boldsymbol{\sigma}. \quad (3.14)$$

From this velocity operator we can see that a nonequilibrium magnon accumulation $\delta\mu$ gives rise to a velocity response $\delta\mathbf{v} = \mathbf{g}'(\mathbf{p}) \cdot \delta\mu$ among the conduction electrons—or, in other words, to a current $\mathbf{J} = ne\langle\delta\mathbf{v}\rangle = ne\langle\mathbf{g}'(\mathbf{p}) \cdot \delta\mu\rangle$. Magnonic charge pumping has been demonstrated in $\text{Ga}_{1-x}\text{Mn}_x\text{As}$ by ferromagnetic resonance [233].

Magnonic charge pumping:



Redrawn after Ref. 233.

3.5 Phenomenology of current-induced spin torques

The Edelstein mechanism can be used to generate spin–orbit torques for all symmetries of the underlying spin–orbit coupling [32]. In the previous section, we saw examples of both Rashba and Dresselhaus spin–orbit torques. The Rashba torque is typically found at interfaces, whereas the Dresselhaus torque is an example of a so-called *bulk spin–orbit torque*. Bulk spin–orbit torques are generated in crystals where global or local structural inversion asymmetry generates a spin polarization that torques the magnetization or the antiferromagnetic Néel order parameter. However, the crystallographic and magnetic point groups host a wide variety of spin–orbit symmetries [183]. A systematic investigation of the possible spin–orbit torques requires a framework that efficiently deals with these symmetries.

Reference 234 comments on the generation of a *local* spin polarization within an inversion-symmetric unit cell.

Fortunately, we have already encountered such a framework in Sect. 2.5 in the context of magnetocrystalline anisotropies. As long as the current-induced torque at (\mathbf{r}, t) only depends on the magnetization at (\mathbf{r}, t) , we can write it as [235, 236]

$$\boldsymbol{\tau}(\mathbf{r}, t) = \gamma \mathbf{m}(\mathbf{r}, t) \times \mathbf{H}(\mathbf{r}, t), \quad H_i = \eta_{ij} J_j, \quad (3.15)$$

where $\mathbf{m} = \mathbf{M}/M$ is the normalized magnetization, \mathbf{J} is the current density and η_{ij} is a second-rank tensor. Just as we did for the magnetocrystalline anisotropies, we can expand the tensor η_{ij} in the magnetization components m_i and their derivatives $\partial_i m_j$. To lowest order we get

$$\eta_{ij} = \Lambda_{ij} + \Gamma_{ijk} m_k + \beta_{ijkl} \partial_k m_l + P_{ijkln} m_k \partial_l m_n + \dots \quad (3.16)$$

Experience from the magnetocrystalline anisotropy shows that the first few terms in the expansion usually captures the experimentally observed behavior [85]. Such an expansion for the current-induced torques was first proposed by Refs. 235 and 236. The effective magnetic field \mathbf{H} and the magnetization \mathbf{m} are axial vectors. Since the current density \mathbf{J} is a polar vector, η_{ij} is an axial tensor, and the tensors Λ_{ij} , Γ_{ijk} , β_{ijkl} , and P_{ijkln} are respectively axial (Λ_{ij}), polar (Γ_{ijk}), polar (β_{ijkl}), and axial (P_{ijkln}).

Depending on the relevant point-group symmetry, we can use Eqs. (3.15) and (3.16) to write down any possible current-induced torque. We consider sputtered permalloy and strained $\text{Ga}_{1-x}\text{Mn}_x\text{As}$ as examples.

Permalloy ($\text{Ni}_{80}\text{Fe}_{20}$) is a disordered magnetic alloy [26]. When deposited by sputtering, permalloy can have relatively low crystallinity. Sputtered permalloy is therefore an approximately isotropic material with negligible spin-orbit coupling.

The only isotropic second-rank tensor is the Kronecker delta, δ_{ij} [237]. Since Λ_{ij} is an axial tensor and δ_{ij} is a polar tensor

$$\Lambda_{ij} = 0 \quad \forall i, j.$$

The only isotropic third-rank tensor is the Levi–Civita symbol, ϵ_{ijk} [237]. Since Γ_{ijk} is a polar tensor and ϵ_{ijk} is an axial tensor

$$\Gamma_{ijk} = 0 \quad \forall i, j, k.$$

There are three fourth-rank isotropic tensors, namely [237]

$$\delta_{ij}\delta_{kl}, \quad \delta_{ik}\delta_{jl}, \quad \text{and} \quad \delta_{il}\delta_{jk}.$$

These are all polar tensors, like β_{ijkl} . However, whereas $\delta_{ij}\delta_{kl}$ and $\delta_{ik}\delta_{jl}$ describe simultaneous spin-space and real-space rotations, $\delta_{il}\delta_{jk}$ describes separate spin-space and real-space rotations. (For β_{ijkl} , the indices j and k are real-space indices and the indices i and l are spin-space indices.) Consequently, if spin–orbit coupling can be neglected, β_{ijkl} is on the form

$$\beta_{ijkl} = \beta_0 \delta_{il} \delta_{jk}.$$

Similarly, there are six fifth-rank isotropic tensors, namely [237]

$$\begin{aligned} &\epsilon_{ijk}\delta_{ln}, \quad \epsilon_{ijl}\delta_{kn}, \quad \epsilon_{ijn}\delta_{kl}, \\ &\epsilon_{ikl}\delta_{jn}, \quad \epsilon_{ikn}\delta_{jl}, \quad \text{and} \quad \epsilon_{iln}\delta_{jk}. \end{aligned}$$

These are all axial fifth-rank tensors, like P_{ijkln} . However, only $\epsilon_{ikn}\delta_{jl}$ describes separate spin-space and real-space rotations. (For P_{ijkln} , the indices j and l are real-space indices and the indices i , k , and n are spin-space indices.) Consequently, P_{ijkln} is on the form

$$P_{ijkln} = P_0 \epsilon_{ikn} \delta_{jl}.$$

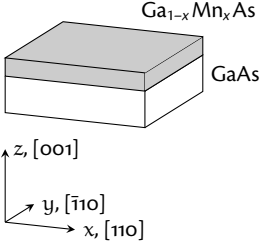
Using these expressions for the tensors Λ_{ij} , Γ_{ijk} , β_{ijkl} , and P_{ijkln} , the possible current-induced torques in sputtered permalloy are

$$\boldsymbol{\tau} = \gamma \beta_0 \mathbf{m} \times (\mathbf{J} \cdot \nabla) \mathbf{m} - \gamma P_0 (\mathbf{J} \cdot \nabla) \mathbf{m}. \quad (3.17)$$

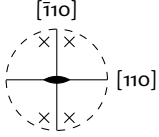
An isotropic system is, necessarily, inversion symmetric.

The tensors Λ_{ij} and Γ_{ijk} are both zero in any inversion-symmetric system, as is the spin–orbit coupling.

Strained $\text{Ga}_{1-x}\text{Mn}_x\text{As}$ epilayer:



Stereographic projection:



Redrawn after Ref. 236.

We recognize these torques as the spin-transfer torques from Eq. (3.6). Consequently, we can identify the coefficients P_0 and β_0 as $P_0 = -uM/\gamma$ and $\beta_0 = -\beta uM/\gamma$.

Strained $\text{Ga}_{1-x}\text{Mn}_x\text{As}$ grown epitaxially on a GaAs (001) substrate has point-group symmetry $mm2$ (C_{2v}) [238]. The epilayer has linear Dresselhaus spin-orbit coupling in the bulk (note on page 44) and Rashba spin-orbit coupling due to the broken symmetry at the interface between the $\text{Ga}_{1-x}\text{Mn}_x\text{As}$ film and the GaAs substrate. Due to shape anisotropy, the magnetization of the epilayer will lie predominantly in the plane, $\mathbf{m} = m_x \mathbf{e}_x + m_y \mathbf{e}_y$. For simplicity, we consider only the case of a uniform magnetization and currents applied in the plane, $\mathbf{J} = J_x \mathbf{e}_x + J_y \mathbf{e}_y$.

Any axial second-rank tensor that is invariant under the symmetry operations of $mm2$ has only two nonzero components [106],

$$\begin{aligned} \Lambda_{xy} &= \Lambda_1, \\ \Lambda_{yx} &= \Lambda_2, \\ \Lambda_{ij} &= 0 \text{ for all other } ij. \end{aligned}$$

Any polar third-rank tensor that is invariant under the symmetry operations of $mm2$ has seven nonzero components, but depends on only three independent parameters [106]:

$$\begin{aligned} \Gamma_{xxz(3)} &= \Gamma_1, \\ \Gamma_{yyz(3)} &= \Gamma_2, \\ \Gamma_{zzz} &= \Gamma_3, \\ \Gamma_{ijk} &= 0 \text{ for all other } ijk \end{aligned}$$

($xxz(3)$ indicates the three tensor elements that are obtained by unrestricted permutation of the indices xxz). Consequently, the possible current-induced torques can be written as

$$\mathbf{H} = \Lambda_1 J_y \mathbf{e}_x + \Lambda_2 J_x \mathbf{e}_y + (\Gamma_1 J_x m_x + \Gamma_2 J_y m_y) \mathbf{e}_z. \quad (3.18)$$

Alternatively, we can introduce the Rashba coefficients $\Lambda_R = \frac{1}{2}(\Lambda_1 - \Lambda_2)$, and $\Gamma_R = \frac{1}{2}(\Gamma_1 + \Gamma_2)$, and the Dresselhaus coefficients $\Lambda_D = \frac{1}{2}(\Lambda_1 + \Lambda_2)$, and $\Gamma_D = \frac{1}{2}(\Gamma_1 - \Gamma_2)$, to write

$$\mathbf{H} = \Lambda_R(J_y \mathbf{e}_x - J_x \mathbf{e}_y) + \Lambda_D(J_y \mathbf{e}_x + J_x \mathbf{e}_y) + [\Gamma_R(J_x m_x + J_y m_y) + \Gamma_D(J_x m_x - J_y m_y)] \mathbf{e}_z. \quad (3.19)$$

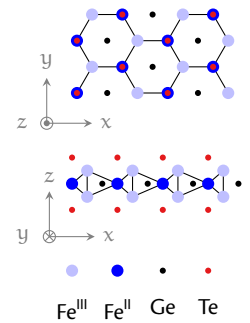
We recognize the first term from Eq. (3.12). The remaining terms have also been derived from microscopic models by respectively Ref. 239, Refs. 219 and 220, and Ref. 228.

3.6* Spin–orbit torques in Fe_3GeTe_2

In Sect. 2.4 we saw that a continuous symmetry in spin space cannot be broken by exchange interactions with a finite range in two dimensions. This is a statement of the Hohenberg–Mermin–Wagner theorem [89, 97, 98]. A two-dimensional material must therefore exhibit a strong easy-axis anisotropy to order magnetically. Although theoretical models with long-range magnetic order—such as the Ising model [99, 100]—have been known for a long time, it was not until 2016 that truly two-dimensional materials with sufficiently strong anisotropy were discovered [72]. The discovery of these materials has inspired efforts to characterize them, to gain an understanding of their large anisotropies, and to find technological applications for them in, for instance, van der Waals heterostructures [72].

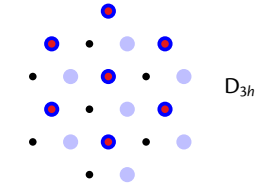
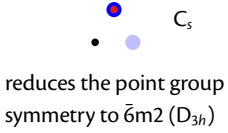
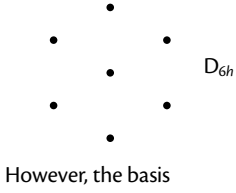
The compound Fe_3GeTe_2 was among the first two-dimensional magnetic materials to be discovered [73, 240]. It is metallic, and the bulk van der Waals crystal can be exfoliated down to the monolayer limit. As a metallic magnet without inversion symmetry, Fe_3GeTe_2 is a candidate material for hosting interesting bulk spin–orbit torques. The strong magnetocrystalline anisotropy as well as the presence of the heavy element tellurium makes it plausible that the spin–orbit torques in Fe_3GeTe_2 may be relatively strong.

Crystal structure of Fe_3GeTe_2 :

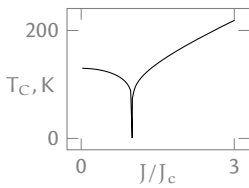


Redrawn after Ref. 73.

Fe_3GeTe_2 crystallizes in the hexagonal system, space group 194, point group $6/m\ 2/m\ 2/m$ (D_{6h}) [241].



T_C of Fe_3GeTe_2 v. current:



In paper II we consider the bulk spin-orbit torques in Fe_3GeTe_2 . We find that despite the low symmetry of its point group $\bar{6}m2$, the spin-orbit torque can be described by a single parameter Γ_0 ,

$$\mathbf{H} = \Gamma_0 [(J_x m_x - J_y m_y) \mathbf{e}_x - (J_x m_y + J_y m_x) \mathbf{e}_y]. \quad (3.20)$$

This effective field is the derivative of the functional

$$\begin{aligned} \mathcal{U} &= + \int d\mathbf{r} \frac{\Gamma_0}{M} [J_y M_x M_y - \frac{1}{2} J_x (M_x^2 - M_y^2)] \\ &= - \int d\mathbf{r} \frac{1}{2} \Gamma_0 J M \sin^2 \vartheta \cos(2\varphi + \varphi_J). \end{aligned} \quad (3.21)$$

Here, ϑ is the polar angle of the magnetization and φ is the azimuthal angle of the magnetization, $(m_x, m_y, m_z) = (\cos \varphi \sin \vartheta, \sin \varphi \sin \vartheta, \cos \vartheta)$, J is the magnitude of the current, and $\varphi_J = \arctan(J_y/J_x)$ is the angle the current makes with the x axis. Comparing this functional to the magnetic energy density of the out-of-plane easy axis,

$$u = -\frac{1}{2} K_z \cos^2 \vartheta,$$

($K_z > 0$) we see that the spin-orbit torque in Fe_3GeTe_2 acts as a pair of in-plane anisotropy axes, one easy axis at $\varphi = n\pi - \varphi_J/2$ and one hard axis at $\varphi = (n + \frac{1}{2})\pi - \varphi_J/2$ (assuming $\Gamma_0 > 0$). In particular, by applying the current along, say, the x axis and varying its magnitude J , the spin-orbit torque can be used to tune Fe_3GeTe_2 from an easy- z -axis magnet to an easy- xz -plane magnet to an easy- x -axis magnet.

In paper II we demonstrate that by using the spin-orbit torque to control the anisotropy of Fe_3GeTe_2 , it is possible to explore phenomena that are unique for two-dimensional magnetic systems. In particular, at the critical current density $J_c = K_z/|\Gamma_0|M$, Fe_3GeTe_2 becomes an easy-plane magnet with a continuous $O(2)$ symmetry. Consequently, the long-range magnetic order disappears at this point. By tuning the applied current

through the critical current density it is therefore possible to tune the Curie temperature T_C .

Although there is no long-range order at the critical current density, this is still an interesting region for studying the magnetic properties. The easy-plane magnet at $J = J_c$ is a physical realization of the universality class of the two-dimensional XY model. As a function of temperature, the two-dimensional XY model features a topological phase transition known as the Berezinskii–Kosterlitz–Thouless transition [242–245]. This phase transition cannot be associated with a local order parameter, but is nonetheless a genuine phase transition [245].

The best-known physical realization of the two-dimensional XY model is the superfluidity of thin films of ^4He . However, easy-plane Fe_3GeTe_2 offers several advantages over superfluid ^4He in terms of tunability, temperature, and accessibility of the physical observables. For instance, in the low-temperature phase of the XY model the spin–spin correlation function $\langle \mathbf{S}_r \cdot \mathbf{S}_{r'} \rangle$ features a temperature-dependent anomalous dimension η , $\langle \mathbf{S}_r \cdot \mathbf{S}_{r'} \rangle \sim 1/|r - r'|^\eta$ [244, 245]. At the critical current density J_c in Fe_3GeTe_2 , this nonuniversal anomalous dimension can be mapped out by measuring the spin–spin correlation function as a function of temperature using for instance polarized small-angle neutron scattering. In contrast, the anomalous dimension η is not experimentally accessible in superfluid ^4He . A measurement of η in Fe_3GeTe_2 would be the first test of the prediction $\eta = \kappa_B T / 4\pi J$ of the XY model [244]. (Here, J is the exchange coupling.)

We also expect easy-plane Fe_3GeTe_2 to exhibit a universal jump in the spin stiffness [245], similar to the universal jump in the superfluid density of ^4He [246, 247]. The spin stiffness may be measured in spin-wave resonance experiments. However, in contrast to ^4He , in which the BKT transition occurs at 1.2 K [247], the Curie temperature of Fe_3GeTe_2 indicates that the jump in spin stiffness would occur at liquid nitrogen or oxygen temperatures.

In addition to Fe_3GeTe_2 , the family of 2D materials with $\bar{6}m2$ symmetry also includes the 2H polymorph of the transition-metal dichalcogenides [248]. Spin–orbit-induced phenomena in these materials have been considered by Ref. 249, which identifies an interesting Dzyaloshinskii–Moriya interaction.

Magnon-induced spin torques

4.1 Magnons as spin waves

The classical interpretation of magnons is spin waves, which are wave solutions to the magnetization's classical equation of motion, namely the Landau–Lifshitz–Gilbert equation [116]. We are now going to consider spin waves in more detail.

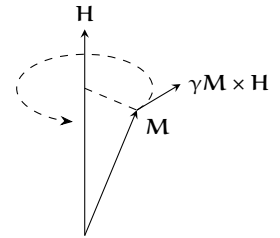
We consider a uniaxial ferromagnet with magnetic energy density

$$u = A \frac{\partial m_i}{\partial x_j} \frac{\partial m_i}{\partial x_j} - K_z m_z^2. \quad (4.1)$$

In the ground state the magnetization aligns with the easy z axis. If the magnetization deviates slightly from $\mathbf{M} = M\mathbf{e}_z$, the magnet will precess about the easy axis. In the presence of magnetic damping the precessing magnetization will relax towards the minimum-energy configuration, but in the absence of damping the precession will persist indefinitely. This precession is known as the *uniform mode* or the *Kittel mode* [26]. If the magnetization is nonuniform, for instance if the magnetization points along the z axis in most of the sample, but deviates slightly in a small region, the ensuing dynamics is more complicated. The local precession of the magnetization will then spread to the rest of the sample as wavelike ripples—spin waves. We parameterize the smallness of the deviation from the z axis using the small parameter λ ,

$$\mathbf{M}(\mathbf{r}, t) = \lambda M_x(\mathbf{r}, t)\mathbf{e}_x + \lambda M_y(\mathbf{r}, t)\mathbf{e}_y + M\mathbf{e}_z. \quad (4.2)$$

Uniform precession:

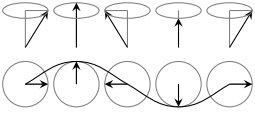


For simplicity, we consider only variations in the magnetization along one spatial direction, x . To first order in λ , the LLG equation gives two nontrivial equations,

$$\frac{\partial M_x}{\partial t} = -\frac{2\gamma}{M} \left(A \frac{\partial^2}{\partial x^2} - K_z \right) M_y, \quad \frac{\partial M_y}{\partial t} = +\frac{2\gamma}{M} \left(A \frac{\partial^2}{\partial x^2} - K_z \right) M_x.$$

(Here, we have neglected damping, $\alpha = 0$, for simplicity.) These equations cannot be separated. Consequently, ferromagnetic spin waves cannot be linearly polarized. However, we can combine the equations for M_x and M_y into a single equation by introducing the auxiliary variable $\psi = M_x - iM_y$. The factor of i signifies that there is a phase shift of $\pi/2$ between the x and the y component of the magnetization. In other words, the spin waves are circularly polarized. Physically, this can be understood as the circular precession of the individual spins. The resulting equation,

Ferromagnetic spin waves:



$$i \frac{\partial \psi}{\partial t} = \frac{2\gamma}{M} \left(A \frac{\partial^2}{\partial x^2} - K_z \right) \psi,$$

admits, as anticipated, solutions that are waves, $\psi = \rho \exp i(kx - \omega t)$. Here, ρ is the spin-wave amplitude, k is the spin-wave wave number, and ω is the spin-wave angular frequency. Substituting this *ansatz* into the equation of motion gives the spin-wave dispersion

$$\omega = -\frac{2\gamma}{M} (Ak^2 + K_z), \quad \gamma < 0. \quad (4.3)$$

We recognize this as the long-wavelength magnon spectrum in Eq. (2.20). However, unlike the magnon spectrum of the isotropic Heisenberg model, the spin-wave spectrum of a uniaxial ferromagnet has a gap that is proportional to the uniaxial anisotropy. Oscillations with frequency less than $\omega_0 = -2\gamma K_z/M$ have an imaginary wave number and do not propagate, but fall off exponentially.

4.2* Spin-wave spin current and spin transfer

An individual magnon carries a spin \hbar [78]. Since magnons carry spin, a net flow of magnons is a pure spin current. The classical analog of such a magnon-mediated spin current can be derived from the LLG equation.

The effective field of a uniaxial ferromagnet is

$$\mathbf{H} = \frac{2A}{M^2} \frac{\partial^2 \mathbf{M}}{\partial x^2} + \frac{2K}{M^2} M_z \mathbf{e}_z. \quad (4.4)$$

Consequently, if we neglect magnetic damping the LLG equation can be written as

$$\frac{\partial \mathbf{M}}{\partial t} = \frac{2\gamma A}{M^2} \mathbf{M} \times \frac{\partial^2 \mathbf{M}}{\partial x^2} + \frac{2\gamma K}{M^2} M_z (\mathbf{M} \times \mathbf{e}_z).$$

The z component of this equation contains no contributions from the magnetic anisotropy, and can be written as

$$\frac{\partial M_z}{\partial t} = \frac{\partial J_s^z}{\partial x}, \quad (4.5)$$

where

$$\mathbf{J}_s = \frac{2\gamma A}{M^2} \mathbf{M} \times \frac{\partial \mathbf{M}}{\partial x}. \quad (4.6)$$

Equation (4.5) is a continuity equation, and \mathbf{J}_s is known as the *spin-wave spin current*. Using Eq. (4.2) and $M_x = \text{Re } \psi$ and $M_y = -\text{Im } \psi$, the spin-wave spin current can be written as

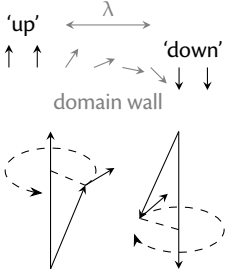
$$J_s^z = \frac{2\gamma A k \rho^2}{M^2} \quad (4.7)$$

in terms of the spin-wave amplitude ρ and the spin-wave wave number k .

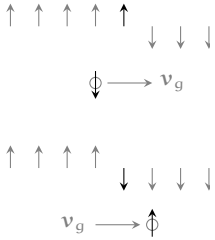
Just like a spin current carried by electrons, the spin-wave spin current can transfer spin to the magnetization. The resulting torque on the magnetization is known as the *magnonic spin-transfer torque* [35, 37]. Spin transfer

In more complicated systems than the isotropic Heisenberg model, the magnon spin can deviate from \hbar [11, 250]. Nonetheless, as long as the magnons carry *some* spin, transfer of spin from the magnons to the magnetization is a viable concept.

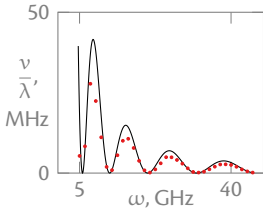
sw helicity in a dw:



sw-induced DW motion:



DW velocity v. drive frequency:



from spin waves can for instance be used to move a domain wall. As an example, we consider an up–down wall in a uniaxial ferromagnet. The handedness of the circularly polarized spin waves changes as they pass through the domain wall. This is the classical analog of the fact that the magnon spin flips as a magnon propagates through a domain wall. Changing the handedness of the spin waves ($M_y \rightarrow +\text{Im} \psi$) changes the sign of the spin-wave spin current, $J_s^z \rightarrow -J_s^z$. To absorb this transfer of spin, the domain wall must move towards the spin-wave source with a velocity

$$v = \frac{|J_s^z|}{M} = -\frac{2\gamma Ak\rho^2}{M^3} = -\frac{v_g \rho^2}{2M^2}, \quad (4.8)$$

where v_g is the spin-wave group velocity $v_g = d\omega/dk = -4\gamma Ak/M$.

Spin-wave-induced domain wall motion was first considered by Ref. 251. Several numerical studies considered different aspects of the interaction between spin waves and domain walls [252–257] before the results of Ref. 251 were independently reproduced analytically [35, 36] and numerically [37]. The numerical studies of spin-wave-induced domain wall motion revealed that the domain wall velocity was very sensitive to the frequency of the locally applied magnetic field acting as a spin-wave source [256–263].

Experimental studies of magnon-induced domain wall motion have mainly focused on thermal magnons [38, 39]. However, a domain wall in a temperature gradient can experience additional torques besides the purely magnonic ones, for instance, the exchange stiffness can vary with temperature [37, 264–269]. Characteristically, these torques can induce a Walker breakdown.

In paper III we consider Walker breakdown and the frequency-dependence of the wall velocity both analytically and numerically. By deriving the equations of motion for a domain wall driven by spin transfer from magnons we show that the magnonic torque does not induce Walker breakdown. Furthermore, we show that much of the frequency dependence of the domain wall velocity found numerically [256–258, 260] can

be attributed to the frequency dependence of the spin-wave-generation efficiency of the spin-wave source, and not to the magnonic spin-transfer torque. Simplistic models for the spin-wave source can therefore introduce spurious frequency dependence that will not be observed experimentally.

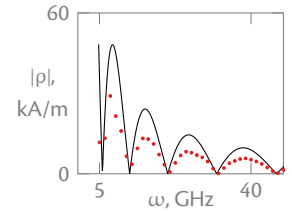
4.3 Classifying multiferroic materials

Multiferroic materials are materials with multiple *ferroic* orders, such as ferromagnetism (spontaneous magnetization), ferroelectricity (spontaneous electric polarization), or ferroelasticity (spontaneous mechanical deformation) [41, 42]. The term is most often used for materials that combine ferromagnetism and ferroelectricity, with a preference for materials that exhibit a *magnetolectric coupling* between the two orders [42].

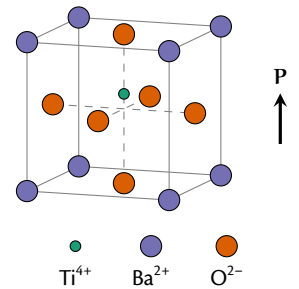
Multiferroic materials are often classified as type-I or type-II multiferroics [270]. Type-I multiferroics are usually good ferroelectrics, and order magnetically at low temperatures ($T \ll T^*$, where T^* is the ferroelectric Curie temperature). Because the origins of magnetism and ferroelectricity in these materials are usually unrelated, there is a weak coupling between the two orders. A case in point are the multiferroic perovskites, such as BaTiO_3 and $\text{Pb}(\text{Zr}_x\text{Ti}_{1-x})\text{O}_3$. The ferroelectricity of these materials is the result of an off-center shift of the transition-metal ion [270, 271], which forms strong covalent bonds to the oxygen ions using its empty d orbitals. This process is suppressed if the d orbitals are partially filled, as is the case for the magnetic transition metals. This antagonism of magnetism and ferroelectricity is why there are so few magnetic ferroelectrics [272].

Type-II multiferroics are magnets in which the magnetic order gives rise to charge order and a spontaneous electric polarization (so-called *improper* ferroelectricity [273]). This gives rise to a strong coupling between the two orders, but the electric polarization is usually much smaller than in type-I multiferroics. Most of the type-II multiferroics are so-called spiral multiferroics, such as TbMnO_3 , $\text{Ni}_3\text{V}_2\text{O}_6$, and MnWO_4 . Terbium

sw amplitude v. drive freq.:

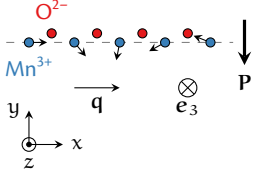


Ferroelectricity in BaTiO_3 :



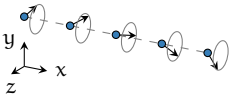
Redrawn after Ref. 271.

Improper ferroelectricity in
TbMnO₃:

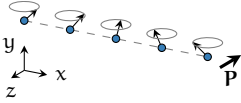


Redrawn after Ref. 273.

Applied field $H \parallel q$,
 $e_3 \parallel q \Rightarrow P = 0$:



Applied field $H \perp q$,
 $e_3 \perp q \Rightarrow P \neq 0$:



manganite provides a good illustration of this mode of multiferroicity. Due to magnetic frustration in the low-temperature magnetic phase, the manganese spins form a spin cycloid in the xy plane which is incommensurate with the crystal lattice [274–276]. Due to the Dzyaloshinskii–Moriya interaction, the spin cycloid can lower its energy by slightly displacing the oxygen atoms from the manganese chain, which can be seen as a form of exchange striction [273, 277]. This intimate connection between the electric polarization and magnetic order gives rise to large magnetoelectric effects. Applying a strong magnetic field H perpendicular to the hard z axis will for instance flop the spin rotation axis e_3 , which is initially parallel to z , to point parallel to the applied field, $e_3 \parallel H$ [278]. Depending on whether the field is applied parallel (x) or perpendicular (y) to the cycloid wave vector q , the resulting polarization is either zero ($H \parallel q$) or flops with the magnetization to point along the z direction ($H \perp q$) [278].

Similar mechanisms can operate independent of crystal symmetry. If the crystal has cubic symmetry ($m\bar{3}m, O_h$), the expression for the electric polarization is particularly simple [278]. Due to the essential role of the spin cycloid in the case of TbMnO₃, we look for terms that couple the polarization to the gradient of the magnetization. Expanding the energy density u in powers of the polarization P_i , the normalized magnetization $m_i = M_i/M$, and gradients of the magnetization $\partial_i m_j$, there are only two terms that contain gradients of the magnetization and respect time-reversal symmetry up to third order,

$$u = \eta_{ijk} m_i \partial_j m_k + \xi_{ijkl} m_i P_j \partial_k m_l .$$

Assuming that the system does not have an instability towards ferroelectricity in the absence of magnetism, we include only the term $\epsilon_{ij} P_i P_j$ in the electric part of the expansion. Thus we consider

$$u = \epsilon_{ij} P_i P_j + \eta_{ijk} m_i \partial_j m_k + \xi_{ijkl} m_i P_j \partial_k m_l . \quad (4.9)$$

The energy density is a proper scalar, the gradient and the polarization are

polar vectors, whereas the magnetization is an axial vector. Consequently, all the tensors ϵ_{ij} , η_{ijk} , and ξ_{ijkl} are polar tensors.

There are no nonzero polar tensors of odd rank that are invariant under $m\bar{3}m$ symmetry. Thus $\eta_{ijk} = 0$ for all i, j , and k . The only invariant polar second-rank tensor is the Kronecker delta [106]. Thus

$$\begin{aligned}\epsilon_{ii} &= 1/2\epsilon_0, \\ \epsilon_{ij} &= 0 \quad \forall i \neq j.\end{aligned}$$

The polar fourth-rank tensor that is invariant under $m\bar{3}m$ has 21 nonzero elements, but only two free parameters [106],

$$\begin{aligned}\xi_{iiii} &= \xi_1, \\ \xi_{xxyy(6)} = \xi_{xxzz(6)} = \xi_{yyzz(6)} &= \xi_2, \\ \xi_{ijkl} &= 0 \text{ for all other } ijkl.\end{aligned}$$

Together, the tensors

$$\delta_{ii}\delta_{jj}, \quad \delta_{ij}\delta_{ij}, \quad \text{and} \quad \delta_{ij}\delta_{ji}$$

generate all these elements. With $i \neq j$, they give the elements $\xi_{xxyy(6)}$, $\xi_{xxzz(6)}$, and $\xi_{yyzz(6)}$, and with $i = j$, they all give the elements ξ_{iiii} . Thus, assuming that $\xi_1 = \xi_2 = \xi$, the tensor ξ_{ijkl} can be written as

$$\xi(\delta_{ii}\delta_{jj} - \delta_{ij}\delta_{ij} + \delta_{ij}\delta_{ji}).$$

Since

$$\delta_{ij}\delta_{ji}m_i\partial_j m_i = \mathbf{m} \cdot (\mathbf{P} \cdot \nabla)\mathbf{m} = 0$$

because $\mathbf{m}^2 = 1$, the energy density can be written as

$$u = \frac{\mathbf{P}^2}{2\epsilon_0} + \xi\mathbf{P} \cdot [\mathbf{m}(\nabla \cdot \mathbf{m}) - (\mathbf{m} \cdot \nabla)\mathbf{m}]. \quad (4.10)$$

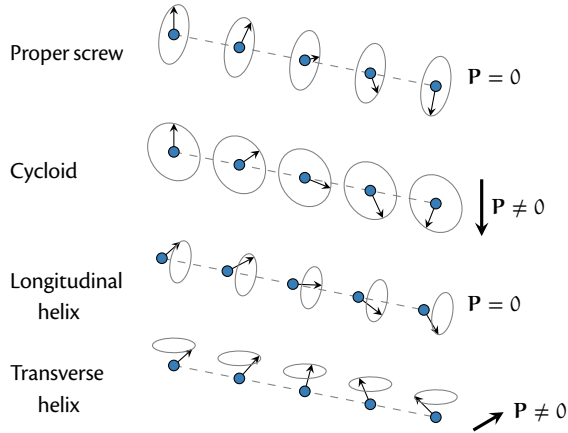
The induced polarization must be such that the energy U is minimal. The condition $\delta U/\delta \mathbf{P} = 0$ gives

$$\mathbf{P} = \gamma_0 [(\mathbf{M} \cdot \nabla)\mathbf{M} - \mathbf{M}(\nabla \cdot \mathbf{M})], \quad (4.11)$$

where we introduced $\gamma_0 = 2\epsilon_0\xi/M^2$.

This coupling between the electric polarization and the magnetization gradient is known as the *inhomogeneous magnetoelectric coupling* or a *flexoelectric coupling* [279]. Figure 4.1 shows a selection of spin structures and the resulting polarization. We recognize the cycloid and the longitudinal and transverse helices from our discussion of TbMnO_3 .

Figure 4.1 Spiral spin structures and the resulting electric polarization, \mathbf{P} , due to the inhomogeneous magneto-electric interaction. In the low-temperature phase, the Mn spins in TbMnO_3 order in a spin cycloid, but application of a magnetic field $\mathbf{H} \perp \mathbf{e}_3$ flops the spiral into the longitudinal helix ($\mathbf{H} \parallel \mathbf{q}$) or the transverse helix ($\mathbf{H} \perp \mathbf{q}$). Redrawn after Ref. 277.

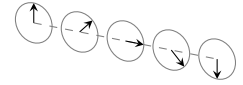


4.4* Magnetization dynamics in type-II multiferroics

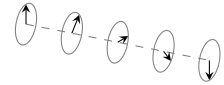
The spin structures in Fig. 4.1 are also familiar from our discussion of domain walls in Chap. 3 and spin waves in the previous sections. A so-called Néel domain wall can be seen as part of a spin cycloid. Thus, even in the uniformly magnetized state, materials with an inhomogeneous magnetoelectric interaction will exhibit an electric polarization at the magnetic domain walls if the walls are of the Néel type [280–282]. Spin waves in the forward-volume geometry (out-of-plane magnetization) will also exhibit an electric polarization [270, 283–286].

Inspired by these results, we consider in paper IV both spin waves in the backward-volume geometry and spin-wave-induced domain wall motion in a ferromagnet with inhomogeneous magnetoelectric coupling. We find that in the presence of magnetic damping, even backward-volume waves give rise to an electric polarization. By applying an electric field, we can use this effect to apply a torque on a homogeneously magnetized sample. However, because the polarization is proportional to the Gilbert damping, this effect is rather small. On the other hand, we find that the magnetoelectric torque can be the dominant factor in spin-wave-induced domain wall motion. By applying an electric field, we are able to control the domain wall velocity as well as its direction of motion (towards or away from the spin-wave source).

Néel wall:



Bloch wall:



Forward-volume waves:



Backward-volume waves:

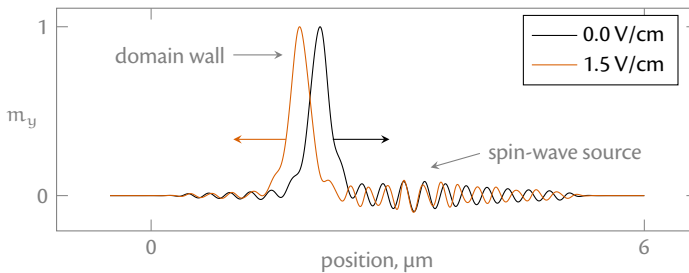
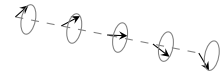


Figure 4.2 Electric-field-controlled domain wall motion in $(\text{BiLu})_3(\text{FeGa})_5\text{O}_{12}$.

Superconductivity

5.1 The Cooper problem

Superconductivity in conventional superconductors is understood in terms of the BCS theory developed by Bardeen, Cooper, and Schrieffer [51]. The BCS superconductor is a momentum-space condensate of pairs of electrons. To better understand this pairing mechanism, we start by considering the one-pair problem, which was first considered by Cooper [50].

The Cooper problem consists of a Fermi sea of noninteracting electrons, to which we add a pair of electrons that interact only with each other. The interaction is described by a potential $V(\mathbf{r})$, where $\mathbf{r} = \mathbf{r}_2 - \mathbf{r}_1$ is the distance between the two electrons. The two interacting electrons must necessarily occupy states above the Fermi level. Their wave function ψ can be written as a product of the plane-wave states that diagonalize the kinetic part of their Hamiltonian,

$$\psi = \sum_{\mathbf{k}_1 > \mathbf{k}_F} a_{\mathbf{k}_1} e^{i\mathbf{k}_1 \cdot \mathbf{r}_1} \sum_{\mathbf{k}_2 > \mathbf{k}_F} b_{\mathbf{k}_2} e^{i\mathbf{k}_2 \cdot \mathbf{r}_2} = \sum_{\mathbf{k}} c_{\mathbf{k}} e^{i\mathbf{k} \cdot \mathbf{r}} \sum_{\mathbf{Q}} d_{\mathbf{Q}} e^{i\mathbf{Q} \cdot \mathbf{R}}. \quad (5.1)$$

Here, we introduced the center-of-mass and relative coordinates and momenta, $\mathbf{r} = \mathbf{r}_2 - \mathbf{r}_1$, $\mathbf{k} = \mathbf{k}_1 + \mathbf{k}_2$, $\mathbf{R} = \frac{1}{2}(\mathbf{r}_1 + \mathbf{r}_2)$, and $\mathbf{Q} = \frac{1}{2}(\mathbf{k}_2 - \mathbf{k}_1)$. We assume that the system is translation invariant, in which case the two-particle wave function ψ cannot depend on the center-of-mass coordinate \mathbf{R} . Thus $d_{\mathbf{Q}} = 0$ for all $\mathbf{Q} \neq 0$. For convenience of notation, we take $d_0 = 1$.

Isolating the potential term, the Schrödinger equation of the two interacting electrons can be written as

$$(E - T)\psi = V(\mathbf{r})\psi, \quad (5.2)$$

where T is $T = -(\nabla_1^2 + \nabla_2^2)/2m$. To determine ψ , we need to find expressions for the coefficients $c_{\mathbf{k}}$. We are also interested in finding the eigenenergy E . To accomplish this, we multiply the Schrödinger equation from the left with ψ^* and integrate over \mathbf{r} . Using the orthogonality of the plane-wave states the Schrödinger equation simplifies to

$$\sum_{\mathbf{k}} |c_{\mathbf{k}}|^2 (E - 2\epsilon_{\mathbf{k}}) = \sum_{\mathbf{k}, \mathbf{k}'} V_{\mathbf{k}, \mathbf{k}'} c_{\mathbf{k}}^* c_{\mathbf{k}'},$$

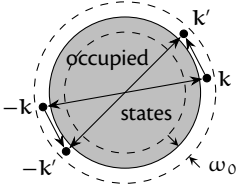
where

$$V_{\mathbf{k}, \mathbf{k}'} = \frac{1}{\Omega} \int d\mathbf{r} e^{-i\mathbf{k} \cdot \mathbf{r}} V(\mathbf{r}) e^{i\mathbf{k}' \cdot \mathbf{r}}$$

and $\epsilon_{\mathbf{k}} = k^2/2m$, with m being the electron mass. Setting the two summands equal we obtain

$$c_{\mathbf{k}} (E - 2\epsilon_{\mathbf{k}}) = \sum_{\mathbf{k}'} V_{\mathbf{k}, \mathbf{k}'} c_{\mathbf{k}'}. \quad (5.3)$$

States coupled by $V_{\mathbf{k}, \mathbf{k}'}$:



The electrons attract inside a thin shell around the Fermi surface. Redrawn after Ref. 45.

We now assume that the matrix element $V_{\mathbf{k}, \mathbf{k}'}$ is

$$V_{\mathbf{k}, \mathbf{k}'} = \begin{cases} -V, & |\epsilon_{\mathbf{k}} - \epsilon_F| < \omega_0 \text{ and } |\epsilon_{\mathbf{k}'} - \epsilon_F| < \omega_0 \\ 0, & \text{otherwise.} \end{cases} \quad (5.4)$$

Converting the sum over \mathbf{k}' to an integral over ϵ we then obtain

$$c(\epsilon) (2\epsilon - E) = V \int_{\epsilon_F}^{\epsilon_F + \omega_0} d\epsilon' N(\epsilon') c(\epsilon') = W,$$

where we wrote $\epsilon = \epsilon_{\mathbf{k}}$ and introduced the density of states $N(\epsilon)$. Since W is independent of ϵ , this equation gives the expression

$$c(\epsilon) = \frac{W}{2\epsilon - E}, \quad (5.5)$$

for the coefficients $c(\epsilon)$. Seeing that the coefficients c only depend on the wave vector \mathbf{k} through the energy $\epsilon_{\mathbf{k}} = k^2/2m$, we have $c_{\mathbf{k}} = c_{-\mathbf{k}}$. The two-particle wave function is therefore symmetric in the spatial coordinate. Thus, to preserve overall antisymmetry we must choose an antisymmetric spin state, the singlet state.

Inserting the expression for $c(\epsilon)$ into the definition of W , we obtain the self-consistency relation

$$1 = V \int_{\epsilon_F}^{\epsilon_F + \omega_0} d\epsilon' \frac{N(\epsilon')}{2\epsilon' - E} = \lambda \ln \frac{2(\epsilon_F + \omega_0) - E}{2\epsilon_F - E} = \lambda \ln \left(1 + \frac{2\omega_0}{\Delta} \right), \quad (5.6)$$

which determines E . Here we made the approximation $N(\epsilon') \approx N(\epsilon_F)$ and introduced $\lambda = VN(\epsilon_F)$ and the binding energy of the pair, $\Delta = 2\epsilon_F - E$. When V is positive, so that the interaction between the two additional electrons is attractive, Δ must be positive for the self-consistency relation to have a solution. But a positive Δ means that the eigenenergy E is smaller than twice the Fermi energy, $E < 2\epsilon_F$. In other words, for an arbitrarily weak attractive interaction the two electrons occupy a state below the Fermi surface, seemingly in violation of the Pauli principle. It would appear that under such an attractive interaction the Fermi sea somehow collapses [287].

5.2 Fermi-liquid theory

Conventional superconductivity arises out of a real metal where the electrons interact with each other through the Coulomb interaction. Since

the Coulomb interactions are finite, we would expect the arbitrarily weak interaction from the Cooper problem to be inconsequential in the real world.

This expectation turns out to be wrong. Fermi-liquid theory [288, 289] has proven to be a good description of the normal-metal state. Because of the effective screening of the Coulomb interaction by the electron liquid, the quasiparticle excitations of Fermi-liquid theory behave as free electron-like fermions except for, for instance, a renormalized mass. Therefore, the free-electron states we used in the Cooper problem turn out to be good states to start from when constructing the superconducting state [45].

The wave function ψ that we used in the Cooper problem is a product state. It can be written out as

$$\psi = \sum_{\mathbf{k}} c_{\mathbf{k}} e^{i\mathbf{k}\cdot\mathbf{r}} = \sum_{\mathbf{k}} c_{\mathbf{k}} e^{i\mathbf{k}\cdot\mathbf{r}_2} e^{-i\mathbf{k}\cdot\mathbf{r}_1}.$$

Since the factors $e^{i\mathbf{k}\cdot\mathbf{r}_2}$ and $e^{-i\mathbf{k}\cdot\mathbf{r}_1}$ can be thought of as single-particle states of momentum \mathbf{k} and $-\mathbf{k}$, the wave function of the pair is a superposition of product states in which the electrons move in diametrically opposite directions. As a result, different pairs will soon overlap. The concept of bound pairs would be destroyed if the quasiparticles of different overlapping pairs interacted strongly. The BCS theory of superconductivity works because the Fermi-liquid quasiparticles are essentially noninteracting.

5.3 Phonon-mediated attractive interactions

The mechanism that gives rise to the attractive interaction between the electrons is an exchange of phonons. Such a phonon-mediated mechanism is supported by the observation of the so-called *isotope effect*: the critical temperature T_c at which the normal metal passes into the superconducting phase varies with the isotope mass M as [290–293]

$$M^\alpha T_c = \text{const.} \quad (5.7)$$

Typical critical temperatures for the elemental metals and their alloys are 1–10 K [48].

The observation of the isotope effect can only be explained if superconductivity depends critically on the electron–phonon interactions [294–296].

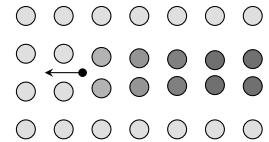
The attractive electron–electron interaction mediated by phonons can be understood by a classical analogy [297]. When a negatively charged electron travels through a lattice of positively charged ions, the electron–ion attraction will move the ions out of their equilibrium positions, and bring them closer to the path of the electron. However, the large ratio of the ion to the electron mass implies that the electron and ion dynamics take place on different time scales. The light electron moves much faster than the heavy ions. As a result, the disturbance of the lattice remains for much longer than the passage of the electron, thus creating a positively charged wake behind it. This wake can attract a second electron. Consequently, by interacting with the same phonon, the electrons experience an attractive interaction that is nonlocal in time, a so-called *retarded interaction*.

The phonon-mediated interaction is maximized if the second electron travels in the opposite direction of the first. Following the trail of the other electron, each of the two electrons is also protected from scattering by an energy barrier. This protection from scattering makes dissipationless conduction in the superconducting state possible.

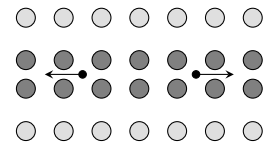
The retardation of the interaction, that is, the time it takes for the ions to relax back into their equilibrium positions, determines the range of the interaction in energy space, ω_0 . Mutual interaction with a phonon cannot give rise to an attraction between electrons separated by an energy larger than the maximal phonon frequency.

The phonon-based mechanism also explains why superconductivity is a low-temperature phenomenon. At high temperatures the presence of thermal phonons disturbs the phonon exchange between the electrons.

An electron traveling through the lattice produces a wake of positive charge:



Another electron traveling in the opposite direction is attracted to the positive charge:



The result is an effective retarded interaction mediated by the phonon. Redrawn after Ref. 298.

5.4 The effective Hamiltonian

In the Cooper problem we considered a system of N free electrons, to which we added two interacting electrons. In a real superconductor *all* the electrons interact attractively. Consequently, the Hamiltonian of the system is

$$\mathcal{H} = \sum_{\mathbf{k}, \sigma} \epsilon_{\mathbf{k}} c_{\mathbf{k}, \sigma}^{\dagger} c_{\mathbf{k}, \sigma} + \sum_{\substack{\mathbf{k}_1, \mathbf{k}_2, \mathbf{q} \\ \sigma_1, \sigma_2}} V_{\mathbf{k}_1, \mathbf{k}_2, \mathbf{q}} c_{\mathbf{k}_1 + \mathbf{q}, \sigma_1}^{\dagger} c_{\mathbf{k}_2 - \mathbf{q}, \sigma_2}^{\dagger} c_{\mathbf{k}_2, \sigma_2} c_{\mathbf{k}_1, \sigma_1},$$

where \mathbf{q} is the momentum exchange between the electrons and $\epsilon_{\mathbf{k}} = k^2/2m - \mu$, with μ being the chemical potential. This Hamiltonian can be considerably simplified by making the same approximation for the matrix element $V_{\mathbf{k}_1, \mathbf{k}_2, \mathbf{q}}$ as we did for the one-pair problem, namely

$$V_{\mathbf{k}_1, \mathbf{k}_2, \mathbf{q}} = \begin{cases} -V, & |\epsilon_{\mathbf{k}} - \epsilon_{\mathbf{F}}| < \omega_0, \text{ for } \mathbf{k} = \mathbf{k}_1, \mathbf{k}_2, \mathbf{k}_1 + \mathbf{q}, \mathbf{k}_2 - \mathbf{q} \\ 0, & \text{otherwise.} \end{cases}$$

Provided that $\omega_0 \ll \epsilon_{\mathbf{F}}$, this approximation implies that the phase space of scattering vectors \mathbf{q} is negligible unless $\mathbf{k}_1 = -\mathbf{k}_2 = \mathbf{k}$. Looking back at the Cooper problem, we also see that since $V_{\mathbf{k}_1, \mathbf{k}_2, \mathbf{q}}$ only depends on the momenta through the energy, the two electrons must have opposite spins, $\sigma_1 = -\sigma_2 = \sigma$. The result is the so-called *pairing Hamiltonian* or *BCS Hamiltonian*:

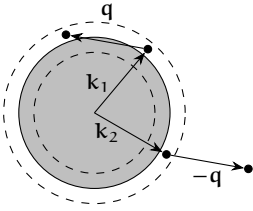
$$\mathcal{H} = \sum_{\mathbf{k}, \sigma} \epsilon_{\mathbf{k}} c_{\mathbf{k}, \sigma}^{\dagger} c_{\mathbf{k}, \sigma} + \sum_{\mathbf{k}, \mathbf{k}'} V_{\mathbf{k}, \mathbf{k}'} c_{\mathbf{k}, \uparrow}^{\dagger} c_{-\mathbf{k}, \downarrow}^{\dagger} c_{-\mathbf{k}', \downarrow} c_{\mathbf{k}', \uparrow}, \quad (5.8)$$

where we renamed $\mathbf{k} + \mathbf{q} \rightarrow \mathbf{k}$ and $\mathbf{k} \rightarrow \mathbf{k}'$ and absorbed the factor of 2 from the sum over σ into $V_{\mathbf{k}, \mathbf{k}'}$.

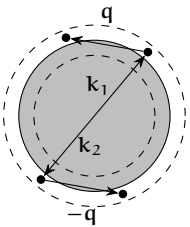
The kinetic term of the BCS Hamiltonian can be rewritten as

$$\sum_{\mathbf{k}, \sigma} \epsilon_{\mathbf{k}} c_{\mathbf{k}, \sigma}^{\dagger} c_{\mathbf{k}, \sigma} = - \sum_{\mathbf{k}} \epsilon_{\mathbf{k}} (1 - n_{\mathbf{k}, \uparrow} - n_{-\mathbf{k}, \downarrow}),$$

If there is no definite relation between \mathbf{k}_1 and \mathbf{k}_2 , the phase space of scattering vectors \mathbf{q} is negligible:



Only for $\mathbf{k}_1 = -\mathbf{k}_2$ is there a large phase space of scattering vectors \mathbf{q} :



Redrawn after Ref. 48.

where $n_{\mathbf{k},\uparrow} = c_{\mathbf{k},\uparrow}^\dagger c_{\mathbf{k},\uparrow}$ and $n_{-\mathbf{k},\downarrow} = c_{-\mathbf{k},\downarrow}^\dagger c_{-\mathbf{k},\downarrow}$. Here, we used $\epsilon_{\mathbf{k}} = \epsilon_{-\mathbf{k}}$ and the fact that the additive constant $-\sum_{\mathbf{k}} \epsilon_{\mathbf{k}}$ does not affect the dynamics. In order to identify the ordered state that solves this Hamiltonian, we make the following useful observation [94, 299]: Acting with $(1 - n_{\mathbf{k},\uparrow} - n_{-\mathbf{k},\downarrow})$ on the state

$$|\cdots, 1_{\mathbf{k},\uparrow}, 1_{-\mathbf{k},\downarrow}, \cdots\rangle = |1\rangle$$

gives

$$(1 - n_{\mathbf{k},\uparrow} - n_{-\mathbf{k},\downarrow})|1\rangle = -|1\rangle,$$

whereas acting on the state

$$|\cdots, 0_{\mathbf{k},\uparrow}, 0_{-\mathbf{k},\downarrow}, \cdots\rangle = |0\rangle$$

gives

$$(1 - n_{\mathbf{k},\uparrow} - n_{-\mathbf{k},\downarrow})|0\rangle = |0\rangle.$$

Thus, if we represent $|0\rangle$ by $(1, 0)$ and $|1\rangle$ by $(0, 1)$, we may write

$$1 - n_{\mathbf{k},\uparrow} - n_{-\mathbf{k},\downarrow} = \begin{pmatrix} 1 & \\ & -1 \end{pmatrix} = \tau_{\mathbf{k}}^z.$$

We can treat the interaction term in the same fashion. Since

$$c_{\mathbf{k},\uparrow}^\dagger c_{-\mathbf{k},\downarrow}^\dagger |1\rangle = 0 \quad \text{and} \quad c_{\mathbf{k},\uparrow}^\dagger c_{-\mathbf{k},\downarrow}^\dagger |0\rangle = |1\rangle$$

we get

$$c_{\mathbf{k},\uparrow}^\dagger c_{-\mathbf{k},\downarrow}^\dagger = \frac{1}{2} \tau_{\mathbf{k}}^- = \tau_{\mathbf{k}}^x - i \tau_{\mathbf{k}}^y.$$

By Hermitian conjugation,

$$c_{-\mathbf{k},\downarrow} c_{\mathbf{k},\uparrow} = \frac{1}{2} \tau_{\mathbf{k}}^+ = \tau_{\mathbf{k}}^x + i \tau_{\mathbf{k}}^y.$$

Here, τ_k^x , τ_k^y , and τ_k^z are the Pauli matrices. We can then conclude that the Hamiltonian can be written as

$$\mathcal{H} = - \sum_{\mathbf{k}} \epsilon_{\mathbf{k}} \tau_{\mathbf{k}}^z + \frac{1}{4} \sum_{\mathbf{k}, \mathbf{k}'} V_{\mathbf{k}, \mathbf{k}'} (\tau_{\mathbf{k}}^x \tau_{\mathbf{k}'}^x + \tau_{\mathbf{k}}^y \tau_{\mathbf{k}'}^y). \quad (5.9)$$

On this form, which is known as the *pseudospin model*, we recognize the Hamiltonian as an XY model with an applied field in the z direction. An important difference between the pseudospin model and the usual XY model is that the real-space lattice indices have been replaced by k-space indices. This points to the fact that we alluded to at the beginning of this chapter, namely that superconductivity is a momentum-space phenomenon.

The XY model has global $O(2)$ symmetry, but in the ordered phase this symmetry is spontaneously broken. Consequently, we can expect to solve this model using a mean-field approach with the order parameter

$$\langle \tau_{\mathbf{k}}^x \rangle = \langle c_{\mathbf{k}, \uparrow}^\dagger c_{-\mathbf{k}, \downarrow}^\dagger \rangle + \langle c_{-\mathbf{k}, \downarrow} c_{\mathbf{k}, \uparrow} \rangle.$$

With this in mind, we write

$$c_{-\mathbf{k}, \downarrow} c_{\mathbf{k}, \uparrow} = b_{\mathbf{k}} + \delta b_{\mathbf{k}} \quad \text{and} \quad c_{\mathbf{k}, \uparrow}^\dagger c_{-\mathbf{k}, \downarrow}^\dagger = b_{\mathbf{k}}^\dagger + \delta b_{\mathbf{k}}^\dagger,$$

where $b_{\mathbf{k}} = \langle c_{-\mathbf{k}, \downarrow} c_{\mathbf{k}, \uparrow} \rangle$ and $\delta b_{\mathbf{k}} = c_{-\mathbf{k}, \downarrow} c_{\mathbf{k}, \uparrow} - \langle c_{-\mathbf{k}, \downarrow} c_{\mathbf{k}, \uparrow} \rangle$, and $b_{\mathbf{k}}^\dagger$ and $\delta b_{\mathbf{k}}^\dagger$ can be obtained by Hermitian conjugation. Substituting these expressions for $c_{-\mathbf{k}, \downarrow} c_{\mathbf{k}, \uparrow}$ and $c_{\mathbf{k}, \uparrow}^\dagger c_{-\mathbf{k}, \downarrow}^\dagger$ into the BCS Hamiltonian, we obtain

$$\mathcal{H} = \sum_{\mathbf{k}, \sigma} \epsilon_{\mathbf{k}} c_{\mathbf{k}, \sigma}^\dagger c_{\mathbf{k}, \sigma} + \sum_{\mathbf{k}, \mathbf{k}'} V_{\mathbf{k}, \mathbf{k}'} (b_{\mathbf{k}}^\dagger c_{-\mathbf{k}', \downarrow} c_{\mathbf{k}', \uparrow} + b_{\mathbf{k}'} c_{\mathbf{k}, \uparrow}^\dagger c_{-\mathbf{k}, \downarrow}^\dagger - b_{\mathbf{k}}^\dagger b_{\mathbf{k}'})$$

to first order in $\delta b_{\mathbf{k}}$. By defining the parameters

$$\Delta_{\mathbf{k}} = - \sum_{\mathbf{k}'} V_{\mathbf{k}, \mathbf{k}'} b_{\mathbf{k}'} \quad \text{and} \quad \Delta_{\mathbf{k}}^\dagger = - \sum_{\mathbf{k}'} V_{\mathbf{k}, \mathbf{k}'} b_{\mathbf{k}'}^\dagger \quad (5.10)$$

this mean-field single-particle Hamiltonian can be written as

$$\mathcal{H} = \sum_{\mathbf{k}, \sigma} \epsilon_{\mathbf{k}} c_{\mathbf{k}, \sigma}^\dagger c_{\mathbf{k}, \sigma} - \sum_{\mathbf{k}} (\Delta_{\mathbf{k}}^\dagger c_{-\mathbf{k}, \downarrow} c_{\mathbf{k}, \uparrow} + \Delta_{\mathbf{k}} c_{\mathbf{k}, \uparrow}^\dagger c_{-\mathbf{k}, \downarrow}^\dagger - b_{\mathbf{k}}^\dagger \Delta_{\mathbf{k}}). \quad (5.11)$$

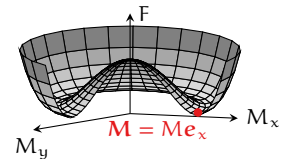
The parameter $\Delta_{\mathbf{k}}$ is called the *superconducting gap* because it, as we will see below, introduces a gap $E_g = 2|\Delta_{\mathbf{k}}|$ in the spectrum.

The BCS Hamiltonian in Eq. (5.8) has global $U(1)$ symmetry—that is, it is unchanged by a transformation $c_{\mathbf{q},\sigma} \rightarrow c_{\mathbf{q},\sigma} e^{i\theta}$ and $c_{\mathbf{q},\sigma}^\dagger \rightarrow c_{\mathbf{q},\sigma}^\dagger e^{-i\theta}$ because there is an equal number of creation and annihilation operators. In the mean-field Hamiltonian in Eq. (5.11), this symmetry is spontaneously broken. So is quasiparticle conservation—Eq. (5.11) contains the terms $c_{\mathbf{k},\uparrow}^\dagger c_{-\mathbf{k},\downarrow}^\dagger$ and $c_{-\mathbf{k},\downarrow} c_{\mathbf{k},\uparrow}$. Both these results are a consequence of the formation of a phase-coherent condensate of Cooper pairs parameterized by the gap $\Delta_{\mathbf{k}}$. The choice of phase for the gap breaks the global $U(1)$ symmetry. The existence of a condensate also enables quasiparticle nonconservation. Two quasiparticles can be annihilated by forming a Cooper pair, or created by breaking an existing pair.

The spontaneously broken global $O(3)$ symmetry of the Heisenberg model in Sect. 2.4 gave rise to gapless excitations—the magnons. The gaplessness of the magnon spectrum is not incidental. The Goldstone theorem states, under quite general conditions, that if the ground state spontaneously breaks a global continuous symmetry of the Hamiltonian, there exist gapless Goldstone modes [89, 300]. Consequently, the spontaneously broken global $U(1)$ symmetry of the BCS Hamiltonian should also give rise to Goldstone modes.

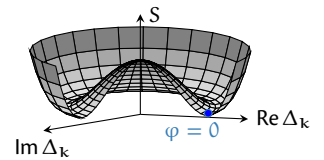
To identify the nature of the Goldstone modes in a superconductor, we can make use of the analogy with the XY model. The Goldstone modes of the XY model are transverse spin fluctuations, magnons. Similarly, the Goldstone modes of a superconductor must be transverse phase fluctuations. However, unlike the XY model, the Cooper pair condensate is charged and couples to the vector potential \mathbf{A} . The gauge freedom of electromagnetism, which is a *local* $U(1)$ symmetry, makes it possible to choose a gauge where there are no phase fluctuations, contingent that the \mathbf{A} field acquires a *mass term* [301–303]. This finite photon mass is responsible for the Meissner effect, which we identified in Sect. 1.4 as one of defining characteristics of a superconductor.

The Landau free energy of the XY model:



Transverse spin fluctuations are gapless for $q \rightarrow 0$.

The effective action for the gap $\Delta_{\mathbf{k}}$:



Transverse phase fluctuations are gapless for $q \rightarrow 0$.

5.5 The BCS gap equation

To identify the spectrum and the equation for the gap, the mean-field Hamiltonian must be diagonalized. For this purpose, we introduce the so-called Nambu spinors

$$\varphi_{\mathbf{k}}^{\dagger} = \left(c_{\mathbf{k},\uparrow}^{\dagger} \quad c_{-\mathbf{k},\downarrow} \right) \quad \text{and} \quad \varphi_{\mathbf{k}} = \begin{pmatrix} c_{\mathbf{k},\uparrow} \\ c_{-\mathbf{k},\downarrow}^{\dagger} \end{pmatrix}$$

to get

$$\mathcal{H} = \sum_{\mathbf{k}} \varphi_{\mathbf{k}}^{\dagger} \begin{pmatrix} +\epsilon_{\mathbf{k}} & -\Delta_{\mathbf{k}} \\ -\Delta_{\mathbf{k}}^{\dagger} & -\epsilon_{\mathbf{k}} \end{pmatrix} \varphi_{\mathbf{k}} + \sum_{\mathbf{k}} (\epsilon_{\mathbf{k}} + b_{\mathbf{k}}^{\dagger} \Delta_{\mathbf{k}}). \quad (5.12)$$

The matrix is Hermitian and can be diagonalized as $U_{\mathbf{k}} D_{\mathbf{k}} U_{\mathbf{k}}^{-1}$ where $D_{\mathbf{k}}$ is diagonal and real and $U_{\mathbf{k}}$ is unitary, $U_{\mathbf{k}}^{-1} = U_{\mathbf{k}}^{\dagger}$. Such a similarity transform is known as a Bogoliubov transform [304]. We choose

$$U_{\mathbf{k}} = \begin{pmatrix} u_{\mathbf{k}} & v_{\mathbf{k}} e^{i\chi} \\ -v_{\mathbf{k}} e^{-i\chi} & u_{\mathbf{k}} \end{pmatrix} \quad \text{where} \quad \begin{aligned} u_{\mathbf{k}} &= \cos \vartheta_{\mathbf{k}}, \\ v_{\mathbf{k}} &= \sin \vartheta_{\mathbf{k}}. \end{aligned}$$

If $\Delta_{\mathbf{k}}$ is not real, it can always be made so by a transformation $c_{\mathbf{q},\sigma} = e^{i\chi/2} c_{\mathbf{q},\sigma}$ and $c_{\mathbf{q},\sigma}^{\dagger} = e^{-i\chi/2} c_{\mathbf{q},\sigma}^{\dagger}$.

Here, χ is the phase of the gap, $\Delta_{\mathbf{k}} = |\Delta_{\mathbf{k}}| e^{i\chi}$. To simplify the remaining calculation, we choose the gap to be real. For $U_{\mathbf{k}}$ to diagonalize the Hamiltonian, we must demand that the off-diagonal elements of $D_{\mathbf{k}}$ vanish identically,

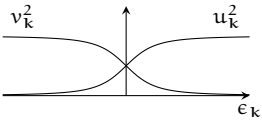
$$2u_{\mathbf{k}}v_{\mathbf{k}}\epsilon_{\mathbf{k}} - (u_{\mathbf{k}}^2 - v_{\mathbf{k}}^2)\Delta_{\mathbf{k}} \stackrel{!}{=} 0.$$

Using the trigonometric identities $2u_{\mathbf{k}}v_{\mathbf{k}} = \sin 2\vartheta_{\mathbf{k}}$ and $u_{\mathbf{k}}^2 - v_{\mathbf{k}}^2 = \cos 2\vartheta_{\mathbf{k}}$, this determines $\vartheta_{\mathbf{k}}$:

$$\tan 2\vartheta_{\mathbf{k}} = \frac{\Delta_{\mathbf{k}}}{\epsilon_{\mathbf{k}}}. \quad (5.13)$$

In turn, $\vartheta_{\mathbf{k}}$ determines $u_{\mathbf{k}}$ and $v_{\mathbf{k}}$. Since $\cos(\arctan \alpha) = 1/\sqrt{1+\alpha^2}$ and $\cos 2\vartheta_{\mathbf{k}} = 2u_{\mathbf{k}}^2 - 1$ we have

$$u_{\mathbf{k}}^2 = \frac{1}{2} \left(1 + \frac{\epsilon_{\mathbf{k}}}{E_{\mathbf{k}}} \right) = 1 - v_{\mathbf{k}}^2, \quad (5.14)$$



where we defined $E_k = \sqrt{\epsilon_k^2 + \Delta_k^2}$. The factors u_k and v_k are known as *coherence factors*. Their existence has experimentally observable consequences in ultrasound attenuation, nuclear magnetic resonance (NMR), and electromagnetic absorption in superconductors [45]. Using the values of the coherence factors, we can calculate the spectrum of \mathcal{H} by writing out the diagonal elements of $D_k = \text{diag}(E_1, E_2)$:

$$E_{1,2} = \pm(u_k^2 - v_k^2)\epsilon_k \pm 2u_k v_k \Delta_k = \pm E_k, \quad E_k = \sqrt{\epsilon_k^2 + \Delta_k^2}.$$

Using the definition

$$\gamma_k = \begin{pmatrix} \gamma_{1,k} \\ \gamma_{2,k}^\dagger \end{pmatrix} = \begin{pmatrix} u_k & -v_k \\ v_k & u_k \end{pmatrix} \begin{pmatrix} c_{k,\uparrow} \\ c_{-k,\downarrow}^\dagger \end{pmatrix}$$

This gives the diagonal Hamiltonian

$$\mathcal{H} = \sum_k E_k (\gamma_{1,k}^\dagger \gamma_{1,k} + \gamma_{2,k}^\dagger \gamma_{2,k}) + \sum_k (\epsilon_k - E_k + b_k^\dagger \Delta_k) \quad (5.15)$$

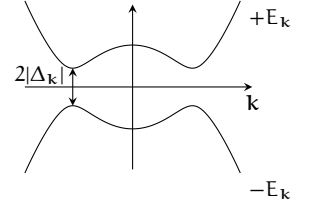
on the form of a free fermion gas. The new fermions created by $\gamma_{1,k}^\dagger$ and $\gamma_{2,k}^\dagger$ are known as *Bogoliubov quasiparticles*.

The superconducting gap is defined using the mean-field parameter $b_k = \langle c_{-k,\downarrow} c_{k,\uparrow} \rangle$. By inverting the definition of γ_k we obtain expressions for the electron operators $c_{-k,\downarrow}$ and $c_{k,\uparrow}$ in terms of the Bogoliubov quasiparticles. Inserting these into the definition of the gap we get

$$\Delta_k = - \sum_{k'} V_{k,k'} u_k v_{k'} \langle 1 - \gamma_{1,k'}^\dagger \gamma_{1,k'} - \gamma_{2,k'}^\dagger \gamma_{2,k'} \rangle.$$

Since the Bogoliubov quasiparticles are free fermions, combined quantum-mechanical and thermal averaging gives

$$\langle \gamma_{1,k}^\dagger \gamma_{1,k} \rangle = \langle \gamma_{2,k}^\dagger \gamma_{2,k} \rangle = f(E_k),$$



where $f(E_k)$ is the Fermi function. Together with $2u_k v_k = \sin 2\theta_k = \Delta_k/E_k$ this gives the *BCS gap equation*,

$$\Delta_k = - \sum_{k'} V_{k,k'} \frac{\Delta_{k'}}{2E_{k'}} \tanh \frac{1}{2} \beta E_{k'}, \quad (5.16)$$

where $\beta = 1/k_B T$. Since $\Delta_{k'}$ appears on the right-hand side, this is a self-consistency relation for the gap.

5.6 Pairing symmetries

As it is written in Eq. (5.16), the gap equation takes into account the possibility that the attractive interaction may vary over the Fermi surface since we carried $V_{k,k'}$ through the calculation. If we make use of the approximation that $V_{k,k'}$ is a constant over the Fermi surface, $V_{k,k'} = -V$, the gap is independent of k , $\Delta_k = \Delta$, which gives

$$1 = V \sum_{\mathbf{k}} \frac{\tanh \frac{1}{2} \beta \sqrt{\epsilon_{\mathbf{k}}^2 + \Delta^2}}{2\sqrt{\epsilon_{\mathbf{k}}^2 + \Delta^2}}. \quad (5.17)$$

When the gap is independent of k , it is spherically symmetric. In other words, it has *s-wave* symmetry. The conventional superconductors are therefore referred to as *s-wave* superconductors.

In unconventional superconductors [305, 306] where the interaction $V_{k,k'}$ varies significantly with momentum, the gap can take on other symmetries. Copper oxides, cuprates, can be superconducting with very high transition temperatures. They are therefore referred to as *high- T_c superconductors* [46, 48, 308]. The high- T_c cuprates are believed to be *d-wave* superconductors [309–314].

Both *s-wave* and *d-wave* superconductors are symmetric in the spatial coordinates. To preserve overall antisymmetry, we therefore chose an antisymmetric spin state, the singlet state. Although we did not take

Typical critical temperatures for the high- T_c superconductors are 30–120 K [48]. The world record at ambient pressure belongs to $\text{HgBa}_2\text{Ca}_2\text{Cu}_3\text{O}_8$ at 133 K [307].

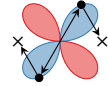
the possibility of the symmetric spin-triplet states into account in the derivation of the gap equation, there exist superconductors which are believed to host spin-triplet superconductivity, such as strontium ruthenate, Sr_2RuO_4 [320–323]. To preserve antisymmetry, the superconducting state must be antisymmetric in the spatial coordinates. The simplest antisymmetric orbital state is the p-wave state, and indeed Sr_2RuO_4 is believed to be a p-wave superconductor [319, 322, 323].

Our discussion of the pairing symmetry tacitly assumes that the correlation between the two quasiparticles in the Cooper pair is even in time (or frequency). Another way to fulfill the constraints of Fermi statistics is for the correlation to be odd in frequency [324, 325]. Odd-frequency correlations can be induced by explicitly breaking the time-reversal symmetry, for instance by applying a magnetic field. It has been suggested that magnesium diboride, MgB_2 —which is a conventional s-wave spin-singlet superconductor [326, 327]—hosts an s-wave spin-triplet odd-frequency phase in an applied magnetic field [328].

Instead of applying a magnetic field, the time-reversal symmetry can also be broken by a ferromagnet. Superconducting correlations will be induced in a material that is proximitized to a superconductor due to the superconducting proximity effect [55, 59, 60]. (The proximity effect will be discussed in the next chapter.) In a s/F heterostructure with a conventional s-wave spin-singlet superconductor and a ferromagnet, there will be induced odd-frequency s-wave spin-triplet correlations in the ferromagnet [61–63, 329, 331–335].

However, breaking the time-reversal symmetry is not a requirement for odd-frequency superconductivity [325]. Odd-frequency correlations can appear even in a s/N heterostructure provided that *two* of the parities of the even-frequency s-wave spin-singlet pairs change simultaneously. For instance, changing both the orbital and frequency parities can give rise to odd-frequency p-wave spin-singlet correlations in the normal metal [330].

Superconductivity with spatial symmetries other than s wave (p wave and d wave) are very sensitive to disorder because impurity scattering can easily break up the Cooper pair:



Impurity concentrations as small as 1 % can be detrimental [315–319].

Pairing symmetries, examples:

Ref.		S	P	T	tot.
51	BCS	–	+	+	–
309	high- T_c	–	+	+	–
322	Sr_2RuO_4	+	–	+	–
328	MgB_2	+	+	–	–
329	s/F	+	+	–	–
330	s/N	–	–	–	–

S: spin; P: parity; T: time

The physical origin of the scattering-matrix elements that link s-wave to p-wave pairing is in this case the broken translation symmetry at the interface [330].

Superconducting spintronics

6.1 Andreev reflection and the proximity effect

The BCS Hamiltonian in the mean-field approximation is an effective single-particle description of a superconductor. In other words, it is a Hamiltonian for the quasiparticles in the superconductor. The effects of the condensate of Cooper pairs enters the problem through the gap parameter, $\Delta_{\mathbf{k}}$. Many of the properties of the normal phase—such as simple band structures and metallic/insulating behavior—can be understood in terms of the Schrödinger equation [78]. Similarly, many of the properties of superconductors can be understood in terms of the first-quantized wave equation for the quasiparticles [47, 336, 337]. The wave equation that corresponds to the mean-field Hamiltonian in Eq. (5.11) is [336]

$$\begin{aligned} i \frac{\partial f}{\partial t} &= -\frac{1}{2m} \frac{\partial^2 f}{\partial x^2} - \mu f - \Delta g, \\ i \frac{\partial g}{\partial t} &= +\frac{1}{2m} \frac{\partial^2 g}{\partial x^2} + \mu g - \Delta^* f, \end{aligned} \quad (6.1)$$

as can be checked by the usual procedure $T_2 = \sum_{\mu, \nu} \langle \mu | T_1 | \nu \rangle a_{\mu}^{\dagger} a_{\nu}$, where T_1 is a first-quantized and T_2 is a second-quantized single-particle operator. This equation is known as the *Bogoliubov–de Gennes equation* [47]. In the normal state the gap vanishes, $\Delta = 0$, and the two components of the Nambu spinor uncouple. In that case, the equation for g is the time-reversed partner of the equation for f and we call f the electron component and g the hole component. In the presence of a gap, the time-independent

Bogoliubov–de Gennes equation is solved by

$$\begin{pmatrix} u \\ -ve^{-ix} \end{pmatrix} e^{ik_+x} \quad \text{and} \quad \begin{pmatrix} ve^{ix} \\ u \end{pmatrix} e^{ik_-x}$$

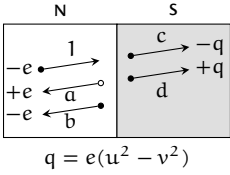
where

$$k_{\pm} = \sqrt{2m[\mu \pm \sqrt{(E^2 - \Delta^2)}]}$$

and we dropped the subscripts k . The first of these solutions is known as an electronlike quasiparticle and the second is known as a holelike quasiparticle because their charges are, respectively, $-e(u^2 - v^2)$ and $+e(u^2 - v^2)$, which reduce to $-e$ and $+e$ when $\Delta \rightarrow 0$, giving $u^2 \rightarrow 1$ and $v^2 \rightarrow 0$.

In a N/s bilayer we must match the wave functions from the normal-metal and superconducting sides at the interface. We consider the case of an electron coming in from the normal side, $f = e^{iq_+x}$, where $q_{\pm} = \sqrt{2m[\mu \pm \epsilon]}$. In general, the wave function on the normal-metal side is then

Scattering in a N/s bilayer:



$$\psi_N = \begin{pmatrix} 1 \\ 0 \end{pmatrix} e^{iq_+x} + \begin{pmatrix} 0 \\ a \end{pmatrix} e^{iq_-x} + \begin{pmatrix} b \\ 0 \end{pmatrix} e^{-iq_+x}$$

and the wave function on the superconducting side is

$$\psi_S = c \begin{pmatrix} u \\ -ve^{-ix} \end{pmatrix} e^{ik_+x} + d \begin{pmatrix} ve^{ix} \\ u \end{pmatrix} e^{-ik_-x}.$$

Matching the wave function and its derivative at $x = 0$ gives

$$a = -\frac{v}{u} e^{-ix}, \quad b = 0, \quad c = \frac{1}{u}, \quad \text{and} \quad d = 0$$

in the approximation where $q_+ = q_- = k_+ = k_- = k$. We see that the incoming electron can be transmitted to the superconductor as an electronlike quasiparticle, or be reflected as a hole. Such a reflection process is known as *Andreev reflection* [338–342].

If the energy of the incoming quasiparticle is smaller than the gap, the wave number k_+ of the electronlike quasiparticle will have a small imaginary component, which gives rise to a decay on the length scale λ ,

$$\frac{1}{\lambda} = \frac{\Delta}{\hbar v_F} \sqrt{1 - \frac{E^2}{\Delta^2}}.$$

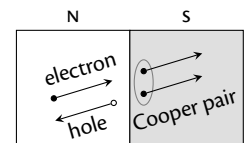
The characteristic length $\xi = \hbar v_F / \pi \Delta$ is known as the *superconducting coherence length*, and is a rough measure of the size of a Cooper pair and a typical length scale for spatial variations in the gap. Beyond about one coherence length, the current carried by a quasiparticle with an energy smaller than the gap is converted to a supercurrent carried by the condensate [336]. Taking this conversion into account, we can gain an intuitive understanding of Andreev reflection: In a typical Andreev process, the incident electron picks up another electron at the interface and forms a Cooper pair. The hole that is left by the second electron is reflected into the normal metal.

The Andreev-reflected hole picks up a phase $-\chi$, where χ is the phase of the superconductor at the interface. Hence, Andreev processes carry phase information about the superconductor into the normal metal. In the zero-temperature limit, such as in the calculation above, the phase information is carried infinitely far into the normal metal [343]. At finite temperature the Andreev-reflected particle will scatter off, say, phonons and lose the phase information beyond the phase-relaxation length [59, 343–345].

The phase information carried into the normal metal by Andreev-reflected particles induces superconducting correlations $\langle c_{-k,\downarrow} c_{k,\uparrow} \rangle$ inside the normal metal. This is the proximity effect that we alluded to in Sect. 5.6. Depending on the scattering matrix at the interface, most of the induced Cooper pairs may have the same symmetry as those of the superconductor itself, or there might be induced a significant amount of, say, odd-frequency p-wave correlations.

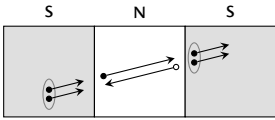
Typical coherence lengths for the elemental metals are $10^1 - 10^3$ nm [78].

Andreev reflection:



Redrawn after Ref. 298.

Josephson effect:



Redrawn after Ref. 298.

In a s/N/s trilayer a hole that impinges on one of the superconductors may be Andreev reflected as an electron. This process destroys one Cooper pair in the first superconductor. The electron may then propagate all the way to the other superconductor and be Andreev reflected as a hole. This process creates one Cooper pair in the second superconductor. Consequently, the overall result is that a Cooper pair is transferred from the first superconductor to the second superconductor. Since the processes are phase-coherent, they will also transfer phase information between the two superconductors. Depending on the phase difference $\delta\chi = \chi_1 - \chi_2$ between the superconductors there might be an equal number of Cooper pairs transferred from left to right and from right to left ($\delta\chi = 0$), or the Andreev processes may carry a net current between the two superconductors. This effect is known as the *Josephson effect*, and the s/N/s trilayer is an example of a *Josephson junction* [346–348].

6.2 Josephson junctions

This assumption is the basis for the phenomenological Ginzburg–Landau theory of superconductivity [46, 54]. The phenomenological theory can be derived from BCS theory [349, 350], in which case ψ is proportional to the gap Δ .

The junction originally considered by Josephson was a s/I/s junction where I is an insulator, or in other words, a tunneling barrier. If we *assume* that the Cooper-pair condensate in each superconductor can be described by a wave function ψ , then tunneling across such a barrier can be described by the coupled equations [80]

$$\begin{aligned} i\hbar \frac{\partial \psi_1}{\partial t} &= H_1 \psi_1 + T \psi_2, \\ i\hbar \frac{\partial \psi_2}{\partial t} &= T \psi_1 + H_2 \psi_2, \end{aligned}$$

where H_i is the Hamiltonian of superconductor i and T is a scalar. Writing out

$$\psi_1 = \sqrt{\rho_1} e^{i\chi_1} \quad \text{and} \quad \psi_2 = \sqrt{\rho_2} e^{i\chi_2},$$

substituting ψ_1 and ψ_2 back into the set of coupled equations, and taking the real and imaginary part of each equation we get

$$\begin{aligned}\hbar \frac{\partial \rho_1}{\partial t} &= +2T\sqrt{\rho_1\rho_2} \sin \delta\chi, & \hbar \frac{\partial \chi_1}{\partial t} &= -T\sqrt{\frac{\rho_2}{\rho_1}} \cos \delta\chi - E_1, \\ \hbar \frac{\partial \rho_2}{\partial t} &= -2T\sqrt{\rho_1\rho_2} \sin \delta\chi, & \hbar \frac{\partial \chi_2}{\partial t} &= -T\sqrt{\frac{\rho_1}{\rho_2}} \cos \delta\chi - E_2,\end{aligned}$$

where the energy E_i is defined by $H_i\psi_i = E_i\psi_i$. The amplitudes ρ_i are proportional to the superfluid density, consequently $\partial\rho_i/\partial t$ is proportional to the current density. The current through the s/I/s Josephson junction is thus

$$I(\delta\chi) = I_0 \sin \delta\chi. \quad (6.2)$$

The maximal current supported by this current–phase relation is I_0 . Attempts to push a larger current through the junction result in a resistive component as well as the dissipationless supercurrent. The current I_0 is therefore known as the *critical current* of the junction.

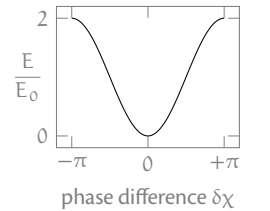
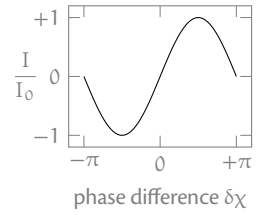
By subtracting the equations of motion of χ_1 and χ_2 , we find

$$\hbar \frac{\partial \delta\chi}{\partial t} = -(E_1 - E_2). \quad (6.3)$$

If the superconductors are identical except for a voltage V applied across the junction this energy difference is $2eV$, where $2e$ is the charge of a Cooper pair. Integrating up the electrical work of done by the applied voltage $\int dt IV = \int d\delta\chi \hbar I/2e$, we see that the energy stored in the junction is [46]

$$E(\delta\varphi) = E_0(1 - \cos \delta\chi), \quad (6.4)$$

where we chose the zero on the energy axis to be such that the integration constant equals $E_0 = \hbar I_0/2e$.



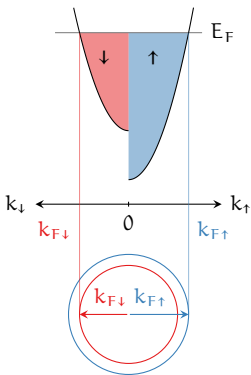
The s/I/s junction is called a 0 junction because its energy is minimal at $\delta\chi = 0$ (modulo 2π) [62, 63, 351, 352]. More complicated Josephson junctions can have more complicated current–phase relations [348, 353, 354]. In ballistic systems, higher harmonics can for instance occur at low temperatures. These higher harmonics are a result of Andreev-reflected electrons or holes that bounce several times back and forth between the superconductors. Consider the s/N/s trilayer we discussed on page 80. When the hole that impinges on the left superconductor is Andreev reflected as an electron, it picks up a phase χ_1 . The Andreev-reflected electron propagates to the right superconductor, and picks up a phase $-\chi_2$ when it is Andreev reflected as a hole. When this hole has completed the round trip and reaches the first superconductor it has accumulated a dynamic phase $q_+L - q_-L \approx 0$, where L is the length of the normal metal, and a scattering phase $\delta\chi$. Multiple round trips give rise to phases of $2\delta\chi$, $3\delta\chi$, and so on and so forth. The result is a current–phase relation on the form [351, 355]

$$I = I_1 \sin \delta\chi + I_2 \sin 2\delta\chi + I_3 \sin 3\delta\chi + \dots$$

In the next sections we will see that ferromagnetic interlayers can also modify the current–phase relation of a Josephson junction. This gives rise to exotic junction such as π junctions and ϕ_0 junctions.

6.3 Spin mixing and π junctions

In itinerant ferromagnets the majority and minority bands are spin split. Consequently, the Fermi wave number is smaller for minority electrons (\downarrow) than for the majority electrons (\uparrow). Let k_F be the Fermi wave number in absence of magnetism. With a finite exchange splitting the majority and minority Fermi wave numbers are, respectively, $k_{F\uparrow} = k_F + Q/2$ and $k_{F\downarrow} = k_F - Q/2$. A Cooper pair formed from two electrons with opposite spins will therefore acquire a center-of-mass momentum Q . In



Redrawn after Ref. 352.

a s/F proximity structure a singlet Cooper pair entering the ferromagnet will oscillate into a spin-0 triplet pair because of the interference between its $\uparrow\downarrow$ and $\downarrow\uparrow$ constituents [352, 356–358].

$$\begin{aligned} (\uparrow\downarrow - \downarrow\uparrow) &\rightarrow (\uparrow\downarrow e^{iQ} - \downarrow\uparrow e^{-iQ}) \\ &= (\uparrow\downarrow - \downarrow\uparrow) \cos Q + i(\uparrow\downarrow + \downarrow\uparrow) \sin Q. \end{aligned} \quad (6.5)$$

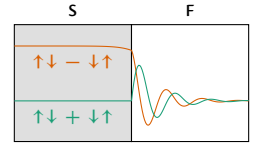
This process is known as *spin mixing* [359]. In principle, the triplet component of the Cooper pair can become either an even-frequency p-wave pair, or an odd-frequency s-wave pair. In practice, p-wave correlations can often be neglected because the relevant experimental samples are disordered.

The wavelength of the singlet–triplet oscillations is $2\pi/Q$, and decreases with increasing exchange splitting. In a s/F/s Josephson junction the number of wavelengths that fit inside the ferromagnet will depend on its length L . If the length of the ferromagnet equals an even number of half wavelengths, $L = 2n\pi/Q$, the singlet components on each side will have the same sign at equilibrium. On the other hand, if the length of the ferromagnet equals an odd number of half wavelengths, $L = (2n + 1)\pi/Q$, the singlet components will have opposite signs at equilibrium, corresponding to a phase shift by $\delta\chi = \pi$ [360–362]. Such a junction is therefore known as a π junction. By changing the length of the junction or its temperature (thus changing effective center-of-mass momentum Q), it is possible to create 0 – π oscillations, going from a 0 to a π ground state [363, 364].

6.4 Spin rotation and spin supercurrents

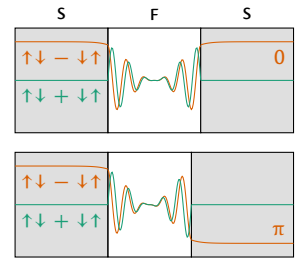
Due to the pair-breaking effect of the magnetic exchange, both the singlet and spin-0-triplet correlations decay rapidly into the magnet, even more so than in a disordered s/N bilayer [62]. The critical currents of such junctions are therefore relatively small, and decrease with larger exchange

Singlet–triplet mixing:



Redrawn after Ref. 352.

0 and π junctions:



Redrawn after Ref. 352.

splittings. The equal-spin triplets, $\uparrow\uparrow$ and $\downarrow\downarrow$, are however not affected by the magnetic exchange. Josephson junctions based on these correlations thus promise higher critical currents. A supercurrent carried by equal-spin triplets will also be spin polarized. Besides the fundamental interest in dissipationless spin currents [365], spin-polarized supercurrents also have potential applications in spintronics [366].

The simplest way—conceptually—to make equal-spin triplets is to use a magnetic inhomogeneity [61, 329, 331, 333, 334]. Using the z axis as quantization axis, we have expressed the spin-0 triplet as $(\uparrow\downarrow + \downarrow\uparrow)_z$. The same spin state can be expressed as $i(\uparrow\uparrow + \downarrow\downarrow)_y$ by quantizing the spin along the y axis. To see this we consider the quantum-mechanical rotation operator. Spin- $1/2$ is rotated by [367]

$$R(\vartheta) = \exp\left(-\frac{i}{2}\vartheta \boldsymbol{\sigma} \cdot \mathbf{n}\right),$$

where ϑ is the rotation angle, \mathbf{n} is the rotation axis, and $\boldsymbol{\sigma}$ is the vector of Pauli matrices. Since the square of a Pauli matrix is the identity, odd and even powers of $(\boldsymbol{\sigma} \cdot \mathbf{n})$ separate:

$$(\boldsymbol{\sigma} \cdot \mathbf{n})^\ell = \begin{cases} I, & \ell \text{ even,} \\ \boldsymbol{\sigma} \cdot \mathbf{n}, & \ell \text{ odd.} \end{cases}$$

Hence, by Taylor-expanding the exponential the rotation operator can be written as

$$R(\vartheta) = I \cos \frac{1}{2}\vartheta - i(\boldsymbol{\sigma} \cdot \mathbf{n}) \sin \frac{1}{2}\vartheta$$

and the rotation operator that takes the quantization axis from z to y is

$$R(z \rightarrow y) = \frac{\sqrt{2}}{2} \begin{pmatrix} 1 & i \\ i & 1 \end{pmatrix}.$$

Consequently, the state $(\uparrow\downarrow + \downarrow\uparrow)_z$ can be written as

$$R_1 R_2 (\uparrow\downarrow + \downarrow\uparrow)_z = i(\uparrow\uparrow + \downarrow\downarrow)_y.$$

Whereas the $(\uparrow\downarrow + \downarrow\uparrow)_z$ pair is short-ranged in a z -polarized magnet, the $i(\uparrow\uparrow)_y$ part of the pair is long-ranged in a y -polarized magnet. Using a magnet where the magnetization rotates from z to y at the S/F interface, the short-ranged $(\uparrow\downarrow + \downarrow\uparrow)_z$ pair generated by singlet–triplet mixing can therefore be converted to a long-ranged $(\uparrow\uparrow)_y$ pair in the bulk of the magnet. This process is known as *spin rotation*. Equal-spin triplets have been generated experimentally using both intrinsic [331, 368] and engineered [369–371] magnetic inhomogeneities.

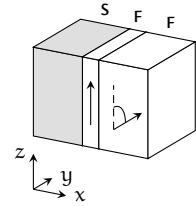
Spin–orbit coupling mixes spin up and spin down, just like the spin-rotation operator. Spin–orbit coupling in combination with a *homogeneous* magnet can therefore be an alternative way to generate long-ranged equal-spin triplets [372, 373]. The advantage of using spin–orbit coupling would be to reduce the experimental complexity related to magnetic control in multilayer structures [370, 371]. It comes, however, with its own set of challenges. With pure Rashba spin–orbit coupling the magnet is required to have both an in-plane (IP) and an out-of-plane (OOP) component for equal-spin triplets to appear [374, 375]. Repeated experimental efforts to realize a long-ranged supercurrent in such systems have yet to succeed [376, 377].

6.5 φ_0 junctions

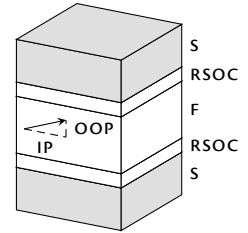
For long-range triplet generation in a $S/F_1/F_2/F_3/S$ junction, a coplanar magnetization texture will suffice [369]. Depending on the exact parameters of the junction, its ground state may be either the 0 or π state. However, if the magnetizations of the three magnets are *not* coplanar, $\mathbf{M}_1 \cdot (\mathbf{M}_2 \times \mathbf{M}_3) \neq 0$, the ground state of the junction is found at a phase difference of $\delta\chi = \varphi_0$, where φ_0 is *not* an integer multiple of π [378]. Such a junction is known as a φ_0 junction.

The origin of the anomalous phase φ_0 can be understood in terms of Andreev processes [378]. We consider a trilayer junction with magnetiza-

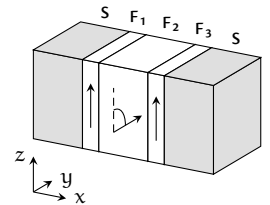
Generation of equal-spin triplets by a magnetic inhomogeneity:



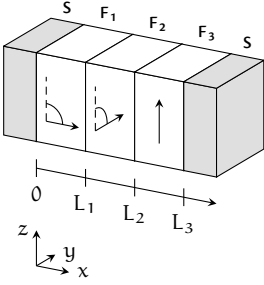
Long-range triplet generation by Rashba coupling:



A $S/F_1/F_2/F_3/S$ junction with long-ranged triplets:



A φ_0 junction:



tions along the x , y , and z axes, $\mathbf{M}_1 = M\mathbf{e}_x$, $\mathbf{M}_2 = M\mathbf{e}_y$, and $\mathbf{M}_3 = M\mathbf{e}_z$. The spin-resolved Bogoliubov–de Gennes equation is

$$\begin{aligned} i\frac{\partial f}{\partial t} &= -\frac{1}{2m}\frac{\partial^2 f}{\partial x^2} - \mu f + D\mathbf{M} \cdot \boldsymbol{\sigma} f + \Delta g, \\ i\frac{\partial g}{\partial t} &= +\frac{1}{2m}\frac{\partial^2 g}{\partial x^2} + \mu g - D\mathbf{M} \cdot \boldsymbol{\sigma}^* g + \Delta^\dagger f, \end{aligned} \quad (6.6)$$

where f and g are two-component spinors and $\Delta = \text{antidiag}(+\Delta, -\Delta)$. Since σ_y has eigenvectors

$$\begin{pmatrix} -i \\ 1 \end{pmatrix} \quad (\text{eigenvalue } +1); \quad \begin{pmatrix} +i \\ 1 \end{pmatrix} \quad (\text{eigenvalue } -1),$$

a spin-up electron at $x = L_1 + 0^+$ can be written as

$$(1 \ i \ 0 \ 0)^T.$$

If the electron moves to the right it has accumulated a phase $k_\uparrow L_2$ upon reaching $x = L_1 + L_2$,

$$(1 \ i \ 0 \ 0)^T e^{ik_\uparrow L_2}.$$

Here, $k_\uparrow = k + Q/2$ and $k_\downarrow = k - Q/2$ are the wave numbers of up and down electrons, respectively. Since σ_z has eigenvectors

$$\begin{pmatrix} 1 \\ 0 \end{pmatrix} \quad (\text{eigenvalue } +1); \quad \begin{pmatrix} 0 \\ 1 \end{pmatrix} \quad (\text{eigenvalue } -1),$$

the electron is in a superposition of the up and down states once it enters F_3 . The two components pick up different phases $k_\uparrow L_3$ and $k_\downarrow L_3$ in F_3 , giving

$$\left[(1 \ 0 \ 0 \ 0)^T e^{ik_\uparrow L_3} + (0 \ i \ 0 \ 0)^T e^{ik_\downarrow L_3} \right] e^{ik_\uparrow L_2}.$$

We can interpret this as the y -up electron precessing about the z axis. When the electron is Andreev reflected at the right superconductor, its

spin flips and it picks up a phase $-\chi_2$, thus the Andreev-reflected hole has the wave function

$$\frac{v}{u} e^{-i\chi_2} \left[(0 \ 0 \ i \ 0)^T e^{ik_\downarrow L_3} + (0 \ 0 \ 0 \ -1)^T e^{ik_\uparrow L_3} \right] e^{ik_\uparrow L_2}.$$

This superposition of a spin-up and a spin-down hole propagates back to $x = L_1 + L_2$, accumulating phases $-k_\uparrow L_2$ and $-ik_\downarrow L_3$. Thus, at $x = L_1 + L_2$ we have the state

$$\frac{v}{u} e^{-i\chi_2} \left[(0 \ 0 \ i \ 0)^T e^{-iQL_3} + (0 \ 0 \ 0 \ -1)^T e^{iQL_3} \right] e^{ik_\uparrow L_2}.$$

Assuming that the total precession angle is $QL_3 = \pi/2$, we can rewrite this state as a spin-up hole quantized along the y axis,

$$\frac{v}{u} e^{-i\chi_2} (0 \ 0 \ 1 \ -i)^T e^{ik_\uparrow L_2}.$$

The hole propagates through F_2 accumulating a phase $-k_\uparrow L_2$, giving

$$\frac{v}{u} e^{-i\chi_2} (0 \ 0 \ 1 \ -i)^T$$

at $x = L_1$. Since σ_x has eigenvectors

$$\begin{pmatrix} +1 \\ 1 \end{pmatrix} \quad (\text{eigenvalue } +1); \quad \begin{pmatrix} -1 \\ 1 \end{pmatrix} \quad (\text{eigenvalue } -1),$$

this state corresponds to a superposition of a spin up and a spin down hole. Upon propagating through F_1 , the up component picks up a phase $-k_\uparrow L_1$ and the down component picks up a phase $-k_\downarrow L_1$. This gives the wave function

$$\frac{v}{u} e^{-i\chi_2} \left[\frac{1-i}{2} (0 \ 0 \ 1 \ 1)^T e^{-ik_\uparrow L_1} + \frac{1+i}{2} (0 \ 0 \ 1 \ -1)^T e^{-ik_\downarrow L_1} \right]$$

at $x = 0$. The Andreev-reflected electron has its spin flipped and picks up a scattering phase χ_1 . Using $\delta\chi = \chi_1 - \chi_2$, the outgoing wave function is

$$\left(\frac{v}{u}\right)^2 e^{i\delta\chi} \left[\frac{1-i}{2} (-1 \ 1 \ 0 \ 0)^T e^{-ik_\uparrow L_1} + \frac{1+i}{2} (1 \ 1 \ 0 \ 0)^T e^{-ik_\downarrow L_1} \right].$$

Completing the round trip, we obtain the state

$$\left(\frac{v}{u}\right)^2 e^{i\delta\chi} \left[\frac{1-i}{2} (-1 \ 1 \ 0 \ 0)^T e^{-iQL_1} + \frac{1+i}{2} (1 \ 1 \ 0 \ 0)^T e^{iQL_1} \right].$$

If the total precession angle accumulated to and fro through F_1 is also $QL_1 = \pi/2$, the result is

$$\left(\frac{v}{u}\right)^2 e^{i\delta\chi} e^{i\pi/2} (1 \ i \ 0 \ 0)^T$$

at $\chi = L_1$. This is precisely the spin-up electron we started with, except for a phase $\delta\chi + \pi/2$. Comparing this result with our discussion in Sect. 6.2, we see that the y-up electron carries a current $I_\uparrow = I_{\uparrow 0} \sin(\delta\chi + \pi/2)$. A similar treatment of the y-down electron gives a current $I_\downarrow = I_{\downarrow 0} \sin(\delta\chi - \pi/2)$. In a junction with perfectly transparent F/F interfaces, the two contributions to the current cancel, $I_\uparrow + I_\downarrow = 0$, leaving only the current from the second-harmonic contribution. However, in a real junction more of the spin-up component than the spin-down component will be transmitted through each F/F interface. Hence, $I_{\uparrow 0} \neq I_{\downarrow 0}$ and the junction exhibits an anomalous phase shift φ_0 . This is known as the *anomalous Josephson effect*.

The anomalous Josephson effect has also been predicted to exist in Josephson junctions made from unconventional superconductors [379–382], in ordinary s/N/s junctions with spin–orbit coupling and a suitably oriented Zeeman field [383–385], and in s/F/s junctions on a topological insulator [386]. Furthermore, it has been predicted [387–389] as well as experimentally confirmed [390] for the Josephson current through a quantum dot. The exact mechanism that gives rise to the anomalous phase φ_0 in each of these cases is different from the one we described above, but in each case time-reversal symmetry and chiral symmetry is broken [383, 391, 392].

Time-reversal symmetry requires that $I(-\delta\chi) = -I(\delta\chi)$, forcing the current at $\delta\chi = 0$ to zero. Broken time-reversal symmetry is therefore a requirement for the anomalous Josephson effect, but not in itself enough.

In, say, the ferromagnetic 0 and π junctions we considered in Sect. 6.3, time-reversal symmetry is broken, but $I(0) = 0$. However, combined with a broken chiral symmetry, broken time-reversal symmetry allows for an anomalous phase φ_0 . Above, the chiral symmetry is broken by the triple product $\mathbf{M}_1 \cdot (\mathbf{M}_2 \times \mathbf{M}_3) \neq 0$. In, say, the $s/N/s$ junction, the chiral symmetry is broken by the triple product $\mathbf{n} \cdot (\mathbf{B} \times \mathbf{J})$ [385]. Here, \mathbf{n} is the direction of broken inversion symmetry, \mathbf{B} is the applied magnetic field, and \mathbf{J} is the current density.

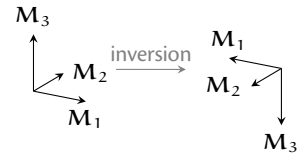
In paper VII we consider a slightly different φ_0 junction. In and of itself, this junction does not exhibit any anomalous phase. However, using a superconducting spin Hall effect and a transverse spin current, we manage to generate a charge current in the weak link and inverse proximity regions. In the absence of external leads the current through the junction must be zero, thus a phase difference φ_0 accumulates over the junction, setting up an oppositely directed supercurrent that exactly cancels the charge current injected from the weak link.

6.6* The superspin Hall effect

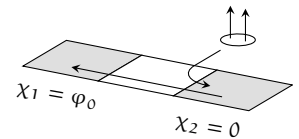
The ordinary spin Hall effect, which we considered in Chap. 3, is a phenomenon that occurs out of equilibrium. The ordinary spin Hall effect in superconducting materials is a quasiparticle effect, and has been considered both theoretically [393–399] and experimentally [400]. Experimentally, it has been found that the spin Hall effect can be enhanced by several orders of magnitude below the critical temperature [400].

In addition to the ordinary spin Hall effect, superconductors can also host magnetoelectric effects in which an equilibrium supercurrent carried by the condensate can give rise to a spin polarization or a transverse spin current, or *vice versa* [401–406]. In paper VI, we consider a transverse equilibrium spin current that is induced by the Josephson current in a $s/N/F/N/s$ junction where the normal metals exhibit Rashba spin–orbit

Broken chiral symmetry:



φ_0 effect induced by a superconducting spin Hall effect:



coupling. In paper VII, we identify the inverse effect: a Josephson current induced by a transverse spin current in the same junction. We refer to this as the *superspin Hall effect*.

The superspin Hall effect is found in clean systems where there are p-wave correlations in addition to the s-wave correlations emanating from the proximitized superconductors [VI]. Even-frequency p-wave correlations must be in one of the triplet states. The interaction between the s- and p-wave correlations can be described in terms of the order parameters Δ_+ and Δ_- , which are the sum and difference of the original s-wave and p-wave order parameters, Δ_s and Δ_k , respectively. Here, k refers to the momentum in the direction transverse to the junction. The relative magnitude of Δ_+ and Δ_- depends on the relative phase of Δ_s and Δ_k :

$$|\Delta_{\pm}|^2 = |\Delta_s|^2 + \Delta_k^2 \pm 2 \operatorname{Re}(\Delta_s \Delta_k^*).$$

When no phase difference is applied over the junction, Δ_s is purely real and Δ_k is purely imaginary, see Fig. 6.1. Consequently, $|\Delta_+| = |\Delta_-|$, and as many Cooper pairs condense in the $|k \uparrow, -k \downarrow\rangle$ state as in the $|k \downarrow, -k \uparrow\rangle$ state. However, when a phase difference is applied over the junction, Δ_s acquires an imaginary component and Δ_k acquires a real component and $|\Delta_+| \neq |\Delta_-|$. Due to the resulting difference in condensation energy, Cooper pairs condense preferentially in $|k \uparrow, -k \downarrow\rangle$ or $|k \downarrow, -k \uparrow\rangle$. The result is an antisymmetric momentum-resolved spin magnetization, or in other words, a transverse equilibrium spin current.

It has been suggested that equilibrium spin currents have observable consequences that can be detected *via* electrical [407, 408] or mechanical [409] means, or through the magnetization dynamics they induce [410, 411]. Nonetheless, experimental detection schemes for equilibrium spin currents have yet to be implemented. However, if we run the spin Hall mechanism in reverse, injection of a transverse equilibrium spin current

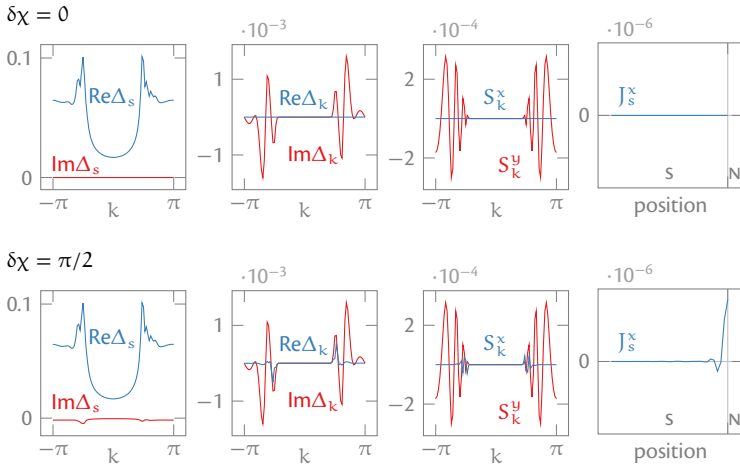


Figure 6.1 Superspin Hall mechanism. At $\delta\chi = 0$, the order parameters Δ_s and Δ_k are purely real and purely imaginary, respectively. Thus $|\Delta_+| = |\Delta_-|$. Since as many pairs condense in $|k \uparrow, -k \downarrow\rangle$ as in $|k \downarrow, -k \uparrow\rangle$, S_k is k -symmetric. At $\delta\chi = \pi/2$, the order parameters Δ_s and Δ_k are both complex. Thus $|\Delta_+| \neq |\Delta_-|$. Since different number of pairs condense in $|k \uparrow, -k \downarrow\rangle$ and $|k \downarrow, -k \uparrow\rangle$, S_k is k -antisymmetric.

into the junction will give rise to an anomalous phase difference in the junction's current-phase relation. In paper VII we suggest that the inverse superspin Hall effect can be demonstrated using a spin-polarized supercurrent.

Outlook

In this thesis I have considered magnetic and superconducting phenomena that fall broadly within the scope of spin-based electronics. I have highlighted some of the main results that I have obtained throughout my graduate studies; these results are elaborated further in the enclosed papers. In retrospect, some of my projects have been more promising or stimulating than others. In the present chapter I conclude the thesis by discussing further projects I would have liked to do.

The low dimensionality of the van der Waals magnets opens for novel ways to couple to their order parameters. Monolayers of the 2H polymorph of the transition-metal dichalcogenides can for instance be both piezoelectric [412–414] and magnetic [415–417]. If the magnetoelastic coupling in these materials is sufficiently strong, would it be possible to induce ferromagnetic resonance using an out-of-plane electric field? These materials also harbor spin–orbit torques with the same symmetry as Fe_3GeTe_2 [249]. Would it be possible for the nonequilibrium magnon accumulation induced by ferromagnetic resonance to give rise to magnonic charge pumping?

Spin-polarized supercurrents are a central theme in superconducting spintronics. Although supercurrents carried by equal-spin Cooper pairs undoubtedly exist [343], the evidence is mostly indirect, such as otherwise inexplicably long-ranged supercurrents [418–421]. To the best of my knowledge, the spin polarization of a supercurrent has yet to be measured directly. In paper VII we suggest that the inverse spin Hall effect can be used for this purpose. Magnetization dynamics induced by

a supercurrent would be another telltale sign of the supercurrent spin-polarization [410, 411]. Insofar none of these schemes have been implemented experimentally, it is interesting to look for other—perhaps more easily accessible—ways to measure the spin-polarization of a supercurrent or an equilibrium spin current in general.

In Chap. 6 we considered the profound effect magnetism can have on superconductivity. Other authors have also considered in what ways supercurrents can affect the magnetization, for instance by inducing magnetization dynamics [410, 411, 422]. The reciprocal action of the two phenomena suggests that a complete theory for S/F proximity structures needs to take into account their dynamic interplay in a coupled set of equations. Such a grand synthesis seems to me to be one of the most outstanding theoretical challenges in the field of superconducting spintronics.



Bibliography

- 1 **C. Yarbrough, A. Thompson.**
*International Human Genome Sequencing Consortium announces
"Working Draft" of human genome*
National Human Genome Research Institute.
<https://www.genome.gov/10001457> (2019).
- 2 **International Human Genome Sequencing Consortium.**
Initial sequencing and analysis of the human genome.
Nature **409**, 860 (2001).
10/bfpgjh.
- 3 **J.C. Venter, M.D. Adams, E.W. Myers, et al.**
The sequence of the human genome.
Science **291**, 1304 (2001).
10/bfkcgk.
- 4 **R.H. Waterston, E.S. Lander, J.E. Sulston.**
On the sequencing of the human genome.
Proceedings of the National Academy of Sciences **99**, 3712 (2002).
10/fkm9pr.
- 5 **D.P. Clark, N.J. Pazdernik.**
Biotechnology. 2nd ed.
(Academic Cell, 2016).

- 6 **G.E. Moore.**
Cramming more components onto integrated circuits.
Electronics **38**, 114 (1965);
Cramming more components onto integrated circuits.
IEEE Solid-State Circuits Society Newsletter **11**, 33 (2006).
10/c36b4b.
- 7 **G.E. Moore.**
Moore's law at 40.
Understanding Moore's Law: Four Decades of Innovation
(Chemical Heritage Foundation, 2006).
- 8 **R.H. Dennard, F.H. Gaensslen, H.-N. Yu, et al.**
Design of ion-implanted MOSFET's with very small physical dimensions.
IEEE Journal of Solid-State Circuits **SC-9**, 256 (1974);
Design of ion-implanted MOSFET's with very small physical dimensions.
IEEE Solid-State Circuits Society Newsletter **12**, 38 (2007).
10/bjjgbt.
- 9 **B.G. Streetman, S. Banerjee.**
Solid State Electronic Devices. 6th ed.
(Pearson/Prentice Hall, 2006).
- 10 **W. Haensch, E.J. Nowak, R.H. Dennard, et al.**
Silicon CMOS devices beyond scaling.
IBM Journal of Research and Development **50**, 339 (2006).
10/bscsfh.

- 11 **W. Arden, M. Brillouët, P. Cogez, et al.**
More than Moore
ITRS White Paper
(ITRS, 2010).
<http://www.itrs2.net/itrs-models-and-papers> (2018).
- 12 **M.M. Waldrop.**
The chips are down for Moore's law.
Nature **530**, 144 (2016).
10/bcf8.
- 13 **K. Bourzac.**
Supercomputing poised for a massive speed boost.
Nature **551**, 554 (2017).
10/gfvttqw.
- 14 **N. Jones.**
How to stop data centres from gobbling up the world's electricity.
Nature **561**, 163 (2018).
10/gd58cv.
- 15 **R.K. Cavin, P. Lugli, V.V. Zhirnov.**
Science and engineering beyond Moore's law.
Proceedings of the IEEE **100**, 1720 (2012).
10/f4c46q.
- 16 **S. Salahuddin, K. Ni, S. Datta.**
The era of hyper-scaling in electronics.
Nature Electronics **1**, 442 (2018).
10/gfvttb.

- 17 **R. Landauer.**
Irreversibility and heat generation in the computing process.
IBM Journal of Research and Development **5**, 183 (1961).
10/drrfmq.
- 18 **A. Bérut, A. Arakelyan, A. Petrosyan, et al.**
Experimental verification of Landauer's principle linking
information and thermodynamics.
Nature **483**, 187 (2012).
10/gdz5j6.
- 19 **S. Moore.**
Computing's power limit demonstrated.
IEEE Spectrum **49**, 14 (2012).
10/gfn7bv.
- 20 **S.A. Wolf, D.D. Awschalom, R.A. Buhrman, et al.**
Spintronics: A spin-based electronics vision for the future.
Science **294**, 1488 (2001).
10/bjgx9x.
- 21 **I. Žutić, J. Fabian, S. Das Sarma.**
Spintronics: Fundamentals and applications.
Reviews of Modern Physics **76**, 323 (2004).
10/bkzd7w.
- 22 **S.D. Bader, S.S.P. Parkin.**
Spintronics.
Annual Review of Condensed Matter Physics **1**, 71 (2010).
10/bwn73n.

- 23 **G.E. Uhlenbeck.**
Fifty years of spin: Personal reminiscences.
Physics Today **29**, 43 (1976).
10/dw735n.
- 24 **C. Chappert, A. Fert, F.N. Van Dau.**
The emergence of spin electronics in data storage.
Nature Materials **6**, 813 (2007).
10/d656rz.
- 25 **S. Bhatti, R. Sbiaa, A. Hirohata, et al.**
Spintronics based random access memory: A review.
Materials Today **20**, 530 (2017).
10/gcqjsz.
- 26 **J.M.D. Coey.**
Magnetism and Magnetic Materials.
(Cambridge University Press, 2010).
10/gdxxkp.
- 27 **R. Waser.**
Nanoelectronics and Information Technology. 3rd ed.
(John Wiley & Sons, 2012).
- 28 **A. Brataas, A.D. Kent, H. Ohno.**
Current-induced torques in magnetic materials.
Nature Materials **11**, 372 (2012).
10/gfvz3p.
- 29 **J. Åkerman.**
Toward a universal memory.
Science **308**, 508 (2005).
10/cwkhk.

- 30 **A.D. Kent, D.C. Worledge.**
A new spin on magnetic memories.
Nature Nanotechnology **10**, 187 (2015).
10/892.
- 31 **R. Mertens.**
Metalgrass, LTD.
<http://www.mram-info.com> (2018).
- 32 **A. Manchon, I.M. Miron, T. Jungwirth, et al.**
Current-induced spin-orbit torques in ferromagnetic and antiferromagnetic systems.
arXiv: 1801.09636.
- 33 **A.V. Chumak, V.I. Vasyuchka, A.A. Serga, B. Hillebrands.**
Magnon spintronics.
Nature Physics **11**, 453 (2015).
10/gfvz4n.
- 34 **Y. Kajiwara, K. Harii, S. Takahashi, et al.**
Transmission of electrical signals by spin-wave interconversion in a magnetic insulator.
Nature **464**, 262 (2010).
10/dpqqxw.
- 35 **P. Yan, X.S. Wang, X.R. Wang.**
All-magnonic spin-transfer torque and domain wall propagation.
Physical Review Letters **107**, 177207 (2011).
10/bx7zq7.
- 36 **X.R. Wang, P. Yan, X.S. Wang.**
Magnonic spin-transfer torque and domain wall propagation.
IEEE Transactions on Magnetics **48**, 4074 (2012).
10/gfvz4x.

- 37 **D. Hinzke, U. Nowak.**
Domain wall motion by the magnonic spin Seebeck effect.
Physical Review Letters **107**, 027205 (2011).
10/cmt6t3.
- 38 **J. Torrejon, G. Malinowski, M. Pelloux, et al.**
Unidirectional thermal effects in current-induced
domain wall motion.
Physical Review Letters **109**, 106601 (2012).
10/gfvz42.
- 39 **W. Jiang, P. Upadhyaya, Y. Fan, et al.**
Direct imaging of thermally driven domain wall motion in
magnetic insulators.
Physical Review Letters **110**, 177202 (2013).
10/gfvz43.
- 40 **W. Eerenstein, N.D. Mathur, J.F. Scott.**
Multiferroic and magnetoelectric materials.
Nature **442**, 759 (2006).
10/fmbt4m.
- 41 **H. Schmid.**
Multi-ferroic magnetoelectrics.
Ferroelectrics **162**, 317 (1994).
10/brm4z6.
- 42 **H. Schmid.**
Multiferroic materials and heterostructures.
Comptes Rendus Physique **16**, 141 (2015).
10/gfv274.

- 43 **H. Kamerlingh Onnes.**
Further experiments with liquid helium. The disappearance of the electrical resistance of mercury.
Proceedings of the Royal Netherlands Academy of Arts and Sciences **14**, 113 (1911).
- 44 **W. Meissner, R. Ochsenfeld.**
Ein neuer Effekt bei Eintritt der Supraleitfähigkeit.
Naturwissenschaften **21**, 787 (1933).
10/d6h3nw.
- 45 **J.R. Schrieffer.**
Theory of Superconductivity.
(Perseus Books, 1999).
- 46 **M. Tinkham.**
Introduction to Superconductivity. 2nd ed.
(McGraw-Hill, 1996).
- 47 **P.G. de Gennes.**
Superconductivity of Metals and Alloys.
(Westview Press, 1999).
- 48 **K. Fossheim, A. Sudbø.**
Superconductivity: Physics and Applications.
(John Wiley & Sons, 2004).
10/fjfvvw.
- 49 **D. van Delft, P. Kes.**
The discovery of superconductivity.
Physics Today **63**, 38 (2010).
10/d9drk9.

- 50 **L.N. Cooper.**
Bound electron pairs in a degenerate Fermi gas.
Physical Review **104**, 1189 (1956).
10/b6wdwt.
- 51 **J. Bardeen, L.N. Cooper, J.R. Schrieffer.**
Theory of superconductivity.
Physical Review **108**, 1175 (1957).
10/fw8k5d.
- 52 **V.L. Ginzburg.**
Ferromagnetic superconductors.
Soviet Physics—JETP **4**, 153 (1957).
- 53 **B.T. Matthias, H. Suhl, E. Corenzwit.**
Spin exchange in superconductors.
Physical Review Letters **1**, 92 (1958).
10/dkk788.
- 54 **Л.Д. Ландау, В.Л. Гинзбург.**
К теории сверхпроводимости.
*Журнал Экспериментальной и
Теоретической Физики* **20**, 1064 (1950);
L.D. Landau, V.L. Ginzburg.
On the theory of superconductivity.
Collected Papers of L. D. Landau
(Pergamon Press, 1965).
10/c5zz.
- 55 **R. Holm, W. Meissner.**
Messungen mit Hilfe von flüssigem Helium. Kontaktwiderstand
zwischen Supraleitern und Nichtsupraleitern.
Zeitschrift für Physik **74**, 715 (1932).
10/fw5d58.

- 56 **P.G. De Gennes, E. Guyon.**
Superconductivity in “normal” metals.
Physics Letters **3**, 168 (1963).
10/d48qw9.
- 57 **N.R. Werthamer.**
Theory of the superconducting transition temperature and energy
gap function of superposed metal films.
Physical Review **132**, 2440 (1963).
10/dzsg95.
- 58 **J.J. Hauser, H.C. Theuerer, N.R. Werthamer.**
Superconductivity in Cu and Pt by means of superimposed films
with lead.
Physical Review **136**, A637 (3A 1964).
10/bns2bd.
- 59 **P.G. de Gennes.**
Boundary effects in superconductors.
Reviews of Modern Physics **36**, 225 (1964).
10/cbbdxk.
- 60 **G. Deutscher, P.G. de Gennes.**
Gapless superconductivity.
Superconductivity
(Marcel Dekker, 1969).
- 61 **F.S. Bergeret, A.F. Volkov, K.B. Efetov.**
Odd triplet superconductivity and related phenomena in
superconductor–ferromagnet structures.
Reviews of Modern Physics **77**, 1321 (2005).
10/bqc4vn.

- 62 **A.I. Buzdin.**
Proximity effects in superconductor–ferromagnet heterostructures.
Reviews of Modern Physics 77, 935 (2005).
10/c3w2rr.
- 63 **I.F. Lyuksyutov, V.L. Pokrovsky.**
Ferromagnet–superconductor hybrids.
Advances in Physics 54, 67 (2005).
10/bwmbvf.
- 64 **J. Linder, J.W.A. Robinson.**
Superconducting spintronics.
Nature Physics 11, 307 (2015).
10/gc4jjv.
- 65 **K.S. Novoselov, A.K. Geim, S.V. Morozov, et al.**
Electric field effect in atomically thin carbon films.
Science 306, 666 (2004).
10/bcqqsc.
- 66 **K.S. Novoselov, D. Jiang, F. Schedin, et al.**
Two-dimensional atomic crystals.
Proceedings of the National Academy of Sciences 102, 10451 (2005).
10/ftg9zh.
- 67 **A.K. Geim, K.S. Novoselov.**
The rise of graphene.
Nature Materials 6, 183 (2007).
10/d3tx8m.

- 68 **K.S. Novoselov, A. Mishchenko, A. Carvalho, et al.**
2D materials and van der Waals heterostructures.
Science **353**, aac9439 (2016).
10/f8w86m.
- 69 **K.S. Novoselov, A.K. Geim, S.V. Morozov, et al.**
Two-dimensional gas of massless Dirac fermions in graphene.
Nature **438**, 197 (2005).
10/bz2jk2.
- 70 **Y. Zhang, Y.-W. Tan, H.L. Stormer, P. Kim.**
Experimental observation of the quantum Hall effect and Berry's
phase in graphene.
Nature **438**, 201 (2005).
10/dgrwrr.
- 71 **J.C.W. Song, N.M. Gabor.**
Electron quantum metamaterials in van der Waals
heterostructures.
Nature Nanotechnology **13**, 986 (2018).
10/gfvvggj.
- 72 **K.S. Burch, D. Mandrus, J.-G. Park.**
Magnetism in two-dimensional van der Waals materials.
Nature **563**, 47 (2018).
10/gfgqj4.
- 73 **Y. Deng, Y. Yu, Y. Song, et al.**
Gate-tunable room-temperature ferromagnetism in
two-dimensional Fe_3GeTe_2 .
Nature **563**, 94 (2018).
10/gffg4n.

- 74 **W. Han, R.K. Kawakami, M. Gmitra, J. Fabian.**
Graphene spintronics.
Nature Nanotechnology **9**, 794 (2014).
10/gd24cf.
- 75 **I. Žutić, A. Matos-Abiague, B. Scharf, et al.**
Proximitized materials.
Materials Today **22**, 85 (2019).
10/czbg.
- 76 **A. Cresti, B.K. Nolić, J.H. Garcia, S. Roche.**
Charge, spin and valley Hall effects in disordered graphene.
Rivista del Nuovo Cimento **39**, 587 (2016).
10/gfv3qd.
- 77 **J.R. Rumble.**
Magnetic susceptibility of the elements and inorganic compounds.
CRC Handbook of Chemistry and Physics 99th ed.
(CRC Press, 2018).
- 78 **C. Kittel.**
Introduction to Solid State Physics. 8th ed.
(John Wiley & Sons, 2005).
- 79 **D.C. Mattis.**
The Theory of Magnetism Made Simple.
(World Scientific, 2006).
- 80 **R.P. Feynman, R.B. Leighton, M.L. Sands.**
The Feynman Lectures on Physics. New millennium ed.
(Basic Books, 2011).
- 81 **J.H. Van Vleck.**
The Theory of Electric and Magnetic Susceptibilities. 1st ed.
(Clarendon Press, 1932).

- 82 **E.U. Condon.**
Wave mechanics and the normal state of the hydrogen molecule.
Proceedings of the National Academy of Sciences **13**, 466 (1927).
10/d5vv77.
- 83 **W. Heitler, F. London.**
Wechselwirkung neutraler Atome und homöopolare Bindung nach
der Quantenmechanik.
Zeitschrift für Physik **44**, 455 (1927).
10/fnjkv.
- 84 **L. Pauling, E.B. Wilson.**
Introduction to Quantum Mechanics. 1st ed.
(McGraw-Hill, 1935).
- 85 **R.C. O'Handley.**
Modern Magnetic Materials: Principles and Applications.
(John Wiley & Sons, 2000).
- 86 **L. Pauling.**
The Nature of the Chemical Bond. 3rd ed.
(Cornell University Press, 1960).
- 87 **D.J. Griffiths.**
Introduction to Quantum Mechanics. 2nd ed.
(Pearson Prentice Hall, 2005).
- 88 **I.N. Levine.**
Quantum Chemistry. 7th ed.
(Pearson, 2014).
- 89 **A. Auerbach.**
Interacting Electrons and Quantum Magnetism.
(Springer, 1998).

- 90 **W. Heisenberg.**
Zur Theorie des Ferromagnetismus.
Zeitschrift für Physik **49**, 619 (1928).
10/fnn9vb.
- 91 **N.F. Mott, R.E. Peierls.**
Obituary: Werner Heisenberg, 5 December 1901–1 February 1976.
Biographical Memoirs of Fellows of the Royal Society **23**, 212 (1977).
10/d53cgp.
- 92 **T. Holstein, H. Primakoff.**
Field dependence of the intrinsic domain magnetization of a
ferromagnet.
Physical Review **58**, 1098 (1940).
10/c6cdgq.
- 93 **T.L. Hill.**
An Introduction to Statistical Thermodynamics.
(Dover Publications, 1986).
- 94 **C. Kittel, C.Y. Fong.**
Quantum Theory of Solids. 2nd ed.
(John Wiley & Sons, 1987).
- 95 **I.S. Gradshteĭn, I.M. Ryzhik (eds D. Zwillinger, V. Moll)**
Table of Integrals, Series, and Products. 8th ed.
(Academic Press, 2015).
- 96 **F. Bloch.**
Zur Theorie des Ferromagnetismus.
Zeitschrift für Physik **61**, 206 (1930).
10/c7mg8d.

- 97 **P.C. Hohenberg.**
Existence of long-range order in one and two dimensions.
Physical Review **158**, 383 (1967).
10/fvvs2.
- 98 **N.D. Mermin, H. Wagner.**
Absence of ferromagnetism or antiferromagnetism in one- or
two-dimensional isotropic Heisenberg models.
Physical Review Letters **17**, 1133 (1966).
10/c7bj43.
- 99 **E. Ising.**
Beitrag zur Theorie des Ferromagnetismus.
Zeitschrift für Physik **31**, 253 (1925).
10/d6b6nj.
- 100 **L. Onsager.**
Crystal statistics. A two-dimensional model with an
order–disorder transition.
Physical Review **65**, 117 (1944).
10/frjf8h.
- 101 **K. Honda, S. Kaya.**
On the magnetisation of single crystals of iron.
Science Reports of Tohoku University **15**, 721 (1926).
- 102 **S. Kaya.**
On the magnetisation of single crystals of nickel.
Science Reports of Tohoku University **17**, 639 (1928).
- 103 **S. Kaya.**
On the magnetisation of single crystals of cobalt.
Science Reports of Tohoku University **17**, 1157 (1928).

- 104 **F.E. Neumann** (ed **O.E. Meyer**)
*Vorlesungen über die Theorie der Elastizität der festen Körper
und des Lichtäthers.*
(B.G. Teubner-Verlag, 1885).
- 105 **P. Curie.**
Sur la symétrie dans les phénomènes physiques, symétrie d'un
champ électrique et d'un champ magnétique.
Journal de Physique Théorique et Appliquée **3**, 393 (1894).
10/dfk9fs.
- 106 **R.R. Birss** (ed **E.P. Wohlfarth**)
Symmetry and Magnetism.
(North-Holland Publishing Company, 1964);
Macroscopic symmetry in space-time.
Reports on Progress in Physics **26**, 307 (1963).
10/bvgzcb.
- 107 **L.H. Thomas.**
The motion of the spinning electron.
Nature **117**, 514 (1926).
10/fp38vv.
- 108 **R.R. Haar, L.J. Curtis.**
The Thomas precession gives $g_e - 1$, not $g_e/2$.
American Journal of Physics **55**, 1044 (1987).
10/c6qmv4.
- 109 **E.T. Jaynes.**
Ferroelectricity.
(Princeton University Press, 1953).

- 110 **H.A. Lorentz.**
The Theory of Electrons. 2nd ed.
(Dover Publications, 2011).
- 111 **J.D. Jackson.**
Classical Electrodynamics. 3rd ed.
(John Wiley & Sons, 1999).
- 112 **W.F. Brown (ed E.P. Wohlfarth)**
Magnetostatic Principles in Ferromagnetism.
(North-Holland Publishing Company, 1962).
- 113 **M.J. Donahue, D.G. Porter.**
OOMMF User's Guide, Version 1.0
NIST Interagency Report, NISTIR 6376
(NIST, Gaithersburg, MD, USA, 1999);
*The object-oriented micromagnetic framework
project at ITL/NIST*
National Institute of Standards and Technology.
<https://math.nist.gov/oommf> (2019).
- 114 **A. Vansteenkiste, J. Leliaert, M. Dvornik, et al.**
The design and verification of MuMax3.
AIP Advances 4, 107133 (2014).
10/f6pp9f;
A. Vansteenkiste.
MuMax3. GPU-accelerated micromagnetism
DyNaMat group, Ghent University.
<http://mumax.github.io> (2019).

- 115 **R.D. McMichael, M.J. Donahue, D.G. Porter, J. Eicke.**
Comparison of magnetostatic field calculation methods on two-dimensional square grids as applied to a micromagnetic standard problem.
Journal of Applied Physics **85**, 5816 (1999).
10/dw4mm9.
- 116 **A.G. Gurevich, G.A. Melkov.**
Magnetization Oscillations and Waves.
(CRC Press, 1996).
- 117 **D.N. Chartoryzhskii, B.A. Kalinikos, O.G. Vendik.**
Parallel pump spin wave instability in thin ferromagnetic films.
Solid State Communications **20**, 985 (1976).
10/b6zkqw.
- 118 **B.A. Kalinikos.**
Excitation of propagating spin waves in ferromagnetic films.
IEE Proceedings H—Microwaves, Optics and Antennas **127**, 4 (1980).
10/bqhht6.
- 119 **S.O. Demokritov, V.E. Demidov, O. Dzyapko, et al.**
Bose–Einstein condensation of quasi-equilibrium magnons at room temperature under pumping.
Nature **443**, 430 (2006).
10/d88bx3.
- 120 **A.A. Serga, V.S. Tiberkevich, C.W. Sandweg, et al.**
Bose–Einstein condensation in an ultra-hot gas of pumped magnons.
Nature Communications **5**, 3452 (2014).
10/gfxj8j.

- 121 **T. Wimmer, M. Althammer, L. Liensberger, et al.**
Spin transport in a charge-current-induced magnon Bose–Einstein condensate at room temperature.
arXiv: 1812.01334.
- 122 **L.D. Landau, E.M. Lifshitz.**
Über die Theorie der Dispersion der magnetischen Permeabilität in ferromagnetischen Körpern.
Physikalische Zeitschrift der Sowjetunion **8**, 153 (1935);
On the theory of the dispersion of magnetic permeability in ferromagnetic bodies.
Collected Papers of L. D. Landau
(Pergamon Press, 1965).
10/c5z2.
- 123 **A. Brataas, Y. Tserkovnyak, G.E.W. Bauer.**
Scattering theory of Gilbert damping.
Physical Review Letters **101**, 037207 (2008).
10/dv7dx4.
- 124 **A. Brataas, Y. Tserkovnyak, G.E.W. Bauer.**
Magnetization dissipation in ferromagnets from scattering theory.
Physical Review B **84**, 054416 (2011).
10/bdhxvw.
- 125 **H. Ebert, S. Mankovsky, D. Ködderitzsch, P.J. Kelly.**
Ab initio calculation of the Gilbert damping parameter via the linear response formalism.
Physical Review Letters **107**, 066603 (2011).
10/d4f4rd.

- 126 **S. Mankovsky, D. Ködderitzsch, G. Woltersdorf, H. Ebert.**
First-principles calculation of the Gilbert damping parameter via the linear response formalism with application to magnetic transition metals and alloys.
Physical Review B **87**, 014430 (2013).
10/gfxqzf.
- 127 **M.A.W. Schoen, D. Thonig, M.L. Schneider, et al.**
Ultra-low magnetic damping of a metallic ferromagnet.
Nature Physics **12**, 839 (2016).
10/f3s7n.
- 128 **T.L. Gilbert.**
Formulation, Foundations and Applications of the Phenomenological Theory of Ferromagnetism
PhD Thesis
(Illinois Institute of Technology, Chicago, IL, USA, 1956).
<http://people.physics.tamu.edu/saslow> (2019);
A phenomenological theory of damping in ferromagnetic materials.
IEEE Transactions on Magnetics **40**, 3443 (2004).
10/d2d2gn.
- 129 **M.A.W. Schoen, J.M. Shaw, H.T. Nembach, et al.**
Radiative damping in waveguide-based ferromagnetic resonance measured via analysis of perpendicular standing spin waves in sputtered permalloy films.
Physical Review B **92**, 184417 (2015).
10/gfxq4x.
- 130 **V.G. Bar'yakhtar, B.A. Ivanov, T.K. Soboleva, A.L. Sukstanskii.**
Theory of dynamical-soliton relaxation in ferromagnets.
Soviet Physics—JETP **64**, 857 (1986).

- 131 **Y. Tserkovnyak, E.M. Hankiewicz, G. Vignale.**
Transverse spin diffusion in ferromagnets.
Physical Review B **79**, 094415 (2009).
10/d87g3x.
- 132 **H.T. Nembach, J.M. Shaw, C.T. Boone, T.J. Silva.**
Mode- and size-dependent Landau–Lifshitz damping in magnetic nanostructures: Evidence for nonlocal damping.
Physical Review Letters **110**, 117201 (2013).
10/gfxrbg.
- 133 **Y. Li, W.E. Bailey.**
Wave-number-dependent Gilbert damping in metallic ferromagnets.
Physical Review Letters **116**, 117602 (2016).
10/gfxrbh.
- 134 **J. Foros, A. Brataas, Y. Tserkovnyak, G.E.W. Bauer.**
Current-induced noise and damping in nonuniform ferromagnets.
Physical Review B **78**, 140402 (2008).
10/c3fz8j.
- 135 **T. Weindler, H.G. Bauer, R. Islinger, et al.**
Magnetic damping: Domain wall dynamics versus local ferromagnetic resonance.
Physical Review Letters **113**, 237204 (2014).
10/gfxrbk.
- 136 **H. Goldstein.**
Classical Mechanics. 2nd ed.
(Addison-Wesley Publishing Company, 1980).

- 137 **J.-E. Wegrowe, M.-C. Ciornei.**
Magnetization dynamics, gyromagnetic relation, and inertial effects.
American Journal of Physics **80**, 607 (2012).
10/f33mgt.
- 138 **O. Tchernyshyov.**
Conserved momenta of a ferromagnetic soliton.
Annals of Physics **363**, 98 (2015).
10/f72kkz.
- 139 **S. Dasgupta, O. Tchernyshyov.**
Energy–momentum tensor of a ferromagnet.
Physical Review B **98**, 224401 (2018).
10/gfxrfw.
- 140 **L. Berger.**
Low-field magnetoresistance and domain drag in ferromagnets.
Journal of Applied Physics **49**, 2156 (1978).
10/b75tz5.
- 141 **L. Berger.**
Domain drag effect in the presence of variable magnetic field or variable transport current.
Journal of Applied Physics **50**, 2137 (1979).
10/dnrq3z.
- 142 **P.P. Freitas, L. Berger.**
Observation of s–d exchange force between domain walls and electric current in very thin permalloy films.
Journal of Applied Physics **57**, 1266 (1985).
10/b6p295.

- 143 **C. Hung, L. Berger.**
Exchange forces between domain wall and electric current in permalloy films of variable thickness.
Journal of Applied Physics **63**, 4276 (1988).
10/cjxpvf.
- 144 **P. Grünberg, R. Schreiber, Y. Pang, et al.**
Layered magnetic structures: Evidence for antiferromagnetic coupling of Fe layers across Cr interlayers.
Physical Review Letters **57**, 2442 (1986).
10/c2s59p.
- 145 **C.F. Majkrzak, J.W. Cable, J. Kwo, et al.**
Observation of a magnetic antiphase domain structure with long-range order in a synthetic Gd–Y superlattice.
Physical Review Letters **56**, 2700 (1986).
10/cfzj2k.
- 146 **M.B. Salamon, S. Sinha, J.J. Rhyne, et al.**
Long-range incommensurate magnetic order in a Dy–Y multilayer.
Physical Review Letters **56**, 259 (1986).
10/bhgp6p.
- 147 **M.N. Baibich, J.M. Broto, A. Fert, et al.**
Giant magnetoresistance of (001)Fe/(001)Cr magnetic superlattices.
Physical Review Letters **61**, 2472 (1988).
10/bwpxzk.
- 148 **G. Binasch, P. Grünberg, F. Saurenbach, W. Zinn.**
Enhanced magnetoresistance in layered magnetic structures with antiferromagnetic interlayer exchange.
Physical Review B **39**, 4828 (1989).
10/fvgvfc.

- 149 **L. Berger.**
Emission of spin waves by a magnetic multilayer traversed
by a current.
Physical Review B **54**, 9353 (1996).
10/dqh7d2.
- 150 **J.C. Slonczewski.**
Current-driven excitation of magnetic multilayers.
Journal of Magnetism and Magnetic Materials **159**, L1 (1996).
10/cbt84c.
- 151 **M. Tsoi, A.G.M. Jansen, J. Bass, et al.**
Excitation of a magnetic multilayer by an electric current.
Physical Review Letters **80**, 4281 (1998).
10/bk5gbf.
- 152 **J.C. Slonczewski.**
Currents and torques in metallic magnetic multilayers.
Journal of Magnetism and Magnetic Materials **247**, 324 (2002).
10/cvf27p.
- 153 **S.H. Strogatz.**
Nonlinear Dynamics and Chaos. 2nd ed.
(Westview Press, 2015).
- 154 **D. Ralph, M. Stiles.**
Spin transfer torques.
Journal of Magnetism and Magnetic Materials **320**, 1190 (2008).
10/ckxzsg.

- 155 **T.J. Silva, W.H. Rippard.**
Developments in nano-oscillators based upon spin-transfer point-contact devices.
Journal of Magnetism and Magnetic Materials **320**, 1260 (2008).
10/dctvfs.
- 156 **J.-V. Kim.**
Spin-torque oscillators.
Solid State Physics **63**, 217–294
(Elsevier, 2012).
10/c5zw.
- 157 **T. Chen, R.K. Dumas, A. Eklund, et al.**
Spin-torque and spin-Hall nano-oscillators.
Proceedings of the IEEE **104**, 1919 (2016).
10/f3s962.
- 158 **S. Zhang, Z. Li.**
Roles of nonequilibrium conduction electrons on the magnetization dynamics of ferromagnets.
Physical Review Letters **93**, 127204 (2004).
10/cpx93m.
- 159 **A. Thiaville, Y. Nakatani, J. Miltat, Y. Suzuki.**
Micromagnetic understanding of current-driven domain wall motion in patterned nanowires.
Europhysics Letters **69**, 990 (2005).
10/dm5f4b.
- 160 **Y. Tserkovnyak, A. Brataas, G.E.W. Bauer.**
Theory of current-driven magnetization dynamics in inhomogeneous ferromagnets.
Journal of Magnetism and Magnetic Materials **320**, 1282 (2008).
10/d2njtk.

- 161 **F. Hellman, A. Hoffmann, Y. Tserkovnyak, et al.**
Interface-induced phenomena in magnetism.
Reviews of Modern Physics **89**, 025006 (2017).
10/gbhvd6.
- 162 **G.S.D. Beach, M. Tsoi, J.L. Erskine.**
Current-induced domain wall motion.
Journal of Magnetism and Magnetic Materials **320**, 1272 (2008).
10/cttgbn.
- 163 **G. Malinowski, O. Boulle, M. Kläui.**
Current-induced domain wall motion in nanoscale
ferromagnetic elements.
Journal of Physics D: Applied Physics **44**, 384005 (2011).
10/c6khjj.
- 164 **J. Shibata, G. Tatara, H. Kohno.**
A brief review of field- and current-driven domain-wall motion.
Journal of Physics D: Applied Physics **44**, 384004 (2011).
10/bjdppg.
- 165 **N.L. Schryer, L.R. Walker.**
The motion of 180° domain walls in uniform dc magnetic fields.
Journal of Applied Physics **45**, 5406 (1974).
10/fbwk7f.
- 166 **S.S.P. Parkin, M. Hayashi, L. Thomas.**
Magnetic domain-wall racetrack memory.
Science **320**, 190 (2008).
10/bpzg6k.

- 167 **M. Hayashi, L. Thomas, R. Moriya, et al.**
Current-controlled magnetic domain-wall nanowire shift register.
Science **320**, 209 (2008).
10/bkxv5k.
- 168 **S. Parkin, S.-H. Yang.**
Memory on the racetrack.
Nature Nanotechnology **10**, 195 (2015).
10/gfx5pt.
- 169 **Y.B. Bazaliy, B.A. Jones, S.-C. Zhang.**
Modification of the Landau–Lifshitz equation in the presence of a
spin-polarized current in colossal- and giant-magnetoresistive
materials.
Physical Review B **57**, R3213 (1998).
10/cf3wjz.
- 170 **J. Fernández-Rossier, M. Braun, A.S. Núñez, A.H. MacDonald.**
Influence of a uniform current on collective magnetization
dynamics in a ferromagnetic metal.
Physical Review B **69**, 174412 (2004).
10/fb67ws.
- 171 **J. Shibata, G. Tatara, H. Kohno.**
Effect of spin current on uniform ferromagnetism:
Domain nucleation.
Physical Review Letters **94**, 076601 (2005).
10/fvqx5n.
- 172 **G. Yu, P. Upadhyaya, K.L. Wong, et al.**
Magnetization switching through spin-Hall-effect-induced chiral
domain wall propagation.
Physical Review B **89**, 104421 (2014).
10/gfx5pz.

- 173 **K. Garello, C.O. Avci, I.M. Miron, et al.**
Ultrafast magnetization switching by spin–orbit torques.
Applied Physics Letters **105**, 212402 (2014).
10/gfx5p2.
- 174 **J.-C. Rojas-Sánchez, P. Laczkowski, J. Sampaio, et al.**
Perpendicular magnetization reversal in Pt/[Co/Ni]₃/Al
multilayers *via* the spin Hall effect of Pt.
Applied Physics Letters **108**, 082406 (2016).
10/gfx5p3.
- 175 **J. Sinova, S.O. Valenzuela, J. Wunderlich, et al.**
Spin Hall effects.
Reviews of Modern Physics **87**, 1213 (2015).
10/gcpdbg.
- 176 **J. Sinova, T. Jungwirth.**
Surprises from the spin Hall effect.
Physics Today **70**, 38 (2017).
10/gfz9jj.
- 177 **Y.K. Kato, R.C. Myers, A.C. Gossard, D.D. Awschalom.**
Observation of the spin Hall effect in semiconductors.
Science **306**, 1910 (2004).
10/fgsr2g.
- 178 **J. Wunderlich, B. Kaestner, J. Sinova, T. Jungwirth.**
Experimental observation of the spin-Hall effect in a
two-dimensional spin–orbit coupled semiconductor system.
Physical Review Letters **94**, 047204 (2005).
10/fhvg8q.

- 179 **A.W. Smith.**
The variation of the Hall effect in metals with change of temperature.
Physical Review **30**, 1 (1910).
10/bkggc8.
- 180 **N. Nagaosa, J. Sinova, S. Onoda, et al.**
Anomalous Hall effect.
Reviews of Modern Physics **82**, 1539 (2010).
10/bkbfwm.
- 181 **R. Karplus, J.M. Luttinger.**
Hall effect in ferromagnetics.
Physical Review **95**, 1154 (1954).
10/c6zv5f.
- 182 **D. Xiao, M.-C. Chang, Q. Niu.**
Berry phase effects on electronic properties.
Reviews of Modern Physics **82**, 1959 (2010).
10/bdr799.
- 183 **K.V. Samokhin.**
Spin-orbit coupling and semiclassical electron dynamics in noncentrosymmetric metals.
Annals of Physics **324**, 2385 (2009).
10/bpvjv7.
- 184 **K. Ando, S. Takahashi, K. Harii, et al.**
Electric manipulation of spin relaxation using the spin Hall effect.
Physical Review Letters **101**, 036601 (2008).
10/dwsx4j.

- 185 **C.-F. Pai, M. Mann, A.J. Tan, G.S.D. Beach.**
Determination of spin torque efficiencies in heterostructures with perpendicular magnetic anisotropy.
Physical Review B **93**, 144409 (2016).
10/gfx8rn.
- 186 **I.E. Dzialoshinskii.**
Thermodynamical theory of “weak” ferromagnetism in antiferromagnetic substances.
Soviet Physics—JETP **5**, 1259 (1957).
- 187 **T. Moriya.**
New mechanism of anisotropic superexchange interaction.
Physical Review Letters **4**, 228 (1960).
10/bkn7wf.
- 188 **T. Moriya.**
Anisotropic superexchange interaction and weak ferromagnetism.
Physical Review **120**, 91 (1960).
10/dhm7wd.
- 189 **A.R. Fert.**
Magnetic and transport properties of metallic multilayers.
Materials Science Forum **59–60**, 439 (1991).
10/c7jt6.
- 190 **C. Bi, H. Almasi, K. Price, et al.**
Anomalous spin-orbit torque switching in synthetic antiferromagnets.
Physical Review B **95**, 104434 (2017).
10/c2xp.

- 191 **G. Yu, P. Upadhyaya, Y. Fan, *et al.***
Switching of perpendicular magnetization by spin-orbit torques in the absence of external magnetic fields.
Nature Nanotechnology **9**, 548 (2014).
10/gfx8rq.
- 192 **J.M. Lee, K. Cai, G. Yang, *et al.***
Field-free spin-orbit torque switching from geometrical domain-wall pinning.
Nano Letters **18**, 4669 (2018).
10/gfbmcw.
- 193 **L. You, O. Lee, D. Bhowmik, *et al.***
Switching of perpendicularly polarized nanomagnets with spin orbit torque without an external magnetic field by engineering a tilted anisotropy.
Proceedings of the National Academy of Sciences **112**, 10310 (2015).
10/f7n8mv.
- 194 **S. Fukami, C. Zhang, S. Duttagupta, *et al.***
Magnetization switching by spin-orbit torque in an antiferromagnet-ferromagnet bilayer system.
Nature Materials **15**, 535 (2016).
10/f8kwwm.
- 195 **A. van den Brink, G. Vermijs, A. Solignac, *et al.***
Field-free magnetization reversal by spin-Hall effect and exchange bias.
Nature Communications **7**, 10854 (2016).
10/f8dj2s.

- 196 **Y.-W. Oh, S.-H. Baek, Y.M. Kim, et al.**
Field-free switching of perpendicular magnetization through spin-orbit torque in antiferromagnet/ferromagnet/oxide structures.
Nature Nanotechnology **11**, 878 (2016).
10/gfx8rt.
- 197 **K. Cai, M. Yang, H. Ju, et al.**
Electric field control of deterministic current-induced magnetization switching in a hybrid ferromagnetic/ferroelectric structure.
Nature Materials **16**, 712 (2017).
10/f9zmp4.
- 198 **M. Wang, W. Cai, D. Zhu, et al.**
Field-free switching of a perpendicular magnetic tunnel junction through the interplay of spin-orbit and spin-transfer torques.
Nature Electronics **1**, 582 (2018).
10/gfx8rv.
- 199 **L. Onsager.**
Reciprocal relations in irreversible processes. I.
Physical Review **37**, 405 (1931).
10/dtx2zs.
- 200 **L. Onsager.**
Reciprocal relations in irreversible processes. II.
Physical Review **38**, 2265 (1931).
10/ds5z6g.
- 201 **S.R. de Groot.**
Thermodynamics of Irreversible Processes.
(North-Holland Publishing Company, 1951).

- 202 **E. Saitoh, M. Ueda, H. Miyajima, G. Tatara.**
Conversion of spin current into charge current at room temperature: Inverse spin-Hall effect.
Applied Physics Letters **88**, 182509 (2006).
10/d7x366.
- 203 **S.O. Valenzuela, M. Tinkham.**
Direct electronic measurement of the spin Hall effect.
Nature **442**, 176 (2006).
10/btqxp7.
- 204 **H. Zhao, E.J. Loren, H.M. van Driel, A.L. Smirl.**
Coherence control of Hall charge and spin currents.
Physical Review Letters **96**, 246601 (2006).
10/b8w9jf.
- 205 **Y. Tserkovnyak, A. Brataas, G.E.W. Bauer.**
Enhanced Gilbert damping in thin ferromagnetic films.
Physical Review Letters **88**, 117601 (2002).
10/bj88jf.
- 206 **Y. Tserkovnyak, A. Brataas, G.E.W. Bauer, B.I. Halperin.**
Nonlocal magnetization dynamics in ferromagnetic heterostructures.
Reviews of Modern Physics **77**, 1375 (2005).
10/cpcph6.
- 207 **K. Uchida, S. Takahashi, K. Harii, et al.**
Observation of the spin Seebeck effect.
Nature **455**, 778 (2008).
10/c3mtgc.

- 208 **S.Y. Huang, X. Fan, D. Qu, et al.**
 Transport magnetic proximity effects in platinum.
Physical Review Letters **109**, 107204 (2012).
 10/gd875g.
- 209 **M. Weiler, M. Althammer, F.D. Czeschka, et al.**
 Local charge and spin currents in magnetothermal landscapes.
Physical Review Letters **108**, 106602 (2012).
 10/gd875h.
- 210 **Э.И. Рашба.**
Физика Твёрдого Тела **1**, 407 (1959);
E.I. Rashba.
 Symmetry of energy bands in crystals of wurtzite type. I.
 Symmetry of bands disregarding spin–orbit interaction.
Soviet Physics—Solid State **1**, 368 (1959).
- 211 **Э.И. Рашба, В. Шека.**
Физика Твёрдого Тела **2**, 162 (1959);
E.I. Rashba, V.I. Sheka.
 Symmetry of energy bands in crystals of wurtzite type. II.
 Symmetry of bands with spin–orbit interaction included.
New Journal of Physics **17**, 050202 (2015).
 10/gfkwz.
- 212 **Э.И. Рашба.**
 Комбинированный резонанс в полупроводниках.
Успехи Физических Наук **84**, 557 (1964);
É.I. Rashba.
 Combined resonance in semiconductors.
Soviet Physics—Uspekhi **7**, 823 (1965).
 10/dbtmck.

- 213 **A. Manchon, H.C. Koo, J. Nitta, et al.**
 New perspectives for Rashba spin–orbit coupling.
Nature Materials **14**, 871 (2015).
 10/gd239n.
- 214 **Е.Л. Ивченко, Г.Е. Пикус.**
 Новый фотогальванический эффект в гиротропных кристаллах.
Письма в ЖЭТФ **27**, 640 (1978);
E.L. Ivchenko, G.E. Pikus.
 New photogalvanic effect in gyrotropic crystals.
JETP Letters **27**, 604 (1978).
- 215 **А.Г. Аронов, Ю.Б. Лянда-Геллер.**
 Ядерный электрический резонанс и ориентация спинов носителей электрическим полем.
Письма в ЖЭТФ **50**, 398 (1989);
A.G. Aronov, Y.B. Lyanda-Geller.
 Nuclear electric resonance and orientation of carrier spins by an electric field.
JETP Letters **50**, 431 (1989).
- 216 **V.M. Edelstein.**
 Spin polarization of conduction electrons induced by electric current in two-dimensional asymmetric electron systems.
Solid State Communications **73**, 233 (1990).
 10/dxp3x3.
- 217 **A. Manchon, S. Zhang.**
 Theory of nonequilibrium intrinsic spin torque in a single nanomagnet.
Physical Review B **78**, 212405 (2008).
 10/bw86g6.

- 218 **A. Manchon, S. Zhang.**
Theory of spin torque due to spin–orbit coupling.
Physical Review B **79**, 094422 (2009).
10/fcdhz8.
- 219 **K.-W. Kim, S.-M. Seo, J. Ryu, et al.**
Magnetization dynamics induced by in-plane currents in ultrathin magnetic nanostructures with Rashba spin–orbit coupling.
Physical Review B **85**, 180404 (2012).
10/gfx83g.
- 220 **A. Qaiumzadeh, R.A. Duine, M. Titov.**
Spin–orbit torques in two-dimensional Rashba ferromagnets.
Physical Review B **92**, 014402 (2015).
10/gfx83h.
- 221 **A. Chernyshov, M. Overby, X. Liu, et al.**
Evidence for reversible control of magnetization in a ferromagnetic material by means of spin–orbit magnetic field.
Nature Physics **5**, 656 (2009).
10/bdffkg.
- 222 **C. Ciccarelli, L. Anderson, V. Tshitoyan, et al.**
Room-temperature spin–orbit torque in NiMnSb.
Nature Physics **12**, 855 (2016).
10/f83ztm.
- 223 **G. Dresselhaus, A.F. Kip, C. Kittel.**
Spin–orbit interaction and the effective masses of holes in germanium.
Physical Review **95**, 568 (1954).
10/b98qv4.

- 224 **G. Dresselhaus, A.F. Kip, C. Kittel.**
Cyclotron resonance of electrons and holes in silicon and germanium crystals.
Physical Review **98**, 368 (1955).
10/cg96cc.
- 225 **G. Dresselhaus.**
Spin-orbit coupling effects in zinc blende structures.
Physical Review **100**, 580 (1955).
10/bf2sh3.
- 226 **M.I. Dyakonov, V.Y. Kachorovskii.**
Spin relaxation of two-dimensional electrons in noncentrosymmetric semiconductors.
Soviet Physics—Semiconductors **20**, 110 (1986).
- 227 **D. Fang, H. Kurebayashi, J. Wunderlich, et al.**
Spin-orbit-driven ferromagnetic resonance.
Nature Nanotechnology **6**, 413 (2011).
10/c6xqr4.
- 228 **H. Kurebayashi, J. Sinova, D. Fang, et al.**
An antidamping spin-orbit torque originating from the Berry curvature.
Nature Nanotechnology **9**, 211 (2014).
10/gfx83s.

- 229 **Е.Л. Ивченко, Ю.Б. Лянда-Геллер, Г.Е. Пикус.**
 Фототок в структурах с квантовыми ямами при оптической ориентации свободных носителей.
Письма в ЖЭТФ 50, 156 (1989);
E.L. Ivchenko, Y.B. Lyanda-Geller, G.E. Pikus.
 Photocurrent in structures with quantum wells with an optical orientation of free carriers.
JETP Letters 50, 175 (1989).
- 230 **S.D. Ganichev, E.L. Ivchenko, S.N. Danilov, et al.**
 Conversion of spin into directed electric current in quantum wells.
Physical Review Letters 86, 4358 (2001).
 10/b48vnr.
- 231 **S.D. Ganichev, E.L. Ivchenko, V.V. Bel'kov, et al.**
 Spin-galvanic effect.
Nature 417, 153 (2002).
 10/ddv2zn.
- 232 **K.M.D. Hals, A. Brataas, Y. Tserkovnyak.**
 Scattering theory of charge-current-induced magnetization dynamics.
Europhysics Letters 90, 47002 (2010).
 10/ckmxwr.
- 233 **C. Ciccarelli, K.M.D. Hals, A. Irvine, et al.**
 Magnonic charge pumping via spin-orbit coupling.
Nature Nanotechnology 10, 50 (2015).
 10/gfx835.
- 234 **X. Zhang, Q. Liu, J.-W. Luo, et al.**
 Hidden spin polarization in inversion-symmetric bulk crystals.
Nature Physics 10, 387 (2014).
 10/f5z5ct.

- 235 **K.M.D. Hals, A. Brataas.**
Phenomenology of current-induced spin–orbit torques.
Physical Review B **88**, 085423 (2013).
10/gfzq9v.
- 236 **K.M.D. Hals, A. Brataas.**
Spin-motive forces and current-induced torques in ferromagnets.
Physical Review B **91**, 214401 (2015).
10/gfzq9w.
- 237 **E.A. Kearsley, J.T. Fong.**
Linearly independent sets of isotropic Cartesian tensors of ranks
up to eight.
J. of Research of the National Bureau of Standards **79B**, 49 (1975).
10/gdgzzf.
- 238 **T. Jungwirth, J. Sinova, J. Mašek, et al.**
Theory of ferromagnetic (III, Mn)V semiconductors.
Reviews of Modern Physics **78**, 809 (2006).
10/bt8g6g.
- 239 **I. Garate, A.H. MacDonald.**
Influence of a transport current on magnetic anisotropy in
gyrotropic ferromagnets.
Physical Review B **80**, 134403 (2009).
10/fj7dgs.
- 240 **Z. Fei, B. Huang, P. Malinowski, et al.**
Two-dimensional itinerant ferromagnetism in atomically thin
Fe₃GeTe₂.
Nature Materials **17**, 778 (2018).
10/gdz3j4.

- 241 **H.-J. Deiseroth, K. Aleksandrov, C. Reiner, et al.**
Fe₃GeTe₂ and Ni₃GeTe₂ – two new layered transition-metal compounds: Crystal structures, HRTEM investigations, and magnetic and electrical properties.
European Journal of Inorganic Chemistry **2006**, 1561 (2006).
10/cd3bsf.
- 242 **V.L. Berezinskiĭ.**
Destruction of long-range order in one-dimensional and two-dimensional systems having a continuous symmetry group. I. Classical systems.
Soviet Physics—JETP **32**, 493 (1971).
- 243 **V.L. Berezinskiĭ.**
Destruction of long-range order in one-dimensional and two-dimensional systems possessing a continuous symmetry group. II. Quantum systems.
Soviet Physics—JETP **34**, 610 (1972).
- 244 **J.M. Kosterlitz, D.J. Thouless.**
Ordering, metastability and phase transitions in two-dimensional systems.
Journal of Physics C: Solid State Physics **6**, 1181 (1973).
10/d6z7hr.
- 245 **N. Goldenfeld.**
Lectures on Phase Transitions and the Renormalization Group.
(Addison-Wesley, 1992).
- 246 **D.R. Nelson, J.M. Kosterlitz.**
Universal jump in the superfluid density of two-dimensional superfluids.
Physical Review Letters **39**, 1201 (1977).
10/b89fh3.

- 247 **D.J. Bishop, J.D. Reppy.**
Study of the superfluid transition in two-dimensional ^4He films.
Physical Review Letters **40**, 1727 (1978).
10/c7hht6.
- 248 **S. Manzeli, D. Ovchinnikov, D. Pasquier, et al.**
2D transition metal dichalcogenides.
Nature Reviews Materials **2**, 17033 (2017).
10/gc5vmz.
- 249 **K.M.D. Hals, K. Everschor-Sitte.**
Twists in ferromagnetic monolayers with trigonal prismatic symmetry.
Physical Review B **99**, 104422 (2019).
10/gf2t8d.
- 250 **A. Kamra, U. Agrawal, W. Belzig.**
Noninteger-spin magnonic excitations in untextured magnets.
Physical Review B **96**, 020411 (2017).
10/gfzvcp.
- 251 **А.В. Михайлов, А.И. Яремчук.**
Вынужденное движение доменной стенки в поле спиновой волны.
Письма в ЖЭТФ **39**, 296 (1984);
A.V. Mikhailov, A.I. Yaremchuk.
Forced motion of a domain wall in the field of a spin wave.
JETP Letters **39**, 354 (1984).
- 252 **S. Yuan, H. De Raedt, S. Miyashita.**
Quantum dynamics of spin wave propagation through domain walls.
Journal of the Physical Society of Japan **75**, 084703 (2006).
10/b2hcfn.

- 253 **R. Hertel, W. Wulfhekel, J. Kirschner.**
Domain-wall induced phase shifts in spin waves.
Physical Review Letters **93**, 257202 (2004).
10/c4zfh4.
- 254 **C. Bayer, H. Schultheiss, B. Hillebrands, R.L. Stamps.**
Phase shift of spin waves traveling through a 180°
Bloch-domain wall.
IEEE Transactions on Magnetics **41**, 3094 (2005).
10/dnxxcx.
- 255 **S. Macke, D. Goll.**
Transmission and reflection of spin waves in the presence
of Néel walls.
Journal of Physics: Conference Series **200**, 042015 (2010).
10/d7369n.
- 256 **D.-S. Han, S.-K. Kim, J.-Y. Lee, et al.**
Magnetic domain-wall motion by propagating spin waves.
Applied Physics Letters **94**, 112502 (2009).
10/cmgz26.
- 257 **M. Jamali, H. Yang, K.-J. Lee.**
Spin wave assisted current induced magnetic domain wall motion.
Applied Physics Letters **96**, 242501 (2010).
10/cfwpjx.
- 258 **S.-M. Seo, H.-W. Lee, H. Kohno, K.-J. Lee.**
Magnetic vortex wall motion driven by spin waves.
Applied Physics Letters **98**, 012514 (2011).
10/d8zf38.

- 259 **X.-G. Wang, G.-H. Guo, Y.-Z. Nie, et al.**
Domain wall motion induced by the magnonic spin current.
Physical Review B **86**, 054445 (2012).
10/gfzvbp.
- 260 **J.-S. Kim, M. Stärk, M. Kläui, et al.**
Interaction between propagating spin waves and domain walls on a ferromagnetic nanowire.
Physical Review B **85**, 174428 (2012).
10/gfzvbq.
- 261 **X.-G. Wang, G.-H. Guo, G.-F. Zhang, et al.**
Spin-wave resonance reflection and spin-wave induced domain wall displacement.
Journal of Applied Physics **113**, 213904 (2013).
10/gfzvbr.
- 262 **K.-W. Moon, B. Sun Chun, W. Kim, C. Hwang.**
Control of domain wall motion by interference of spin wave.
Journal of Applied Physics **114**, 123908 (2013).
10/gfzvbs.
- 263 **H. Hata, T. Taniguchi, H.-W. Lee, et al.**
Spin-wave-induced domain wall motion in perpendicularly magnetized system.
Applied Physics Express **7**, 033001 (2014).
10/gfzvbt.
- 264 **A.A. Kovalev, Y. Tserkovnyak.**
Thermomagnonic spin transfer and Peltier effects in insulating magnets.
Europhysics Letters **97**, 67002 (2012).
10/gfzvbv.

- 265 **A.A. Kovalev.**
Skyrmionic spin Seebeck effect via dissipative thermomagnonic torques.
Physical Review B **89**, 241101 (2014).
10/gfzvbw.
- 266 **X.S. Wang, X.R. Wang.**
Thermodynamic theory for thermal-gradient-driven domain-wall motion.
Physical Review B **90**, 014414 (2014).
10/gfzvbz.
- 267 **F. Schlickeiser, U. Ritzmann, D. Hinzke, U. Nowak.**
Role of entropy in domain wall motion in thermal gradients.
Physical Review Letters **113**, 097201 (2014).
10/gfzvbz.
- 268 **P. Yan, Y. Cao, J. Sinova.**
Thermodynamic magnon recoil for domain wall motion.
Physical Review B **92**, 100408 (2015).
10/gfzvb2.
- 269 **S. Moretti, V. Raposo, E. Martinez, L. Lopez-Diaz.**
Domain wall motion by localized temperature gradients.
Physical Review B **95**, 064419 (2017).
10/gfzvb3.
- 270 **D. Khomskii.**
Classifying multiferroics: Mechanisms and effects.
Physics **2**, 20 (2009).
10/bw5mqr.

- 271 **W.D. Callister, D.G. Rethwisch.**
Materials Science and Engineering. 8th ed.
(John Wiley & Sons, 2011).
- 272 **N.A. Hill.**
Why are there so few magnetic ferroelectrics?
Journal of Physical Chemistry B **104**, 6694 (2000).
10/dnkktc.
- 273 **S.-W. Cheong, M. Mostovoy.**
Multiferroics: A magnetic twist for ferroelectricity.
Nature Materials **6**, 13 (2007).
10/csxvfh.
- 274 **T. Kimura, T. Goto, H. Shintani, et al.**
Magnetic control of ferroelectric polarization.
Nature **426**, 55 (2003).
10/bxpv2n.
- 275 **T. Goto, T. Kimura, G. Lawes, et al.**
Ferroelectricity and giant magnetocapacitance in perovskite
rare-earth manganites.
Physical Review Letters **92**, 257201 (2004).
10/bd4jq6.
- 276 **T. Kimura, G. Lawes, T. Goto, et al.**
Magnetoelectric phase diagrams of orthorhombic RMnO_3
($\text{R} = \text{Gd}, \text{Tb}, \text{and Dy}$).
Physical Review B **71**, 224425 (2005).
10/dpkx2r.

- 277 **Y. Tokura, S. Seki, N. Nagaosa.**
Multiferroics of spin origin.
Reports on Progress in Physics 77, 076501 (2014).
10/gfz3z.
- 278 **M. Mostovoy.**
Ferroelectricity in spiral magnets.
Physical Review Letters 96, 067601 (2006).
10/ff6swm.
- 279 **В.Г. Барьяхтар, В.А. Львов, Д.А. Яблонский.**
Теория неоднородного магнитоэлектрического эффекта.
Письма в ЖЭТФ 37, 565 (1983);
V.G. Bar'yakhtar, V.A. L'vov, D.A. Yablonskii.
Inhomogeneous magnetoelectric effect.
JETP Letters 37, 673 (1983).
- 280 **А.С. Логгинов, Г.А. Мешков, А.В. Николаев, А.П. Пятаков.**
Магнитоэлектрическое управление доменными границами в пленке феррита-граната.
Письма в ЖЭТФ 86, 124 (2007);
A.S. Logginov, G.A. Meshkov, A.V. Nikolaev, A.P. Pyatakov.
Magnetoelectric control of domain walls in a ferrite garnet film.
JETP Letters 86, 115 (2007).
10/c77s9v.

- 281** **А.П. Пятаков, А.С. Сергеев, Е.П. Николаева, et al.**
Микромагнетизм и топологические дефекты в
магнитоэлектрических средах.
Успехи Физических Наук **185**, 1077 (2015);
A.P. Pyatakov, A.S. Sergeev, E.P. Nikolaeva, et al.
Micromagnetism and topological defects in magnetoelectric
media.
Physics-Uspokhi **58**, 981 (2015).
10/gfzx5r.
- 282** **I. Dzyaloshinskii.**
Magnetoelectricity in ferromagnets.
Europhysics Letters **83**, 67001 (2008).
10/djsncv.
- 283** **D.L. Mills, I.E. Dzyaloshinskii.**
Influence of electric fields on spin waves in simple ferromagnets:
Role of the flexoelectric interaction.
Physical Review B **78**, 184422 (2008).
10/cm45sq.
- 284** **T. Liu, G. Vignale.**
Electric control of spin currents and spin-wave logic.
Physical Review Letters **106**, 247203 (2011).
10/dmp9q9.
- 285** **T. Liu, G. Vignale.**
Flexoelectric phase shifter for spin waves.
Journal of Applied Physics **111**, 083907 (2012).
10/gfzx5s.

- 286 X. Zhang, T. Liu, M.E. Flatté, H.X. Tang.**
Electric-field coupling to spin waves in a centrosymmetric ferrite.
Physical Review Letters **113**, 037202 (2014).
10/gfzx5t.
- 287 R. Shankar.**
Renormalization-group approach to interacting fermions.
Reviews of Modern Physics **66**, 129 (1994).
10/cc8vg6.
- 288 L.D. Landau.**
The theory of a Fermi liquid.
Soviet Physics—JETP **3**, 920 (1956);
The theory of a Fermi liquid.
Collected Papers of L. D. Landau
(Pergamon Press, 1965).
10/c5zx.
- 289 P. Nozières.**
Theory of Interacting Fermi Systems.
(Perseus Books, 1997).
- 290 E. Maxwell.**
Isotope effect in the superconductivity of mercury.
Physical Review **78**, 477 (1950).
10/cxvh36.
- 291 C.A. Reynolds, B. Serin, W.H. Wright, L.B. Nesbitt.**
Superconductivity of isotopes of mercury.
Physical Review **78**, 487 (1950).
10/bvt79t.

- 292 **J.W. Garland.**
Isotope effect in superconductivity.
Physical Review Letters **11**, 114 (1963).
10/dvhrbx.
- 293 **B. Serin.**
Superconductivity. Experimental Part.
Encyclopedia of Physics **15**, 210–273
(Springer-Verlag, 1956).
- 294 **J. Bardeen.**
Zero-point vibrations and superconductivity.
Physical Review **79**, 167 (1950).
10/ch6tf9.
- 295 **H. Fröhlich.**
Theory of the superconducting state. The ground state at the
absolute zero of temperature.
Physical Review **79**, 845 (1950).
10/bn594g.
- 296 **J. Bardeen.**
Theory of Superconductivity.
Encyclopedia of Physics **15**, 274–369
(Springer-Verlag, 1956).
- 297 **V.F. Weisskopf.**
The formation of Cooper pairs and the nature of
superconducting currents.
Contemporary Physics **22**, 375 (1981).
10/brjr5z.

- 298 **J.A. Ouassou.**
Manipulating Superconductivity in Magnetic Nanostructures in and out of Equilibrium
PhD Thesis
(NTNU, Trondheim, Norway, 2019).
<http://hdl.handle.net/11250/2591114> (2019).
- 299 **P.W. Anderson.**
Random-phase approximation in the theory of superconductivity.
Physical Review **112**, 1900 (1958).
10/frgwc9.
- 300 **R.V. Lange.**
Nonrelativistic theorem analogous to the Goldstone theorem.
Physical Review **146**, 301 (1966).
10/fd9x25.
- 301 **P.W. Anderson.**
Coherent excited states in the theory of superconductivity: Gauge invariance and the Meissner effect.
Physical Review **110**, 827 (1958).
10/bgmc9h.
- 302 **P.W. Anderson.**
Plasmons, gauge invariance, and mass.
Physical Review **130**, 439 (1963).
10/dsgctv.
- 303 **A. Altland, B.D. Simons.**
Condensed Matter Field Theory. 2nd ed.
(Cambridge University Press, 2010).
10/c52f5q.

- 304 **N.N. Bogoljubov.**
On a new method in the theory of superconductivity.
Il Nuovo Cimento **7**, 794 (1958).
10/bkj9dv.
- 305 **A.J. Leggett.**
A theoretical description of the new phases of liquid ^3He .
Reviews of Modern Physics **47**, 331 (1975).
10/dxsc69.
- 306 **M. Sigrist.**
Introduction to unconventional superconductivity.
AIP Conference Proceedings **789**, 165 (2005).
10/cjd7zs.
- 307 **A. Schilling, M. Cantoni, J.D. Guo, H.R. Ott.**
Superconductivity above 130 K in the Hg–Ba–Ca–Cu–O system.
Nature **363**, 56 (1993).
10/dzzkpf.
- 308 **J.G. Bednorz, K.A. Müller.**
Possible high- T_c superconductivity in the Ba–La–Cu–O system.
Zeitschrift für Physik B **64**, 189 (1986).
10/cj434s.
- 309 **C.C. Tsuei, J.R. Kirtley, C.C. Chi, et al.**
Pairing symmetry and flux quantization in a tricrystal
superconducting ring of $\text{YBa}_2\text{Cu}_3\text{O}_{7-\delta}$.
Physical Review Letters **73**, 593 (1994).
10/dqss29.

- 310 **C.C. Tsuei, J.R. Kirtley.**
Phase-sensitive evidence for d-wave pairing symmetry in electron-doped cuprate superconductors.
Physical Review Letters **85**, 182 (2000).
10/c87pjw.
- 311 **C.C. Tsuei, J.R. Kirtley, G. Hammerl, et al.**
Robust $d_{x^2-y^2}$ pairing symmetry in hole-doped cuprate superconductors.
Physical Review Letters **93**, 187004 (2004).
10/bth84x.
- 312 **A.J. Leggett.**
What DO we know about high T_c ?
Nature Physics **2**, 134 (2006).
10/bnggn4.
- 313 **D.A. Bonn.**
Are high-temperature superconductors exotic?
Nature Physics **2**, 159 (2006).
10/cwb6c4.
- 314 **C.C. Tsuei, J.R. Kirtley.**
Pairing symmetry in cuprate superconductors.
Reviews of Modern Physics **72**, 969 (2000).
10/bdcdzt.
- 315 **Y. Dalichaouch, M.C. de Andrade, D.A. Gajewski, et al.**
Impurity scattering and triplet superconductivity in UPt_3 .
Physical Review Letters **75**, 3938 (1995).
10/bxjzqn.

- 316 **C. Geibel, C. Schank, F. Jährling, et al.**
Doping effects on UPd₂Al₃.
Physica B **199–200**, 128 (1994).
10/cdbvqj.
- 317 **S. Onari, H. Kontani.**
Violation of Anderson's theorem for the sign-reversing s-wave state of iron-pnictide superconductors.
Physical Review Letters **103**, 177001 (2009).
10/bfpgqh.
- 318 **Y. Wang, A. Kreisel, P.J. Hirschfeld, V. Mishra.**
Using controlled disorder to distinguish s_± and s₊₊ gap structure in Fe-based superconductors.
Physical Review B **87**, 094504 (2013).
10/c38p.
- 319 **A.P. Mackenzie, R.K.W. Haselwimmer, A.W. Tyler, et al.**
Extremely strong dependence of superconductivity on disorder in Sr₂RuO₄.
Physical Review Letters **80**, 161 (1998).
10/b562dq.
- 320 **Y. Maeno, H. Hashimoto, K. Yoshida, et al.**
Superconductivity in a layered perovskite without copper.
Nature **372**, 532 (1994).
10/dqtw6w.
- 321 **K. Ishida, H. Mukuda, Y. Kitaoka, et al.**
Spin-triplet superconductivity in Sr₂RuO₄ identified by ¹⁷O Knight shift.
Nature **396**, 658 (1998).
10/d2qh9p.

- 322 **F. Laube, G. Goll, H. von Löhneysen, et al.**
Spin-triplet superconductivity in Sr_2RuO_4 probed by
Andreev reflection.
Physical Review Letters **84**, 1595 (2000).
10/c7sjwk.
- 323 **Y. Maeno, T.M. Rice, M. Sigrist.**
The intriguing superconductivity of strontium ruthenate.
Physics Today **54**, 42 (2001).
10/dhgv8.
- 324 **Б.Л. Безрезинский.**
Новая модель анизотропной фазы сверхтекучего He^3 .
Письма в ЖЭТФ **20**, 628 (1974);
V.L. Berezinskii.
New model of the anisotropic phase of superfluid He^3 .
JETP Letters **20**, 287 (1974).
- 325 **J. Linder, A.V. Balatsky.**
Odd-frequency superconductivity.
arXiv: 1709.03986.
- 326 **J. Nagamatsu, N. Nakagawa, T. Muranaka, et al.**
Superconductivity at 39 K in magnesium diboride.
Nature **410**, 63 (2001).
10/c5xzh.
- 327 **C. Buzea, T. Yamashita.**
Review of the superconducting properties of MgB_2 .
Superconductor Science and Technology **14**, R115 (2001).
10/d28ntn.

- 328 **A. Aperis, P. Maldonado, P.M. Oppeneer.**
Ab initio theory of magnetic-field-induced odd-frequency two-band superconductivity in MgB₂.
Physical Review B **92**, 054516 (2015).
10/f3pmjm.
- 329 **F.S. Bergeret, A.F. Volkov, K.B. Efetov.**
Long-range proximity effects in superconductor–ferromagnet structures.
Physical Review Letters **86**, 4096 (2001).
10/bg59wr.
- 330 **Y. Tanaka, Y. Tanuma, A.A. Golubov.**
Odd-frequency pairing in normal-metal/superconductor junctions.
Physical Review B **76**, 054522 (2007).
10/bwhcm5.
- 331 **F.S. Bergeret, A.F. Volkov, K.B. Efetov.**
Josephson current in superconductor–ferromagnet structures with a nonhomogeneous magnetization.
Physical Review B **64**, 134506 (2001).
10/b7v2n5.
- 332 **A. Kadigrobov, R.I. Shekhter, M. Jonson.**
Quantum spin fluctuations as a source of long-range proximity effects in diffusive ferromagnet-superconductor structures.
Europhysics Letters **54**, 394 (2001).
10/d7h6g2.

- 333 **F.S. Bergeret, A.F. Volkov, K.B. Efetov.**
 Manifestation of triplet superconductivity in
 superconductor–ferromagnet structures.
Physical Review B **68**, 064513 (2003).
 10/fhkzkw.
- 334 **A.F. Volkov, F.S. Bergeret, K.B. Efetov.**
 Odd triplet superconductivity in superconductor–ferromagnet
 multilayered structures.
Physical Review Letters **90**, 117006 (2003).
 10/b7nzw6.
- 335 **Y.V. Fominov, A.A. Golubov, M.Y. Kupriyanov.**
 Triplet proximity effect in FSF trilayers.
JETP Letters **77**, 510 (2003).
 10/cj3gvq.
- 336 **G.E. Blonder, M. Tinkham, T.M. Klapwijk.**
 Transition from metallic to tunneling regimes in superconducting
 microconstrictions: Excess current, charge imbalance, and
 supercurrent conversion.
Physical Review B **25**, 4515 (1982).
 10/bwjv89.
- 337 **S. Datta, P.F. Bagwell, M.P. Anantram.**
Scattering Theory of Transport for Mesoscopic Superconductors
 ECE Technical Reports, ECE-107
 (Purdue University, 1996).
<http://docs.lib.purdue.edu/ecetr/107>.
- 338 **A.F. Andreev.**
 The thermal conductivity of the intermediate state in
 superconductors.
Soviet Physics—JETP **19**, 1228 (1964).

- 339 **P.G. de Gennes, D. Saint-James.**
Elementary excitations in the vicinity of a normal-metal–superconducting-metal contact.
Physics Letters **4**, 151 (1963).
10/ck3kxt.
- 340 **D. Saint-James.**
Excitations élémentaires au voisinage de la surface de séparation d'un métal normal et d'un métal supraconducteur.
Journal de Physique **25**, 899 (1964).
10/d74whj.
- 341 **G. Deutscher.**
Andreev–Saint-James reflections: A probe of cuprate superconductors.
Reviews of Modern Physics **77**, 109 (2005).
10/fsm23s.
- 342 **J.A. Sauls.**
Andreev bound states and their signatures.
Phil. Trans. of the Royal Society A **376**, 20180140 (2018).
10/gd876f.
- 343 **M. Eschrig.**
Spin-polarized supercurrents for spintronics: A review of current progress.
Reports on Progress in Physics **78**, 104501 (2015).
10/cwvc.
- 344 **S. Datta.**
Electronic Transport in Mesoscopic Systems.
(Cambridge University Press, 1995).
10/c5zt.

- 345 **T. Heinzel.**
Mesoscopic Electronics in Solid State Nanostructures.
(Wiley-VCH Verlag GmbH, 2006).
10/dzmsvf.
- 346 **B. Josephson.**
Possible new effects in superconductive tunnelling.
Physics Letters **1**, 251 (1962).
10/fbfm9m.
- 347 **P.W. Anderson, J.M. Rowell.**
Probable observation of the Josephson superconducting
tunneling effect.
Physical Review Letters **10**, 230 (1963).
10/c2fppj.
- 348 **K.K. Likharev.**
Superconducting weak links.
Reviews of Modern Physics **51**, 101 (1979).
10/fck7v7.
- 349 **L.P. Gor'kov.**
Microscopic derivation of the Ginzburg–Landau equations in the
theory of superconductivity.
Soviet Physics—JETP **9**, 1364 (1959).
- 350 **A.A. Abrikosov, L.P. Gorkov, I.E. Dzyaloshinskii.**
Methods of Quantum Field Theory in Statistical Physics.
(Dover Publications, 1975).
- 351 **A.A. Golubov, M.Y. Kupriyanov, E. Il'ichev.**
The current–phase relation in Josephson junctions.
Reviews of Modern Physics **76**, 411 (2004).
10/bs7wmz.

- 352 **M. Eschrig.**
Spin-polarized supercurrents for spintronics.
Physics Today **64**, 43 (2011).
10/d8cj2w.
- 353 **И.О. Кулик, А.Н. Омелянчук.**
К микроскопической теории эффекта Джозефсона в
сверхпроводящих мостиках.
Письма в ЖЭТФ **21**, 216 (1975);
I.O. Kulik, A.N. Omel'yanchuk.
Contribution to the microscopic theory of the Josephson effect in
superconducting bridges.
JETP Letters **21**, 96 (1975).
- 354 **И.О. Кулик, А.Н. Омелянчук.**
Свойства сверхпроводящих микромостиков в чистом пределе.
Физика Низких Температур **3**, 945 (1977);
I.O. Kulik, A.N. Omel'yanchuk.
Properties of superconducting microbridges in the pure limit.
Soviet Journal of Low Temperature Physics **3**, 459 (1977).
- 355 **Y. Tanaka, S. Kashiwaya.**
Theory of Josephson effects in anisotropic superconductors.
Physical Review B **56**, 892 (1997).
10/bnxgsp.
- 356 **P. Fulde, R.A. Ferrell.**
Superconductivity in a strong spin-exchange field.
Physical Review **135**, A550 (1964).
10/bjhc54.
- 357 **A.I. Larkin, Y.N. Ovchinnikov.**
Nonuniform state of superconductors.
Soviet Physics—JETP **20**, 762 (1965).

- 358 **T. Kontos, M. Aprili, J. Lesueur, X. Grison.**
 Inhomogeneous superconductivity induced in a ferromagnet by proximity effect.
Physical Review Letters **86**, 304 (2001).
 10/crw6nx.
- 359 **M. Eschrig, J. Kopp, J.C. Cuevas, G. Schön.**
 Theory of half-metal/superconductor heterostructures.
Physical Review Letters **90**, 137003 (2003).
 10/bzkdct.
- 360 **Л.Н. Булаевский, В.В. Кузий, А.А. Собянин.**
 Сверхпроводящая система со слабой связью с током в основном состоянии.
Письма в ЖЭТФ **25**, 314 (1977);
L.N. Bulaevskii, V.V. Kuzii, A.A. Sobyenin.
 Superconducting system with weak coupling to the current in the ground state.
JETP Letters **25**, 290 (1977).
- 361 **V.V. Ryazanov, V.A. Obznov, A.Y. Rusanov, et al.**
 Coupling of two superconductors through a ferromagnet: Evidence for a π junction.
Physical Review Letters **86**, 2427 (2001).
 10/b5vghk.
- 362 **T. Kontos, M. Aprili, J. Lesueur, et al.**
 Josephson junction through a thin ferromagnetic layer: Negative coupling.
Physical Review Letters **89**, 137007 (2002).
 10/fhz36m.

- 363 **Y. Blum, A. Tsukernik, M. Karpovski, A. Palevski.**
Oscillations of the superconducting critical current in
Nb–Cu–Ni–Cu–Nb junctions.
Physical Review Letters **89**, 187004 (2002).
10/ctsjtq.
- 364 **V.A. Oboznov, V.V. Bol'ginov, A.K. Feofanov, et al.**
Thickness dependence of the Josephson ground states of
superconductor–ferromagnet–superconductor junctions.
Physical Review Letters **96**, 197003 (2006).
10/c26568.
- 365 **E. Sonin.**
Spin currents and spin superfluidity.
Advances in Physics **59**, 181 (2010).
10/cjrdr.
- 366 **M.G. Blamire, J.W.A. Robinson.**
The interface between superconductivity and magnetism:
Understanding and device prospects.
Journal of Physics: Condensed Matter **26**, 453201 (2014).
10/gfc8kz.
- 367 **J.J. Sakurai, J. Napolitano.**
Modern Quantum Mechanics. 2nd ed.
(Cambridge University Press, 2017).
10/c5zv.
- 368 **J.W.A. Robinson, J.D.S. Witt, M.G. Blamire.**
Controlled injection of spin-triplet supercurrents into a strong
ferromagnet.
Science **329**, 59 (2010).
10/d9rkh4.

- 369 **M. Houzet, A.I. Buzdin.**
Long range triplet Josephson effect through a
ferromagnetic trilayer.
Physical Review B **76**, 060504 (2007).
10/b2vp9c.
- 370 **T.S. Khaire, M.A. Khasawneh, W.P. Pratt, N.O. Birge.**
Observation of spin-triplet superconductivity in Co-based
Josephson junctions.
Physical Review Letters **104**, 137002 (2010).
10/bkvp93.
- 371 **W.M. Martinez, W.P. Pratt, N.O. Birge.**
Amplitude control of the spin-triplet supercurrent in s/F/s
Josephson junctions.
Physical Review Letters **116**, 077001 (2016).
10/gft6rp.
- 372 **F.S. Bergeret, I.V. Tokatly.**
Singlet–triplet conversion and the long-range proximity effect in
superconductor–ferromagnet structures with generic spin
dependent fields.
Physical Review Letters **110**, 117003 (2013).
10/gc5phk.
- 373 **F.S. Bergeret, I.V. Tokatly.**
Spin–orbit coupling as a source of long-range triplet proximity
effect in superconductor–ferromagnet hybrid structures.
Physical Review B **89**, 134517 (2014).
10/gc5phg.

- 374 **S.H. Jacobsen, I. Kulagina, J. Linder.**
Controlling superconducting spin flow with spin-flip immunity using a single homogeneous ferromagnet.
Scientific Reports **6**, 23926 (2016).
10/f8gss4.
- 375 **M. Amundsen, J. Linder.**
The quasiclassical theory for interfaces with spin-orbit coupling.
arXiv: 1904.11986.
- 376 **N. Satchell, N.O. Birge.**
Supercurrent in ferromagnetic Josephson junctions with heavy metal interlayers.
Physical Review B **97**, 214509 (2018).
10/gf2jrb.
- 377 **N. Satchell, R. Loloee, N.O. Birge.**
Supercurrent in ferromagnetic Josephson junctions with heavy metal interlayers. II. Canted magnetization.
arXiv: 1904.08798.
- 378 **J.-F. Liu, K.S. Chan.**
Anomalous Josephson current through a ferromagnetic trilayer junction.
Physical Review B **82**, 184533 (2010).
10/cgnw3h.
- 379 **В.Б. Гешкенбейн, А.И. Ларкин.**
Эффект Джозефсона в сверхпроводниках с тяжелыми фермионами.
Письма в ЖЭТФ **43**, 306 (1986);
V.B. Geshkenbein, A.I. Larkin.
The Josephson effect in superconductors with heavy fermions.
JETP Letters **43**, 395 (1986).

- 380 **S. Yip.**
Josephson current–phase relationships with unconventional superconductors.
Physical Review B **52**, 3087 (1995).
10/dvnx83.
- 381 **M. Sigrist.**
Time-reversal symmetry breaking states in high-temperature superconductors.
Progress of Theoretical Physics **99**, 899 (1998).
10/b8css8.
- 382 **S. Kashiwaya, Y. Tanaka.**
Tunnelling effects on surface bound states in unconventional superconductors.
Reports on Progress in Physics **63**, 1641 (2000).
10/d8xyp2.
- 383 **I.V. Krive, L.Y. Gorelik, R.I. Shekhter, M. Jonson.**
Chiral symmetry breaking and the Josephson current in a ballistic superconductor–quantum wire–superconductor junction.
Low Temperature Physics **30**, 398 (2004).
10/c62zj9.
- 384 **A.A. Reynoso, G. Usaj, C.A. Balseiro, et al.**
Anomalous Josephson current in junctions with spin polarizing quantum point contacts.
Physical Review Letters **101**, 107001 (2008).
10/fg4znm.

- 385 **A. Buzdin.**
Direct coupling between magnetism and superconducting current in the Josephson φ_0 junction.
Physical Review Letters **101**, 107005 (2008).
10/bq5gsm.
- 386 **Y. Tanaka, T. Yokoyama, N. Nagaosa.**
Manipulation of the Majorana fermion, Andreev reflection, and Josephson current on topological insulators.
Physical Review Letters **103**, 107002 (2009).
10/b6cn3g.
- 387 **L. Dell'Anna, A. Zazunov, R. Egger, T. Martin.**
Josephson current through a quantum dot with spin-orbit coupling.
Physical Review B **75**, 085305 (2007).
10/c2gj28.
- 388 **A. Zazunov, R. Egger, T. Jonckheere, T. Martin.**
Anomalous Josephson current through a spin-orbit coupled quantum dot.
Physical Review Letters **103**, 147004 (2009).
10/d5q9fn.
- 389 **A. Brunetti, A. Zazunov, A. Kundu, R. Egger.**
Anomalous Josephson current, incipient time-reversal symmetry breaking, and Majorana bound states in interacting multilevel dots.
Physical Review B **88**, 144515 (2013).
10/gf2m5r.
- 390 **D.B. Szombati, S. Nadj-Perge, D. Car, et al.**
Josephson φ_0 -junction in nanowire quantum dots.
Nature Physics **12**, 568 (2016).
10/f8p7r7.

- 391 **J.-F. Liu, K.S. Chan.**
Relation between symmetry breaking and the anomalous Josephson effect.
Physical Review B **82**, 125305 (2010).
10/d5bvht.
- 392 **A. Rasmussen, J. Danon, H. Suominen, et al.**
Effects of spin-orbit coupling and spatial symmetries on the Josephson current in SNS junctions.
Physical Review B **93**, 155406 (2016).
10/gffjdb.
- 393 **S. Takahashi, S. Maekawa.**
Hall effect induced by a spin-polarized current in superconductors.
Physical Review Letters **88**, 116601 (2002).
10/fgkzdh.
- 394 **S. Takahashi, S. Maekawa.**
Spin current in metals and superconductors.
Journal of the Physical Society of Japan **77**, 031009 (2008).
10/d5w8xh.
- 395 **S. Takahashi, S. Maekawa.**
Spin Hall effect in superconductors.
Japanese Journal of Applied Physics **51**, 010110 (2012).
10/cjr32s.
- 396 **H. Kontani, J. Goryo, D.S. Hirashima.**
Intrinsic spin Hall effect in the s-wave superconducting state: Analysis of the Rashba model.
Physical Review Letters **102**, 086602 (2009).
10/dzkw59.

- 397 **S. Pandey, H. Kontani, D.S. Hirashima, et al.**
Spin Hall effect in iron-based superconductors:
A Dirac-point effect.
Physical Review B **86**, 060507 (2012).
10/gd4rkw.
- 398 **A.G. Mal'shukov.**
Supercurrent generation by spin injection in an s-wave
superconductor–Rashba metal bilayer.
Physical Review B **95**, 064517 (2017).
10/gd4rk5.
- 399 **C. Espedal, P. Lange, S. Sadjina, et al.**
Spin Hall effect and spin swapping in diffusive superconductors.
Physical Review B **95**, 054509 (2017).
10/gd4vdj.
- 400 **T. Wakamura, H. Akaike, Y. Omori, et al.**
Quasiparticle-mediated spin Hall effect in a superconductor.
Nature Materials **14**, 675 (2015).
10/f7gpd4.
- 401 **A.G. Mal'shukov, C.S. Chu.**
Spin Hall effect in a Josephson contact.
Physical Review B **78**, 104503 (2008).
10/dwgqd3.
- 402 **A.G. Mal'shukov, C.S. Chu.**
Spin-Hall current and spin polarization in an electrically biased
SNS Josephson junction.
Physical Review B **84**, 054520 (2011).
10/bhgdgw.

- 403 **A.G. Mal'shukov, S. Sadjina, A. Brataas.**
Inverse spin Hall effect in superconductor/normal-metal/superconductor Josephson junctions.
Physical Review B **81**, 060502 (2010).
10/fjm2m7.
- 404 **F.S. Bergeret, I.V. Tokatly.**
Manifestation of extrinsic spin Hall effect in superconducting structures: Nondissipative magnetoelectric effects.
Physical Review B **94**, 180502 (2016).
10/gd4rk3.
- 405 **K. Sengupta, R. Roy, M. Maiti.**
Spin Hall effect in triplet chiral superconductors and graphene.
Physical Review B **74**, 094505 (2006).
10/bxt977.
- 406 **Z.-H. Yang, Y.-H. Yang, J. Wang.**
Interfacial spin Hall current in a Josephson junction with Rashba spin-orbit coupling.
Chinese Physics B **21**, 057402 (2012).
10/gd4rkt.
- 407 **V.P. Mineev, G.E. Volovik.**
Electric dipole moment and spin supercurrent in superfluid ^3He .
Journal of Low Temperature Physics **89**, 823 (1992).
10/b3rnzj.
- 408 **F. Meier, D. Loss.**
Magnetization transport and quantized spin conductance.
Physical Review Letters **90**, 167204 (2003).
10/dvvptc.

- 409 **E.B. Sonin.**
Proposal for measuring mechanically equilibrium spin currents in the Rashba medium.
Physical Review Letters **99**, 266602 (2007).
10/drxkps.
- 410 **I. Kulagina, J. Linder.**
Spin supercurrent, magnetization dynamics, and ϕ -state in spin-textured Josephson junctions.
Physical Review B **90**, 054504 (2014).
10/gffh3f.
- 411 **I.V. Bobkova, A.M. Bobkov, M.A. Silaev.**
Spin torques and magnetic texture dynamics driven by the supercurrent in superconductor/ferromagnet structures.
Physical Review B **98**, 014521 (2018).
10/gffh3h.
- 412 **K.-A.N. Duerloo, M.T. Ong, E.J. Reed.**
Intrinsic piezoelectricity in two-dimensional materials.
Journal of Physical Chemistry Letters **3**, 2871 (2012).
10/f4bntv.
- 413 **W. Wu, L. Wang, Y. Li, et al.**
Piezoelectricity of single-atomic-layer MoS₂ for energy conversion and piezotronics.
Nature **514**, 470 (2014).
10/gf2mhw.
- 414 **H. Zhu, Y. Wang, J. Xiao, et al.**
Observation of piezoelectricity in free-standing monolayer MoS₂.
Nature Nanotechnology **10**, 151 (2015).
10/gf2vgm.

- 415 **M. Bonilla, S. Kolekar, Y. Ma, et al.**
Strong room-temperature ferromagnetism in VSe₂ monolayers on van der Waals substrates.
Nature Nanotechnology **13**, 289 (2018).
10/gf2vgrp.
- 416 **D.J. O'Hara, T. Zhu, A.H. Trout, et al.**
Room temperature intrinsic ferromagnetism in epitaxial manganese selenide films in the monolayer limit.
Nano Letters **18**, 3125 (2018).
10/gdkqwr.
- 417 **J. Yang, A. Wang, S. Zhang, et al.**
Coexistence of piezoelectricity and magnetism in two-dimensional vanadium dichalcogenides.
Physical Chemistry Chemical Physics **21**, 132 (2019).
10/gf2vgf.
- 418 **R.S. Keizer, S.T.B. Goennenwein, T.M. Klapwijk, et al.**
A spin triplet supercurrent through the half-metallic ferromagnet CrO₂.
Nature **439**, 825 (2006).
10/bxgrgd.
- 419 **M.S. Anwar, F. Czeschka, M. Hesselberth, et al.**
Long-range supercurrents through half-metallic ferromagnetic CrO₂.
Physical Review B **82**, 100501 (2010).
10/b84b72.
- 420 **M.S. Anwar, J. Aarts.**
Inducing supercurrents in thin films of ferromagnetic CrO₂.
Superconductor Science and Technology **24**, 024016 (2011).
10/cj5kms.

- 421 **M.S. Anwar, M. Veldhorst, A. Brinkman, J. Aarts.**
Long range supercurrents in ferromagnetic CrO₂ using a
multilayer contact structure.
Applied Physics Letters **100**, 052602 (2012).
10/gft6rn.
- 422 **F. Korschelle, A. Buzdin.**
Magnetic moment manipulation by a Josephson current.
Physical Review Letters **102**, 017001 (2009).
10/bkknqs.

I

Reference

V. Risinggård, J. Linder.

Universal absence of Walker breakdown and linear current–velocity relation via spin–orbit torques in coupled and single domain wall motion. *Physical Review B* **95**, 134423 (2017).

10/c2q9

Contributions

JL initiated and supervised the project. VR did the analytical and numerical work. VR realized the relevance of the results to the switching anomaly reported by C. Bi *et al.* (*Phys. Rev. B* **95**, 104434; 2017) and fitted the model to the experiment. All authors contributed to the discussion of the results and the revision of the final manuscript.

Comments

This work was presented at the 2017 APS March Meeting, session R47.6 (New Orleans, LA, USA).

Universal absence of Walker breakdown and linear current-velocity relation via spin-orbit torques in coupled and single domain wall motion

Vetle Risinggård* and Jacob Linder

Department of Physics, NTNU, Norwegian University of Science and Technology, N-7491 Trondheim, Norway

(Received 21 December 2016; published 14 April 2017)

We consider theoretically domain wall motion driven by spin-orbit and spin Hall torques. We find that it is possible to achieve universal absence of Walker breakdown for all spin-orbit torques using experimentally relevant spin-orbit coupling strengths. For spin-orbit torques other than the pure Rashba spin-orbit torque, this gives a linear current-velocity relation instead of a saturation of the velocity at high current densities. The effect is very robust and is found in both soft and hard magnetic materials, as well as in the presence of the Dzyaloshinskii-Moriya interaction and in coupled domain walls in synthetic antiferromagnets, where it leads to very high domain wall velocities. Moreover, recent experiments have demonstrated that the switching of a synthetic antiferromagnet does not obey the usual spin Hall angle dependence, but that domain expansion and contraction can be selectively controlled toggling only the applied in-plane magnetic field magnitude and not its sign. We show that the combination of spin Hall torques and interlayer exchange coupling produces the necessary relative velocities for this switching to occur.

DOI: [10.1103/PhysRevB.95.134423](https://doi.org/10.1103/PhysRevB.95.134423)

I. INTRODUCTION

Domain wall motion in ferromagnetic strips is a central theme in magnetization dynamics and has recently been instrumental to the discovery of several new current-induced effects [1–6]. The attainable velocity of a domain wall driven by conventional spin-transfer torques (STTs) [7–9] is limited by the Walker breakdown [10], upon which the domain wall deforms, resulting in a reduction of its velocity.

Current-induced torques derived from spin-orbit effects (SOTs) such as the spin Hall effect [4–6,11] or an interfacial Rashba spin-orbit coupling [12–14] have enabled large domain wall velocities. We here consider the dependence of the domain wall velocity on the current and find that regardless of the relative importance of the reactive and dissipative components of the torque it is possible to achieve universal absence of Walker breakdown for all current densities for experimentally relevant spin-orbit coupling strengths. For spin-orbit torques other than the pure Rashba SOTs, such as the spin Hall torques, the velocity will not saturate as a function of current, but will increase linearly as long as a conventional spin-transfer torque is present. This behavior is robust against the presence of an interfacial Dzyaloshinskii-Moriya interaction [15–17] and is found both in perpendicular anisotropy ferromagnets, in shape anisotropy-dominated strips and in synthetic antiferromagnets (SAFs) [18–22], where it enables very high domain wall velocities for relatively small current densities. Moreover, the combination of SOTs with the interlayer exchange torque was recently shown experimentally to produce novel switching behavior that circumvents the usual spin Hall angle dependence [22]. We show that the combination of spin Hall torques and interlayer exchange produces the required dependence of the domain wall velocity on the topological charge to qualitatively reproduce the experimental data.

II. UNIVERSAL ABSENCE OF WALKER BREAKDOWN

We consider an ultrathin ferromagnet with a heavy-metal underlayer as shown in Fig. 1. We describe the dynamics of the magnetization $\mathbf{m}(\mathbf{r}, t)$ using the Landau-Lifshitz-Gilbert (LLG) equation [23],

$$\partial_t \mathbf{m} = \gamma \mathbf{m} \times \mathbf{H} - \frac{\alpha}{m} \mathbf{m} \times \partial_t \mathbf{m} + \boldsymbol{\tau}, \quad (1)$$

where $\gamma < 0$ is the gyromagnetic ratio, m is the saturation magnetization, $\alpha < 0$ is the Gilbert damping, $\mathbf{H} = -\delta F / \delta \mathbf{m}$ is the effective field acting on the magnetization, and $\boldsymbol{\tau}$ is the current-induced torques. The free energy F of the ferromagnet is a sum,

$$F = \int d\mathbf{r} (f_Z + f_{\text{ex}} + f_{\text{DM}} + f_a), \quad (2)$$

of the Zeeman energy due to applied magnetic fields, the isotropic exchange, the interfacial Dzyaloshinskii-Moriya interaction, and the magnetic anisotropy.

The Zeeman energy and the isotropic exchange can be written, respectively, as $f_Z = -\mathbf{H}_0 \cdot \mathbf{m}$, where \mathbf{H}_0 is the applied magnetic field, and $f_{\text{ex}} = (A/m^2)[(\nabla m_x)^2 + (\nabla m_y)^2 + (\nabla m_z)^2]$, where A is the exchange stiffness [23]. Inversion symmetry breaking at the interface between the heavy metal and the ferromagnet gives rise to an anisotropic contribution to the exchange known as the Dzyaloshinskii-Moriya interaction, which favors a canting of the spins [15–17]. The resulting contribution to the free energy is $f_{\text{DM}} = (D/m^2)[m_z(\nabla \cdot \mathbf{m}) - (\mathbf{m} \cdot \nabla)m_z]$, where D is the magnitude of the Dzyaloshinskii-Moriya vector. Ultrathin magnetic films are prone to exhibit perpendicular magnetization due to interface contributions to the magnetic anisotropy [24]. Consequently, we write the magnetic anisotropy energy as $f_a = -K_z m_z^2 + K_y m_y^2$, corresponding to an easy axis in the z direction and a hard axis in the y direction.

*vetle.k.risinggard@ntnu.no

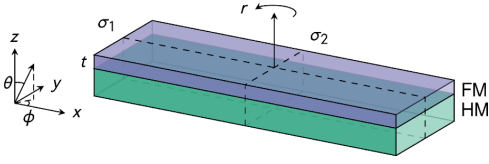


FIG. 1. Ultrathin ferromagnet with a heavy-metal underlayer. We consider transverse domain wall motion along the x axis. r , σ_1 , and σ_2 denote the three nontrivial operations of the symmetry group C_{2v} .

A. Current-induced torques

The current-induced torques τ are conventionally divided into spin-transfer torques and spin-orbit torques. The spin-transfer torques can be written as [7–9]

$$\tau_{\text{STT}} = u \partial_x \mathbf{m} - \frac{\beta u}{m} \mathbf{m} \times \partial_x \mathbf{m}, \quad (3)$$

where $u = \mu_B P j / [em(1 + \beta^2)]$ and j is the electric current, P is its spin polarization, μ_B is the Bohr magneton, e is the electric charge, and β is the nonadiabacity parameter. The spin-orbit torques can be written as [4–6, 11–14]

$$\tau_{\text{R}} = \gamma \mathbf{m} \times H_{\text{R}} \mathbf{e}_y - \gamma \mathbf{m} \times \left(\mathbf{m} \times \frac{\beta H_{\text{R}}}{m} \mathbf{e}_y \right), \quad (4)$$

$$\tau_{\text{SH}} = \gamma \mathbf{m} \times \left(\mathbf{m} \times \frac{H_{\text{SH}}}{m} \mathbf{e}_y \right) + \gamma \mathbf{m} \times \beta_{\text{SH}} H_{\text{SH}} \mathbf{e}_y, \quad (5)$$

where $H_{\text{R}} = \alpha_{\text{R}} P j / [2\mu_B m(1 + \beta^2)]$ and α_{R} is the Rashba parameter and where $H_{\text{SH}} = \hbar \theta_{\text{SH}} j / (2em t)$ and θ_{SH} is the spin Hall angle and t is the magnet thickness. Since the spin Hall effect changes sign upon time reversal, the principal spin Hall torque term is dissipative instead of reactive, in contrast to the principal term of the STTs and the Rashba SOTs.

In fact, assuming that the stack can be described using the C_{2v} symmetry group (see Fig. 1) it can be shown that these torques exhaust the number of possible torque components. Hals and Brataas [25] describe spin-orbit torques and generalized spin-transfer torques in terms of a tensor expansion. Assuming the lowest orders are sufficient to describe the essential dynamics, the reactive and dissipative spin-orbit torques are described by, respectively, an axial second-rank tensor and a polar third-rank tensor while the generalized spin-transfer torques are described using a polar fourth-rank tensor and an axial fifth-rank tensor. The torques that arise in a given structure are limited by the requirement that the tensors must be invariant under the symmetry operations fulfilled by the structure. We have assumed that the physical systems we consider are described by C_{2v} symmetry. Combined with the fact that the current is applied in the x direction only and that $\partial_y \mathbf{m} = 0$ and $\partial_z \mathbf{m} = 0$, this implies that there is only one relevant nonzero element in the axial second-rank tensor, two elements in the polar third-rank tensor, three elements in the polar fourth-rank tensor, and six elements in the axial fifth-rank tensor [26].

The three relevant nonzero elements of the second- and third-rank tensors give rise to three spin-orbit torques. A detailed analysis shows that these torque components are captured by the Rashba and spin Hall torques in Eqs. (4)

and (5). As an aside, we note that although the Rashba and spin Hall effects may not necessarily capture all of the relevant microscopic physics [27–29] these torques can still be used to model the dynamics because they contain three free parameters, α_{R} , θ_{SH} , and β_{SH} .

As has been shown in Ref. [25], the generalized spin-transfer torques reduce to the ordinary STTs in the nonrelativistic limit. Thus, by using the ordinary STTs we neglect possible spin-orbit coupling corrections to these higher-order terms.

B. Collective coordinate model

The magnetization is conveniently parametrized in spherical coordinates as $\mathbf{m}/m = \cos \phi \sin \theta \mathbf{e}_x + \sin \phi \sin \theta \mathbf{e}_y + \cos \theta \mathbf{e}_z$. Using the assumption that there is no magnetic texture along the y and the z axes, $\nabla = \partial_x \mathbf{e}_x$, we can find the domain wall profile by minimizing the free energy. The resulting Euler-Lagrange equations are

$$A(\theta'' \csc \theta \sec \theta - \phi^2) - D\phi' \sin \phi \tan \theta = (K_z + K_y \sin^2 \phi) \quad \text{and}$$

$$A(\phi'' + 2\theta' \phi' \cot \theta) + D\theta' \sin \phi = K_y \cos \phi \sin \phi.$$

One solution of these differential equations is the Néel wall solution $\phi = n\pi$ and $\theta = 2 \arctan \exp[Q(x - X)/\lambda]$, where Q is the topological charge of the wall [30], X is the wall position, and $\lambda = \sqrt{A/K_z}$ is the domain wall width. n is even if $D < 0$ and $Q = +1$, and n is odd if $D < 0$ and $Q = -1$. This domain wall profile is known as the Walker profile [10]. To be sure that $\phi = n\pi$ is really the global minimum, we solve the full LLG equation (1) for a single magnetic layer and let the solution relax without any applied currents or fields. The angle $\phi(x)$ can then be calculated as $\phi(x) = \arctan[m_y(x)/m_x(x)]$. However, $\phi(x)$ is ill defined in the domains where $\theta \rightarrow 0$ or π . Consequently, we consider ϕ only inside the domain wall. As shown in Fig. 2(a), the solution $\phi = 0$ works very well.

Substitution of the Walker profile into the full LLG equation (1) using $\mathbf{H}_0 = H_x \mathbf{e}_x$ and $Q = +1$ gives the collective coordinate equations for the wall position X and tilt ϕ

$$\begin{aligned} \frac{\alpha \dot{X}}{\lambda} - \dot{\phi} &= +\frac{\pi}{2} \gamma (H_{\text{SH}} - \beta H_{\text{R}}) \cos \phi + \frac{\beta u}{\lambda}, \quad (6) \\ (1 + \alpha^2) \dot{\phi} &= -\frac{\alpha \gamma K_y}{m} \sin 2\phi + \frac{\pi \alpha \gamma (D - H_x m \lambda)}{2m\lambda} \sin \phi \\ &\quad - \frac{u(\alpha + \beta)}{\lambda} - \frac{\pi}{2} \gamma [H_{\text{SH}}(1 - \alpha \beta_{\text{SH}}) \\ &\quad - H_{\text{R}}(\alpha + \beta)] \cos \phi. \quad (7) \end{aligned}$$

By doing this substitution, we are assuming that the domain wall moves as a rigid object described by two collective coordinates $X(t)$ and $\phi(t)$ (Ref. [30]). In particular, we are neglecting any position dependence in the domain wall tilt ϕ . The collective coordinate model, or one-dimensional model, has been used previously to explain the qualitative behavior of both spin-transfer and spin-orbit torques [4, 5, 7, 10, 18–20, 28, 30, 31]. However, it is important to remember that the model will always be an approximation, and we cannot necessarily expect quantitative agreement between experimental results and model predictions nor can we completely exclude

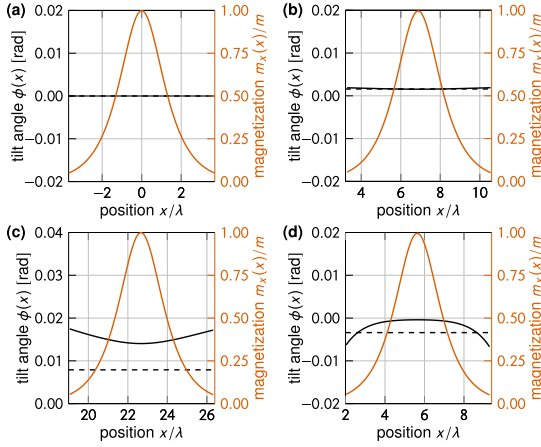


FIG. 2. Position dependence of the domain wall tilt ϕ . In each panel, the orange curve $m_x(x)$ shows the extension of the domain wall while the black solid curve shows the domain wall tilt $\phi(x)$ obtained by solving the full LLG equation (1) and the black dashed line shows the prediction of the collective coordinate model. (a) Equilibrium solution. (b) Spin-transfer torque dynamics. (c) Spin Hall torque dynamics. (d) Rashba spin-orbit torque dynamics. (a)–(d) We use the material parameters supplied in the first column of Table 1 with $j = 5 \text{ MA cm}^{-2}$ except that $J = 0$.

the possibility of dynamics that is not captured by the one-dimensional model [31]. We can nevertheless test the adequacy of the collective coordinate model by calculating $\phi(x)$ from a solution of the full LLG equation for a single magnetic layer, just as we did for the static case. As shown in Fig. 2(b) the x dependence of ϕ is negligible for spin-transfer torques. The x dependence of ϕ is larger for spin Hall [Fig. 2(c)] and Rashba spin-orbit torques [Fig. 2(d)]. Nonetheless, the ability of the collective coordinate model to consistently qualitatively reproduce experimental behavior indicates that it captures the generality, if not all, of the physics in the system.

Equations (6) and (7) can be simplified by introducing $aj = \frac{\pi}{2}\gamma(H_{\text{SH}} - \beta H_{\text{R}})$, $bj = \beta u/\lambda$, $c = -2\alpha\gamma K_y/m$, $d = \pi\alpha\gamma(D - H_x m\lambda)/(2m\lambda)$, $ej = -\frac{\pi}{2}\gamma[H_{\text{SH}}(1 - \alpha\beta_{\text{SH}}) - H_{\text{R}}(\alpha + \beta)]$, and $fj = -u(\alpha + \beta)/\lambda$. Walker breakdown is absent when the time derivative $\dot{\phi}$ vanishes, resulting in the condition

$$0 = c \sin \phi \cos \phi + d \sin \phi + j(e \cos \phi + f). \quad (8)$$

Provided that the transverse domain wall is not transformed into, for instance, a vortex wall [31], Walker breakdown will be universally absent if $e > f$ because this equation always has a solution for ϕ regardless of the value of j . For increasing j , ϕ will level off to a value $\cos \phi = -f/e$. For realistic material values $e > f$ corresponds to a Rashba parameter $\alpha_{\text{R}} > 4\mu_{\text{B}}^2/(\pi e\gamma\lambda) = 1\text{--}6 \text{ meV nm}$ (pure Rashba SOTs) or a spin Hall angle $\theta_{\text{SH}} > 4\mu_{\text{B}}Pt/(\pi\hbar\gamma\lambda) = 0.05\text{--}0.09$ (pure spin Hall torques). To the best of our knowledge, the absence of Walker breakdown for spin Hall torques has not been noted previously, whereas absence of Walker breakdown for

sufficiently strong Rashba spin-orbit coupling was pointed out in Ref. [32], and can also be noted in Refs. [13,33–35].

Let us write $\xi = \cos \phi$ and $\eta = \sin \phi$, so that $\xi^2 + \eta^2 = 1$. Solving Eq. (8) for η to get $\eta = -j(e\xi + f)/(c\xi + d)$, this relation gives a quartic equation

$$c^2\xi^4 + 2cd\xi^3 + [(ej)^2 + d^2 - c^2]\xi^2 + 2(e fj^2 - cd)\xi = d^2 - (fj)^2.$$

The exact solutions of the quartic are hopelessly complicated. However, they all have the same series expansion around $j = 0$ and $j \rightarrow \infty$. We consider first the asymptotic expansion,

$$\xi = -\frac{f}{e} + \frac{S_1}{j} + O(j^{-2}), \quad (9)$$

where S_1 represents the solutions of the quadratic equation $e^6\xi^2 = d^2e^4 + c^2f^4 + (c^2 - d^2)f^2e^2 + 2cdef(f^2 - e^2)$. Using Eq. (6), the wall velocity is then

$$\frac{\alpha\dot{X}}{\lambda} = \left(b - \frac{af}{e}\right)j + aS_1 + aO(j^{-1}). \quad (10)$$

Back substitution of the abbreviations a , b , e , and f shows that for pure Rashba SOTs the coefficient of the linear term reduces to zero because the ratio of the reactive to the dissipative torque is the same for the STTs and the Rashba SOTs. Thus, for large j the domain wall velocity approaches a constant. For pure spin Hall torques we get instead the linear term $-u\alpha(1 + \beta\beta_{\text{SH}})/[\lambda(1 - \alpha\beta_{\text{SH}})]$. This means that for large j the velocity is actually independent of the sign of the spin Hall angle and increases linearly with j . Note the importance of including the STTs—which are always present—in these considerations: in the absence of STTs ($u \rightarrow 0$) both b and f go to zero and the velocity levels off to a constant for large j for any combination of SOTs.

For completeness, we also consider the series expansion about $j = 0$, which gives

$$\xi = -1 + \frac{(e - f)^2}{2(c - d)^2}j^2 + O(j^4) \quad (11)$$

and

$$\frac{\alpha\dot{X}}{\lambda} = (b - a)j + \frac{a(e - f)^2}{2(c - d)^2}j^3 + aO(j^5). \quad (12)$$

The key observation here is that in this regime the velocity does depend on the sign of the spin Hall angle ($a \propto \theta_{\text{SH}}$ for pure spin Hall torques) and increases with the cube of j . Combined with the spin Hall angle independence of the velocity in the $j \rightarrow \infty$ limit, this implies that even in the absence of Walker breakdown a nonmonotonic current-velocity relation is possible. Figure 3(a) shows a numerical solution of the coupled equations (6) and (7) as a function of j for pure Rashba SOTs and for pure spin Hall torques both in the cases of $\theta_{\text{SH}} > 0$ and $\theta_{\text{SH}} < 0$ together with the analytical solutions close to $j = 0$ and for large j for parameters that are typical for a standard cobalt-nickel multilayer. We see that our analytical results successfully approximate the full solution in the expected ranges of validity indicating the absence of Walker breakdown in the numerical solution.

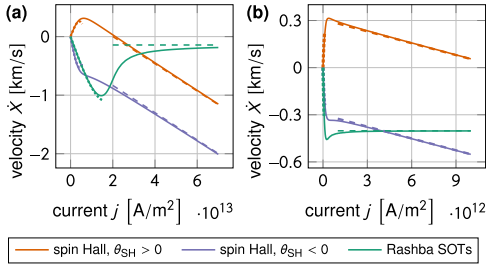


FIG. 3. Current-velocity relation for three different SOTs in the absence of Walker breakdown. The Rashba SOTs level off to a constant velocity at large currents, whereas the spin Hall torques asymptotically approach a linear current-velocity relation. Dashed lines show the asymptotic expansion and dotted curves show the series about $j = 0$. We use the material parameters supplied in the (a) first and (b) second column of Table I except that $J = 0$.

The in-plane hard axis included in the magnetic anisotropy is appropriate for narrow ferromagnetic strips, which generally host Néel walls. Wider strips give Bloch walls [24], and by making the necessary modifications to the above calculations, we find that in this case the domain wall velocity retains the qualitative features elucidated above. This is also true for shape anisotropy-dominated strips, which host head-to-head walls. This shows that universal absence of Walker breakdown is a robust effect that does not depend on the details of the ferromagnetic material, unlike other SOT effects studied previously [36]. This fact is also illustrated by the numerics. In Fig. 3(b) we present numerical results obtained for a Néel wall in a PMA ferromagnet with anisotropies weaker by an order of magnitude, weaker magnetic damping, and much larger Rashba spin-orbit coupling and spin Hall angle in the adjacent heavy metal. The results are qualitatively similar to those obtained in Fig. 3(a).

III. COUPLED DOMAIN WALLS IN A SAF STRUCTURE

We consider next an asymmetric stack of two ultrathin ferromagnets separated by an insulating spacer as shown in Fig. 4(a). We describe the dynamics of each of the ferromagnets using separate LLG equations, but add to the

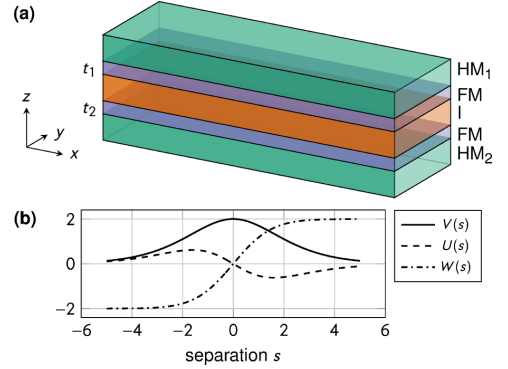


FIG. 4. (a) Two ultrathin ferromagnets separated by an insulating spacer with heavy-metal over- and underlayers. The ferromagnets are identical except for their thicknesses, but the different heavy metals induce different DMIs and SOTs. (b) Dependence of the IEC terms $V(s)$, $U(s)$, and $W(s)$ on the wall separation.

free energy a coupling term,

$$F_{\text{IEC}} = \int \frac{d\mathbf{r}_1}{m^{(1)}} \int \frac{d\mathbf{r}_2}{m^{(2)}} J(\mathbf{r}_1 - \mathbf{r}_2) [\mathbf{m}^{(1)}(\mathbf{r}_1) \cdot \mathbf{m}^{(2)}(\mathbf{r}_2)], \quad (13)$$

representing the interlayer exchange (IEC). We assume that the IEC is local in the plane, $J(\mathbf{r}_1 - \mathbf{r}_2) = J\delta(x_1 - x_2)\delta(y_1 - y_2)$. Equation (13) then represent the lowest-order coupling proposed by Bruno [37].

Following the same procedure as in the previous section we may now derive four coupled collective coordinate equations. With an antiferromagnetic coupling the walls will have opposite topological charges, $Q_2 = -Q_1$. Since a local IEC can only affect the chiralities, and not the profiles of the walls, we can use the static solution derived previously, $\theta = 2 \arctan \exp[Q(x - X)/\lambda]$, where $\lambda = \sqrt{A/K_z}$ is the domain wall width and Q is the topological charge. For a single wall the azimuthal angle ϕ is given by $\phi = n\pi$. n is even if $D < 0$ and $Q = +1$, and n is odd if $D < 0$ and $Q = -1$. To limit the scope of the treatment, we consider only the case where D_1 and D_2 have the same sign, $D_1 < 0$ and $D_2 < 0$. Then the DMI and the IEC cooperate to give the static solution $\phi_1 = 0$ ($Q_1 = +1$) and $\phi_2 = \pi$ ($Q_2 = -1$).

Substituting this static solution into the LLG equations using $\mathbf{H}_0 = H_x \mathbf{e}_x$ gives the collective coordinate equations

$$(1 + \alpha^2) \frac{\dot{X}_1}{\lambda} = -\frac{\gamma K_y}{m} \sin 2\phi_1 + \frac{\pi\gamma(D_1 - H_x m \lambda)}{2m\lambda} \sin \phi_1 + \frac{\gamma J t_2}{2m} [\alpha U(s) \cos(\phi_1 - \phi_2) + \alpha W(s) + V(s) \sin(\phi_1 - \phi_2)] - \frac{u(1 - \alpha\beta)}{\lambda} + \frac{\pi}{2} \gamma [H_{\text{SH}}^{(1)}(\alpha + \beta_{\text{SH}}^{(1)}) + H_{\text{R}}^{(1)}(1 - \alpha\beta)] \cos \phi_1, \quad (14)$$

$$(1 + \alpha^2) \frac{\dot{X}_2}{\lambda} = +\frac{\gamma K_y}{m} \sin 2\phi_2 + \frac{\pi\gamma(D_2 + H_x m \lambda)}{2m\lambda} \sin \phi_2 - \frac{\gamma J t_1}{2m} [\alpha U(s) \cos(\phi_1 - \phi_2) + \alpha W(s) - V(s) \sin(\phi_1 - \phi_2)] - \frac{u(1 - \alpha\beta)}{\lambda} + \frac{\pi}{2} \gamma [H_{\text{SH}}^{(2)}(\alpha + \beta_{\text{SH}}^{(2)}) + H_{\text{R}}^{(2)}(1 - \alpha\beta)] \cos \phi_2, \quad (15)$$

$$(1 + \alpha^2)\dot{\phi}_1 = -\frac{\alpha\gamma K_y}{m} \sin 2\phi_1 + \frac{\pi\alpha\gamma(D_1 - H_x m\lambda)}{2m\lambda} \sin \phi_1 - \frac{\gamma J t_2}{2m} [U(s) \cos(\phi_1 - \phi_2) + W(s) - \alpha V(s) \sin(\phi_1 - \phi_2)] - \frac{u(\alpha + \beta)}{\lambda} - \frac{\pi}{2}\alpha\gamma [H_{\text{SH}}^{(1)}(1 - \alpha\beta_{\text{SH}}^{(1)}) - H_{\text{R}}^{(1)}(\alpha + \beta)] \cos \phi_1, \quad (16)$$

$$(1 + \alpha^2)\dot{\phi}_2 = -\frac{\alpha\gamma K_y}{m} \sin 2\phi_2 - \frac{\pi\alpha\gamma(D_2 + H_x m\lambda)}{2m\lambda} \sin \phi_2 - \frac{\gamma J t_1}{2m} [U(s) \cos(\phi_1 - \phi_2) + W(s) + \alpha V(s) \sin(\phi_1 - \phi_2)] + \frac{u(\alpha + \beta)}{\lambda} + \frac{\pi}{2}\alpha\gamma [H_{\text{SH}}^{(2)}(1 - \alpha\beta_{\text{SH}}^{(2)}) - H_{\text{R}}^{(2)}(\alpha + \beta)] \cos \phi_2. \quad (17)$$

where we have assumed that the bulk parameters of the two ferromagnets are equal and where s is the separation between the two walls, $s = (X_1 - X_2)/\lambda$. The IEC terms are expressed using the three functions $V(s)$, $U(s)$, and $W(s)$:

$$V(s) = 2s \operatorname{csch} s,$$

$$U(s) = 2 \operatorname{csch} s - 2s \operatorname{coth} s \operatorname{csch} s,$$

$$W(s) = 2 \operatorname{coth} s - 2s \operatorname{csch}^2 s.$$

These functions are plotted in Fig. 4(b).

Equations (14) and (16) reduce to Eqs. (6) and (7) when $J \rightarrow 0$. To solve Eqs. (14)–(17) numerically, we rescale the equations to obtain dimensionless variables. The dimension of Eqs. (14)–(17) is Hz. A convenient scaling factor with the same dimensions is $\mu_0\gamma m$. By dividing Eqs. (14)–(17) by $\mu_0\gamma m$ we get the rescaled variables $\tilde{t} = t\mu_0\gamma m$, $\tilde{X}_i = X_i/\lambda$, $\tilde{H}_x = H_x/\mu_0 m$, $\tilde{K}_y = K_y/\mu_0 m^2$, $\tilde{D}_i = D_i/\mu_0 m^2 \lambda$, $\tilde{t}_i = t_i/\lambda$, $\tilde{J} = J\lambda/\mu_0 m^2$, and $\tilde{u} = u/\mu_0\gamma m\lambda$. We solve the equations using an explicit fourth-order Runge-Kutta scheme with adaptive step-size control, implemented as a Dormand-Prince pair [38].

A. Universal absence of Walker breakdown in SAF structures

For parameter values representative of a standard cobalt-nickel multilayer we obtain the current-velocity and current-tilt relations shown in Figs. 5(a) and 5(b) for $t_1/t_2 = 1$ in the case where only STTs are present and in the case where spin Hall torques are additionally present. We see that the presence of the IEC delays Walker breakdown when the wall is driven by ordinary STTs, but the subcritical differential velocity remains unaffected. This can also be shown analytically by solving for the tilt angle of the wall as a function of current. Such a calculation shows that the tilt angle is suppressed by the IEC (but the breakdown angle is still $\pi/4$). Back substitution of this angle into the torque acting on the wall shows that this torque is independent of J , explaining why there is no change in the differential velocity.

When spin Hall torques are included, the domain wall tilt levels off to a finite value and the current-velocity relation is linear in the $j \rightarrow \infty$ limit. This shows that universal absence of Walker breakdown is also found in SAF structures. The effect of the IEC can be understood simply as a rescaling of the constant S_1 and the higher-order constants S_2, S_3, \dots in the expansion (9), making the tilt angle approach its limiting value more slowly. Thus, the effect of the IEC on both the STT and spin Hall results is to suppress the domain wall tilt, as shown in Fig. 5(b). We note that the combination of spin Hall torques and IEC produces much higher domain wall velocities

than in single ferromagnets for comparatively small current densities [20].

In a single ferromagnet the velocity of a wall driven by spin Hall torques decreases with t as $1/t$. When changing t_2 from $t_2 = t_1/2$ to $t_2 = 2t_1$ in a SAF structure, we find that the velocity peaks close to $t_1/t_2 \approx 1$, which maximizes the IEC torque [see Fig. 5(c); the deviation from 1 is due to the DMI]. This can be understood by considering Fig. 5(d); at $t_1/t_2 \approx 1$ the magnetizations in both layers are tilted in the y direction. Increasing (decreasing) t_2 to $t_2 = 2t_1$ ($t_2 = t_1/2$) reduces (increases) $H_{\text{SH}}^{(2)}$ and increases (reduces) $H_{\text{IEC}}^{(1)}$, thus $(\phi_2 - \phi_1)$ approaches π and the IEC torque is reduced.

Just as for the single ferromagnetic layer the results for the coupled walls are robust against a change of parameters, as shown in Figs. 5(e)–5(h).

B. Novel switching behavior in SAF structures

Bi *et al.* [22] have very recently demonstrated completely novel switching behavior in SAF structures. In single ferromagnets, domain walls with one topological charge will travel faster than those with the opposite topological charge if an in-plane magnetic field is applied [39]. If the relative velocity is large enough the favored domains can overcome the destabilizing action of the current (see Refs. [40–43]) and merge [44–46]. The favored magnetization direction is uniquely determined by the spin Hall angle and the applied magnetic field for a fixed direction of the current. Bi *et al.*

TABLE I. Parameters used for the numerical solution of Eqs. (14)–(17) and for analytical estimates in the text.

Parameter	Co-Ni	Strong SOC	Bi <i>et al.</i>	Unit
gyromagnetic ratio γ	−0.19	−0.19	−0.19	THz/T
domain wall width λ	4	16	2	nm
hard axis anisotropy K_y	200	20	2	kJ/m ³
saturation magn. m	1	1	1.1	MA/m
DM constant D	−1.4	−1.0	−0.1	mJ/m ²
Gilbert damping α	−0.25	−0.1	−0.5	
spin-polarization P	0.5	0.5	0.5	
nonadiabacity param. β	0.5	0.4	2	
Rashba parameter α_{R}	6.3	75		meVnm
spin Hall angle θ_{SH}	0.1	0.2	0.12	
spin Hall β -term β_{SH}	0.02	0.02	0.02	
interlayer exchange $J t_1 t_2$	5	5	1.5	mJ/m ²
thickness t_1	1.2	1.2	0.6	nm
thickness t_2	1.2	1.2	1.7	nm

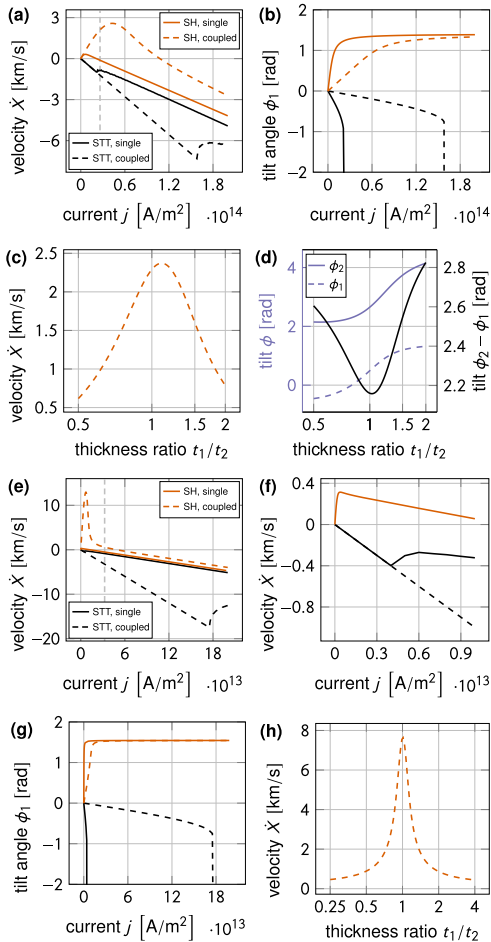


FIG. 5. Domain wall dynamics in interlayer exchange coupled ferromagnets. (a) and (b) The IEC delays Walker breakdown for STT driving, but the subcritical differential velocity remains unaffected. With spin Hall torques the tilt angle stabilizes at a finite value, indicating universal absence of Walker breakdown. The tilt angle approaches its limiting value more slowly in the presence of IEC. (c) and (d) The IEC gives the velocity a nonmonotonic thickness dependence resulting in a peak close to $t_1/t_2 = 1$. [$j = 3 \text{ GAcm}^{-2}$, corresponding to the dashed vertical line in (a).] We use the material parameters supplied in the first column of Table I. (e)–(h) These results are robust against a change in parameters to those in the second column of Table I.

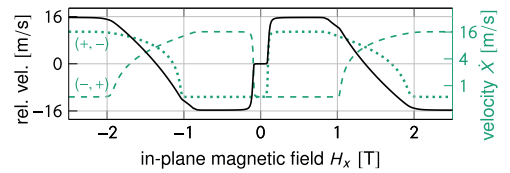


FIG. 6. Qualitative reproduction of the experimental results of Bi *et al.* [22]. The sign of the relative velocity of walls with $(Q_1, Q_2) = (+1, -1)$ and $(Q_1, Q_2) = (-1, +1)$ can be toggled only by changing the magnitude of the applied field. We use the material parameters supplied in the third column of Table I.

observed this behavior in SAF structures for small in-plane fields, but by toggling between large and small values of the in-plane field (same sign), they were able to toggle the sign of the relative velocity of the walls and thereby the favored magnetization direction. Using material parameters that approximate the samples of Bi *et al.*, our model qualitatively reproduces this behavior, as shown in Fig. 6. Under an in-plane field in the range 0.3–1.4 T, walls with $(Q_1, Q_2) = (+1, -1)$ travel faster than walls with $(Q_1, Q_2) = (-1, +1)$ and up magnetization is favored. If the field is increased beyond 1.4 T, the relative velocity changes sign, and down magnetization is favored. (The offset from zero is due to the DMI.)

IV. CONCLUSION

We have shown that complete suppression of Walker breakdown is possible in a wide range of domain wall systems driven by spin-orbit torques, including head-to-head walls in soft magnets, Bloch and Néel walls in perpendicular anisotropy magnets, in the presence of the Dzyaloshinskii-Moriya interaction, and in coupled domain walls in synthetic antiferromagnets. For spin-orbit torques other than pure Rashba spin-orbit torques this leads to a linear current-velocity relation instead of a saturation of the velocity for large currents. In combination with interlayer exchange coupling, spin-orbit torque driven domain wall motion in synthetic antiferromagnets gives rise to novel switching behavior and very high domain wall velocities.

ACKNOWLEDGMENTS

Funding via the “Outstanding Academic Fellows” program at NTNU, the COST Action MP-1201, the NV Faculty, and the Research Council of Norway Grants No. 216700 and No. 240806, is gratefully acknowledged. We thank Morten Amundsen for very useful discussions of the numerics.

- [1] I. M. Miron, P.-J. Zermatten, G. Gaudin, S. Auffret, B. Rodmacq, and A. Schuhl, *Phys. Rev. Lett.* **102**, 137202 (2009).
 [2] I. M. Miron, G. Gaudin, S. Auffret, B. Rodmacq, A. Schuhl, S. Pizzini, J. Vogel, and P. Gambardella, *Nature Mater.* **9**, 230 (2010).

- [3] I. M. Miron, T. Moore, H. Szabolcs, L. D. Buda-Prejbeanu, S. Auffret, B. Rodmacq, S. Pizzini, J. Vogel, M. Bonfim, A. Schuhl, and G. Gaudin, *Nature Mater.* **10**, 419 (2011).
 [4] S. Emori, U. Bauer, S.-M. Ahn, E. Martinez, and G. S. D. Beach, *Nature Mater.* **12**, 611 (2013).

- [5] K.-S. Ryu, L. Thomas, S.-H. Yang, and S. Parkin, *Nature Nanotechnol.* **8**, 527 (2013).
- [6] P. P. J. Haazen, E. Murè, J. H. Franken, R. Lavrijsen, H. J. M. Swagten, and B. Koopmans, *Nature Mater.* **12**, 299 (2013).
- [7] S. Zhang and Z. Li, *Phys. Rev. Lett.* **93**, 127204 (2004).
- [8] D. C. Ralph and M. D. Stiles, *J. Magn. Magn. Mater.* **320**, 1190 (2008).
- [9] A. Brataas, A. D. Kent, and H. Ohno, *Nature Mater.* **11**, 372 (2012).
- [10] N. L. Schryer and L. R. Walker, *J. Appl. Phys.* **45**, 5406 (1974).
- [11] K. Ando, S. Takahashi, K. Harii, K. Sasage, J. Ieda, S. Maekawa, and E. Saitoh, *Phys. Rev. Lett.* **101**, 036601 (2008).
- [12] A. Manchon and S. Zhang, *Phys. Rev. B* **78**, 212405 (2008).
- [13] K.-W. Kim, S.-M. Seo, J. Ryu, K.-J. Lee, and H.-W. Lee, *Phys. Rev. B* **85**, 180404 (2012).
- [14] A. Chernyshov, M. Overby, X. Liu, J. K. Furdyna, Y. Lyanda-Geller, and L. P. Rokhinson, *Nature Phys.* **5**, 656 (2009).
- [15] I. E. Dzyaloshinskii, *Zh. Eksp. Teor. Fiz.* **32**, 1547 (1957) [*J. Exp. Theor. Phys.* **5**, 1259 (1957)].
- [16] T. Moriya, *Phys. Rev. Lett.* **4**, 228 (1960); *Phys. Rev.* **120**, 91 (1960).
- [17] A. Fert, *Mater. Sci. Forum* **59–60**, 439 (1990).
- [18] H. Saarikoski, H. Kohno, C. H. Marrows, and G. Tatara, *Phys. Rev. B* **90**, 094411 (2014).
- [19] S. Lepadatu, H. Saarikoski, R. Beacham, M. J. Benitez, T. A. Moore, G. Burnell, S. Sugimoto, D. Yesudas, M. C. Wheeler, J. Miguel, S. S. Dhesi, D. McGrouther, S. McVitie, G. Tatara, and C. H. Marrows, [arXiv:1604.07992](https://arxiv.org/abs/1604.07992).
- [20] S.-H. Yang, K.-S. Ryu, and S. Parkin, *Nature Nanotechnol.* **10**, 221 (2015).
- [21] R. Tomasello, V. Puliafito, E. Martinez, A. Manchon, M. Ricci, M. Carpentieri, and G. Finocchio, [arXiv:1610.00894](https://arxiv.org/abs/1610.00894).
- [22] C. Bi, H. Almasi, K. Price, T. Newhouse-Illige, M. Xu, S. R. Allen, X. Fan, and W. Wang, *Phys. Rev. B* **95**, 104434 (2017).
- [23] L. D. Landau and E. M. Lifshitz, *Phys. Z. Sowjetunion* **8**, 153 (1935) [*Ukr. J. Phys.* **53**, 14 (2008)]; T. Gilbert, *IEEE Trans. Magn.* **40**, 3443 (2004).
- [24] R. C. O'Handley, *Modern Magnetic Materials. Principles and Applications* (John Wiley & Sons, New York, 2000).
- [25] K. M. D. Hals and A. Brataas, *Phys. Rev. B* **88**, 085423 (2013); **91**, 214401 (2015).
- [26] R. R. Birss, *Symmetry and Magnetism*, 1st ed., edited by E. P. Wohlfarth, Selected Topics in Solid State Physics Vol. 3 (North-Holland, Amsterdam, 1964).
- [27] J. Kim, J. Sinha, M. Hayashi, M. Yamanouchi, S. Fukami, T. Suzuki, S. Mitani, and H. Ohno, *Nature Mater.* **12**, 240 (2012).
- [28] K.-S. Ryu, S.-H. Yang, L. Thomas, and S. S. P. Parkin, *Nature Commun.* **5**, 3910 (2014).
- [29] X. Fan, H. Celik, J. Wu, C. Ni, K.-J. Lee, V. O. Lorenz, and J. Q. Xiao, *Nature Commun.* **5**, 3042 (2014).
- [30] J. Shibata, G. Tatara, and H. Kohno, *J. Phys. D: Appl. Phys.* **44**, 384004 (2011).
- [31] G. Beach, M. Tsoi, and J. Erskine, *J. Magn. Magn. Mater.* **320**, 1272 (2008).
- [32] J. Linder and M. Alidoust, *Phys. Rev. B* **88**, 064420 (2013).
- [33] M. Stier, M. Creutzburg, and M. Thorwart, *Phys. Rev. B* **90**, 014433 (2014).
- [34] O. Boule, L. D. Buda-Prejbeanu, E. Jué, I. M. Miron, and G. Gaudin, *J. Appl. Phys.* **115**, 17D502 (2014).
- [35] P.-B. He, H. Yan, M.-Q. Cai, and Z.-D. Li, *Europhys. Lett.* **114**, 67001 (2016).
- [36] A. V. Khvalkovskiy, V. Cros, D. Apalkov, V. Nikitin, M. Krounbi, K. A. Zvezdin, A. Anane, J. Grollier, and A. Fert, *Phys. Rev. B* **87**, 020402 (2013).
- [37] P. Bruno, *Phys. Rev. B* **52**, 411 (1995).
- [38] J. R. Dormand and P. J. Prince, *J. Comput. Appl. Math.* **6**, 19 (1980).
- [39] S.-G. Je, D.-H. Kim, S.-C. Yoo, B.-C. Min, K.-J. Lee, and S.-B. Choe, *Phys. Rev. B* **88**, 214401 (2013).
- [40] J. Shibata, G. Tatara, and H. Kohno, *Phys. Rev. Lett.* **94**, 076601 (2005).
- [41] Y. Nakatani, J. Shibata, G. Tatara, H. Kohno, A. Thiaville, and J. Miltat, *Phys. Rev. B* **77**, 014439 (2008).
- [42] J. Torrejon, F. Garcia-Sanchez, T. Taniguchi, J. Sinha, S. Mitani, J.-V. Kim, and M. Hayashi, *Phys. Rev. B* **91**, 214434 (2015).
- [43] T. Taniguchi, S. Mitani, and M. Hayashi, *Phys. Rev. B* **92**, 024428 (2015).
- [44] G. Yu, P. Upadhyaya, K. L. Wong, W. Jiang, J. G. Alzate, J. Tang, P. K. Amiri, and K. L. Wang, *Phys. Rev. B* **89**, 104421 (2014).
- [45] K. Garello, C. O. Avci, I. M. Miron, M. Baumgartner, A. Ghosh, S. Auffret, O. Boule, G. Gaudin, and P. Gambardella, *Appl. Phys. Lett.* **105**, 212402 (2014).
- [46] J.-C. Rojas-Sánchez, P. Laczkowski, J. Sampaio, S. Collin, K. Bouzehouane, N. Reyren, H. Jaffrès, A. Mougin, and J.-M. George, *Appl. Phys. Lett.* **108**, 082406 (2016).



Reference

Ø. Johansen, V. Risinggård, A. Sudbø, J. Linder, A. Brataas.
Current control of magnetism in two-dimensional Fe_3GeTe_2 .
Physical Review Letters **122**, 217203 (2019).
10/c6nz

Contributions

AB initiated the project. AB and JL supervised the project. ØJ did the initial literature search. ØJ and VR identified Fe_3GeTe_2 as a suitable material based on symmetry considerations and material parameters. VR derived the spin-orbit torque based on symmetry considerations. ØJ calculated the current-induced magnon populations and identified an effective energy functional for the spin-orbit torque. VR and ØJ conceived that the Curie temperature could be controlled using the current. ØJ calculated the Curie temperature. All authors contributed to the writing of the manuscript and the discussion of the results.

Current Control of Magnetism in Two-Dimensional Fe_3GeTe_2

Øyvind Johansen,^{*} Vette Risinggård,[†] Asle Sudbø, Jacob Linder, and Arne Brataas
 Center for Quantum Spintronics, Department of Physics, Norwegian University of Science and Technology,
 NO-7491 Trondheim, Norway



(Received 13 December 2018; published 31 May 2019)

The recent discovery of magnetism in two-dimensional van der Waals systems opens the door to discovering exciting physics. We investigate how a current can control the ferromagnetic properties of such materials. Using symmetry arguments, we identify a recently realized system in which the current-induced spin torque is particularly simple and powerful. In Fe_3GeTe_2 , a single parameter determines the strength of the spin-orbit torque for a uniform magnetization. The spin-orbit torque acts as an effective out-of-equilibrium free energy. The contribution of the spin-orbit torque to the effective free energy introduces new in-plane magnetic anisotropies to the system. Therefore, we can tune the system from an easy-axis ferromagnet via an easy-plane ferromagnet to another easy-axis ferromagnet with increasing current density. This finding enables unprecedented control and provides the possibility to study the Berezinskii-Kosterlitz-Thouless phase transition in the 2D XY model and its associated critical exponents.

DOI: [10.1103/PhysRevLett.122.217203](https://doi.org/10.1103/PhysRevLett.122.217203)

Introduction.—Magnetism in lower dimensions hosts interesting physics that has been studied theoretically for many decades. Examples include the intriguing physics of the exactly solvable 2D Ising model [1] and the Berezinskii-Kosterlitz-Thouless (BKT) phase transition in the 2D XY model [2–4]. However, experimentally realizing the details of these theoretical predictions has proven difficult. One reason for this difficulty is that fabricating atomically thin films is challenging. The isolation of graphene in 2004 provided a path for exploring two-dimensional van der Waals materials [5]. Creating two-dimensional films that have long-range magnetic order at finite temperatures is more challenging because of the Mermin-Wagner theorem [6]. This theorem states that long-range magnetic order does not exist at finite temperatures below three dimensions when the exchange interaction has a finite range and the material has a continuous symmetry in spin space. Consequently, realizing two-dimensional magnetic materials requires breaking the continuous symmetry of the system, e.g., by a uniaxial magnetocrystalline anisotropy. This provides an energy cost (also known as a magnon gap) to suppress long-range fluctuations that can destroy the magnetic order. The recent discovery of magnetic order in two-dimensional van der Waals materials has therefore led to a large number of studies of magnetism in atomically thin films [7]. Magnetic order has been reported in FePS_3 [8], Cr_2GeTe_6 [9], CrI_3 [10], VSe_2 [11], MSe_x [12], and Fe_3GeTe_2 [13,14]. In addition, multiferroicity has been identified in CuCrP_2S_6 [15]. These new two-dimensional magnets are amenable to electrical control [14,16–18] and produce record-high tunnel magnetoresistances [19].

Currents can induce torques in magnetic materials [20]. In ferromagnets with broken inversion symmetry, the spin-orbit interaction leads to spin-orbit torques (SOTs) [21]. These torques can be present even in the bulk of the materials without requiring additional spin-polarizing elements. The effects of SOTs are typically sufficiently large to induce magnetization switching or motion of magnetic textures [22]. With the rich physics that is known to exist in two-dimensional magnetic systems, we explore how currents can provide additional control over the magnetic state via SOTs.

Although many of the newly discovered two-dimensional magnetic systems exhibit SOTs, we find that in one material the torque is particularly simple and powerful. The form of the torque is simple because it is determined by a single parameter. The torque is also influential in determining the magnetic state of the system. In contrast to many other systems, we can describe the current-induced effects via an effective out-of-equilibrium free energy. Therefore, the SOT enables unprecedented control over the magnetic state via the current. We will demonstrate how the current can drive the system from having easy-axis anisotropy along one direction to anisotropy along a different axis by proceeding via an intermediate state with easy-plane anisotropy.

Interestingly, the current-induced easy-plane configuration provides the possibility to study the BKT phase transition in this system. The BKT transition is an example of a so-called conformal phase transition in which the scale invariance of a topologically ordered state, i.e., conformal invariance, is lost at the (topological) phase transition [23]. When driven by a current, we realize a 2D conformal field

theory in the low-temperature phase, with conformality being lost [23] at the transition to the paramagnetic phase. Additionally, it was recently discovered that an ionic gate considerably increases the critical temperature [14]. Consequently, two-dimensional Fe_3GeTe_2 forms an ideal and very rich laboratory for studying fundamental problems of broad current interest in condensed matter physics and beyond at elevated temperatures.

System.—We consider a monolayer of Fe_3GeTe_2 . Figure 1 shows the crystal structure of this material. Fe_3GeTe_2 crystallizes in the hexagonal system, space group 194, point group $\mathbf{6}/\mathbf{m}2/\mathbf{m}2/\mathbf{m}$, known as D_{6h} in the Schönflies notation [24]. However, the basis reduces the point group symmetry to $\mathbf{6m}2$ (D_{3h}). Placing a Fe_3GeTe_2 monolayer on a substrate may reduce the symmetry even further (point group $\mathbf{3m}$) if the bottom tellurium layer hybridizes with the surface. Here, we assume that a possible monolayer-substrate interaction is weak. In the case of a strong monolayer-substrate interaction, we can preserve the out-of-plane mirror symmetry by suspending the monolayer between two electrodes [25] or encapsulating it in another van der Waals material, such as hexagonal boron nitride.

The SOT can be written as [26]

$$\boldsymbol{\tau} = -|\gamma|\mathbf{m} \times \mathbf{H}_{\text{SOT}}, \quad (1)$$

where γ is the gyromagnetic ratio and \mathbf{m} is the magnetization unit vector. For a spatially uniform magnetization, the effective magnetic field \mathbf{H}_{SOT} due to the SOT in a Fe_3GeTe_2 monolayer is [27]

$$\mathbf{H}_{\text{SOT}} = \Gamma_0[(m_x J_x - m_y J_y)\mathbf{e}_x - (m_y J_x + m_x J_y)\mathbf{e}_y] \quad (2)$$

for current densities and magnetizations in any direction. Here, m_i are magnetization components, and J_i are components of the current density. Γ_0 is a free parameter that is determined by the spin-orbit coupling.

We provide a rigorous derivation of the effective field \mathbf{H}_{SOT} based on Neumann's principle in the Supplemental Material [27]. In Fe_3GeTe_2 , we can understand the

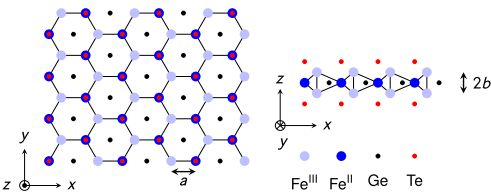


FIG. 1. Crystal structure of a Fe_3GeTe_2 monolayer. (Left) View along \mathbf{e}_z . (Right) View along \mathbf{e}_y . a is the in-plane bond length between Fe^{III} and Fe^{II} . $2b$ is the out-of-plane distance between the two Fe^{III} sublattices. Fe^{III} and Fe^{II} represent the two inequivalent Fe sites in oxidation states +3 and +2, respectively. Redrawn after Ref. [14].

dependence of the SOT on the magnetization and currents in Eq. (2) as follows. The crystal structure in Fig. 1 is invariant under a threefold rotation about the z axis ($\mathbf{3}_z$), an inversion of the y axis (\mathbf{m}_y), and an inversion of the z axis (\mathbf{m}_z). These symmetry operations generate the point group $\mathbf{6m}2$. Since \mathbf{H}_{SOT} only contains terms that are quadratic in y , it is invariant under the operation \mathbf{m}_y . The operation $\mathbf{3}_z$ transforms (m_x, m_y) into

$$\frac{1}{2} \begin{pmatrix} -1 & \sqrt{3} \\ -\sqrt{3} & -1 \end{pmatrix} \begin{pmatrix} m_x \\ m_y \end{pmatrix} = \frac{1}{2} \begin{pmatrix} -m_x + \sqrt{3}m_y \\ -\sqrt{3}m_x - m_y \end{pmatrix}, \quad (3)$$

and similarly for (J_x, J_y) and $(\mathbf{e}_x, \mathbf{e}_y)$. Backsubstitution of the transformation in Eq. (3) into Eq. (2) shows that \mathbf{H}_{SOT} is also invariant under this operation. The effective field \mathbf{H}_{SOT} is invariant under \mathbf{m}_z since neither m_z nor \mathbf{e}_z appear in Eq. (2).

Micromagnetics.—The magnetization dynamics can be described by the semiclassical Landau-Lifshitz-Gilbert equation

$$\dot{\mathbf{m}} = -|\gamma|\mathbf{m} \times \mathbf{H}_{\text{eff}} + \alpha \mathbf{m} \times \dot{\mathbf{m}} + \boldsymbol{\tau}. \quad (4)$$

Here, $\alpha > 0$ is the dimensionless Gilbert damping parameter, $\mathbf{H}_{\text{eff}} = -M_s^{-1} \delta f[\mathbf{m}] / \delta \mathbf{m}$ is an effective magnetic field that describes the magnetization direction \mathbf{m} that minimizes the free energy density functional $f[\mathbf{m}]$, and M_s is the saturation magnetization. Interestingly, we note that a functional exists that generates the effective SOT field in Eq. (2), which is given by

$$f_{\text{SOT}}[\mathbf{m}] = M_s \Gamma_0 \left[J_y m_x m_y - \frac{1}{2} J_x (m_x^2 - m_y^2) \right]. \quad (5)$$

The out-of-equilibrium current-induced SOT can therefore be absorbed into an effective field $\tilde{\mathbf{H}}_{\text{eff}}$ that minimizes the effective free energy density $f_{\text{eff}}[\mathbf{m}] = f[\mathbf{m}] + f_{\text{SOT}}[\mathbf{m}]$.

The 2D ferromagnet Fe_3GeTe_2 is a uniaxial ferromagnet with an out-of-plane easy axis [13,14,29]. The contribution of the dipole-dipole interaction to the spin wave spectrum can be neglected for a monolayer system [30–34]. If we consider a spatially uniform magnetization and use a spherical basis, $(m_x, m_y, m_z) = (\sin\theta\cos\phi, \sin\theta\sin\phi, \cos\theta)$, the effective free energy becomes

$$f_{\text{eff}}[\theta, \phi] = -\frac{M_s}{2} [K_z \cos^2 \theta + \Gamma_0 |J| \sin^2 \theta \cos(2\phi + \phi_J)]. \quad (6)$$

Here, $K_z > 0$ is the out-of-plane anisotropy constant, and $|J|$ and $\phi_J = \arctan(J_y/J_x)$ are the magnitude and azimuthal angle of the applied current, respectively. From this, we find that the SOT effectively acts as in-plane magnetocrystalline anisotropies. The anisotropy originating from the SOT always comes in a pair of perpendicular easy and hard axes.

The directions of the anisotropy axes depend on the direction of the applied current. For weak currents ($|\Gamma_0 J| < K_z$), the magnetization of Fe_3GeTe_2 remains out of plane ($\theta = 0, \pi$). However, for sufficiently strong currents ($|\Gamma_0 J| > K_z$), an in-plane configuration of the magnetization becomes more energetically favorable. Assuming that $\Gamma_0 > 0$, the effective free energy is then minimized by $\theta = \pi/2$ and $\phi = n\pi - \phi_J/2$ ($n = 0, 1, 2, \dots$). When $\Gamma_0 < 0$, the easy and hard axes are interchanged, and the minima are $\phi = (n + 1/2)\pi - \phi_J/2$. The easy and hard axes also interchange upon reversal of the applied current.

Magnon gap.—Because the SOT can effectively be considered a current-controlled magnetocrystalline anisotropy, we can electrically control the magnon gap in Fe_3GeTe_2 . The magnon gap is governed by the energy difference between the out-of-plane and in-plane magnetization configurations, i.e., $|K_z - |\Gamma_0 J||$. At the critical current $|J_c| = K_z/|\Gamma_0|$, the magnon gap vanishes as the magnetic easy axis transitions from an out-of-plane axis to an in-plane axis. Exactly at this transition point, we obtain a magnetic easy plane. Below the critical current, the magnon gap decreases monotonically with the applied current, whereas it increases monotonically above the critical current. The ability to electrically tune the magnon gap in a 2D magnetic material opens the door for exploring a wide variety of effects in magnetism in two dimensions.

Curie temperature.—The first effect that is characteristic of a two-dimensional system that we will now illustrate is the dependence of the Curie temperature on the magnon gap. Because the Curie temperature in 2D is primarily governed by the magnon gap, unlike in 3D [35], we will study its behavior as we tune the SOT-controlled magnon gap through the transition from an out-of-plane easy axis to an in-plane easy axis. To illustrate the basic aspects of current control of the Curie temperature, we make a few simplifications to reduce the number of free parameters and the complexity of the calculations. Fe_3GeTe_2 is an itinerant ferromagnet, and its magnetic interactions are therefore described by the Stoner model [29]. The Stoner model can in our system be transformed into a Ruderman-Kittel-Kasuya-Yosida (RKKY) exchange interaction between the iron atoms [36]. We assume that the exchange interaction in a Fe_3GeTe_2 monolayer has a finite range and therefore obeys the Mermin-Wagner theorem. To simplify the calculations, we replace the Stoner or RKKY exchange interaction by a simple nearest-neighbor interaction between the Fe^{II} and Fe^{III} atoms (i.e., there is no exchange interaction within each sublattice or between the two different Fe^{III} sublattices). This will also obey the Mermin-Wagner theorem, and this system will consequently also exhibit the same qualitative dependence on the magnon gap as other finite-range interactions. We also assume that the magnetic anisotropy constants are identical at all sites. Consequently, we consider the model Hamiltonian

$$\mathcal{H} = -\frac{\epsilon_J}{2\hbar^2} \sum_{\mathbf{r}} \sum_{\delta} \mathbf{S}_{\mathbf{r}} \cdot \mathbf{S}_{\mathbf{r}+\delta} - \frac{\epsilon_z}{2\hbar^2} \sum_{\mathbf{r}} (S_{r,z})^2 - \frac{\epsilon_x}{2\hbar^2} \sum_{\mathbf{r}} [(S_{r,x})^2 - (S_{r,y})^2]. \quad (7)$$

Here, $\epsilon_J > 0$ is an energy constant that describes the nearest-neighbor exchange interactions of spins separated by δ , $\epsilon_z > 0$ is an energy constant that describes the out-of-plane anisotropy, and $\epsilon_x \propto \Gamma_0 J_x > 0$ is an energy constant that describes the effective in-plane anisotropies caused by the SOT. $S_{r,i}$ ($i = x, y, z$) describes the i th component of the spin operator located at position \mathbf{r} . We split the Fe_3GeTe_2 monolayer into three distinct sublattices: one for the Fe^{II} atoms, one for the Fe^{III} atoms at $z = +b$, and one for the Fe^{III} atoms at $z = -b$.

We proceed by performing a Holstein-Primakoff transformation of the spin operators around the equilibrium spin direction. This is in the z direction below the critical current J_c and along the x direction above the critical current. Because of the anomalous Hall effect in Fe_3GeTe_2 [14,37,38], applying the current exactly along the x direction can be experimentally challenging. However, as can be deduced from Eq. (6), a scenario in which the current is applied in a different direction can be achieved by a rotation of the unit cell or Brillouin zone. Since it is the magnons closest to the Γ point that dominate the calculation of the Curie temperature, we expect the results to be very similar for an off-axis current.

In our calculations, we keep terms to the second order in the Holstein-Primakoff magnon operators. We expect this to be a good qualitative approximation, although it will not be a very good quantitative approximation because the magnon population diverges at the critical point. However, keeping terms to, for instance, the fourth order in the magnon operators to include magnon-magnon interactions [9] would be complicated because Eq. (7) does not conserve the magnon number for finite currents.

Following the Holstein-Primakoff transformation, we perform a Fourier transformation of the magnon operators to momentum space. We then diagonalize the Hamiltonian by a Bogoliubov transformation such that it takes the form [27]

$$\mathcal{H} = \sum_{\mathbf{k}, \mu} \epsilon_{\mathbf{k}, \mu} \alpha_{\mathbf{k}, \mu}^{\dagger} \alpha_{\mathbf{k}, \mu}. \quad (8)$$

Here, the operator $\alpha_{\mathbf{k}, \mu}^{(\dagger)}$ annihilates (creates) an eigenmagnon with a momentum \mathbf{k} and energy $\epsilon_{\mathbf{k}, \mu}$. There are three different modes ($\mu = \text{I, II, III}$) of the eigenmagnons. We have imposed the constraint on the Bogoliubov transformation that the new operators have to satisfy bosonic commutation relations: $[\alpha_{\mathbf{k}, \mu}, \alpha_{\mathbf{k}', \mu'}^{\dagger}] = \delta_{\mathbf{k}\mathbf{k}'} \delta_{\mu\mu'}$.

From the energy spectrum of the eigenmagnons in Fe_3GeTe_2 , we can estimate the Curie temperature T_c . To determine T_c , we use the fact that the magnetization along

the equilibrium direction of the spins vanishes at this temperature. Because we consider a monolayer system, we only have magnons with in-plane momenta. Balancing the magnetic moments, we find the constraint

$$\sum_{\nu} s_{\nu} - \sum_{\mu} \frac{1}{A_{\text{BZ}}} \int_{A_{\text{BZ}}} d^2k \frac{S_{k,\mu}/\hbar}{\exp(\epsilon_{k,\mu}/k_B T_c) - 1} = 0. \quad (9)$$

Here, s_{ν} is the dimensionless spin number of the magnetic moments in sublattice ν (where $\nu = 2$ for the Fe^{II} atoms, and $\nu = 3_{\pm}$ for the Fe^{III} atoms located at $z = \pm b$), and $A_{\text{BZ}} = \sqrt{3}\pi^2/(2a^2)$ is the (reciprocal) area of the first Brillouin zone. $S_{k,\mu}$ is the spin of the eigenmagnons, which is *not* an integer for finite SOT because of magnon squeezing [39]. The spin of the eigenmagnons depends on the parameters of the Bogoliubov transformation and is given in the Supplemental Material [27].

We can now calculate the Curie temperature numerically based on Eq. (9). In our calculations, we set the out-of-plane anisotropy constant to be $\epsilon_z = 0.335$ meV [29]. The value of the nearest-neighbor exchange coupling is set to be $\epsilon_J = 0.705$ meV to reproduce the experimental T_c of a monolayer of ~ 130 K [13] (note, however, that a different experiment determined the T_c of a monolayer to be ~ 68 K [14]). The real value of ϵ_J is in all likelihood larger [14] because the linear response method typically overestimates T_c . The dimensionless spin numbers s_{ν} for the spins in sublattice ν are $s_2 = 2$ and $s_{3_{-}}, s_{3_{+}} = 5/2$ [40]. We plot the Curie temperature as a function of the applied current in Fig. 2.

Because we only kept terms to the second order in the magnon operators, we do not expect that our calculation of T_c will be quantitatively correct. However, the qualitative features of our result appear to be physically reasonable. When we apply a SOT below the critical current $|J_c|$, we

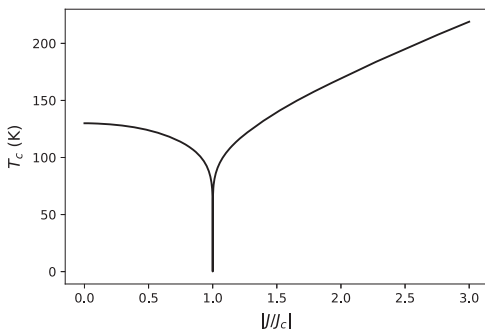


FIG. 2. Numerical calculation of T_c for a spontaneous magnetization based on a simple linear response model of the magnon spectrum. The result is identical for any direction of the applied current \mathbf{J} . Below $|J_c|$, the magnetization is along the z axis, whereas above $|J_c|$, the magnetization is along an in-plane axis determined by the direction of the applied current.

effectively reduce the magnon gap by creating a pair of easy and hard axes perpendicular to the out-of-plane magnetization. Because the Curie temperature in 2D materials is governed by the magnon gap, this also reduces T_c . At the critical current strength, we obtain a continuous symmetry in the form of an easy plane when the in-plane easy axis induced by the SOT becomes equal to the out-of-plane magnetocrystalline anisotropy. Because of the Mermin-Wagner theorem, there can be no long-range magnetic order at finite temperatures in this scenario, and T_c drops to zero. Above the critical current, we now increase the magnon gap for an in-plane magnetization configuration, and T_c increases accordingly. T_c will then saturate at the Curie temperature of the Ising model for large currents, which our model does not capture [41].

In addition to the current affecting the Curie temperature through a SOT, the current will also increase the temperature in the material due to joule heating, which needs to be taken into account when measuring the Curie temperature of the material. The joule heating increases quadratically with the applied current. Conversely, the SOT is linear in the applied current, but its effect on the Curie temperature depends on whether we are above or below the critical current. Consequently, if the critical current is sufficiently small, then the effect of the SOT will dominate that of the joule heating. In this case, the magnetic ordering exhibits reentrant behavior as a function of the applied current. Notably, above the critical current, when the magnetization is in the plane, the easy and hard axes are interchanged upon reversal of the current direction. A reversal of the applied current would therefore lead to a 90° rotation of the magnetization.

2D XY model.—Although the spontaneous magnetization vanishes for finite temperatures at the critical current density $|J_c|$, this regime remains an interesting region for studying the magnetic properties. At the critical current density ($|\epsilon_x| = \epsilon_z$), the model in Eq. (7) becomes, quite remarkably, a 2D easy-plane ferromagnet, where the easy plane is perpendicular to the plane of the monolayer. Therefore, at this current density, the model features a critical phenomenon in the universality class of the 2D XY model. Consequently, the system has a topological phase transition rather than the more conventional phase transition of the 2D Ising model [1]. The 2D Ising universality class falls within the framework of the Landau-Ginzburg-Wilson paradigm of phase transitions of an order-disorder transition monitored by a local order parameter [42,43]. The spin-spin correlation length diverges from above and below T_c as $\xi \sim |T - T_c|^{-\nu}$, where ν is a universal critical exponent. There is true long-range order in the low-temperature phase, short-range order in the high-temperature phase, and power-law spin-spin correlations precisely at the critical point. In contrast, the 2D XY model features a genuine phase transition with no local order parameter. At this phase transition, the spin-spin correlation

length diverges as $\xi \sim \exp(\text{const}/\sqrt{T - T_{\text{BKT}}})$ from the high-temperature side only [4], where T_{BKT} is the critical temperature of the BKT transition. The high-temperature phase has short-range order, and the entire low-temperature phase is critical with a spin-spin correlation function featuring a nonuniversal temperature-dependent anomalous dimension η , $\langle \mathbf{S}_r \cdot \mathbf{S}_{r'} \rangle \sim 1/|\mathbf{r} - \mathbf{r}'|^\eta$ [4].

In 2D Fe_3GeTe_2 , we may realize this type of highly nontrivial behavior by tuning the electric current to the critical value and then drive the system through the phase transition by varying the temperature. Moreover, below the BKT transition, the temperature dependence of the non-universal anomalous dimension η of the 2D XY model can be mapped by varying the temperature and measuring the spin-spin correlation function by polarized small-angle neutron scattering, which is particularly well suited for ultrathin films [44]. The present system is also amenable to studying the universal anomalous dimension of the 2D Ising model at $T = T_c$, $\eta = 1/4$ [45]. The prediction for the 2D XY model, $\eta = k_B T / 4\pi J$ [4], where J is the effective exchange coupling and k_B is Boltzmann's constant, has not been tested in real 2D magnetic systems to our knowledge.

Examples of real physical systems with this level of control over such phenomena are very rare, particularly for systems where the phenomena are accessible at relatively elevated temperatures. The most well-known example is superfluidity in thin films of ^4He , where the BKT transition occurs below 1.2 K [46]. In that context, the remarkable prediction and experimental verification of a universal jump in the superfluid density of the system [46,47] is also worth noting. We expect the corresponding physics of a universal jump in the spin stiffness of the system to occur at liquid nitrogen or oxygen temperatures in the system studied here. The spin stiffness may be measured in spin wave resonance experiments [48]. Furthermore, and in contrast to our present case, η is not experimentally accessible in superfluid thin films of ^4He .

The parameter Γ_0 determines the magnitude of the critical current and thus the accessibility of the effects that we discuss. This value cannot be obtained purely from symmetry considerations but rather needs to be determined experimentally or by *ab initio* calculations. In light of the exciting physics that can be realized and the flexibility of the system, determining its value would be very interesting. Based on the strong magnetic anisotropy of the material, we believe that the spin-orbit coupling is sufficiently strong. Paired with the observation that SOTs are typically sufficiently large to induce magnetization switching in other materials [22], we have reason to believe that reentrant magnetism and topological phase transitions can be experimentally observed in Fe_3GeTe_2 .

The authors thank Alireza Qaiumzadeh for helpful discussions. We gratefully acknowledge funding via the "Outstanding Academic Fellows" program at NTNU, the Research Council of Norway Grants No. 240806,

No. 239926, and No. 250985, and the Research Council of Norway through its Centres of Excellence funding scheme, Project No. 262633, "QuSpin."

Ø. J. and V. R. contributed equally to this work.

* oyvinjoh@ntnu.no

† vetle.k.risinggard@ntnu.no

- [1] L. Onsager, Crystal statistics. I. A two-dimensional model with an order-disorder transition, *Phys. Rev.* **65**, 117 (1944).
- [2] V. L. Berezinskii, Destruction of long-range order in one-dimensional and two-dimensional systems having a continuous symmetry group I. Classical systems, *Sov. Phys. JETP* **32**, 493 (1971).
- [3] V. L. Berezinskii, Destruction of long-range order in one-dimensional and two-dimensional systems possessing a continuous symmetry group. II. Quantum systems, *Sov. Phys. JETP* **34**, 610 (1972).
- [4] J. M. Kosterlitz and D. J. Thouless, Ordering, metastability and phase transitions in two-dimensional systems, *J. Phys. C* **6**, 1181 (1973).
- [5] K. S. Novoselov, A. K. Geim, S. V. Morozov, D. Jiang, Y. Zhang, S. V. Dubonos, I. V. Grigorieva, and A. A. Firsov, Electric field effect in atomically thin carbon films, *Science* **306**, 666 (2004).
- [6] N. D. Mermin and H. Wagner, Absence of Ferromagnetism or Antiferromagnetism in One- or Two-Dimensional Isotropic Heisenberg Models, *Phys. Rev. Lett.* **17**, 1133 (1966).
- [7] K. S. Burch, D. Mandrus, and J.-G. Park, Magnetism in two-dimensional van der Waals materials, *Nature (London)* **563**, 47 (2018).
- [8] J. U. Lee, S. Lee, J. H. Ryoo, S. Kang, T. Y. Kim, P. Kim, C.-H. Park, J.-G. Park, and H. Cheong, Ising-type magnetic ordering in atomically thin FePS_3 , *Nano Lett.* **16**, 7433 (2016).
- [9] C. Gong *et al.*, Discovery of intrinsic ferromagnetism in two-dimensional van der Waals crystals, *Nature (London)* **546**, 265 (2017).
- [10] B. Huang *et al.*, Layer-dependent ferromagnetism in a van der Waals crystal down to the monolayer limit, *Nature (London)* **546**, 270 (2017).
- [11] M. Bonilla, S. Kolekar, Y. Ma, H. C. Diaz, V. Kalappattil, R. Das, T. Eggers, H. R. Gutierrez, M.-H. Phan, and M. Batzill, Strong room-temperature ferromagnetism in VSe_2 monolayers on van der Waals substrates, *Nat. Nanotechnol.* **13**, 289 (2018).
- [12] D. J. O'Hara *et al.*, Room temperature intrinsic ferromagnetism in epitaxial manganese selenide films in the monolayer limit, *Nano Lett.* **18**, 3125 (2018).
- [13] Z. Fei *et al.*, Two-dimensional itinerant ferromagnetism in atomically thin Fe_3GeTe_2 , *Nat. Mater.* **17**, 778 (2018).
- [14] Y. Deng *et al.*, Gate-tunable room-temperature ferromagnetism in two-dimensional Fe_3GeTe_2 , *Nature (London)* **563**, 94 (2018).
- [15] Y. Lai, Z. Song, Y. Wan, M. Xue, Y. Ye, L. Dai, W. Yang, H. Du, and J. Yang, Discovery of two-dimensional multi-ferroicity in van der Waals CuCrP_2S_6 layers, *arXiv*: 1805.04280.

- [16] B. Huang *et al.*, Electrical control of 2D magnetism in bilayer CrI_3 , *Nat. Nanotechnol.* **13**, 544 (2018).
- [17] S. Jiang, L. Li, Z. Wang, K. F. Mak, and J. Shan, Controlling magnetism in 2D CrI_3 by electrostatic doping, *Nat. Nanotechnol.* **13**, 549 (2018).
- [18] Z. Wang *et al.*, Electric-field control of magnetism in a few-layered van der Waals ferromagnetic semiconductor, *Nat. Nanotechnol.* **13**, 554 (2018).
- [19] H. H. Kim, B. Yang, T. Patel, F. Sfigakis, C. Li, S. Tian, H. Lei, and A. W. Tsen, One million percent tunnel magneto-resistance in a magnetic van der Waals heterostructure, *Nano Lett.* **18**, 4885 (2018).
- [20] A. Brataas, A. D. Kent, and H. Ohno, Current-induced torques in magnetic materials, *Nat. Mater.* **11**, 372 (2012).
- [21] A. Manchon and S. Zhang, Theory of nonequilibrium intrinsic spin torque in a single nanomagnet, *Phys. Rev. B* **78**, 212405 (2008).
- [22] A. Manchon, I. M. Miron, T. Jungwirth, J. Sinova, J. Zelenzý, A. Thiaville, K. Garello, and P. Gambardella, Current-induced spin-orbit torques in ferromagnetic and antiferromagnetic systems, arXiv:1801.09636.
- [23] D. B. Kaplan, J.-W. Lee, D. T. Son, and M. A. Stephanov, Conformality lost, *Phys. Rev. D* **80**, 125005 (2009).
- [24] H.-J. Deiseroth, K. Aleksandrov, C. Reiner, L. Kienle, and R. K. Kremer, Fe_3GeTe_2 and Ni_3GeTe_2 — two new layered transition-metal compounds: Crystal structures, HRTEM investigations, and magnetic and electrical properties, *Eur. J. Inorg. Chem.* **2006**, 1561 (2006).
- [25] J. C. Meyer, A. K. Geim, M. I. Katsnelson, K. S. Novoselov, T. J. Booth, and S. Roth, The structure of suspended graphene sheets, *Nature (London)* **446**, 60 (2007).
- [26] K. M. D. Hals and A. Brataas, Phenomenology of current-induced spin-orbit torques, *Phys. Rev. B* **88**, 085423 (2013); Spin-motive forces and current-induced torques in ferromagnets, *Phys. Rev. B* **91**, 214401 (2015).
- [27] See Supplemental Material at <http://link.aps.org/supplemental/10.1103/PhysRevLett.122.217203> for a derivation of the spin-orbit torques and the details of the critical-temperature calculation, which includes Ref. [28].
- [28] R. R. Birss, in *Symmetry and Magnetism*, edited by E. P. Wohlfarth, Selected Topics in Solid State Physics, Vol. 3, 1st ed. (North-Holland Publishing Company, Amsterdam, 1964).
- [29] H. L. Zhuang, P. R. C. Kent, and R. G. Hennig, Strong anisotropy and magnetostriction in the two-dimensional Stoner ferromagnet Fe_3GeTe_2 , *Phys. Rev. B* **93**, 134407 (2016).
- [30] D. N. Chartoryzhskii, B. A. Kalinikos, and O. G. Vendik, Parallel pump spin wave instability in thin ferromagnetic films, *Solid State Commun.* **20**, 985 (1976).
- [31] B. A. Kalinikos, Excitation of propagating spin waves in ferromagnetic films, *IEE Proc. H* **127**, 4 (1980).
- [32] B. A. Kalinikos, Spectrum and linear excitation of spin waves in ferromagnetic films, *Sov. Phys. J.* **24**, 718 (1981).
- [33] B. A. Kalinikos and A. N. Slavin, Theory of dipole-exchange spin wave spectrum for ferromagnetic films with mixed exchange boundary conditions, *J. Phys. C* **19**, 7013 (1986).
- [34] B. A. Kalinikos, M. P. Kostylev, N. V. Kozhus, and A. N. Slavin, The dipole-exchange spin wave spectrum for anisotropic ferromagnetic films with mixed exchange boundary conditions, *J. Phys. Condens. Matter* **2**, 9861 (1990).
- [35] A. Auerbach, *Interacting Electrons and Quantum Magnetism*, Graduate Texts in Contemporary Physics (Springer-Verlag, Berlin, 1994).
- [36] R. E. Prange and V. Korenman, Local-band theory of itinerant ferromagnetism. IV. Equivalent Heisenberg model, *Phys. Rev. B* **19**, 4691 (1979).
- [37] C. Tan, J. Lee, S.-G. Jung, T. Park, S. Albarakati, J. Partridge, M. R. Field, D. G. McCulloch, L. Wang, and C. Lee, Hard magnetic properties in nanoflake van der Waals Fe_3GeTe_2 , *Nat. Commun.* **9**, 1554 (2018).
- [38] N. Nagaosa, J. Sinova, S. Onoda, A. H. MacDonald, and N. P. Ong, Anomalous Hall effect, *Rev. Mod. Phys.* **82**, 1539 (2010).
- [39] A. Kamra, U. Agrawal, and W. Belzig, Noninteger-spin magnonic excitations in untextured magnets, *Phys. Rev. B* **96**, 020411(R) (2017).
- [40] J. H. Rodriguez, H. N. Ok, Y.-M. Xia, P. G. Debrunner, B. E. Hinrichs, T. Meyer, and N. H. Packard, Mössbauer spectroscopy of the spin-coupled Fe^{3+} - Fe^{2+} center of reduced uteroferrin, *J. Phys. Chem.* **100**, 6849 (1996).
- [41] D. Torelli and T. Olsen, Calculating critical temperatures for ferromagnetic order in two-dimensional materials, *2D Mater.* **6**, 015028 (2019).
- [42] L. D. Landau, E. M. Lifshitz, and E. M. Pitaevskii, *Statistical Physics*, 1st ed. (Butterworth and Heinemann, London, 1999).
- [43] K. G. Wilson and J. B. Kogut, The renormalization group and the ϵ expansion, *Phys. Rep.* **12**, 75 (1974).
- [44] T. Maurer, S. Gautrot, F. Ott, G. Chaboussant, F. Zighem, L. Cagnon, and O. Fruchart, Ordered arrays of magnetic nanowires investigated by polarized small-angle neutron scattering, *Phys. Rev. B* **89**, 184423 (2014).
- [45] C. Itzykson and J.-M. Drouffe, *Statistical Field Theory*, Cambridge Monographs on Mathematical Physics (Cambridge University Press, Cambridge, England, 1989), Vol. 1.
- [46] D. J. Bishop and J. D. Reppy, Study of the Superfluid Transition in Two-Dimensional ^4He Films, *Phys. Rev. Lett.* **40**, 1727 (1978).
- [47] D. R. Nelson and J. M. Kosterlitz, Universal Jump in the Superfluid Density of Two-Dimensional Superfluids, *Phys. Rev. Lett.* **39**, 1201 (1977).
- [48] M. Golosovsky, P. Monod, P. K. Muduli, and R. C. Budhani, Spin-wave resonances in $\text{La}_{0.7}\text{Sr}_{0.3}\text{MnO}_3$ films: Measurement of spin-wave stiffness and anisotropy field, *Phys. Rev. B* **76**, 184413 (2007).

Supplementary Material to “Current Control of Magnetism in Two-Dimensional Fe₃GeTe₂”

Øyvind Johansen,^{*} Vetle Risinggård,[†] Asle Sudbø, Jacob Linder, and Arne Brataas

*Center for Quantum Spintronics, Department of Physics, NTNU,
Norwegian University of Science and Technology, N-7491 Trondheim, Norway*

(Dated: December 19, 2018)

I. DERIVATION OF SPIN-ORBIT TORQUES IN Fe₃GeTe₂

Ref. [1] has shown that in the linear response regime under the local approximation, the current-induced torques can be written as

$$\boldsymbol{\tau}(\mathbf{r}, t) = -|\gamma|\mathbf{m}(\mathbf{r}, t) \times \mathbf{H}_{\text{SOT}}, \quad H_{\text{SOT},i} = \eta_{ij} J_j, \quad (1)$$

where \mathbf{m} is the magnetization unit vector, \mathbf{J} is the current density applied to the system, and η is a second-rank tensor. (Summation over repeated indices is implied.) Which elements of η_{ij} that are nonzero is determined by the symmetry of the system. The tensor η can be expanded in the magnetization components m_i and their derivatives $\partial_i m_j$. If we only consider a uniform magnetization, one obtains to lowest order

$$\eta_{ij} = \Lambda_{ij} + \Gamma_{ijk} m_k + \dots \quad (2)$$

where Λ_{ij} is an axial second-rank tensor, and Γ_{ijk} is a polar third-rank tensor.

To determine which contributions to the tensors Λ_{ij} and Γ_{ijk} that are allowed by symmetry, Ref. [1] imposes the criterion that these tensors must be invariant under all transformations R in the point group G of the structure. This amounts to demanding that the relations

$$\Lambda_{ij} = |R| R_{i'i''} R_{j'j''} \Lambda_{i''j''}, \quad (3)$$

$$\Gamma_{ijk} = R_{i'i''} R_{j'j''} R_{k'k''} \Gamma_{i''j''k''}, \quad (4)$$

are fulfilled for all $R \in G$.

Monolayer Fe₃GeTe₂ crystallizes in point group $\bar{6}m2$ (D_{3h}) [2]. Since this group is generated by the elements $\bar{6}_z$, \mathbf{m}_y , and $\mathbf{2}_x$, it is sufficient to impose that η_{ij} should be invariant under these operations [3]. The representing matrices of these symmetry operations are

$$\mathbf{m}_y = \begin{pmatrix} 1 & & \\ & -1 & \\ & & 1 \end{pmatrix}, \quad \mathbf{2}_x = \begin{pmatrix} 1 & & \\ & -1 & \\ & & -1 \end{pmatrix}, \quad \bar{6}_z = \frac{1}{2} \begin{pmatrix} -1 & -\sqrt{3} & \\ \sqrt{3} & -1 & \\ & & -2 \end{pmatrix}.$$

Eq. (3) with $R = \mathbf{2}_x$ implies that Λ_{ij} vanishes when x appears an odd number of times in the indices ij . (That is, $\Lambda_{xj} = \Lambda_{ix} = 0$ for $i, j = y, z$.) Similarly, $R = \mathbf{m}_y$ implies that Λ_{ij} vanishes when y appears an even number of times in the indices ij . (That is, $\Lambda_{ij} = 0$ for $i, j = x, z$ and $\Lambda_{yy} = 0$.) Consequently, only

Λ_{yz} and Λ_{zy} are invariant under the symmetry operations $\mathbf{2}_x$ and \mathbf{m}_y . The operation $\bar{6}_z$ gives

$$\Lambda_{yz} = -\frac{1}{2}\Lambda_{zy} \quad \text{and} \quad \Lambda_{zy} = -\frac{1}{2}\Lambda_{yz}$$

for these elements. These relations can only hold for $\Lambda_{ij} = 0$. Thus we conclude that $\Lambda_{ij} = 0 \forall i, j$.

Repeating the analysis for Γ_{ijk} with Eq. (4), $R = \mathbf{2}_x$ implies that Γ_{ijk} vanishes when x appears an even number of times in the indices ijk , and $R = \mathbf{m}_y$ implies that Γ_{ijk} vanishes when y appears an odd number of times in the indices ijk . Consequently, only Γ_{yyx} , Γ_{xzz} , Γ_{xxx} , and the four other elements generated by freely permuting the indices yyx and xzz are invariant under the symmetry operations $\mathbf{2}_x$ and \mathbf{m}_y . The operation $\bar{6}_z$ gives

$$\Gamma_{xzz} = -\frac{1}{2}\Gamma_{xzz}, \quad \Gamma_{zxx} = -\frac{1}{2}\Gamma_{zxx}, \quad \text{and} \quad \Gamma_{zzx} = -\frac{1}{2}\Gamma_{zzx},$$

which implies that $\Gamma_{xzz} = \Gamma_{zxx} = \Gamma_{zzx} = 0$. Furthermore,

$$\Gamma_{yyx} = \frac{1}{8}(-\Gamma_{yyx} + 3\Gamma_{yxy} + 3\Gamma_{xyy} - 3\Gamma_{xxx}),$$

$$\Gamma_{yxy} = \frac{1}{8}(+3\Gamma_{yyx} - \Gamma_{yxy} + 3\Gamma_{xyy} - 3\Gamma_{xxx}),$$

$$\Gamma_{xyy} = \frac{1}{8}(+3\Gamma_{yyx} + 3\Gamma_{yxy} - \Gamma_{xyy} - 3\Gamma_{xxx}),$$

and

$$\Gamma_{xxx} = -\frac{1}{8}[\Gamma_{xxx} + 3(\Gamma_{yyx} + \Gamma_{yxy} + \Gamma_{xyy})].$$

Together these relations imply $\Gamma_{yyx} = \Gamma_{yxy} = \Gamma_{xyy} = -\Gamma_{xxx}$. We conclude that Γ_{ijk} has four nonzero components, but only one free parameter, $\Gamma_{xxx} = \Gamma_0$. The effective field corresponding to the spin-orbit torque in Fe₃GeTe₂ is thus

$$\mathbf{H}_{\text{SOT}} = \Gamma_0[(m_x J_x - m_y J_y)\mathbf{e}_x - (m_y J_x + m_x J_y)\mathbf{e}_y]. \quad (5)$$

II. MAGNON SPIN AND ENERGY SPECTRUM

Using the result that the spin-orbit torque leads to a set of perpendicular in-plane easy and hard axes, as derived in the manuscript, we can write a model Hamiltonian in zero-external field,

$$\mathcal{H} = -\frac{\epsilon_J}{2\hbar^2} \sum_{\mathbf{r}} \sum_{\delta} \mathbf{S}_{\mathbf{r}} \cdot \mathbf{S}_{\mathbf{r}+\delta} - \frac{\epsilon_z}{2\hbar^2} \sum_{\mathbf{r}} (S_{\mathbf{r},z})^2 - \frac{\epsilon_x}{2\hbar^2} \sum_{\mathbf{r}} [(S_{\mathbf{r},x})^2 - (S_{\mathbf{r},y})^2]. \quad (6)$$

Here we only consider nearest-neighbour exchange interaction between sites separated by δ , and only consider a current in the x -direction ($\epsilon_x \propto \Gamma_0 J_x > 0$), as the anisotropy behaves similarly (just with different axes) if we have a y -component of the current.

^{*} oyvinjoh@ntnu.no

[†] vetle.k.risinggard@ntnu.no

A. Below the critical current

Below the critical current, the equilibrium configuration is along the z axis. We do a Holstein–Primakoff transformation of the spin operators, defined by

$$S_{i,\nu,+} = \hbar\sqrt{2s_\nu}a_{i,\nu}^\dagger \sqrt{1 - \frac{a_{i,\nu}^\dagger a_{i,\nu}}{2s_\nu}} \approx \hbar\sqrt{2s_\nu}a_{i,\nu}^\dagger, \quad (7)$$

$$S_{i,\nu,-} = \hbar\sqrt{2s_\nu} \sqrt{1 - \frac{a_{i,\nu}^\dagger a_{i,\nu}}{2s_\nu}} a_{i,\nu} \approx \hbar\sqrt{2s_\nu}a_{i,\nu}, \quad (8)$$

$$S_{i,\nu,z} = \hbar \left(a_{i,\nu}^\dagger a_{i,\nu} - s_\nu \right), \quad (9)$$

where $S_\pm = S_x \pm iS_y$, i is the label of the unit cell, and $\nu = 2, 3_\pm$ indicates the sublattice of the Fe^{II} and Fe^{III} atoms, respectively, where sublattice $\nu = 3_+$ ($\nu = 3_-$) consists of the Fe^{III} atoms located at $z = +b$ ($z = -b$). We assume the nearest-neighbor exchange interaction is only between sublattice $\nu = 2$ and $\nu = 3_\pm$, and that there is no exchange interaction between the Fe^{III} atoms. Rewriting the Hamiltonian to the S_\pm basis, we get

$$\begin{aligned} \mathcal{H} = & -\frac{\varepsilon_J}{2\hbar^2} \sum_{r,\delta} \left[\frac{1}{2} (S_{r,+}S_{r+\delta,-} + S_{r,-}S_{r+\delta,+}) + S_{r,z}S_{r+\delta,z} \right] \\ & - \frac{\varepsilon_x}{2\hbar^2} \sum_r (S_{r,z})^2 - \frac{\varepsilon_x}{4\hbar^2} \sum_r \sum_{m=\pm} (S_{r,m})^2. \end{aligned} \quad (10)$$

Inserting the Holstein–Primakoff transformation, keeping terms to second order in the magnon operators, we get

$$\begin{aligned} \mathcal{H} = & -\varepsilon_J \sum_i \sum_{r_j=r_i+\delta} \sum_{\nu=3_\pm} \left[\sqrt{2s_\nu} (a_{i,2}^\dagger a_{j,\nu} + a_{j,\nu}^\dagger a_{i,2}) \right. \\ & \left. - s_\nu a_{i,2}^\dagger a_{i,2} - s_2 a_{j,\nu}^\dagger a_{j,\nu} \right] + \varepsilon_z \sum_{i,\nu} s_\nu a_{i,\nu}^\dagger a_{i,\nu} \\ & - \frac{\varepsilon_x}{2} \sum_{i,\nu} s_\nu (a_{i,\nu}^\dagger a_{i,\nu} + a_{i,\nu} a_{i,\nu}), \end{aligned} \quad (11)$$

disregarding any constant terms, where r_j is the position of the nearest-neighbor atom of the atom located in unit cell i and sublattice $\nu = 2$. Next we perform a Fourier transform to momentum space, defined by

$$a_{i,\nu} = \frac{1}{\sqrt{N}} \sum_{\mathbf{k}} a_{\mathbf{k},\nu} e^{-i\mathbf{k}\cdot\mathbf{r}_{i,\nu}}, \quad a_{i,\nu}^\dagger = \frac{1}{\sqrt{N}} \sum_{\mathbf{k}} a_{\mathbf{k},\nu}^\dagger e^{i\mathbf{k}\cdot\mathbf{r}_{i,\nu}}, \quad (12)$$

with N being the number of unit cells, and \mathbf{k} the wave vector running over the first Brillouin zone. The Hamiltonian then becomes (disregarding any constant terms)

$$\begin{aligned} \mathcal{H} = & \sum_{\mathbf{k}} \sum_{z=\pm} \varepsilon_J \left[3s_3 a_{\mathbf{k},2}^\dagger a_{\mathbf{k},2} + 3s_2 a_{\mathbf{k},3_z}^\dagger a_{\mathbf{k},3_z} \right. \\ & \left. - \sqrt{s_2 s_3} \left(\gamma_{-\mathbf{k}}^z a_{\mathbf{k},2}^\dagger a_{\mathbf{k},3_z} + \gamma_{\mathbf{k}}^z a_{\mathbf{k},3_z}^\dagger a_{\mathbf{k},2} \right) \right] + \varepsilon_z \sum_{\mathbf{k},\nu} s_\nu a_{\mathbf{k},\nu}^\dagger a_{\mathbf{k},\nu} \\ & - \frac{\varepsilon_x}{2} \sum_{\mathbf{k},\nu} s_\nu \left(a_{\mathbf{k},\nu}^\dagger a_{-\mathbf{k},\nu}^\dagger + a_{\mathbf{k},\nu} a_{-\mathbf{k},\nu} \right). \end{aligned} \quad (13)$$

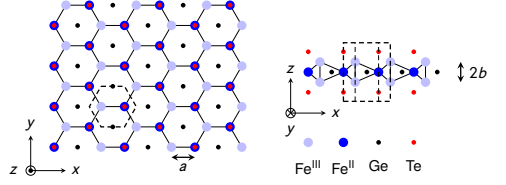


Figure 1. Crystal structure of monolayer Fe_3GeTe_2 . All the drawn in-plane bindings are at a 120° (in-plane) angle relative the neighboring bindings. Dashed lines denote the unit cell. Left: view along e_z ; right: view along e_y . Fe^{III} and Fe^{II} represent the two inequivalent Fe sites in oxidation states +3 and +2, respectively. Redrawn after Ref. [4].

Here we have introduced the structure factor

$$\gamma_{\mathbf{k}} = \sum_{\delta} e^{i\mathbf{k}\cdot\delta}, \quad (14)$$

which becomes

$$\gamma_{\mathbf{k}}^\pm = e^{\pm ik_z b} \left[e^{-ik_x a} + 2e^{ik_x a/2} \cos\left(\frac{\sqrt{3}}{2} k_y a\right) \right] \quad (15)$$

for Fe_3GeTe_2 between the $\nu = 2$ and $\nu = 3_\pm$ sublattices, as can be seen from Fig. 1. Here a is the in-plane lattice constant between the Fe^{II} and Fe^{III} atoms, and $2b$ the separation between two Fe^{III} atoms in the z direction. We have also used that there are three nearest neighbors in each sublattice. We can write the Hamiltonian on the form

$$\begin{aligned} \mathcal{H} = & \sum_{\mathbf{k}} \left(\frac{A}{2} a_{\mathbf{k},2}^\dagger a_{\mathbf{k},2} + \frac{B}{2} a_{\mathbf{k},3_-}^\dagger a_{\mathbf{k},3_-} + \frac{B}{2} a_{\mathbf{k},3_+}^\dagger a_{\mathbf{k},3_+} \right. \\ & \left. + C_{\mathbf{k}} a_{\mathbf{k},2}^\dagger a_{\mathbf{k},3_-} + D_{\mathbf{k}} a_{\mathbf{k},2}^\dagger a_{\mathbf{k},3_+} + \sum_{\nu} E_{\nu} a_{\mathbf{k},\nu} a_{-\mathbf{k},\nu} \right) + \text{H.c.} \end{aligned} \quad (16)$$

The coefficients A , B , $C_{\mathbf{k}}$, $D_{\mathbf{k}}$, and E_{ν} are given in Table I.

We now have to diagonalize the Hamiltonian. This can be done by a six-dimensional Bogoliubov transformation, defined by the matrix \underline{B}_6

$$\begin{aligned} \alpha_{\mathbf{k}} = & \begin{pmatrix} \alpha_{\mathbf{k},\text{I}} \\ \alpha_{\mathbf{k},\text{II}} \\ \alpha_{\mathbf{k},\text{III}} \\ \alpha_{-\mathbf{k},\text{I}}^\dagger \\ \alpha_{-\mathbf{k},\text{II}}^\dagger \\ \alpha_{-\mathbf{k},\text{III}}^\dagger \end{pmatrix} = \underline{B}_6 \begin{pmatrix} a_{\mathbf{k},2} \\ a_{\mathbf{k},3_-} \\ a_{\mathbf{k},3_+} \\ a_{-\mathbf{k},2}^\dagger \\ a_{-\mathbf{k},3_-}^\dagger \\ a_{-\mathbf{k},3_+}^\dagger \end{pmatrix} \equiv \underline{B}_6 \mathbf{a}_{\mathbf{k}} \\ = & \sum_{\nu} \begin{pmatrix} u_{\text{I},\nu} & v_{\text{I},\nu} \\ u_{\text{II},\nu} & v_{\text{II},\nu} \\ u_{\text{III},\nu} & v_{\text{III},\nu} \\ \tilde{v}_{\text{I},\nu}^* & \tilde{u}_{\text{I},\nu}^* \\ \tilde{v}_{\text{II},\nu}^* & \tilde{u}_{\text{II},\nu}^* \\ \tilde{v}_{\text{III},\nu}^* & \tilde{u}_{\text{III},\nu}^* \end{pmatrix} \begin{pmatrix} a_{\mathbf{k},\nu} \\ a_{-\mathbf{k},\nu}^\dagger \end{pmatrix}, \end{aligned} \quad (17)$$

Table I. The coefficients for the Fourier transformed Hamiltonian in Eq. (16) below and above the critical current $|J_c|$.

Coefficient	$ J < J_c $	$ J > J_c $
A	$6s_3\varepsilon_J + s_2\varepsilon_z$	$6s_3\varepsilon_J + \frac{1}{2}s_2(3\varepsilon_x - \varepsilon_z)$
B	$3s_2\varepsilon_J + s_3\varepsilon_z$	$3s_2\varepsilon_J + \frac{1}{2}s_3(3\varepsilon_x - \varepsilon_z)$
C_k	$-\sqrt{s_2s_3}\gamma_{-k}^- \varepsilon_J$	$-\sqrt{s_2s_3}\gamma_{-k}^- \varepsilon_J$
D_k	$-\sqrt{s_2s_3}\gamma_{-k}^+ \varepsilon_J$	$-\sqrt{s_2s_3}\gamma_{-k}^+ \varepsilon_J$
E_ν	$-\frac{1}{2}s_\nu\varepsilon_x$	$-\frac{1}{4}s_\nu(\varepsilon_x + \varepsilon_z)$

where κ now only runs over half the vector space of \mathbf{k} , so that the Hamiltonian can be written as

$$\mathcal{H} = \sum_{\kappa,\mu} \left(\varepsilon_{\kappa,\mu} \alpha_{\kappa,\mu}^\dagger \alpha_{\kappa,\mu} + \varepsilon_{-\kappa,\mu} \alpha_{-\kappa,\mu}^\dagger \alpha_{-\kappa,\mu} \right). \quad (18)$$

The Bogoliubov coefficients with a tilde, e.g. $\tilde{v}_{1,2}$, are evaluated at $-\kappa$ while the coefficients without tilde are evaluated at κ . To diagonalize the Hamiltonian we impose bosonic commutation relations ($[\alpha_{\kappa,\mu}, \alpha_{\kappa',\mu'}^\dagger] = \delta_{\kappa,\kappa'} \delta_{\mu,\mu'}$) as well as the relation $[\alpha_{\kappa,\mu}, \mathcal{H}] = \varepsilon_{\kappa,\mu} \alpha_{\kappa,\mu}$. The bosonic commutation relation leads to the constraint

$$[\alpha_{\kappa}, \alpha_{\kappa}^\dagger] = \underline{B}_6 [\mathbf{a}_{\kappa}, \mathbf{a}_{\kappa}^\dagger] \underline{B}_6^\dagger = \underline{B}_6 \underline{Y} \underline{B}_6^\dagger = \underline{Y}, \quad (19)$$

where we have introduced the matrix

$$\underline{Y} = \text{diag}(1, 1, 1, -1, -1, -1). \quad (20)$$

The relation in Eq. (19) requires the normalization

$$\sum_{\nu} \left(|u_{\mu\nu}|^2 - |v_{\mu\nu}|^2 \right) = 1. \quad (21)$$

The relation from the commutation with the Hamiltonian leads to the eigenvalue problem

$$\begin{pmatrix} A & C_{\kappa}^* & D_{\kappa}^* & -2E_2 & & \\ C_{\kappa} & B & & & -2E_{3-} & \\ D_{\kappa} & & B & & & -2E_{3+} \\ 2E_2 & & & -A & -C_{-\kappa} & -D_{-\kappa} \\ & 2E_{3-} & & -C_{-\kappa}^* & -B & \\ & & 2E_{3+} & -D_{-\kappa}^* & & -B \end{pmatrix} \mathbf{e}_{\mu} = \varepsilon_{\kappa,\mu} \mathbf{e}_{\mu}, \quad (22)$$

where $\mathbf{e}_{\mu} = (u_{\mu,2}, u_{\mu,3-}, u_{\mu,3+}, v_{\mu,2}, v_{\mu,3-}, v_{\mu,3+})^T$. We note that $C_{-\kappa} = C_{\kappa}^*$ and $D_{-\kappa} = D_{\kappa}^*$ and all other elements in the matrix are real and independent of κ . Consequently, we therefore have that $\tilde{u}_{\mu,\nu} = u_{\mu,\nu}^*$ and $\tilde{v}_{\mu,\nu} = v_{\mu,\nu}^*$. We also have that $\varepsilon_{\kappa,\mu} = \varepsilon_{-\kappa,\mu}$, and as $\varepsilon_{\kappa,\mu}$ is a real quantity, we therefore also have $\varepsilon_{-\kappa,\mu} = \varepsilon_{\kappa,\mu}$.

In addition to finding the energy of the eigenmagnons, we also wish to determine their spin, as these are not integer due to squeezing from the SOT-induced anisotropy [5]. Using Eq. (17) and Eq. (19) we see that $\mathbf{a}_{\kappa} = \underline{B}_6^{-1} \alpha_{\kappa} = \underline{Y} \underline{B}_6^\dagger \underline{Y}^{-1}$. This can be written explicitly as

$$a_{\kappa,\nu} = \sum_{\mu} \left(u_{\mu,\nu} \alpha_{\kappa,\mu} - v_{\mu,\nu} \alpha_{-\kappa,\mu}^\dagger \right), \quad (23)$$

$$a_{\kappa,\nu}^\dagger = \sum_{\mu} \left(u_{\mu,\nu}^* \alpha_{\kappa,\mu}^\dagger - v_{\mu,\nu}^* \alpha_{-\kappa,\mu} \right). \quad (24)$$

Together with the fact that non-diagonal expectation values of the product of two eigenmagnon operators vanish, we see from Eq. (9) and Eq. (21) that

$$\begin{aligned} \sum_{i,\nu} \langle S_{i,\nu,z} \rangle &= \sum_{\kappa,\mu} \hbar \sum_{\nu} \left(|u_{\mu,\nu}|^2 + |v_{\mu,\nu}|^2 \right) \sum_{m=\pm} \langle \alpha_{m\kappa,\mu}^\dagger \alpha_{m\kappa,\mu} \rangle \\ &= \sum_{\kappa,\mu} \hbar \left(1 + 2 \sum_{\nu} |v_{\mu,\nu}|^2 \right) \langle \alpha_{\kappa,\mu}^\dagger \alpha_{\kappa,\mu} \rangle, \end{aligned} \quad (25)$$

where we have disregarded all constant terms. We can then see that the eigenmagnon spin contribution is

$$S_{\kappa,\mu} = \hbar \left(1 + 2 \sum_{\nu} |v_{\mu,\nu}|^2 \right). \quad (26)$$

B. Above the critical current

Above the critical current, the lowest energy configuration of the spins is along the x axis. We therefore have to change the Holstein–Primakoff transformation to reflect this, with the following transformation:

$$\tilde{S}_{i,\nu,+} = \hbar \sqrt{2s_\nu} a_{i,\nu}^\dagger \sqrt{1 - \frac{a_{i,\nu}^\dagger a_{i,\nu}}{2s_\nu}} \approx \hbar \sqrt{2s_\nu} a_{i,\nu}^\dagger, \quad (27)$$

$$\tilde{S}_{i,\nu,-} = \hbar \sqrt{2s_\nu} \sqrt{1 - \frac{a_{i,\nu}^\dagger a_{i,\nu}}{2s_\nu}} a_{i,\nu} \approx \hbar \sqrt{2s_\nu} a_{i,\nu}, \quad (28)$$

$$\tilde{S}_{i,\nu,x} = \hbar \left(a_{i,\nu}^\dagger a_{i,\nu} - s_\nu \right), \quad (29)$$

with $\tilde{S}_{\pm} = -\tilde{S}_z \pm i\tilde{S}_y$. Using this transformation in the Hamiltonian in Eq. (6), we get

$$\begin{aligned} \mathcal{H} &= -\varepsilon_J \sum_i \sum_{r_j=r_i+\delta} \sum_{\nu=3_{\pm}} \left[\sqrt{s_2 s_\nu} \left(a_{i,2}^\dagger a_{j,\nu} + a_{j,\nu}^\dagger a_{i,2} \right) \right. \\ &\quad \left. - s_\nu a_{i,2}^\dagger a_{i,2} - s_2 a_{j,\nu}^\dagger a_{j,\nu} \right] \\ &\quad - \frac{\varepsilon_z}{4} \sum_{i,\nu} s_\nu \left(a_{i,\nu}^\dagger a_{i,\nu}^\dagger + 2a_{i,\nu}^\dagger a_{i,\nu} + a_{i,\nu} a_{i,\nu} \right) \\ &\quad + \frac{\varepsilon_x}{4} \sum_{i,\nu} s_\nu \left(6a_{i,\nu}^\dagger a_{i,\nu} - a_{i,\nu}^\dagger a_{i,\nu}^\dagger - a_{i,\nu} a_{i,\nu} \right). \end{aligned} \quad (30)$$

We again do a Fourier transformation as before, and find the Hamiltonian to be on the form (again disregarding any constant terms)

$$\begin{aligned} \mathcal{H} &= + \sum_{\mathbf{k}} \sum_{z=\pm} \varepsilon_J \left[3s_3 a_{\mathbf{k},2}^\dagger a_{\mathbf{k},2} + 3s_2 a_{\mathbf{k},3_z}^\dagger a_{\mathbf{k},3_z} \right. \\ &\quad \left. - \sqrt{s_2 s_3} \left(\gamma_{\mathbf{k},2}^z a_{\mathbf{k},2}^\dagger a_{\mathbf{k},3_z} + \gamma_{\mathbf{k},2}^z a_{\mathbf{k},3_z}^\dagger a_{\mathbf{k},2} \right) \right] \\ &\quad - \frac{\varepsilon_z}{4} \sum_{\mathbf{k},\nu} s_\nu \left(2a_{\mathbf{k},\nu}^\dagger a_{\mathbf{k},\nu} + a_{\mathbf{k},\nu}^\dagger a_{-\mathbf{k},\nu}^\dagger + a_{\mathbf{k},\nu} a_{-\mathbf{k},\nu} \right) \\ &\quad + \frac{\varepsilon_x}{4} \sum_{\mathbf{k},\nu} s_\nu \left(6a_{\mathbf{k},\nu}^\dagger a_{\mathbf{k},\nu} - a_{\mathbf{k},\nu}^\dagger a_{-\mathbf{k},\nu}^\dagger - a_{\mathbf{k},\nu} a_{-\mathbf{k},\nu} \right). \end{aligned} \quad (31)$$

From this expression we can read off the coefficients in Eq. (16), and use the results in the previous subsection for the case below

the critical current to determine the energy and spin of the eigenmagnons. The coefficients in Eq. (16) are given in Table I both above and below the critical current.

-
- [1] K. M. D. Hals and A. Brataas, "Phenomenology of current-induced spin-orbit torques," *Phys. Rev. B* **88**, 085423 (2013); "Spin-motive forces and current-induced torques in ferromagnets," *Phys. Rev. B* **91**, 214401 (2015).
- [2] H.-J. Deiseroth, K. Aleksandrov, C. Reiner, L. Kienle, and R. K. Kremer, " Fe_3GeTe_2 and Ni_3GeTe_2 – two new layered transition-metal compounds: Crystal structures, HRTEM investigations, and magnetic and electrical properties," *Eur. J. Inorg. Chem.* **2006**, 1561–1567 (2006).
- [3] R. R. Birss, *Symmetry and Magnetism*, 1st ed., edited by E. P. Wohlfarth, Selected Topics in Solid State Physics, Vol. 3 (North-Holland Publishing Company, 1964).
- [4] Y. Deng, Y. Yu, Y. Song, J. Zhang, N. Z. Wang, Z. Sun, Y. Yi, Y. Z. Wu, S. Wu, J. Zhu, J. Wang, X. H. Chen, and Y. Zhang, "Gate-tunable room-temperature ferromagnetism in two-dimensional Fe_3GeTe_2 ," *Nature* **563**, 94–99 (2018).
- [5] A. Kamra, U. Agrawal, and W. Belzig, "Noninteger-spin magnonic excitations in untextured magnets," *Phys. Rev. B* **96**, 020411 (2017).



Reference

V. Risinggård, E.G. Tveten, A. Brataas, J. Linder.
Equations of motion and frequency dependence
of magnon-induced domain wall motion.
Physical Review B **96**, 174441 (2017).
10/c2q8

Contributions

JL initiated and supervised the project. VR derived the equations of motion based on previous work by EGT (*Phys. Rev. Lett.* **112**, 147204; 2014). VR derived the frequency-dependence of the spin-wave amplitude based on discussions with EGT. VR performed the numerical work and drafted the manuscript. All authors contributed to the discussion of the results and the revision of the final manuscript.

Equations of motion and frequency dependence of magnon-induced domain wall motion

Vetle Risinggård,* Erlend G. Tveten, Arne Brataas, and Jacob Linder

Department of Physics, Center for Quantum Spintronics, NTNU, Norwegian University of Science and Technology, N-7491 Trondheim, Norway

(Received 5 June 2017; revised manuscript received 19 September 2017; published 30 November 2017)

Spin waves can induce domain wall motion in ferromagnets. We derive the equations of motion for a transverse domain wall driven by spin waves. Our calculations show that the magnonic spin-transfer torque does not cause rotation-induced Walker breakdown. The amplitude of spin waves that are excited by a localized microwave field depends on the spatial profile of the field and the excitation frequency. By taking this frequency dependence into account, we show that a simple one-dimensional model may reproduce much of the puzzling frequency dependence observed in early numerical studies.

DOI: 10.1103/PhysRevB.96.174441

I. INTRODUCTION

Magnon-induced domain wall motion has recently been studied analytically [1–4], numerically [5–13], and experimentally [14,15]. The numerical analyses have uncovered a wide range of domain wall behaviors. The domain wall velocity depends on the frequency of the locally applied magnetic field acting as the spin-wave source in a complicated and nonmonotonic way. For some frequencies, it is even possible to reverse the direction of the domain wall motion. This complicated behavior can be explained as a competition between angular and linear momentum transfer: Conservation of angular momentum causes a domain wall to move *towards* the spin-wave source via a magnonic torque [1,2]. On the other hand, conservation of linear momentum causes a domain wall to propagate *away* from the spin-wave source [3,4].

So far, experimental investigations of magnon-induced domain wall motion have mainly focused on dynamics induced by thermal magnons [14,15]. However, a domain wall in a temperature gradient can experience additional torques besides the purely magnonic ones, for instance, the exchange stiffness can vary with temperature [5,16–21]. Characteristically, these torques can induce a Walker breakdown, upon which the domain wall is deformed as it moves [22].

In ferromagnets, previous studies of domain wall dynamics due to magnonic torques have considered the response of a *static* wall to *first-order* spin-wave excitations. In such a scheme, global conservation laws determine the resulting domain wall velocity [1–4]. However, understanding *dynamic* phenomena, such as a Walker breakdown, requires knowledge about the dynamics of the collective coordinates that represent the domain wall [23]. Spin-wave-induced domain wall motion is a result of the back action of the spin waves on the magnetic texture [1]. Consequently, the soft modes of the domain wall are quadratic in the spin-wave amplitude. Deriving the equations of motion of the collective coordinates, therefore, requires an expansion to *second order* in the spin-wave amplitudes. This principle is the basis for understanding how spin waves induce domain wall motion in antiferromagnets [24].

In this article, we apply the same method to ferromagnets. We derive the collective coordinate equations of a spin-wave-driven domain wall from the ferromagnetic Landau-Lifshitz-Gilbert (LLG) equation. Our approach enables the inclusion of dissipative torques into the dynamic equations of the domain wall position X and the tilt angle ϕ .

In the perturbative regime, the absence of Walker breakdown amounts to requiring that the domain wall tilt is stationary $\dot{\phi} = 0$. We show that, in practice, the domain wall rotation is always negligibly small in, e.g., yttrium iron garnet (YIG). Thus, Walker breakdown is absent in domain wall motion driven purely by magnonic spin transfer.

In our simulations, a localized magnetic field excites the spin waves that in turn drive the domain wall motion. Understanding the domain wall motion then requires knowing both the frequency-dependent magnonic torques as well as the generated spin-wave amplitude. The spatial profile of the microwave source determines how the spin-wave amplitude depends on the driving frequency [25–28]. We derive a special case of Kalinikos' general formula [25] and show that the spin-wave amplitude is proportional to the Fourier sine transform of the source profile. We then use the dependence of the spin-wave amplitude on the microwave frequency to find consistent results for how the domain wall velocity depends on the driving frequency in the numerical and analytical calculations.

Reference [29] has recently considered the linear-response spin-wave emission from a stationary domain wall in a uniform microwave field. We consider a different problem—spin-wave-induced domain wall motion—which is a second-order effect.

II. EQUATIONS OF MOTION

We consider an effectively one-dimensional ferromagnet as shown in Fig. 1. The LLG equation determines the magnetization dynamics [30,31],

$$\partial_t \mathbf{m} = \gamma \mathbf{m} \times \mathbf{H} + \frac{\alpha}{m} \mathbf{m} \times \partial_t \mathbf{m}, \quad (1)$$

where $\mathbf{m}(\mathbf{r}, t)$ is the magnetization, m is its magnitude, $\gamma < 0$ is the gyromagnetic ratio, $\mathbf{H}(\mathbf{r}, t) = -\delta F(\mathbf{r}, t)/\delta \mathbf{m}(\mathbf{r}, t)$ is the effective magnetic field, and $\alpha > 0$ is the Gilbert damping constant.

*vetle.k.risinggard@ntnu.no

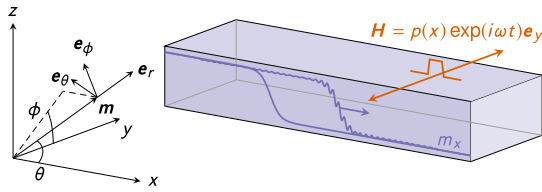


FIG. 1. Magnonic spin transfer induces a motion of the domain wall. We consider transverse domain wall motion along the x axis. The spatial profile of the applied magnetic field influences the amplitude of the excited spin waves and subsequently the resulting domain wall velocity.

The free energy F consists of the exchange, the dipole-dipole interaction, and the magnetic anisotropy. In a magnetic wire, the dipole-dipole interaction favors a magnetization direction along the long axis. Taking this into account in the simplest approximation, we model the dipole-dipole interaction as an effective easy-axis anisotropy. The free energy is then

$$F = \int dr \left(\frac{A(\partial_x \mathbf{m})^2}{m^2} - \frac{K m_x^2}{m^2} \right), \quad (2)$$

where A is the exchange stiffness and K is the effective uniaxial anisotropy constant. As shown numerically in the Appendix, our results are unchanged by an additional hard axis.

The LLG equation (1) conserves the magnitude of the magnetization $|\mathbf{m}| = m$, which makes it convenient to express the magnetization in spherical coordinates (see Fig. 1),

$$\mathbf{m} = m(\cos \theta \mathbf{e}_x + \cos \phi \sin \theta \mathbf{e}_y + \sin \phi \sin \theta \mathbf{e}_z). \quad (3)$$

In terms of the angles θ and ϕ a solution of the static ($\partial_t \mathbf{m} = 0$) LLG equation (1) is the Néel wall $\theta = 2 \arctan \exp[Q(x - X)/\lambda]$, where X is the domain wall position, $\lambda = \sqrt{A/K}$ is the domain wall width, and $Q = \pm 1$ is the topological charge [32]. In the absence of a hard axis, ϕ can take any value.

We calculate the magnon-induced dynamics perturbatively. The small parameter h parametrizes deviations from the equilibrium magnetization in the spherical frame, see Fig. 1. To second order in h , the magnetization is [24]

$$\begin{aligned} \mathbf{m} &= \left(m - \frac{h^2}{2m} [m_\theta^{(2)} + m_\phi^{(2)}] \right) \mathbf{e}_r \\ &+ (hm_\theta^{(1)} + h^2 m_\theta^{(2)}) \mathbf{e}_\theta + (hm_\phi^{(1)} + h^2 m_\phi^{(2)}) \mathbf{e}_\phi \\ &= \left(m - \frac{h^2}{2m} [m_\theta^2 + m_\phi^2] \right) \mathbf{e}_r + hm_\theta \mathbf{e}_\theta + hm_\phi \mathbf{e}_\phi. \end{aligned} \quad (4)$$

The second line follows from the normalization criterion $\mathbf{m} \cdot \mathbf{m} = m^2$, and we have written $m_{\theta/\phi} = m_{\theta/\phi}^{(1)}$ for simplicity. The second-order contributions to the transverse components \mathbf{e}_θ and \mathbf{e}_ϕ have been dropped since it turns out that carrying them through the following calculation does not change Eqs. (14) and (15).

Substituting the expansion (4) into the LLG equation (1) and equating like orders of h gives three equations that determine the magnetization dynamics to zeroth, first, and second orders

in h . Because we are considering the *dynamic* reaction of the magnetization texture, θ depends on position, and both θ and ϕ depend on time. By assuming that the dynamics of the domain wall collective coordinates is quadratic in the spin-wave excitations, we obtain two equations to linear order,

$$\partial_t m_\theta = \left(-\frac{2\gamma A}{m} \partial_x^2 + \frac{2\gamma K}{m} \cos 2\theta - \alpha \partial_t \right) m_\phi, \quad (5a)$$

and

$$\partial_t m_\phi = \left(+\frac{2\gamma A}{m} \partial_x^2 - \frac{2\gamma K}{m} \cos 2\theta + \alpha \partial_t \right) m_\theta. \quad (5b)$$

As pointed out in Ref. [33], the introduction of the auxiliary function $\psi = m_\theta - im_\phi$ simplifies Eqs. (5). Assuming that $\psi(x, t) = \psi(x) \exp(-i\omega t)$ and using $\sin \theta = \text{sech } \xi$, we obtain

$$q^2 \psi = (-\partial_\xi^2 - 2 \text{sech}^2 \xi) \psi, \quad (6)$$

where we defined the dimensionless length $\xi = Q(x - X)/\lambda$ and the dimensionless wave number,

$$q^2 = -m\omega(1 + i\alpha)/2\gamma K - 1. \quad (7)$$

Equation (6) is a Schrödinger equation with a reflectionless Pöschl-Teller potential [34]. It has two solutions, a bound state $\psi = \rho \text{sech } \xi$ for $q = -i$ (implying $\omega = 0$) and a traveling wave [35,36],

$$\psi(\xi, t) = \rho \left(\frac{\tanh \xi - iq}{1 + iq} \right) \exp i(q\xi - \omega t). \quad (8)$$

The amplitude ρ is arbitrary, and, as is easily checked by back substitution, the solution (8) holds for any complex q . We need a second equation to determine m_θ and m_ϕ . A reasonable condition is that they should both be real, which in turn ensures that the magnetization (4) is real. Thus we write

$$m_\theta = +\text{Re } \psi, \quad (9a)$$

$$m_\phi = -\text{Im } \psi. \quad (9b)$$

To calculate the real and imaginary parts of ψ , it is useful to rewrite the wave number q in terms of a real part κ and an imaginary part $1/\Gamma$. In Eq. (7), we insert the real and imaginary parts of $q = \kappa + i/\Gamma$ and expand to the lowest nonvanishing order in α . We then find the well-known dispersion,

$$\omega = -\frac{2\gamma K(\kappa^2 + 1)}{m}, \quad (10)$$

and damping length [37],

$$\Gamma = -\frac{4\gamma K\kappa}{m\omega\alpha}. \quad (11)$$

The dispersion relation and the damping length are both plotted in Fig. 2. (We use a convention so that $\gamma < 0$ and $\alpha > 0$.)

The solution (8) is well known and was used in Ref. [2] to derive the domain wall velocity using conservation of

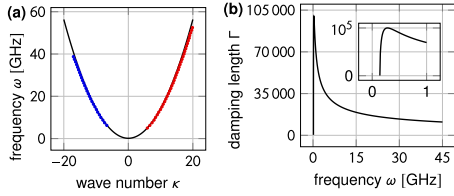


FIG. 2. (a) Dispersion and (b) damping length of the spin waves to lowest order in α . The solid curves are the analytical results of Eqs. (10) and (11). The dotted lines are numerical solutions using a square box (red) and a Gaussian (blue) source. The dimensionless wave number κ is given in units of $1/\lambda$, and the dimensionless damping length Γ is given in units of λ . The inset in (b) shows a zoom in on $\omega < 1$ GHz. Note that the damping length vanishes as the frequency approaches the gap $\omega_0 = -2\gamma K/m = 0.14$ GHz from above. We use material parameters corresponding to YIG: $\gamma = -26$ GHz/T, $A = 4$ pJ/m, $K = 0.4$ kJ/m³, $m = 150$ kA/m, and $\alpha = 10^{-5}$.

angular momentum. It is implicit in the results of Ref. [2] that the collective coordinates are quadratic in the spin-wave excitations. Thus, to obtain the main result in this paper, which is the equations of motion for \dot{X} and $\dot{\phi}$, we consider the

$$\int d\xi \operatorname{sech} \xi \left(\frac{\dot{X}}{\lambda} - \alpha \dot{\phi} \right) = \frac{2\gamma A \rho^2 \kappa}{m^3 \lambda^2} \int d\xi \exp\left(-\frac{2(\xi + \xi_0)}{\Gamma}\right) \frac{[(\kappa^2 + 1)\Gamma^2 + 1] \operatorname{sech} \xi + 2\Gamma \tanh \xi \operatorname{sech} \xi}{[(\kappa^2 + 1)\Gamma^2 + 1 - 2\Gamma]}, \quad (13a)$$

$$\int d\xi \operatorname{sech} \xi \left(\frac{\alpha \dot{X}}{\lambda} + \dot{\phi} \right) = \frac{2\gamma A \rho^2}{m^3 \lambda^2 \Gamma} \int d\xi \exp\left(-\frac{2(\xi + \xi_0)}{\Gamma}\right) \frac{[(\kappa^2 - 1)\Gamma^2 + 1] \operatorname{sech} \xi - \Gamma[(\kappa^2 + 1)\Gamma^2 - 1] \tanh \xi \operatorname{sech} \xi}{[(\kappa^2 + 1)\Gamma^2 + 1 - 2\Gamma]}. \quad (13b)$$

Here, the factor $\exp(-2\xi_0/\Gamma)$, where ξ_0 is the distance between the domain wall and the spin-wave source, takes into account the damping of the spin waves. Because the dynamics of the collective coordinates is quadratic in the spin-wave components, their motion decays twice as fast as the spin waves with increasing distance from the spin-wave source. Carrying out the spatial integrals in Eqs. (13) then gives the equations of motion. However, direct spatial integration produces β functions [38]. To express the integrals over ξ in terms of elementary functions, we assume that ξ/Γ is small and expand the exponential damping factor $\exp(-2\xi/\Gamma)$ on the right-hand side to first order in ξ/Γ . For moderate ξ , this assumption is valid for large Γ . This is the case for low damping and frequencies comparable to the gap, see Fig. 2. When ξ is large, the smallness of ξ/Γ is unimportant because the error we introduce is suppressed by the hyperbolic secant.

To linear order in α , the resulting equations of motion are

$$\frac{\dot{X}}{\lambda} = \frac{2\gamma A \kappa \rho^2 \exp(-2\xi_0/\Gamma)(\kappa^2 + 1 + 2/\Gamma)}{\lambda^2 m^3 (\kappa^2 + 1)}, \quad (14)$$

and

$$\dot{\phi} = \frac{2\gamma A \kappa \rho^2 \exp(-2\xi_0/\Gamma)(\alpha \kappa^2 + \alpha - 3\kappa/\Gamma - 1/\kappa\Gamma)}{\lambda^2 m^3 (\kappa^2 + 1)}. \quad (15)$$

Equations (14) and (15) are our main analytical results. As expected, in the limit of no damping $\alpha \rightarrow 0$ and $\Gamma \rightarrow \infty$, we

recover the result of Ref. [2],

$$\int d\xi \operatorname{sech} \xi \left(\frac{\dot{X}}{\lambda} - \alpha \dot{\phi} \right) = \int d\xi \frac{4\gamma K \operatorname{sech} \xi}{m^3} (m_\phi m_\theta \tanh \xi + m_\phi \partial_\xi m_\theta), \quad (12a)$$

$$\int d\xi \operatorname{sech} \xi \left(\frac{\alpha \dot{X}}{\lambda} + \dot{\phi} \right) = \int d\xi \frac{4\gamma K \operatorname{sech} \xi}{m^3} (m_\theta^2 \tanh \xi - m_\phi \partial_\xi m_\phi). \quad (12b)$$

Since all terms except $X(t)$ and $\phi(t)$ are known, Eqs. (12) constitute a set of coupled ordinary temporal differential equations that determine the dynamics of the collective coordinates.

Equations (12) contain two different time scales. The fast time scale is set by the period of the spin waves. The slow time scale is associated with the dynamics of the domain wall. Our focus is on the second and slower time scale. Therefore, we substitute the spin-wave components into the right-hand side of Eqs. (12) and average over one spin-wave period, giving

recover the result of Ref. [2],

$$\frac{\dot{X}}{\lambda} = \frac{2\gamma A \kappa \rho^2}{\lambda^2 m^3}. \quad (16)$$

In addition, the equation of motion for ϕ gives

$$\dot{\phi} = 0, \quad (17)$$

in this limit.

We have calculated the spin-wave-induced magnetization dynamics perturbatively, cf. Eq. (4). It is then reasonable to assume that the transverse wall will not be transformed into, for instance, a vortex wall [39]. Thus, the absence of Walker breakdown amounts to requiring that the domain wall tilt is stationary $\dot{\phi} = 0$ [22]. Equation (17) shows that this is always the case for purely magnonic torques. In the presence of a finite damping, $\dot{\phi} = 0$ does not hold identically [cf. Eq. (15)], but when evaluating this expression with material parameters typical of low-damping magnetic garnets (Fig. 3), we discover that the rotation rate, although finite, is negligible. Consequently, purely magnonic torques do not induce Walker breakdown in realistic materials.

The dynamics of the domain wall collective coordinates explicitly depends on the frequency of the spin waves through κ and Γ . Assuming the spin-wave amplitude ρ is constant, the domain wall velocity increases monotonically with increasing frequencies as shown in Fig. 3. This is understood most easily

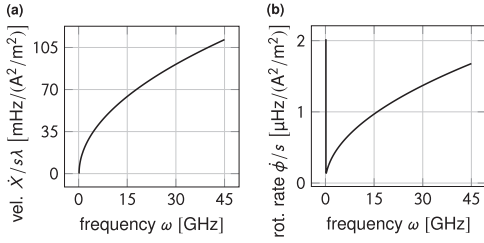


FIG. 3. The dependence of (a) the domain wall velocity \dot{X}/λ and (b) the rotation rate $\dot{\phi}$ on the spin-wave frequency. Both plots are normalized to the spin-wave amplitude $s = \rho^2 \exp(-2\xi_0/\Gamma)$. The frequency dependence of the wall velocity is monotonic. Because of the low damping, the wall rotation rate is five orders of magnitude smaller than the wall velocity and almost vanishes throughout the interval. We use the same parameters as in Fig. 2.

in the absence of magnetic damping. Domain wall motion occurs in our model because angular momentum is transferred from the spin waves to the magnetic texture. The group velocity $v_g = d\omega/d\kappa = -4\gamma A\kappa/m\lambda^2$ is a monotonically increasing function of frequency. A higher group velocity implies that more spin waves pass through the domain wall per unit time, so the rate of angular momentum transfer from the spin waves to the domain wall is higher. A higher rate of angular momentum transfer gives a higher domain wall velocity. This is manifest in Eq. (16), which can be written as $\dot{X}/\lambda = -\frac{1}{2}v_g\rho^2/m^2$.

The monotonic increase in domain wall velocity with increasing frequency contrasts with the nonmonotonic dependence on the excitation frequency observed in numerical simulations [6–13]. However, the dynamics of the collective coordinates also depends strongly on the spin-wave amplitude ρ . Since the spin-wave amplitude depends on the frequency of the applied excitation field [25–28], it is the spatial profile of the applied excitation field that plays the main role in determining the frequency dependence of the domain wall velocity in some of these studies.

III. FREQUENCY DEPENDENCE OF THE SPIN-WAVE AMPLITUDE

We now consider the generation of the spin waves. The microwave source is assumed to be far into the domain. It is then sufficient to only consider the interaction between the source and a homogenous magnetization. Furthermore, we assume that the dominant effect of the damping is an exponential decrease in the spin-wave amplitude as the spin waves move away from the source. This allows us to neglect the damping in the following analysis of the spin-wave generation.

We calculate the disturbance of the homogeneous magnetization caused by the source perturbatively. The small excitation parameter h parametrizes a locally applied magnetic-field $\mathbf{H} = hp(x)\exp(-i\omega t)\mathbf{e}_y$. Anticipating a propagating wave solution, we substitute the *ansatz*,

$$\mathbf{m} = m\mathbf{e}_x + hm_y(x,t)\mathbf{e}_y + hm_z(x,t)\mathbf{e}_z, \quad (18)$$

which is accurate to first order in h , into the LLG equation (1). This gives two equations to first order in h ,

$$\partial_t m_y = \left(-\frac{2\gamma A}{m} \partial_x^2 + \frac{2\gamma K}{m} \right) m_z, \quad (19)$$

$$\partial_t m_z = \left(+\frac{2\gamma A}{m} \partial_x^2 - \frac{2\gamma K}{m} \right) m_y + \gamma mp(x)\exp(-i\omega t). \quad (20)$$

Again, introducing the auxiliary variable $\psi = m_y - im_z$ and using $\psi(x,t) = \psi(x)\exp(-i\omega t)$, we obtain

$$-\gamma mp(\xi) = \left(\frac{2\gamma K}{m} \partial_\xi^2 - \frac{2\gamma K}{m} - \omega \right) \psi(\xi), \quad (21)$$

where we introduced the dimensionless length $\xi = x/\lambda$. To obtain the solution to the differential equation (21) for different spatial profiles of the applied magnetic-field $p(\xi)$, we solve for the Green function. The Green function G of Eq. (21) is defined by [40]

$$-\gamma m\delta(\xi) = \left(\frac{2\gamma K}{m} \partial_\xi^2 - \frac{2\gamma K}{m} - \omega \right) G(\xi). \quad (22)$$

By spatial Fourier transformation, we obtain an algebraic equation that can be solved to give

$$g(\xi') = \frac{\gamma m^2}{2\gamma K(\xi'^2 + 1) + m\omega}, \quad (23)$$

where ξ' is the Fourier conjugate variable of ξ . The inverse Fourier transform gives

$$G = -\frac{m^2 \sin \kappa \xi}{4\kappa K} (2\Theta(\xi) - 1), \quad (24)$$

where κ is the dimensionless wave number from Eq. (10) and $\Theta(\xi)$ is the Heaviside step function. The spin-wave $\psi(\xi)$ then is given by the convolution of the Green function and the source profile p ,

$$\begin{aligned} \psi(\xi) &= \int_{-\infty}^{+\infty} d\xi'' G(\xi - \xi'') p(\xi'') \\ &= 2 \int_0^{+\infty} d\xi'' G(\xi - \xi'') p(\xi''), \end{aligned} \quad (25)$$

where the last expression, valid only for symmetrical sources $p(-\xi) = p(\xi)$, is proportional to a Fourier sine transform.

Different source profiles can be obtained by tuning the relative widths of the conducting stripes of a coplanar waveguide [26,27]. In particular, we are interested in the square box source p_1 and a Gaussian source p_2 ,

$$p_1(\xi) = \frac{H}{2\sigma} [\Theta(\xi - \mu + \sigma) - \Theta(\xi - \mu - \sigma)], \quad (26a)$$

$$p_2(\xi) = \frac{H}{\sqrt{2\pi}\sigma} \exp\left(-\frac{(\xi - \mu)^2}{2\sigma^2}\right), \quad (26b)$$

where μ is the source position and σ is the source half-width. Substituting p_1 and p_2 into Eq. (25), we obtain the spin-wave

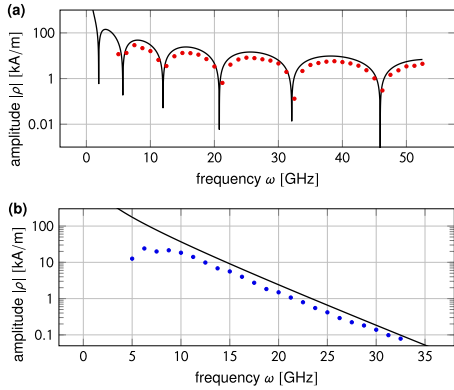


FIG. 4. Spin-wave amplitude as a function of the driving frequency for different spatial profiles of the applied magnetic field. (a) The amplitude due to the square box source dies off as $|\sin \kappa \sigma / (\kappa^2 \sigma)|$, whereas (b) the Gaussian source dies off as $\exp(-\kappa^2 \sigma^2 / 2) / \kappa$. We use the same parameters as in Fig. 2 with $H = 0.2$ T and (a) $\sigma = 1.02\lambda = 102$ nm and (b) $\sigma = \lambda/4 = 25$ nm. The wave number $\kappa(\omega)$ used to calculate the analytical curves is estimated by performing a least-squares fit to the numerical dispersions in Fig. 2.

amplitudes,

$$\rho_1 = \pm \frac{Hm^2 \sin \kappa \sigma}{4K\kappa \kappa \sigma}, \quad (27a)$$

$$\rho_2 = \pm \frac{Hm^2}{4K\kappa} \exp\left(-\frac{1}{2}\kappa^2 \sigma^2\right), \quad (27b)$$

far away from the source ($|\mu| \rightarrow \infty$).

Equations (27) can be derived as special cases of Kalinikos' general formula [25]. As illustrated in Fig. 4, the spin-wave amplitudes depend strongly on the driving frequency and the spatial profile of the applied magnetic field. The square box source (26a) has sharply defined ends. Thus, at every frequency where an integer number of wavelengths fits inside the box, we excite standing waves within the box, and the spin-wave amplitude far away from the box is practically zero. The zeros of the amplitude at 5.63, 11.90, 21.25, 32.50, and 46.25 GHz, correspond to two to six wavelengths, respectively, fitting inside the box width of 2σ . The intermittent peaks in the amplitude correspond to a half-integer number of wavelengths fitting inside the box, giving maximum emission of spin waves. On the other hand, the Gaussian source (26b) falls off exponentially, and spin waves will leak out of the source region at every frequency. However, the width of the box introduces a length scale in the problem, thus determining the slope of the amplitude in the log plot found in Fig. 4(b). Although our analytical calculation readily reproduces the frequency dependence observed in the full numerical solution, it overestimates the amplitude roughly by a factor of 1.6.

As shown in Fig. 5, the substitution of the amplitudes (27a) and (27b) into the equation of motion for X , Eq. (14), accounts for the frequency dependence of the domain wall velocity

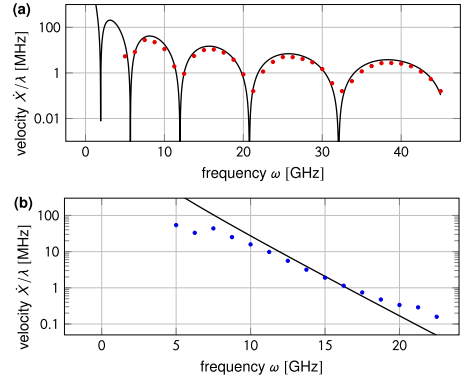


FIG. 5. Domain wall velocity as a function of the driving frequency for different spatial profiles of the applied magnetic field. We use the same parameters as in Fig. 2 with $H = 0.2$ T and (a) $\sigma = 1.02\lambda = 102$ nm and (b) $\sigma = \lambda/4 = 25$ nm. The analytical curves are calculated by substituting Eqs. (27) into Eq. (14), the wave number $\kappa(\omega)$ is estimated by performing a least-squares fit to the numerical dispersions in Fig. 2, and the overestimate of the amplitude has been corrected by a factor of $1.6^2 = 2.6$.

in the corresponding one-dimensional numerical model. The Appendix describes the numerical calculations.

Our results illustrate that a critical assessment of the impact of the source is vital to extract information about the frequency dependence of magnonic spin-transfer torques from micromagnetic simulations, such as those presented in Refs. [6–13]. For example, studies that use square box sources need to take into account the well-known artifacts [25] thus introduced in the frequency dependence of the domain wall velocity. The results presented above should serve to illustrate that the frequency dependence introduced by the square box source may account for some of the effects previously attributed to the internal modes of the domain wall [6,8–11]. However, there are also clear indications that the internal modes of the domain wall affect the magnon-induced domain wall motion when the two-dimensional character of the system is important [13]. Reference [41] reports the first steps towards an analytical treatment of magnon-domain wall interaction in two dimensions.

Figure 6 plots the spin-wave amplitude as a function of the strength of the applied field magnitude H . As expected, for small applied fields, there is a linear regime where perturbation theory works well. We observe that a magnetic field of 0.2 T as applied in Figs. 4 and 5 is well within this perturbative regime. For applied magnetic fields above this regime, the amplitude of the mode oscillating at the excitation frequency decreases due to the appearance of higher-frequency modes [42,43].

IV. CONCLUSION

We have derived the equations of motion for the collective coordinates of a transverse domain wall driven by spin waves. We used this description to demonstrate that magnonic spin transfer does not induce Walker breakdown. For spin waves

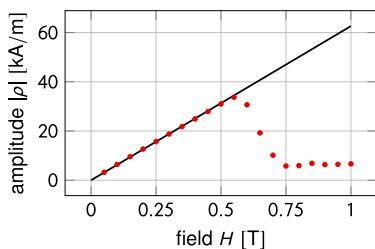


FIG. 6. Spin-wave amplitude as a function of the magnitude of the applied magnetic-field H at $\omega = 15$ GHz. We use the square box source ($\sigma = 1.02\lambda = 102$ nm) and the same parameters as in Fig. 2, and the overestimate of the amplitude has been corrected by a factor of $1.6^2 = 2.6$.

excited by a localized microwave field the spatial profile of the applied field strongly affects the frequency dependence of the spin-wave amplitude. Taking this frequency dependence into account, we have explained how pure spin transfer may still result in a domain wall velocity with a nonmonotonic dependence on the excitation frequency in a one-dimensional model. In particular, the frequency dependence of the spin-wave amplitude arising from a square box source can account for some of the frequency dependence of the domain wall velocity that has previously been attributed to internal modes of the domain wall.

ACKNOWLEDGMENTS

We would like to thank A. Qauiumzadeh for useful discussions. Funding via the “Outstanding Academic Fellows” program at NTNU, the COST Action MP-1201, the NV Faculty, the Research Council of Norway Grants No. 216700 and No. 240806, and the Research Council of Norway through its Centres of Excellence funding scheme, Project No. 262633, “QuSpin” is gratefully acknowledged.

APPENDIX: NUMERICS

We solve the Landau-Lifshitz-Gilbert equation (1) numerically. To this end, we apply a spatiotemporal discretization

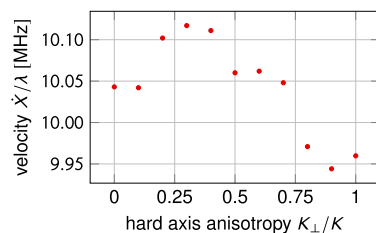


FIG. 7. Domain wall velocity as a function of hard-axis anisotropy for $H = 0.2$ T and $\omega = 15$ GHz. We use the square box source ($\sigma = 1.02\lambda = 102$ nm) and the same parameters as in Fig. 2.

using a centered implicit scheme in Maple [44]. The effective field is

$$\mathbf{H} = \frac{2A}{m^2} \partial_x^2 \mathbf{m} + \frac{2}{m^2} (K m_x \mathbf{e}_x - K_\perp m_z \mathbf{e}_z), \quad (\text{A1})$$

as derived from the free-energy (2) with an additional hard-axis anisotropy. The system is a $3\text{-}\mu\text{m}$ grid with grid points spaced 4 nm apart. The initial magnetization profile is a domain wall with positive topological charge ($Q = +1$) and positive chirality ($\phi = 0$) centered at the origin. An additional magnetic-field $p(x) \exp(-i\omega t) \mathbf{e}_y$, centered at $x = 1 \mu\text{m}$, excites the spin waves. We insert absorbing boundary conditions at the sample ends to avoid interference phenomena due to spin-wave reflections. In doing so, the Gilbert damping parameter increases to $\alpha = 1$ inside $0.3\text{-}\mu\text{m}$ -wide regions at both ends of the sample [37].

The hard-axis anisotropy K_\perp in Eq. (A1) is set to zero in the analytical treatment and in the numerical results in the main text. However, we have verified numerically that the results in Figs. 2 and 4–6 are essentially unchanged in the presence of a hard-axis anisotropy of magnitude $K_\perp = K/2$. As shown in Fig. 7 for one frequency and applied field magnitude, the additional hard-axis anisotropy only leads to slight changes in the domain wall velocity. (This should be expected—in the absence of domain wall rotation, the hard axis will not affect the domain wall dynamics.)

-
- [1] A. V. Mikhailov and A. I. Yaremchuk, *JETP Lett.* **39**, 354 (1984).
 - [2] P. Yan, X. S. Wang, and X. R. Wang, *Phys. Rev. Lett.* **107**, 177207 (2011); X. R. Wang, P. Yan, and X. S. Wang, *IEEE Trans. Magn.* **48**, 4074 (2012).
 - [3] D. Wang, X.-G. Wang, and G.-H. Guo, *Europhys. Lett.* **101**, 27007 (2013); X.-G. Wang, G.-H. Guo, G.-F. Zhang, Y.-Z. Nie, and Q.-L. Xia, *Appl. Phys. Lett.* **102**, 132401 (2013).
 - [4] P. Yan, A. Kamra, Y. Cao, and G. E. W. Bauer, *Phys. Rev. B* **88**, 144413 (2013).
 - [5] D. Hinzke and U. Nowak, *Phys. Rev. Lett.* **107**, 027205 (2011).
 - [6] D.-S. Han, S.-K. Kim, J.-Y. Lee, S. J. Hermsdoerfer, H. Schultheiss, B. Leven, and B. Hillebrands, *Appl. Phys. Lett.* **94**, 112502 (2009).
 - [7] M. Jamali, H. Yang, and K.-J. Lee, *Appl. Phys. Lett.* **96**, 242501 (2010).
 - [8] S.-M. Seo, H.-W. Lee, H. Kohno, and K.-J. Lee, *Appl. Phys. Lett.* **98**, 012514 (2011).
 - [9] X.-G. Wang, G.-H. Guo, Y.-Z. Nie, G.-F. Zhang, and Z.-X. Li, *Phys. Rev. B* **86**, 054445 (2012).
 - [10] J.-S. Kim, M. Stärk, M. Kläui, J. Yoon, C.-Y. You, L. Lopez-Diaz, and E. Martinez, *Phys. Rev. B* **85**, 174428 (2012).
 - [11] X.-G. Wang, G.-H. Guo, G.-F. Zhang, Y.-Z. Nie, and Q.-L. Xia, *J. Appl. Phys.* **113**, 213904 (2013).
 - [12] K.-W. Moon, B. Sun Chun, W. Kim, and C. Hwang, *J. Appl. Phys.* **114**, 123908 (2013).
 - [13] H. Hata, T. Taniguchi, H.-W. Lee, T. Moriyama, and T. Ono, *Appl. Phys. Express* **7**, 033001 (2014).

- [14] J. Torrejon, G. Malinowski, M. Pelloux, R. Weil, A. Thiaville, J. Curiale, D. Lacour, F. Montaigne, and M. Hehn, *Phys. Rev. Lett.* **109**, 106601 (2012).
- [15] W. Jiang, P. Upadhyaya, Y. Fan, J. Zhao, M. Wang, L.-T. Chang, M. Lang, K. L. Wong, M. Lewis, Y.-T. Lin, J. Tang, S. Cherepov, X. Zhou, Y. Tserkovnyak, R. N. Schwartz, and K. L. Wang, *Phys. Rev. Lett.* **110**, 177202 (2013).
- [16] A. A. Kovalev and Y. Tserkovnyak, *Europhys. Lett.* **97**, 67002 (2012).
- [17] A. A. Kovalev, *Phys. Rev. B* **89**, 241101 (2014).
- [18] X. S. Wang and X. R. Wang, *Phys. Rev. B* **90**, 014414 (2014).
- [19] F. Schlickeiser, U. Ritzmann, D. Hinzke, and U. Nowak, *Phys. Rev. Lett.* **113**, 097201 (2014).
- [20] P. Yan, Y. Cao, and J. Sinova, *Phys. Rev. B* **92**, 100408 (2015).
- [21] S. Moretti, V. Raposo, E. Martinez, and L. Lopez-Diaz, *Phys. Rev. B* **95**, 064419 (2017).
- [22] N. L. Schryer and L. R. Walker, *J. Appl. Phys.* **45**, 5406 (1974).
- [23] O. A. Tretiakov, D. Clarke, G.-W. Chern, Y. B. Bazaliy, and O. Tchernyshyov, *Phys. Rev. Lett.* **100**, 127204 (2008).
- [24] E. G. Tveten, A. Qaiumzadeh, and A. Brataas, *Phys. Rev. Lett.* **112**, 147204 (2014).
- [25] B. A. Kalinikos, *Sov. Phys. J.* **24**, 718 (1981).
- [26] P. Gruszecki, M. Kasprzak, A. E. Serebryannikov, M. Krawczyk, and W. Śmigaj, *Sci. Rep.* **6**, 22367 (2016).
- [27] H. S. Körner, J. Stigloher, and C. H. Back, *Phys. Rev. B* **96**, 100401 (2017).
- [28] M. Fazlali, M. Dvornik, E. Iacocca, P. Dürrenfeld, M. Haidar, J. Åkerman, and R. K. Dumas, *Phys. Rev. B* **93**, 134427 (2016).
- [29] N. J. Whitehead, S. A. R. Horsley, T. G. Philbin, A. N. Kuchko, and V. V. Kruglyak, *Phys. Rev. B* **96**, 064415 (2017).
- [30] L. D. Landau and E. M. Lifshitz, *Phys. Z. Sowjetunion* **8**, 153 (1935); *Ukr. J. Phys.* **53**, 14 (2008).
- [31] T. Gilbert, *IEEE Trans. Magn.* **40**, 3443 (2004).
- [32] J. Shibata, G. Tatara, and H. Kohno, *J. Phys. D: Appl. Phys.* **44**, 384004 (2011).
- [33] C. Bayer, H. Schultheiss, B. Hillebrands, and R. Stamps, *IEEE Trans. Magn.* **41**, 3094 (2005).
- [34] G. Pöschl and E. Teller, *Z. Phys.* **83**, 143 (1933).
- [35] A. A. Thiele, *Phys. Rev. B* **7**, 391 (1973).
- [36] J. Lekner, *Am. J. Phys.* **75**, 1151 (2007).
- [37] S.-M. Seo, K.-J. Lee, H. Yang, and T. Ono, *Phys. Rev. Lett.* **102**, 147202 (2009).
- [38] I. S. Gradshteyn and I. M. Ryzhik, *Table of Integrals, Series, and Products*, 8th ed., edited by D. Zwillinger and V. Moll (Academic Press, Waltham, MA, 2015).
- [39] G. Beach, M. Tsoi, and J. Erskine, *J. Magn. Magn. Mater.* **320**, 1272 (2008).
- [40] M. L. Boas, *Mathematical Methods in the Physical Sciences*, 3rd ed. (John Wiley & Sons, Hoboken, NJ, 2006).
- [41] P. Yan and G. E. W. Bauer, *IEEE Trans. Magn.* **49**, 3109 (2013).
- [42] G. A. Melkov and D. V. Slobodianiuk, *Ukr. J. Phys.* **58**, 189 (2013).
- [43] V. E. Demidov, H. Ulrichs, S. O. Demokritov, and S. Urazhdin, *Phys. Rev. B* **83**, 020404 (2011).
- [44] A. Heck, *Introduction to Maple*, 3rd ed. (Springer Science+Business Media, New York, NY, 2003).

IV

Reference

V. Risinggård, I. Kulagina, J. Linder.
Electric field control of magnon-induced magnetization dynamics
in multiferroics.
Scientific Reports **6**, 31800 (2016).
10/f8zhsc


Contributions

JL and IK conceived the study. IK carried out the preliminary investigation of current- and magnon-induced magnetization dynamics, and found that the domain wall velocity could be controlled with an applied electric field. VR limited the scope of the project to magnon-induced dynamics. VR derived the electric polarization due to spin waves in a homogeneous magnet; conceived of a physical mechanism to explain this result; and identified suitable materials and proposed an experimental setup. VR independently reproduced the electric-field dependence of the domain-wall velocity and conceived of a physical mechanism to explain this result. JL supervised the project. VR wrote the manuscript. All authors commented on the final version of the manuscript.

Comments

This work was presented at the 2016 APS March Meeting, session V6.1 (Baltimore, MD, USA).

SCIENTIFIC REPORTS



OPEN

Electric field control of magnon-induced magnetization dynamics in multiferroics

Vetle Risinggård^{*}, Iryna Kulagina[†] & Jacob Linder

Received: 31 May 2016

Accepted: 25 July 2016

Published: 24 August 2016

We consider theoretically the effect of an inhomogeneous magnetoelectric coupling on the magnon-induced dynamics of a ferromagnet. The magnon-mediated magnetoelectric torque affects both the homogeneous magnetization and magnon-driven domain wall motion. In the domains, we predict a reorientation of the magnetization, controllable by the applied electric field, which is almost an order of magnitude larger than that observed in other physical systems via the same mechanism. The applied electric field can also be used to tune the domain wall speed and direction of motion in a linear fashion, producing domain wall velocities several times the zero field velocity. These results show that multiferroic systems offer a promising arena to achieve low-dissipation magnetization rotation and domain wall motion by exciting spin-waves.

Multiferroic materials are materials that exhibit simultaneously two or more ferroic order parameters (ferroelectric, (anti)ferromagnetic, ferroelastic and ferrotoroidic order)¹. The term *multiferroics* has also been used more generally to refer to materials that exhibit a magnetoelectric coupling—that is, materials with a free energy functional that contains terms dependent on both the magnetization and the polarization^{2–4}.

If the cross-terms in the free energy only depend on the magnetization itself—and not its derivatives—the material is said to exhibit the homogeneous magnetoelectric effect. The first detailed investigation of this effect was made by Dzyaloshinskii⁵ for Cr₂O₃. An essential aspect of the homogeneous magnetoelectric effect is that an effect that is first order in both the polarization and the magnetization (linear magnetoelectric effect) cannot occur in materials where the free energy has time-reversal and spatial inversion symmetry⁶.

If the cross-terms in the free energy depend on the gradient of the magnetization, the material is said to exhibit the inhomogeneous magnetoelectric effect, or the flexoelectric effect. The existence of this effect was first pointed out by Bar'yakhtar *et al.*⁷. The inhomogeneous magnetoelectric effect can be present even in inversion symmetric systems. The study of the inhomogeneous magnetoelectric effect has seen a revival after the work of Mostovoy⁸ on the rare earth manganites. Several authors have contributed to an extension of these results to the dynamic regime^{9–16}.

In this work, we determine how the magnetization dynamics of multiferroic materials are influenced by injecting spin-waves. Magnon spintronics is an emerging subfield of the field of spintronics which applies spin-waves for information transport and processing^{17,18}. By carrying spin currents using magnons rather than electrons, large scale charge transport and the associated Joule heating is avoided. Magnons can propagate over centimeter distances in low-damping magnetic insulators¹⁹, while spin-currents carried by electrons are limited by the spin-diffusion length, which is on the order of microns. Magnons also offer exciting possibilities exploiting wave-based and nonlinear phenomena, such as the majority gate^{20–22} and parallel computing²³.

One of the principal advantages of magnon spintronics is the wide variety of available magnetic materials and interactions, and the large number of other magnetic excitations such as domain walls, vortices and skyrmions. For instance, there are obvious opportunities for creating nonvolatile memories based on magnons interacting with domain walls^{24,25} or skyrmions^{26,27}. The properties of such systems can be tuned by exploiting higher order magnetic interactions such as the Dzyaloshinskii–Moriya interaction (DMI)^{28,29}, not to mention magnon band structure engineering in magnonic crystals¹⁸.

We will first consider the effect of an inhomogeneous magnetoelectric coupling on magnetization dynamics induced by magnon injection. We demonstrate analytically and numerically that this term produces a reorientation of the time-averaged magnetization, see Fig. 1. A similar reorientation has been identified previously by

NTNU, Norwegian University of Science and Technology, Department of Physics, N-7491 Trondheim, Norway.

^{*}These authors contributed equally to this work. Correspondence and requests for materials should be addressed to V.R. (email: vetle.m.risinggard@ntnu.no)

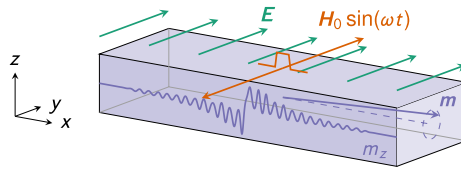


Figure 1. Magnetization reorientation by the magnon-mediated magnetoelectric torque. When an electric field is applied to a homogeneously magnetized sample, nothing happens. When a magnetic inhomogeneity is introduced in the form of spin-waves, the interaction between the applied electric field and the induced electric polarization produces a shift in the time-averaged magnetization that is linear in the applied electric field.

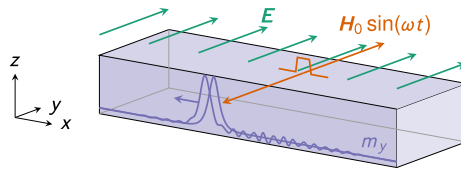


Figure 2. Controlling the domain wall velocity by the magnon-mediated magnetoelectric torque. In the absence of an applied electric field, the magnetic domain wall travels towards the spin-wave source. The magnitude of the velocity is determined by the spin-wave excitation amplitude, the distance from the source and the spin-wave frequency. By application of an electric field the domain wall can be made to stop and change direction of motion. The velocity of the domain wall is linear in the electric field.

Manchon *et al.*³⁰ for a Dzyaloshinskii–Moriya ferromagnet and by Linder³¹ for a topological insulator–ferromagnet heterostructure. Unlike these previous results, the magnitude and direction of the reorientation of the magnetization that is due to the inhomogeneous magnetoelectric effect is controllable by the applied electric field; not fixed by the material constants. Moreover, the effect is quantitatively much larger than in the Dzyaloshinskii–Moriya case.

Second, we determine how the inhomogeneous magnetoelectric effect alters magnetic domain wall motion. The case of magnetic field-driven domain wall motion has been considered previously by Chen *et al.*³², whereas Dzyaloshinskii³³ and Logginov *et al.*^{34,35} have considered domain wall motion driven by an inhomogeneous electric field. Magnon-induced domain wall motion in ordinary ferromagnets was first considered by Mikhailov and Yaremchuk³⁶, and more recently by Yan *et al.*²⁴ who showed that conservation of angular momentum will drive the domain wall towards the spin-wave source. In response to puzzling numerical results showing domain wall motion away from the spin-wave source, Yan *et al.*³⁷ have developed a theory of linear momentum transfer from spin-waves to domain walls. Linear momentum transfer has later been used to explain the dependence of the direction of domain wall motion in Dzyaloshinskii–Moriya ferromagnets on the sign of the material dependent DMI constant³⁸. Interestingly, we find that for magnon-induced domain wall motion the inhomogeneous magnetoelectric effect enables electric field control of both the sign and magnitude of the domain wall velocity, see Fig. 2. The domain wall velocity scales linearly with the applied electric field.

Magnon-induced dynamics in homogeneously magnetized multiferroics

As shown in Fig. 1, we consider a ferromagnetic wire that exhibits the inhomogeneous magnetoelectric effect. In the continuum limit, the magnetization can be described by a vector field $\mathbf{m}(\mathbf{r}, t)$. The free energy of this system can be written as

$$F[\mathbf{m}] = \frac{A}{m^2} \int [(\nabla m_x)^2 + (\nabla m_y)^2 + (\nabla m_z)^2] d\mathbf{r} - m^{-2} \int (K m_x^2 - K_{\perp} m_z^2) d\mathbf{r} - \int (\mathbf{E} \cdot \mathbf{P}) d\mathbf{r}. \quad (1)$$

Here, A is the exchange stiffness, m is the saturation magnetization, K is the easy axis anisotropy constant and K_{\perp} is the hard axis anisotropy constant. The easy axis of magnetization is taken to be along the length of the wire and is dominated by shape anisotropy. If the wire cross-section is not circular, the shape anisotropy will also contribute a perpendicular hard axis anisotropy. The effective constant K_{\perp} can also contain contributions from magnetocrystalline anisotropy. The final term is the inhomogeneous magnetoelectric interaction⁸. \mathbf{E} is the applied electric field and \mathbf{P} is the induced electric polarization⁸,

$$\mathbf{P} = \gamma_0 [\mathbf{m}(\nabla \cdot \mathbf{m}) - (\mathbf{m} \cdot \nabla) \mathbf{m}]. \quad (2)$$

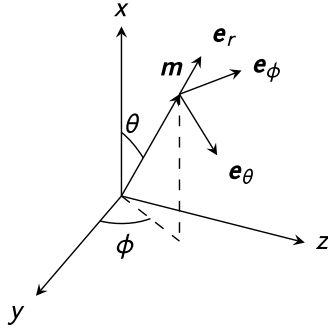


Figure 3. For the spin-wave perturbation theory the magnetization is most conveniently written out in a spherical coordinate system. When the magnetization is homogeneous, θ and ϕ are assumed to be independent of position and time. In the case of a domain wall our objective is to consider the *dynamic* response of a *nonuniform* magnetization texture. Consequently, θ and ϕ must be position- and time-dependent.

γ_0 is the inhomogeneous magnetoelectric coupling constant.

We describe the time dynamics of the magnetization using the Landau–Lifshitz–Gilbert (LLG) equation^{39–41},

$$\partial_t \mathbf{m} = \gamma \mathbf{m} \times \mathbf{H} - \frac{\alpha}{m} \mathbf{m} \times \partial_t \mathbf{m}, \quad (3)$$

where $\mathbf{H}(\mathbf{r}, t)$ is the effective magnetic field acting on the magnetization, γ is the gyromagnetic ratio and α is the Gilbert damping parameter. We assume that $\gamma < 0$ and $\alpha < 0$. The effective magnetic field is given by the functional derivative of the free energy with respect to the magnetization, $\mathbf{H} = -\delta F / \delta \mathbf{m}$. This gives rise to the effective field

$$\mathbf{H} = \frac{2A}{m^2} \nabla^2 \mathbf{m} + \frac{2K}{m^2} m_x \mathbf{e}_x - \frac{2K_{\perp}}{m^2} m_z \mathbf{e}_z + 2\gamma_0 [(\nabla \cdot \mathbf{m}) \mathbf{E} - \nabla(\mathbf{E} \cdot \mathbf{m})], \quad (4)$$

where we have assumed that the electric field is independent of position.

Perturbation theory. We calculate the magnon-induced dynamics perturbatively by considering deviations from a homogeneous magnetization parametrized in the small excitation parameter h . For this purpose the magnetization is most conveniently written out in a spherical frame as shown in Fig. 3. To second order in h the magnetization is⁴²

$$\begin{aligned} \mathbf{m}(\mathbf{r}, t) &= \left(m - h^2 [s_{\theta}^{(2)}(\mathbf{r}, t) + s_{\phi}^{(2)}(\mathbf{r}, t)] \right) \mathbf{e}_r + [hs_{\theta}^{(1)}(\mathbf{r}, t) + h^2 \Delta m_{\theta}(\mathbf{r})] \mathbf{e}_{\theta} \\ &\quad + [hs_{\phi}^{(1)}(\mathbf{r}, t) + h^2 \Delta m_{\phi}(\mathbf{r})] \mathbf{e}_{\phi} \\ &= \left(m - \frac{h^2}{2m} [s_{\theta}^2(\mathbf{r}, t) + s_{\phi}^2(\mathbf{r}, t)] \right) \mathbf{e}_r + [hs_{\theta}(\mathbf{r}, t) + h^2 \Delta m_{\theta}(\mathbf{r})] \mathbf{e}_{\theta} \\ &\quad + [hs_{\phi}(\mathbf{r}, t) + h^2 \Delta m_{\phi}(\mathbf{r})] \mathbf{e}_{\phi}. \end{aligned} \quad (5)$$

$s_{\theta/\phi}^{(1)/(2)}(\mathbf{r}, t)$ is the first (second) order spin-wave excitations in the θ - (ϕ)-direction. For small h the linear terms dominate, reproducing the usual spin-wave expansion²⁴. The second order excitations take into account the fact that the magnetization along the r -direction is reduced for stronger excitation³⁰. $\Delta m_{\theta/\phi}(\mathbf{r})$ correspond to a steady-state reorientation of the magnetization that might be induced by the spin-waves. Since spin-waves in an ordinary ferromagnet do not induce such deviations, these deviations must be of second order in h or higher³⁰. The second equality follows from the micromagnetic normalization criterion $\mathbf{m} \cdot \mathbf{m} = m^2$ and is accurate to second order in h . For ease of notation, we have written $s_{\theta/\phi}^{(1)}(\mathbf{r}, t) = s_{\theta/\phi}(\mathbf{r}, t)$.

Static magnetization. For simplicity, we assume that our system is one-dimensional so that $\nabla = \partial_x \mathbf{e}_x$ and $\nabla^2 = \partial_x^2$. We consider now in turn the equations of our perturbation theory. By inserting the *ansatz* (5) into the LLG equation (3) using the effective field (4) we get two nontrivial equations to zeroth order,

$$\begin{aligned} 2\gamma K_{\perp} \sin \theta \cos \phi \sin \phi &= 0, \\ 2\gamma \cos \theta \sin \theta (K + K_{\perp} \sin^2 \phi) &= 0. \end{aligned}$$

These are the θ - and the ϕ - component, respectively. The zeroth order equations give the static magnetization direction. We see that one solution is to set both angles to zero, $\theta = 0$ and $\phi = 0$. This solution is unchanged by adding an integer multiple of π to either angle.

Spin-wave amplitudes. As in any perturbation theory⁴³, the first and higher order equations vanish identically when the excitation parameter h goes to zero. Thus, $h \rightarrow 0$ leaves us with the static problem. For first and higher orders of the perturbation theory the excitation parameter h is merely a convenient accounting device and can be treated as $h \rightarrow 1$. To first order in h we once more get two nontrivial equations corresponding to the θ - and ϕ -components,

$$\partial_t s_\theta = -\frac{2\gamma}{m} \left(A \partial_x^2 - K - K_\perp - \frac{m\alpha}{2\gamma} \partial_t \right) s_\phi, \tag{6}$$

$$\partial_t s_\phi = +\frac{2\gamma}{m} \left(A \partial_x^2 - K - \frac{m\alpha}{2\gamma} \partial_t \right) s_\theta. \tag{7}$$

To solve these equations we make the assumption that the time-dependence is purely harmonic, $s_{\theta/\phi}(x, t) = s_{\theta/\phi}(x) \times \exp(-i\omega t)$. Equations (6) and (7) can be recast into one single equation by introducing the auxiliary variable $\psi(x) = s_\theta(x) + i c s_\phi(x)$. We multiply equation (6) by ic and subtract equation (7). By requiring that the coefficient of s_ϕ is ic times that of s_θ we get a second order equation in c . Solving this equation we find that $c = -[\gamma K_\perp \pm (\gamma^2 K_\perp^2 + m^2 \omega^2)^{1/2}] / m\omega$. Although both signs are allowed mathematically, we must choose the one that makes sense physically. By choosing the minus sign we get real wave numbers in the intermediate steps leading up to the dispersion relation in equation (10). Thus, keeping to this choice we find the equation

$$\frac{2\gamma A}{m} \partial_x^2 \psi = \frac{\gamma}{m} \left(2K + K_\perp - \gamma^{-1} \sqrt{\gamma^2 K_\perp^2 + m^2 \omega^2} - im\alpha\omega/\gamma \right) \psi \tag{8}$$

for $\psi(x)$. This equation is solved by the *ansatz* that $\psi(x)$ is a damped harmonic, $\psi(x) = \rho \exp(ikx) \exp(-\eta x/\Gamma)$. Here, ρ is the amplitude of the excited spin-waves at the spin-wave source; $\eta = \text{sgn}(x)$, and by choosing $k > 0$ we ensure that ψ represents damped waves traveling away from a source at the origin. If we substitute our *ansatz* for ψ back into equation (8) and separate the real and imaginary part we find expressions for the damping length⁴⁴

$$\Gamma = \frac{4\gamma Ak}{m\alpha\omega} \tag{9}$$

and for the dispersion relation²⁴

$$\omega^2 = \frac{4\gamma^2}{m^2} (Ak^2 + K + K_\perp)(Ak^2 + K). \tag{10}$$

The dispersion relation we have obtained is the usual dispersion relation for an ordinary ferromagnet. We do not observe the linear shift reported by Mills and Dzyaloshinskii¹³ because the spin-wave propagation direction is parallel to the direction of the static magnetization. We make further comments on the case where the wave vector, the applied electric field and the static magnetization are mutually orthogonal at the end of this section.

Having obtained a solution for ψ we need a second condition to solve for the spin-wave components. A reasonable condition is that they should be real, which gives

$$s_\theta(x, t) = +\rho \cos(kx - \omega t) \exp(-\eta x/\Gamma), \tag{11}$$

$$s_\phi(x, t) = -\frac{\rho m\omega \sin(kx - \omega t) \exp(-\eta x/\Gamma)}{\gamma K_\perp - \sqrt{\gamma^2 K_\perp^2 + m^2 \omega^2}}. \tag{12}$$

Magnetization reorientation. Only the θ - and the ϕ -components contribute nontrivial equations to second order in h ,

$$\frac{2\gamma}{m} \left(A \frac{d^2}{dx^2} - K \right) \Delta m_\theta = 2\gamma\gamma_0 (E_y s_\phi \partial_x s_\phi - E_z s_\theta \partial_x s_\phi) \tag{13}$$

$$\frac{2\gamma}{m} \left(A \frac{d^2}{dx^2} - K - K_\perp \right) \Delta m_\phi = 2\gamma\gamma_0 (E_z s_\theta \partial_x s_\theta - E_y s_\phi \partial_x s_\theta) \tag{14}$$

As we have already obtained expressions for the spin-wave components from the first order equations, these are ordinary differential equations on Δm_θ and Δm_ϕ . By assumption, these are time-independent and we remove

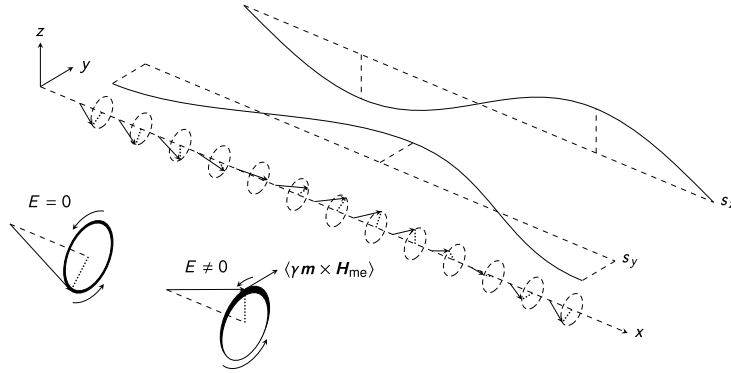


Figure 4. A spin-wave in a homogeneously magnetized sample. In the inset (down left) the weight of the stroke in the circle indicates the average time spent in that part of the circle over one period.

the time-dependence from the right-hand side by averaging over one spin-wave period $2\pi/\omega$. The fact that the spin-waves are exponentially damped provides us with the boundary conditions $\lim_{x \rightarrow \pm\infty} \Delta m_{\theta\phi}(x) = 0$. The resulting solutions are

$$\Delta m_y(x) = - \frac{\eta \rho^2 m^2 \omega \Gamma \gamma_0 [E_z (Ak^2 + K) \Gamma k + E_y m \omega / 2\gamma]}{4\gamma K_{\perp} (m^2 \omega^2 / 4\gamma^2 K_{\perp} - Ak^2 - K) (4A - \Gamma^2 K)}, \quad (15)$$

$$\Delta m_z(x) = - \frac{\eta \rho^2 m^2 \omega \Gamma \gamma_0 [E_z (Ak^2 + K) / m \omega - E_y \Gamma k / 2\gamma]}{(Ak^2 + K) (4A - \Gamma^2 (K + K_{\perp}))}, \quad (16)$$

where we have switched to Cartesian coordinates for clarity.

This demonstrates the existence of a magnon-mediated magnetoelectric torque acting on the homogeneous magnetization. Within the limits of validity of a perturbative theory, the magnitude of this torque scales linearly with the applied electric field. Its direction is controlled by the direction of the applied field. In the absence of a perpendicular anisotropy the relative magnitude of the two reorientation components is

$$\frac{\Delta m_y}{\Delta m_z} = - \frac{E_y + E_z \Gamma k}{E_y \Gamma k - E_z}$$

For relevant damping lengths and wave numbers Δm_z dominates Δm_y by a factor of $\sim 10^6$ when the electric field is applied in the y -direction and *vice versa* when the electric field is applied in the z -direction.

Induced polarization. The induced time-averaged electric polarization is directly proportional to the reorientation of the magnetization

$$\mathbf{P} = \frac{2\eta m \gamma_0}{\Gamma} \Delta \mathbf{m}. \quad (17)$$

However, while the reorientation of the magnetization changes sign at the origin (position of the source), the polarization does not due to the extra factor of $\eta = \text{sgn}(x)$.

Although the polarization is directly proportional to the magnetization reorientation, their behavior in the limit $\alpha \rightarrow 0$ differs due to the extra factor of $1/\Gamma$. In the limit where the damping is large ($\alpha \rightarrow \infty$ and $\Gamma \rightarrow 0$) all dynamics is quenched, and both $\Delta \mathbf{m}$ and \mathbf{P} go to zero. However, in the limit where there is no damping ($\alpha \rightarrow 0$ and $\Gamma \rightarrow \infty$) the time-averaged polarization goes to zero, as pointed out by Mostovoy⁸, but we still observe a finite magnetization reorientation.

Simplified mechanism. The simplest possible system that exhibits a magnon-mediated magnetoelectric torque is a homogeneously magnetized sample. The spin-wave propagation in this system is illustrated by the dampingless spin-chain in Fig. 4. Writing the magnetization of this chain as $\mathbf{m}(x, t) = m\mathbf{e}_x + s_y(x, t)\mathbf{e}_y + s_z(x, t)\mathbf{e}_z$ we get a contribution

$$\mathbf{H}_{me} = 2\gamma_0 E (\partial_x m \mathbf{e}_y - \partial_x s_y \mathbf{e}_x) = -2\gamma_0 E \partial_x s_y \mathbf{e}_x$$

Parameter	Value	Unit
Gyromagnetic ratio, γ	-26	GHz/T
Magnetization, m	6	kA/m
Exchange stiffness, A	5	pJ/m
Easy axis anisotropy, K	0.5	kJ/m ³
Gilbert damping parameter, α	-0.05	1
Inhomogeneous magnetoelectric coupling, γ_0	0.1	psm/A

Table 1. Material constants used in the numerical solution of the LLG equation. These values correspond to the iron garnets (BiR)₃(FeGa)₅O₁₂ (R = Lu, Tm) considered by Logginov *et al.*^{34,35}.

to the effective field from the inhomogeneous magnetoelectric effect when $\mathbf{E} = E\mathbf{e}_y$. If this contribution to the effective field had been constant on the time-scale of the spin-waves, it would only have changed the precession frequency. However, it is not. The torque exerted on the magnetization is

$$\gamma \mathbf{m} \times \mathbf{H}_{\text{me}} = 2\gamma\gamma_0 E (s_y \partial_x s_y \mathbf{e}_z - s_z \partial_x s_y \mathbf{e}_y).$$

When averaging over one oscillation period the z -component vanishes; thus, the magnetization experiences a net torque in the positive y -direction ($\gamma < 0$),

$$\langle \gamma \mathbf{m} \times \mathbf{H}_{\text{me}} \rangle = -2\gamma\gamma_0 E \langle s_z \partial_x s_y \rangle \mathbf{e}_y. \quad (18)$$

As illustrated in the inset of Fig. 4, this torque opposes the precession of the spin when it moves in the negative y -direction and boosts the precession of the spin when it moves in the positive y -direction. When the spins precess in the counterclockwise direction, $s_z > 0$ in the half-period where the spins are slowed by the magnetoelectric torque and $s_z < 0$ in the half-period where the spins are accelerated by the magnetoelectric torque. If we average over one period, the spins spend more time having $s_z > 0$ than $s_z < 0$, so the end result is that the system has acquired a net magnetic moment in the positive z -direction.

This mechanism can also be used to explain the results of Manchon *et al.*³⁰ and Linder³¹, as is easily seen by repeating the calculation above using the effective fields employed in these papers. As such, it represents a unifying framework for magnon-mediated torques on the homogeneous magnetization. In particular, it identifies the following criterion for a system to exhibit similar magnon-mediated torques: That the effective field should contain a gradient of one of the transverse magnetization components.

Upon introducing the expansion (5) of the magnetization in h , we stated that the reorientations of the magnetization $\Delta m_{\theta/\phi}(\mathbf{r})$ are of second order in h or higher since spin-waves in an ordinary ferromagnet do not induce such deviations. The fact that equation (18) is second order in the spin-wave amplitudes provides justification that $\Delta m_{\theta/\phi}(\mathbf{r})$ are in fact exactly of second order.

Full numerical solution. To get further insight into the properties of the magnon-mediated magnetoelectric torque we solve the LLG equation numerically using an adaptive centered implicit scheme for time and space discretization in Maple⁴⁵. We use the effective field given in equation (4) and material constants corresponding to the iron garnets (BiR)₃(FeGa)₅O₁₂ (R = Lu, Tm) considered by Logginov *et al.*^{34,35}, see Table 1. We solve the system on a grid that is 8 μm long at grid-points spaced 4 nm apart. The system is initially homogeneously magnetized in the x -direction. Spin-waves are excited by applying a magnetic field $\mathbf{H}(t) = H_0 \sin(2\pi f t) \mathbf{e}_y$ to 24 grid-points at either side of the origin. The excitation amplitude is $H_0 = 0.2$ T and the excitation frequency is kept at 5 GHz. To avoid spin-wave reflection at the sample ends, we implement absorbing boundary conditions by increasing the Gilbert damping to $|\alpha| = 1$ inside 1 μm wide regions at either end of the sample⁴⁴. The electric field is applied in the y -direction, $\mathbf{E} = E\mathbf{e}_y$, and we set the perpendicular anisotropy to zero.

Figure 5(a) illustrates the symmetry of the effect. These steady-state magnetization profiles have been obtained for an applied electric field of ± 1.5 V/cm. As can also be seen from equation (16) the sign of the torque is determined by the propagation direction of the spin-waves, thus the resulting magnetization is antisymmetric about the spin-wave source. The torque also scales linearly with the applied electric field, so switching the sign of the field switches the sign of the magnetization reorientation.

Figure 5(b) through Fig. 5(d) shows a plots of the time-averaged analytical expression (16) versus the corresponding numerical profile for three different field values. The perturbation theory successfully predicts the magnitude and spatial decay of the torque. As can be seen from equation (16), the decay length of the magnetization reorientation is half that of the spin-waves as the reorientation is second order in h . The perturbative calculation predicts that the torque should scale linearly with the applied electrical field. Plotting the magnetization shift at a fixed position ($x = 0.25 \mu\text{m}$) as a function of the applied electrical field we indeed observe a linear field-dependence, see Fig. 5(e).

Comment on the linear shift of the dispersion. Mills and Dzyaloshinskii¹³ have pointed out that the inhomogeneous magnetoelectric effect will produce a shift of the spin-wave frequency with respect to that of an ordinary ferromagnet on the form

$$\Delta\omega = -C(\mathbf{E} \times \mathbf{M}_s) \cdot \mathbf{k}. \quad (19)$$

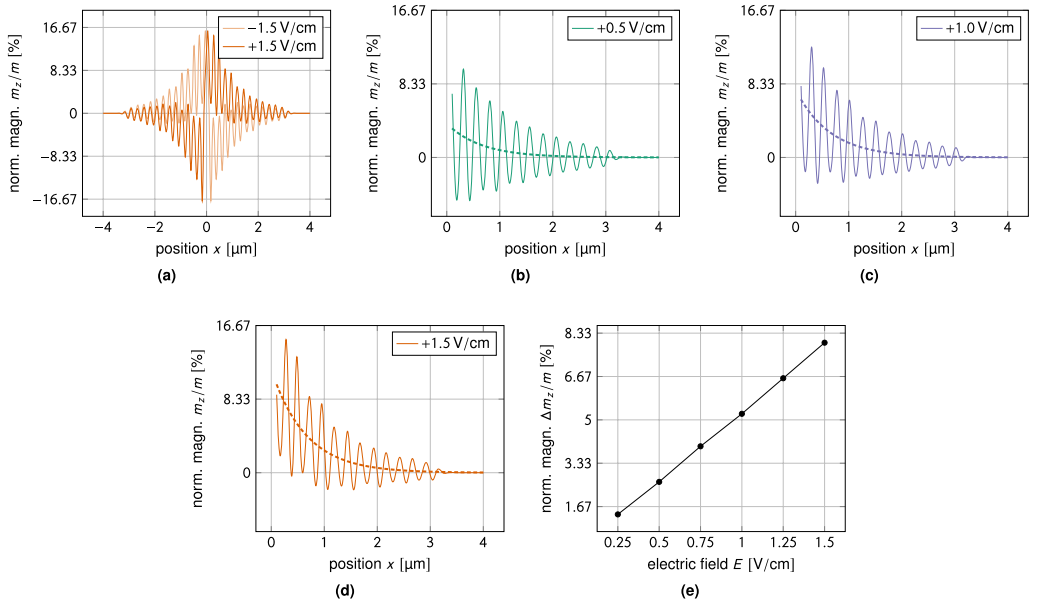


Figure 5. Numerical results for magnon-mediated magnetoelectric torque. When the electric field is applied in the y -direction the magnetization reorientation takes place in the z -direction. (a) Symmetry of the effect. Steady-state magnetization profiles obtained for $E = \pm 1.5$ V/cm. The sign of the torque is determined by the propagation direction of the spin-waves, thus the resulting magnetization is antisymmetric about the spin-wave source ($x = 0$). The torque also scales linearly with the applied electric field, so switching the sign of the field switches the sign of the magnetization reorientation. (b) through (d) Time-averaged analytical fit to the numerical profiles. The analytical theory successfully predicts the magnitude and spatial decay of the torque. The decay length of the spin-waves is twice that of the torque. (e) Linear dependence on applied field. Plotting the magnetization shift at a fixed position ($x = 0.25 \mu\text{m}$) as a function of the applied electrical field we observe a linear field-dependence.

Here E is the applied electric field, M_s is the saturation magnetization, k is the spin-wave wave vector and C is some positive constant. Liu and Vignale^{14,15} have established in a microscopic calculation that yttrium iron garnet (YIG; $\text{Y}_3\text{Fe}_5\text{O}_{12}$) hosts the inhomogeneous magnetoelectric effect and that the phase shift should be observable. This experiment was carried out by Zhang *et al.*¹⁶, showing good agreement between theory and experiment. In the notation of Liu and Vignale¹⁵ the constant C is written

$$C = \frac{|\gamma|eJ}{E_{\text{so}}},$$

where γ is the gyromagnetic ratio, e is the electron charge, $J = 1.6 \cdot 10^{-22} \text{ Jm/A}^2$ is the YIG exchange coupling and the energy $E_{\text{so}} = 4.8 \cdot 10^{-19} \text{ J}$ is inversely proportional to the strength of the YIG spin-orbit coupling.

In the notation of Mills and Dzyaloshinskii¹³, which is closer to our notation, the constant C can be written $C = -|\gamma|b$, where b is the inhomogeneous magnetoelectric coupling constant $b = b_1 + b_2$ used by Mills and Dzyaloshinskii. Thus, for YIG we can calculate $\gamma_0 = b_1 = b_2$ to be

$$\gamma_0 = \frac{eJ}{2E_{\text{so}}} = 2.7 \cdot 10^{-23} \text{ sm/A}.$$

While this value is large enough to produce a measurable spin-wave phase shift, it is far too small to produce a measurable reorientation of the time-averaged magnetization in YIG without exceeding the dielectric breakdown field. However, by turning this argument around, the difference of about ten orders of magnitude indicates that it should be possible to observe gigantic phase shifts if one were to redo the experiment of Zhang *et al.* using the iron garnets of Logginov *et al.*

Writing out the frequency shift as a triple product on the form of equation (19), as was done by Mills and Dzyaloshinskii¹³, emphasizes the importance of the experimental geometry in order to observe this effect. Such geometrical considerations will also be of importance for observing the magnetization reorientation, as is easily seen by repeating the perturbative calculation leading up to equations (15) and (16) for perpendicular m and k . In this geometry, which is the geometry of Liu and Vignale¹⁵ and of Zhang *et al.*¹⁶, no magnetization reorientation is observed.

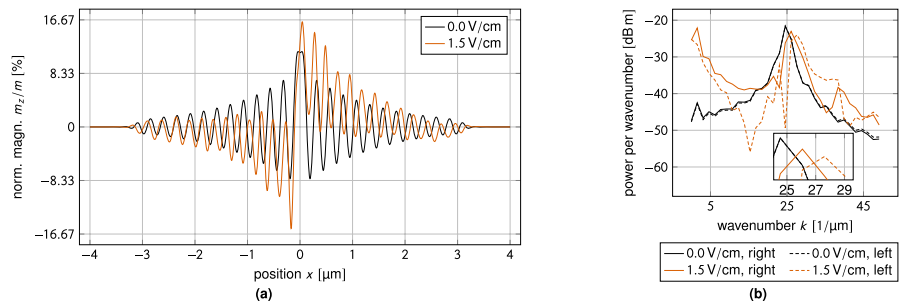


Figure 6. Higher order phase shift due to the magnon-mediated magnetoelectric torque. (a) Visibility of phase shift in magnetization profiles. Steady-state magnetization profiles obtained for $E = 1.5$ V/cm and in the absence of an applied electric field. A higher order correction of the ordinary ferromagnetic dispersion relation induces a phase shift when the electric field is applied. (b) Power spectral density of the magnetization profiles in (a) computed from the data to the right (left) of the source. In the presence of an applied electric field the power spectrum exhibits two peaks. The peak to the left is an artifact introduced by the magnetization reorientation. The one to the right—which corresponds to the spin-wave—is slightly displaced towards higher wavenumbers (smaller wavelengths) as compared to the zero field case.

Further insight can be gained by a closer inspection of the magnetization curves in Fig. 6(a). Here, an electric field-dependent phase shift can be observed which does not follow from the first order dispersion relation (10), but which is a higher order effect. This field-dependent difference in wavelength is easily recognized in the power spectrum shown in Fig. 6(b), which reveals an increase in wavenumber (decrease in wavelength) at $E = 1.5$ V/cm as compared to zero applied field.

Proposals for experiments. The effect we predict is dependent on a reasonable value for the inhomogeneous magnetoelectric coupling constant. One particular class of such materials are the rare earth manganites considered by Mostovoy⁸, which have a spiral magnetization. Another class of materials which potentially hosts the inhomogeneous magnetoelectric effect is the iron garnets studied by Logginov and co-workers^{34,35}, which admit a homogeneous magnetization. We have used material values corresponding to these garnets in the numerical part of this work. The mechanism behind the experimental observations of Logginov *et al.* is currently debated^{35,46}. Whether or not it turns out that these iron garnets host an inhomogeneous magnetoelectric effect is irrelevant to the main message in the present paper. We only use these compounds as an example.

In materials with the Dzyaloshinskii–Moriya interaction the crystal structure favors a canted spin structure^{28,29}. Sergienko and Dagotto^{3,47} have suggested how the inverse mechanism, a form of exchange striction, can give rise to the inhomogeneous magnetoelectric effect. This model is usually applied to large magnetic structures such as magnetic spirals and domain walls, which are on the energy scale of the demagnetization field. To carry this—or any other ionic displacement mechanism⁴⁸—over to weaker magnetic inhomogeneities such as spin-waves is not trivial. It is not obvious that a coupling constant measured using a domain wall³⁴ should be applicable to spin-waves, although that is what we assume by using these values.

To detect the magnon-mediated magnetoelectric torque we propose to either measure the magnetization reorientation directly or to measure the induced polarization. As pointed out previously, the reorientation scales linearly as a function of the electric field and decays exponentially away from the source. Using the example values from Fig. 5(e), a reorientation on the order of 480 A/m should be unproblematic at a distance of $0.25 \mu\text{m}$ away from the source for an applied electric field of 1.5 V/cm. Polar MOKE (magneto-optic Kerr effect) techniques have previously been successfully applied to measure magnetization reorientations on the order of 56 A/m by Fan *et al.*⁴⁹ during their study of the spin-orbit torque. As pointed out in the previous section, the wave vector of the spin-waves must be parallel to the saturation magnetization to observe the magnetization reorientation due to the magnetoelectric torque. An experimental set-up must then use the less sensitive longitudinal MOKE⁵⁰, as illustrated in Fig. 7. However, the effect should still be within the reach of current experimental techniques.

The second possibility is to measure the induced polarization. When averaging over the period of oscillation of the spin-waves, we find that the time-averaged polarization is proportional to the induced magnetization shift, see equation (17). For the material values we have considered, a reorientation of 480 A/m corresponds to a time-averaged polarization on the order of $40 \mu\text{C}/\text{cm}^2$. To measure the polarization, the MOKE laser in Fig. 7 would have to be replaced by localized electrodes on the top and on the bottom of the structure.

Magnon-induced domain wall motion in a multiferroic

As shown in Fig. 2, we consider the same ferromagnetic wire as in the previous section, but assume now that it contains a Néel domain wall. (Bloch domain walls induce no electric polarization and are immune to magnetoelectric effects^{7,8}).

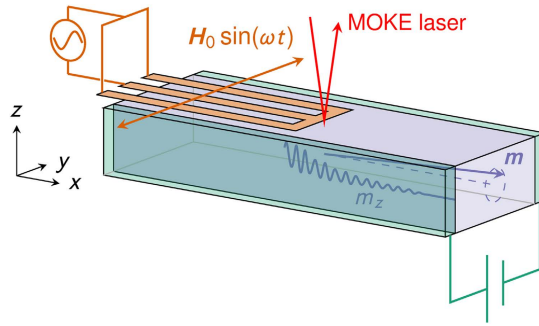


Figure 7. Longitudinal MOKE measurement of the magnetization reorientation. Spin-waves are injected using a coplanar waveguide as used in PSWS (propagating spin-wave spectroscopy^{56,57}) and the electric field is generated by a parallel plate capacitor. The magnetization reorientation decays exponentially away from the spin-wave source, but scales linearly with the applied electric field.

Perturbation theory. We first perform analytical calculations for the magnon-induced domain wall dynamics using a perturbation theory, completely analogous to what we did for the homogeneously magnetized ferromagnet. However, this time we let the angles θ and ϕ from Fig. 3 be time- and position-dependent.

Static magnetization. Just as before, we obtain the equations of our perturbation theory by inserting the *ansatz* (5) into the LLG equation (3) using the effective field (4). To zeroth order in h there is no time-dependence in the problem, and we obtain two nontrivial equations,

$$A\partial_x^2\theta = \cos\theta \sin\theta(K + K_{\perp} \sin^2\phi), \quad (20)$$

$$\gamma_0 E_y(\partial_x\theta) \sin\phi - \gamma_0 E_z(\partial_x\theta) \cos\phi - \frac{2K_{\perp}}{m} \cos\phi \sin\phi = 0. \quad (21)$$

Equation (20) gives us the well known Walker domain wall profile⁵¹ for θ . Thus, the ground state of the system is a head-to-head or a tail-to-tail Néel wall. For $\phi = n\pi$, $n = 0, 1, 2, \dots$, which minimizes the perpendicular anisotropy energy, equation (21) demands that $E_z = 0$, that is, no electric field component along the hard axis. For $K_{\perp} = 0$ equation (21) can be solved to give $\phi = n\pi + \arctan(E_z/E_y)$, $n = 0, 1, 2, \dots$. We conclude that unless the electric field is applied perpendicular to the hard axis, the inhomogeneous magnetoelectric torque and the perpendicular anisotropy torque will compete. For simplicity, we set $K_{\perp} \equiv 0$ and $E_z \equiv 0$ in the remainder of this section.

Spin-wave amplitudes. Assuming that the domain wall position $X(t)$ is second order in h^2 , we obtain two nontrivial equations to first order in h ,

$$\partial_t s_{\theta} = -\frac{2\gamma}{m} \left[A\partial_x^2 + K[1 - 2\cos^2\theta] + \frac{(-1)^n \gamma_0 E_y m^2}{\lambda} \sin\theta - \frac{m\alpha}{2\gamma} \partial_t \right] s_{\phi}, \quad (22)$$

$$\partial_t s_{\phi} = +\frac{2\gamma}{m} \left[A\partial_x^2 + K[1 - 2\cos^2\theta] - \frac{m\alpha}{2\gamma} \partial_t \right] s_{\theta}. \quad (23)$$

We can get rid of the angle θ using the identities $\sin\theta = \text{sech}\xi$ and $\cos\theta = \tanh\xi$ which are valid for a Walker domain wall⁵². Here, $\xi = [x - X(t)]/\lambda$ and $\lambda = \sqrt{A/K}$ is the domain wall width. Using the same trick as before, we can recast these two equations into one equation by introducing the auxiliary variable $\psi(x) = s_{\theta}(x) + i c s_{\phi}(x)$. However, this time we find that $c = \text{sech}\xi \left[(-1)^n \gamma_0 E_y m \pm (\gamma^2 \gamma_0^2 E_y^2 m^2 + \lambda^2 \omega^2 \cosh^2 \xi)^{1/2} \right] / \lambda \omega$ and that

$$\begin{aligned} \frac{2\gamma K}{m} \partial_{\xi}^2 \psi &= \frac{\gamma}{m} \left[2K[1 - 2\text{sech}^2 \xi] - \frac{(-1)^n \gamma_0 E_y m^2}{\lambda} \text{sech}\xi \right. \\ &\quad \left. \pm \frac{m}{\gamma \lambda} \text{sech}\xi \sqrt{\gamma^2 \gamma_0^2 E_y^2 m^2 + \lambda^2 \omega^2 \cosh^2 \xi} \right] \psi. \end{aligned} \quad (24)$$

This is a Schrödinger-like equation, but in the presence of an electric field the potential deviates from the reflectionless potential of Yan *et al.*²⁴. The equation is even in ξ , so there is no dependence on the topological charge of the wall. However, the factor $(-1)^n$ ($n = 0, 1, 2, \dots$) reveals that the potential is chirality-dependent. Chirality dependence was also observed for domain wall motion driven by a magnetic field by Chen *et al.*³².

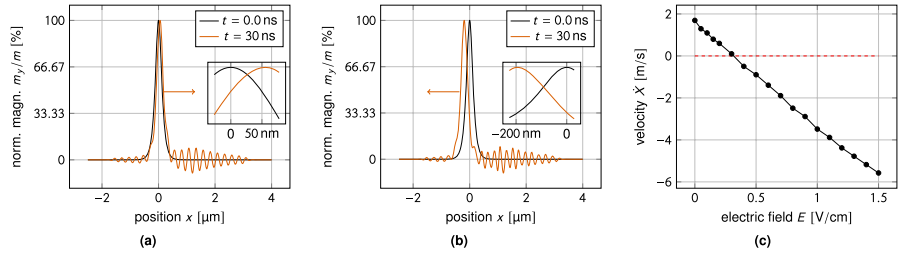


Figure 8. Numerical results for electric field-controlled domain wall motion in a multiferroic. The applied electric field can control both the direction and the velocity of the domain wall. (a) Zero applied field. In the absence of an applied electric field the domain wall moves towards the spin-wave source to conserve angular momentum. (b) Applied electric field. With an applied electric field the domain wall can be made to move away from the spin-wave source. (c) Linear dependence of the domain wall velocity on the applied electric field. The domain wall velocity is a linear function of the applied electric field. For some critical field the domain wall stops and its direction of motion is reversed.

Full numerical solution. The complicated potential in equation (24) makes it difficult to continue the analytical calculation. However, by solving the LLG equation numerically we can get further insight into the domain wall dynamics. We continue to use the iron garnet values from Table 1. We solve the system on an asymmetric grid that is $6.5 \mu\text{m}$ long at grid-points spaced 4 nm apart. The initial profile is a domain wall with positive topological charge ($\partial_x \theta > 0$) and positive chirality ($\phi = 0$) centered at the origin. Spin-waves are excited by applying a magnetic field $\mathbf{H}(t) = H_0 \sin(2\pi f t) \mathbf{e}_y$, to 24 grid-points at either side of $x = 1.2 \mu\text{m}$. The excitation amplitude is $H_0 = 0.2 \text{ T}$ and the excitation frequency is kept at 5 GHz . To avoid spin-wave reflection at the sample ends, we implement absorbing boundary conditions by increasing the Gilbert damping to $|\alpha| = 1$ inside $1 \mu\text{m}$ wide regions at either end of the sample⁴⁴. The electric field is applied in the y -direction, $\mathbf{E} = E \mathbf{e}_y$, and the perpendicular anisotropy is set to zero.

Figure 8(a) is a reproduction of the well-known results of Yan *et al.*²⁴. In the absence of an applied electric field the domain wall moves towards the spin-wave source in order to conserve angular momentum. Figure 8(b) shows that the magnon-mediated magnetoelectric torque can be used to reverse the velocity of the domain wall and make it travel away from the spin-wave source. The domain wall velocity is a linear function of the applied electric field, as shown in Fig. 8(c). At a critical applied electric field the domain wall stops and its direction of motion is reversed.

As suggested by Yan *et al.*³⁷, domain wall motion away from the spin-wave source is caused by linear momentum transfer, with linear momentum formally defined as the generator of magnetic translations^{53,54}. To identify the momentum of a magnetization texture is not trivial, and an essential first step is to realize that the linear momentum of a ferromagnetic soliton is not directly related to its velocity, but to its configuration. This gives the conserved momentum of a domain wall some counter-intuitive properties—for instance, the momentum of a stationary domain wall can be nonzero^{37,53}. Following Tchernyshyov⁵³ we calculate the conserved linear momenta of a magnetization texture consisting of circularly polarized spin-waves superposed on a Walker domain wall (axially symmetric system). The conserved linear momentum attributable to the domain wall and the spin-waves is, respectively

$$P_{\text{DW}} = C + 2m\phi/\gamma, \quad (25)$$

$$P_{\text{SW}} = C - \frac{\rho^2}{2\gamma m} \left(2\phi - \int_{-\infty}^{+\infty} k dx \right), \quad (26)$$

where C denotes the momentum of the reference magnetization profile. Conservation of momentum, $0 = dP/dt = dP_{\text{DW}}/dt + dP_{\text{SW}}/dt$, allows us to solve for the rate of change of the azimuthal angle,

$$\dot{\phi} = \frac{\rho^2}{2(\rho^2 - 2m^2)} \int_{-\infty}^{+\infty} k dx,$$

where the dot denotes a time-derivative. Thus, a change in the linear momentum (wavenumber) of the spin-waves generates domain wall rotation. This suggests that an effective description of the induced dynamics can be made in terms of an applied magnetic field^{37,38}. In an axially symmetric system (no perpendicular anisotropy) the collective coordinate equations of a Walker domain wall subject to an applied magnetic field read⁵⁵,

$$(1 + \alpha^2) \dot{\phi} = -\gamma H, \quad (27)$$

$$(1 + \alpha^2) \frac{\dot{X}}{\lambda} = +\alpha \gamma H, \quad (28)$$

($\gamma < 0, \alpha < 0$). This gives

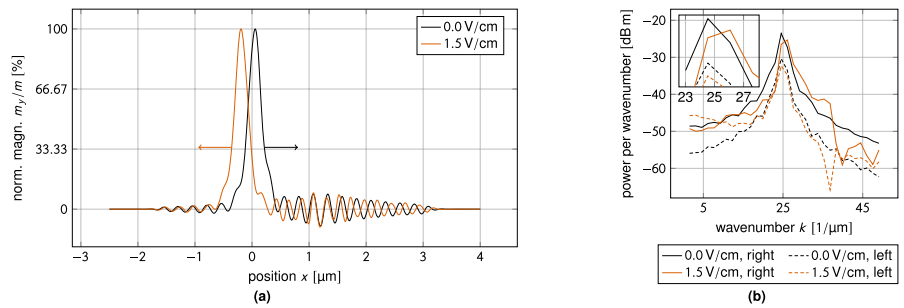


Figure 9. Electric field-dependent linear momentum transfer to the domain wall. (a) Phase shift difference before and after domain wall transmission. Steady-state magnetization profiles obtained for $E = 1.5$ V/cm and in the absence of an applied electric field. To the right of the wall (before transmission through the domain wall) there is a pronounced phase shift between the spin-waves in the two magnetization profiles. To the left of the wall (after domain wall transmission) the wavelengths of the spin-waves are practically identical. (b) Power spectral density of the magnetization profiles in (a) computed from the data to the right (left) of the source. The spurious peak in the power spectrum is now absent as there is no reorientation of the y -component of the magnetization. Whereas the position of the peak in the power spectrum is unchanged upon spin-wave transmission through the domain wall in the zero field case, the peak is shifted towards smaller wavenumbers in the presence of an applied electric field. This corresponds to a transfer of linear momentum to the domain wall.

$$H_{\text{eff}} = \frac{\rho^2(1 + \alpha^2)}{2\gamma(2m^2 - \rho^2)} \int_{-\infty}^{+\infty} k dx. \quad (29)$$

The resulting domain wall velocity, \dot{X} , is small since it is proportional to the Gilbert damping. In the case of a domain wall driven by an applied magnetic field, the domain wall velocity can be increased drastically at small driving fields by breaking the axial symmetry of the system using a perpendicular anisotropy. Wang *et al.*³⁸ argued that the above effective description of linear momentum transfer can be carried over to this case and that an equation similar to equation (29) is valid even in the presence of a perpendicular anisotropy. Using this description they were able to explain domain wall motion driven by linear momentum transfer from spin-waves in a Dzyaloshinskii–Moriya ferromagnet.

In the present case, the axial symmetry of the system is broken by the applied electric field. Since we have not been able to solve equation (24) for the spin-wave amplitudes, we are not able to repeat the analysis leading up to equation (29) in the presence of the inhomogeneous magnetoelectric effect. However, we argue that—just as for the Dzyaloshinskii–Moriya ferromagnet—the underlying physics is the same and that linear momentum transfer from the spin-waves leads to domain wall motion that can be described using an effective Zeeman field.

The mechanism of momentum transfer from the spin-waves to the domain wall is somewhat similar to the one suggested by Wang *et al.*³⁸ for linear momentum transfer in the presence of the Dzyaloshinskii–Moriya interaction. As can be seen in Fig. 9(a) the application of an electric field does not cause significant spin-wave reflection off the domain wall. However, in the presence of an electric field the wavelength changes upon spin-wave transmission through the domain wall. This is captured by the power spectrum in Fig. 9(b). The reduction of the spin-wave wavenumber upon transmission implies that the transmitted spin-waves carry less linear momentum. This change in linear momentum is absorbed by the domain wall.

Since the effective Zeeman field is linear in the momentum transfer^{37,38} and the domain wall velocity is a linear function of the applied magnetic field below Walker breakdown^{32,51}, the linear dependence of the domain wall velocity on the electric field in Fig. 8(c) must be taken as a sign that the momentum transfer is linear in the applied electric field, just as it is linear in the DMI constant³⁸. This is not too surprising, given the linear dependence on the electric field found in equation (24). The dependence of the momentum transfer on the electric field can also be observed in a sequence of power spectrums like the one in Fig. 9(b) taken at increasing electric fields. As the electric field is increased, the wavenumber of the spin-waves to the right of the domain wall is shifted away from the zero field peak, which is just what we pointed out for the homogeneously magnetized case in Fig. 6(b).

Conclusion

To conclude, we have demonstrated analytically and numerically that the inhomogeneous magnetoelectric effect induces a magnon-mediated reorientation of a homogeneous magnetization, and we have provided an explanation of the mechanism behind this effect. This reorientation is not fixed by material constants like the ones discovered for Dzyaloshinskii–Moriya ferromagnets by Manchon *et al.*³⁰ and for topological insulator–ferromagnet heterostructures by Linder³¹, but is tunable by the applied electric field. Its magnitude increases linearly with the electric field and an effect on the order of 8% of the saturation magnetization should not be problematic. This is almost an order of magnitude larger than the reorientation reported by Manchon *et al.* for Dzyaloshinskii–Moriya ferromagnets.

We have also shown that the sign and magnitude of the velocity of a magnon-driven domain wall can be controlled by the applied electric field in the presence of the inhomogeneous magnetoelectric interaction. Domain wall motion towards the spin-wave source is due to angular momentum conservation while domain wall motion away from the source is due to linear momentum transfer. The mechanism of linear momentum transfer is quite similar to the mechanism suggested by Wang *et al.*³⁸ for Dzyaloshinskii–Moriya ferromagnets, and the domain wall velocity scales linearly with the electric field.

References

- Eerenstein, W., Mathur, N. D. & Scott, J. F. Multiferroic and magnetoelectric materials. *Nature* **442**, 759–765, URL <http://www.nature.com/doi/10.1038/nature05023> (2006).
- Spaldin, N. A. The renaissance of magnetoelectric multiferroics. *Science* **309**, 391–392, URL <http://www.sciencemag.org/cgi/doi/10.1126/science.1113357> (2005).
- Cheong, S.-W. & Mostovoy, M. Multiferroics: A magnetic twist for ferroelectricity. *Nat. Mater.* **6**, 13–20, URL <http://www.nature.com/doi/10.1038/nmat1804> (2007).
- Dong, S., Liu, J.-M., Cheong, S.-W. & Ren, Z. Multiferroic materials and magnetoelectric physics: Symmetry, entanglement, excitation, and topology. *Adv. Phys.* **64**, 519–626, URL <http://www.tandfonline.com/doi/full/10.1080/00018732.2015.1114338> (2015).
- Dzyaloshinskii, I. E. On the magneto-electrical effect in antiferromagnets. *J. Exp. Theor. Phys.* **10**, 628–629, URL <http://www.jetp.ac.ru/cgi-bin/e/index/e/10/3/p628?a=list> (1960).
- Schmid, H. Some symmetry aspects of ferroics and single phase multiferroics. *J. Phys. Condens. Mat.* **20**, 434201, URL <http://stacks.iop.org/0953-8984/20/i=43/a=434201?key=crossref.13df1153dc47706416fa3f17637a8224> (2008).
- Bar'yakhtar, V. G., Lvov, V. A. & Yablonskii, D. A. Inhomogeneous magnetoelectric effect. *JETP Lett.* **37**, 673–675, URL http://www.jetpletters.ac.ru/ps/1499/article_22895.shtml (1983).
- Mostovoy, M. Ferroelectricity in spiral magnets. *Phys. Rev. Lett.* **96**, 067601, URL <http://link.aps.org/doi/10.1103/PhysRevLett.96.067601> (2006).
- Cano, A. & Kats, E. I. Electromagnon excitations in modulated multiferroics. *Phys. Rev. B* **78**, 012104, URL <http://link.aps.org/doi/10.1103/PhysRevB.78.012104> (2008).
- Tewari, S., Zhang, C., Toner, J. & Das Sarma, S. Goldstone modes and electromagnon fluctuations in the conical cycloid state of a multiferroic. *Phys. Rev. B* **78**, 144427, URL <http://link.aps.org/doi/10.1103/PhysRevB.78.144427> (2008).
- Cano, A. Theory of electromagnon resonances in the optical response of spiral magnets. *Phys. Rev. B* **80**, 180416, URL <http://link.aps.org/doi/10.1103/PhysRevB.80.180416> (2009).
- Zvezdin, A. K. & Mukhin, A. A. On the effect of inhomogeneous magnetoelectric (flexomagnetolectric) interaction on the spectrum and properties of magnons in multiferroics. *JETP Lett.* **89**, 328–332, URL <http://link.springer.com/10.1134/S0021364009070042> (2009).
- Mills, D. L. & Dzyaloshinskii, I. E. Influence of electric fields on spin waves in simple ferromagnets: Role of the flexoelectric interaction. *Phys. Rev. B* **78**, 184422, URL <http://link.aps.org/doi/10.1103/PhysRevB.78.184422> (2008).
- Liu, T. & Vignale, G. Electric control of spin currents and spin-wave logic. *Phys. Rev. Lett.* **106**, 247203, URL <http://link.aps.org/doi/10.1103/PhysRevLett.106.247203> (2011).
- Liu, T. & Vignale, G. Flexoelectric phase shifter for spin waves. *J. Appl. Phys.* **111**, 083907, URL <http://scitation.aip.org/content/aip/journal/jap/111/8/10.1063/1.4703925> (2012).
- Zhang, X., Liu, T., Flatté, M. E. & Tang, H. X. Electric-field coupling to spin waves in a centrosymmetric ferrite. *Phys. Rev. Lett.* **113**, 037202, URL <http://link.aps.org/doi/10.1103/PhysRevLett.113.037202> (2014).
- Chumak, A. V., Serga, A. A. & Hillebrands, B. Magnon transistor for all-magnon data processing. *Nat. Commun.* **5**, 4700, URL <http://www.nature.com/doi/10.1038/ncomms5700> (2014).
- Chumak, A. V., Vasyuchka, V. I., Serga, A. A. & Hillebrands, B. Magnon spintronics. *Nat. Phys.* **11**, 453–461, URL <http://www.nature.com/doi/10.1038/nphys3347> (2015).
- Serga, A. A., Chumak, A. V. & Hillebrands, B. YIG magnonics. *J. Phys. D Appl. Phys.* **43**, 264002, URL <http://stacks.iop.org/0022-3727/43/i=26/a=264002?key=crossref.6a073bfc1c8ba106fa1ba87bbfe37d3f> (2010).
- Khitun, A., Bao, M. & Wang, K. L. Magnonic logic circuits. *J. Phys. D Appl. Phys.* **43**, 264005, URL <http://stacks.iop.org/0022-3727/43/i=26/a=264005?key=crossref.f9dd566068384c0f843c64d4110dbb4d> (2010).
- Khitun, A. & Wang, K. L. Non-volatile magnonic logic circuits engineering. *J. Appl. Phys.* **110**, 034306, URL <http://scitation.aip.org/content/aip/journal/jap/110/3/10.1063/1.3609062> (2011).
- Klingler, S. *et al.* Design of a spin-wave majority gate employing mode selection. *Appl. Phys. Lett.* **105**, 152410, URL <http://scitation.aip.org/content/aip/journal/apl/105/15/10.1063/1.4898042> (2014).
- Khitun, A. Multi-frequency magnonic logic circuits for parallel data processing. *J. Appl. Phys.* **111**, 054307, URL <http://scitation.aip.org/content/aip/journal/jap/111/5/10.1063/1.3689011> (2012).
- Yan, P., Wang, X. S. & Wang, X. R. All-magnonic spin-transfer torque and domain wall propagation. *Phys. Rev. Lett.* **107**, 177207, URL <http://link.aps.org/doi/10.1103/PhysRevLett.107.177207> (2011).
- Urazhka, Y., Imamura, K., Oyabu, S., Tanaka, T. & Matsuyama, K. Successive logic-in-memory operation in spin wave-based devices with domain wall data coding scheme. *IEEE Trans. Magn.* **50**, 1–3, URL <http://ieeexplore.ieee.org/lpdocs/epic03/wrapper.htm?arnumber=6971479> (2014).
- Fert, A., Cros, V. & Sampaio, J. Skyrmions on the track. *Nat. Nanotechnol.* **8**, 152–156, URL <http://www.nature.com/doi/10.1038/nnano.2013.29> (2013).
- Schütte, C. & Garst, M. Magnon-skyrmion scattering in chiral magnets. *Phys. Rev. B* **90**, 094423, URL <http://link.aps.org/doi/10.1103/PhysRevB.90.094423> (2014).
- Dzyaloshinskii, I. E. A thermodynamic theory of “weak” ferromagnetism of antiferromagnetics. *J. Phys. Chem. Solids* **4**, 241–255, URL <http://linkinghub.elsevier.com/retrieve/pii/0022369758900763> (1958).
- Moriya, T. Anisotropic superexchange interaction and weak ferromagnetism. *Phys. Rev.* **120**, 91–98, URL <http://link.aps.org/doi/10.1103/PhysRev.120.91> (1960).
- Manchon, A., Ndiaye, P. B., Moon, J.-H., Lee, H.-W. & Lee, K.-J. Magnon-mediated Dzyaloshinskii–Moriya torque in homogeneous ferromagnets. *Phys. Rev. B* **90**, 224403, URL <http://link.aps.org/doi/10.1103/PhysRevB.90.224403> (2014).
- Linder, J. Improved domain-wall dynamics and magnonic torques using topological insulators. *Phys. Rev. B* **90**, 041412, URL <http://link.aps.org/doi/10.1103/PhysRevB.90.041412> (2014).
- Chen, H.-B., Liu, Y.-H. & Li, Y.-Q. Electric field control of multiferroic domain wall motion. *J. Appl. Phys.* **115**, 133913, URL <http://scitation.aip.org/content/aip/journal/jap/115/13/10.1063/1.4870711> (2014).
- Dzyaloshinskii, I. E. Magnetoelectricity in ferromagnets. *Europhys. Lett.* **83**, 67001, URL <http://stacks.iop.org/0295-5075/83/i=6/a=67001?key=crossref.4c3468a7a6c2ca649e3b02617a3ffd64> (2008).
- Logginov, A. S., Meshkov, G. A., Nikolaev, A. V. & Pyatakov, A. P. Magnetoelectric control of domain walls in a ferrite garnet film. *JETP Lett.* **86**, 115–118, URL <http://link.springer.com/10.1134/S0021364007140093> (2007).

35. Pyatakov, A. P. *et al.* Micromagnetism and topological defects in magnetoelectric media. *Phys.-Usp.* **58**, 981–992, URL <http://stacks.iop.org/1063-7869/58/i=10/a=981?key=crossref.62c38296ce954ae637088d70bb2c471d> (2015).
36. Mikhailov, A. V. & Yaremchuk, A. I. Forced motion of a domain wall in the field of a spin wave. *JETP Lett.* **39**, 354–357, URL http://www.jetpletters.ac.ru/ps/1299/article_19617.shtml (1984).
37. Yan, P., Kamra, A., Cao, Y. & Bauer, G. E. W. Angular and linear momentum of excited ferromagnets. *Phys. Rev. B* **88**, 144413, URL <http://link.aps.org/doi/10.1103/PhysRevB.88.144413> (2013).
38. Wang, W. *et al.* Magnon-driven domain-wall motion with the Dzyaloshinskii-Moriya interaction. *Phys. Rev. Lett.* **114**, 087203, URL <http://link.aps.org/doi/10.1103/PhysRevLett.114.087203> (2015).
39. Landau, L. D. & Lifshitz, E. M. On the theory of the dispersion of magnetic permeability in ferromagnetic bodies. *Phys. Zeitsch. der Sow.* **8**, 153–169 (1935).
40. Landau, L. D. & Lifshitz, E. M. On the theory of the dispersion of magnetic permeability in ferromagnetic bodies. *Ukr. J. Phys.* **53**, 14–22, URL <http://ujp.bitp.kiev.ua/files/journals/53/si/53SI06p.pdf> (2008).
41. Gilbert, T. A phenomenological theory of damping in ferromagnetic materials. *IEEE Trans. Magn.* **40**, 3443–3449, URL <http://ieeexplore.ieee.org/lpdocs/epic03/wrapper.htm?arnumber=1353448> (2004).
42. Tveten, E. G., Qaiumzadeh, A. & Brataas, A. Antiferromagnetic domain wall motion induced by spin waves. *Phys. Rev. Lett.* **112**, 147204, URL <http://link.aps.org/doi/10.1103/PhysRevLett.112.147204> (2014).
43. Griffiths, D. J. *Introduction to Quantum Mechanics*, 2 edn (Pearson, 2013).
44. Seo, S.-M., Lee, K.-J., Yang, H. & Ono, T. Current-induced control of spin-wave attenuation. *Phys. Rev. Lett.* **102**, 147202, URL <http://link.aps.org/doi/10.1103/PhysRevLett.102.147202> (2009).
45. Waterloo Maple, *pdsolve*. Available at: <http://www.maplesoft.com/support/help/Maple/view.aspx?path=pdsolve> (Accessed: May 6, 2016) (2016).
46. Kabychenkov, A. F., Lisovskii, F. V. & Mansvetova, E. G. Magnetolectric effect in garnet films with the induced magnetic anisotropy in a nonuniform electric field. *JETP Lett.* **97**, 265–269, URL <http://link.springer.com/10.1134/S0021364013050081> (2013).
47. Sergienko, I. A. & Dagotto, E. Role of the Dzyaloshinskii-Moriya interaction in multiferroic perovskites. *Phys. Rev. B* **73**, 094434, URL <http://link.aps.org/doi/10.1103/PhysRevB.73.094434> (2006).
48. Barone, P. & Picozzi, S. Mechanisms and origin of multiferroicity. *C. R. Phys.* **16**, 143–152, URL <http://linkinghub.elsevier.com/retrieve/pii/S1631070515000109> (2015).
49. Fan, X. *et al.* Quantifying interface and bulk contributions to spin-orbit torque in magnetic bilayers. *Nat. Commun.* **5**, 3042, URL <http://www.nature.com/doi/10.1038/ncomms4042> (2014).
50. Jiles, D. *Introduction to Magnetism and Magnetic Materials*, 1 edn. (Springer-Science+Business Media, 1991).
51. Schryer, N. L. & Walker, L. R. The motion of 180° domain walls in uniform dc magnetic fields. *J. Appl. Phys.* **45**, 5406–5421, URL <http://scitation.aip.org/content/aip/journal/jap/45/12/10.1063/1.1663252> (1974).
52. Tatara, G., Kohno, H. & Shibata, J. Microscopic approach to current-driven domain wall dynamics. *Phys. Rep.* **468**, 213–301, URL <http://linkinghub.elsevier.com/retrieve/pii/S0370157308002597> (2008).
53. Tchernyshyov, O. Conserved momenta of a ferromagnetic soliton. *Ann. Phys.* **363**, 98–113, URL <http://linkinghub.elsevier.com/retrieve/pii/S0003491615003395> (2015).
54. Zak, J. Magnetic translation group. *Phys. Rev.* **134**, A1602–A1606, URL <http://link.aps.org/doi/10.1103/PhysRev.134.A1602> (1964).
55. Shibata, J., Tatara, G. & Kohno, H. A brief review of field- and current-driven domain-wall motion. *J. Phys. D: Appl. Phys.* **44**, 384004, URL <http://stacks.iop.org/0022-3727/44/i=38/a=384004?key=crossref.030ab431503338459b13bb288cf61a54> (2011).
56. Bailleul, M., Olligs, D. & Fermon, C. Propagating spin wave spectroscopy in a permalloy film: A quantitative analysis. *Appl. Phys. Lett.* **83**, 972, URL <http://scitation.aip.org/content/aip/journal/apl/83/5/10.1063/1.1597745> (2003).
57. Sekiguchi, K. *et al.* Nonreciprocal emission of spin-wave packet in FeNi film. *Appl. Phys. Lett.* **97**, 022508, URL <http://scitation.aip.org/content/aip/journal/apl/97/2/10.1063/1.3464569> (2010).

Acknowledgements

We thank M. Mostovoy and T. Liu for helpful comments, and acknowledge support from the Outstanding Academic Fellows programme at NTNU and the Norwegian Research Council Grant No. 205591, No. 216700 and No. 240806.

Author Contributions

J.L. and I.K. conceived the study. I.K. carried out the preliminary investigation. V.R. substantially expanded and shaped the project and wrote the manuscript. All authors reviewed the manuscript.

Additional Information

Competing financial interests: The authors declare no competing financial interests.

How to cite this article: Risinggård, V. *et al.* Electric field control of magnon-induced magnetization dynamics in multiferroics. *Sci. Rep.* **6**, 31800; doi: 10.1038/srep31800 (2016).



This work is licensed under a Creative Commons Attribution 4.0 International License. The images or other third party material in this article are included in the article's Creative Commons license, unless indicated otherwise in the credit line; if the material is not included under the Creative Commons license, users will need to obtain permission from the license holder to reproduce the material. To view a copy of this license, visit <http://creativecommons.org/licenses/by/4.0/>

© The Author(s) 2016

V

Reference

Y. Li, M. Amado, T. Hyart, G.P. Mazur, V. Risinggård, T. Wagner, L. McKenzie-Sell, G. Kimbell, J. Wunderlich, J. Linder, J.W.A. Robinson. Competition between canted antiferromagnetic and spin-polarized quantum Hall states at $\nu = 0$ in graphene on a ferrimagnetic insulator. arXiv: 1905.06866

Contributions

JWAR conceived the experiment and supervised the project. YL and MA contributed equally to the work and both performed the electrical, magnetic, and structural measurements. MA and GK grew the YIG thin films, LMS and GK helped perform magnetic and x-ray characterization, and YL fabricated the devices and performed the Raman spectroscopy. TH developed the theoretical interpretation in terms of a competition between the canted antiferromagnetic and ferromagnetic states. VR and JL provided theoretical support. TW, JW, and GPM supported electrical measurements below 9 K. JW, MA, YL, and TH wrote the paper with support from JL and VR. All authors commented on the manuscript.

Comments

This work was presented at the 2018 International Nanoscience Student Conference (Trondheim, Norway).

Competition between canted antiferromagnetic and spin-polarized quantum Hall states at $\nu = 0$ in graphene on a ferrimagnetic insulator

Y. Li,^{1,2†} M. Amado,^{1†} T. Hyart,³ G. P. Mazur,³ V. Risinggård,^{4,5} T. Wagner,^{1,6} L. McKenzie-Sell,^{1,7}
G. Kimbell,¹ J. Wunderlich,⁶ J. Linder,^{4,5} J. W. A. Robinson^{1*}

¹Department of Materials Science & Metallurgy, University of Cambridge, 27 Charles Babbage Road, Cambridge CB3 0FS, United Kingdom. ²Cambridge Graphene Centre, University of Cambridge, 9 JJ Thomson Avenue, Cambridge CB3 0FA, United Kingdom. ³International Research Centre MagTop, Institute of Physics, Polish Academy of Sciences, Aleja Lotników 32/46, PL-02668 Warsaw, Poland. ⁴Department of Physics, Norwegian University of Science and Technology, N-7491 Trondheim, Norway. ⁵Center for Quantum Spintronics, Department of Physics, Norwegian University of Science and Technology, NO-7491 Trondheim, Norway. ⁶Hitachi Cambridge Laboratory, Cambridge CB3 0HE, United Kingdom. ⁷Cavendish Laboratory, University of Cambridge, Cambridge CB3 0HE, United Kingdom.

The $\nu = 0$ quantum Hall state in graphene has attracted experimental¹⁻¹¹ and theoretical¹²⁻¹⁸ interest. Graphene supports four zero-energy Landau levels which are described by spin and valley degeneracies. These lead to a number of approximately degenerate symmetry-broken states^{12,14}. Electron-electron and electron-phonon interactions break valley-symmetry and determine the ground state of the $\nu = 0$ state. The consensus emerging from theory¹⁶⁻¹⁸ and experiment^{3,8,9,11} is that these interactions favour an antiferromagnetic insulating state which supports long-range spin-polarized edge transport^{3,11}. Here we report a competition between canted antiferromagnetic and ferromagnetic quantum Hall states in graphene placed on a ferrimagnetic insulator $\text{Y}_3\text{Fe}_5\text{O}_{12}$ (YIG), which induces a uniform magnetic exchange field in graphene of the order 60 T. The magnetic order and energy gap of the edge modes in graphene are tunable with an 8 T out-of-plane magnetic field at 2.7 K.

A magnetic field parallel (B_{\parallel}) to the plane of graphene can promote a ferromagnetic (F-) state⁹. In general, however a competition between antiferromagnetic (AF-) and F-states leads to a canted antiferromagnetic (CAF-) state in which the spins are tilted parallel (as preferred by the Zeeman field) and perpendicular (as preferred by the interactions that favour AF order) to the magnetic field, pointing in opposite directions in the two sublattices as schematically illustrated in Fig. 1. The CAF-state continuously interpolates between the AF- ($\theta = \pi/2$) and F-states ($\theta = 0$), where θ is the angle between the spins and magnetic field. In the AF-state, charged edge excitations are gapped, but the F-state supports gapless counterpropagating edge modes^{15,17}. Therefore, in the CAF-state the energy gap of the edge modes is tunable with a magnetic field with a gap at $\theta = \pi/2$ which vanishes at $\theta = 0$ (Ref. 17), and a competition between the CAF- and F-states can be detected by transport measurements⁹. Although a tunable energy

gap is interesting for applications, the magnetic field required to control the energy gap in graphene is of the order 15-30 T (Ref. 9).

Here we induce an intrinsic magnetic exchange field in graphene on YIG of the order 60 T. The magnetic order and the energy gap of the edge modes in graphene can be tuned more efficiently than in the absence of YIG by varying the magnitude and direction of a magnetic field. In particular, out-of-plane magnetic fields (B_{\perp}) excite transitions between different $\nu = 0$ quantum Hall states in graphene. The tunability of the magnetic order and the energy gap of the edge modes in graphene are probed through nonlocal resistance (R_{nl}) vs. gate voltage (V_{TG}) measurements as a function of B_{\perp} and temperature (T) in Hall bars. The functional form of $R_{nl}(B_{\perp})$ is found to evolve from a single- to a double-peak structure, which is consistent with theory and demonstrates a competition between F- and CAF-states (Fig. 1) in magnetized graphene.

Edge states in graphene lead to nonlocal transport and invalidate the concept of a local resistivity tensor¹⁹. For ballistic transport, R_{nl} is quantized to values which depend on device geometry¹⁹, but in graphene on YIG the edge modes are not fully protected against backscattering and device dimensions are larger than the mean free path for charge scatter meaning values of R_{nl} are non-universal. Nevertheless, they provide a robust signature for the presence of edge modes as we explain here. The edge spectrum for AF-, CAF- and F-states are different and distinguishable by measuring $R_{nl}(V_{TG})$: the AF-state does not support edge modes and R_{nl} is zero; however, the CAF- and F-states do support edge modes meaning R_{nl} is nonzero. For the CAF-state (F-state), the edge mode is gapped (gapless) and $R_{nl}(V_{TG})$ has a double-peak (single-peak) structure (Fig. 1). We demonstrate a transition from a single- to a double-peak in $R_{nl}(V_{TG})$ with B_{\perp} from 8 T at 2.7 K. Although these results are consistent with theory¹⁷, values of B_{\perp} are lower than expected for isolated graphene (i.e. in the absence of a magnetic substrate) and T -transition is an order of magnitude higher⁹. From theory we estimate a magnetic exchange field in graphene due to YIG of the order 60 T (consistent with theory²⁰⁻²³), which acts to lower the magnetic field required to interpolate between F- and CAF-states.

Recently, Wei *et al.* probed nonlocal transport in graphene/EuS Hall bars²⁴ in which the EuS is a ferromagnetic semiconductor but the $\nu = 0$ states were not reported. In our experiment, we chose YIG since it has a Curie temperature of 550 K (compared to 16.5 K for EuS), a wide bandgap of 2.84 eV (1.65 eV for EuS) and is chemically stable. Furthermore, YIG has an electrical resistivity of $10^{12} \Omega\text{-cm}$, which isolates electrical transport to graphene.

Atomically flat (110) YIG (84-nm-thick) is grown by pulsed laser deposition (see Fig. 2a and Methods) onto single crystal gadolinium gallium garnet with a volume magnetization of 144 emu cm^{-3} (fig. S3), matching bulk YIG²⁵. Magnetoelectric properties in graphene on YIG are investigated by fabricating Hall bars in several steps involving exfoliation of graphene from graphite and dry transfer onto YIG. Electron beam lithography is used to define Au/Cr electrodes (see Methods). The graphene is capped with thickness of 20-50 nm hexagonal boron nitride (hBN) and has a typical field-effect mobility of $\mu \sim 10,000 \text{ cm}^2 \text{ V}^{-1} \text{ s}^{-1}$ at 9 K with a 40-nm-thick AlO_x top-gate (Fig. 2a, left inset). We note that μ is higher than previous reports for exfoliated²³ or chemical vapour deposited²⁶⁻²⁸ graphene on YIG. Control Hall bars of hBN/graphene/ AlO_x /YIG ($\mu \sim 15,000 \text{ cm}^2 \text{ V}^{-1} \text{ s}^{-1}$ at 9 K) and hBN/graphene/ SiO_2 ($\mu \sim 3,000 \text{ cm}^2 \text{ V}^{-1} \text{ s}^{-1}$ at 9 K) are investigated in which graphene is decoupled from YIG. The AlO_x decoupling layer has a thickness of $\sim 6 \text{ nm}$ while the SiO_2 is a thermally oxidized layer on silicon. Before Hall bar fabrication, Raman spectroscopy is performed on the graphene/ SiO_2 prior to and following transfer onto YIG or AlO_x (Fig. 2b). Both before and following transfer onto YIG, we do not observe smearing of the 2D-peak or an additional D-peak (Fig. 2b). The left inset of Figure 2a shows a representative hBN/graphene/YIG Hall bar (prior to top-gate deposition). Longitudinal resistance (R_{xx}) and R_{nl} are measured using lock-in amplifiers (see Methods). For local measurements, $I_{9,10}$ indicates a current flowing between contacts 9 and 10 and a local voltage $V_{3,5}$ is measured between contacts 3 and 5 giving $R_{xx} = V_{3,5}/I_{9,10}$. For R_{nl} , V is probed away from the current path, e.g. $R_{nl} = R_{34,56} = V_{5,6}/I_{3,4}$.

We first focus on nonlocal measurements of hBN/graphene/YIG Hall bars in zero magnetic field. Figure 2c shows a peak in $R_{nl} \sim 380 \text{ } \Omega$ at the Dirac point (V_D). By normalizing R_{xx} and R_{nl} to their respective values at V_D ($R_{xx,D}$ or $R_{nl,D}$), we observe that $R_{nl}/R_{nl,D}$ is an order of magnitude smaller than $R_{xx}/R_{xx,D}$ and the peak in R_{nl} is sharper than R_{xx} . These indicate a contribution from the ordinary spin Hall effect²⁹ and possibly the Zeeman spin Hall effect since YIG has a small remnant out-of-plane moment²⁷. Ohmic, Joule heating and Ettingshausen contributions to R_{nl} are ruled out as shown in Supplementary Sections 2 and 4. Equivalent zero field measurements on hBN/graphene/ SiO_2 (fig. S7) and hBN/graphene/ AlO_x /YIG (fig. S8) reveal reduced R_{nl} values at V_D (less than $65 \text{ } \Omega$ at 9 K in both cases) compared to hBN/graphene/YIG despite larger mobility.

In Figures 3a,b we have plotted $R_{xx}(B_{\perp})$ and $R_{nl}(B_{\perp})$ for a hBN/graphene/YIG Hall bar. Shubnikov-de Haas oscillations are clearly visible in R_{xx} and R_{nl} (Fig. 3a) where $R_{nl}/R_{nl,D}$ falls two orders of magnitude below $R_{xx}/R_{xx,D}$, consistent with induced magnetism in graphene²⁴. The Onsager relation $R_{56,78}(B_{\perp}) = R_{78,56}$

$(-B_{\perp}) \neq R_{78,56}(B_{\perp})$ holds for R_{nl} (Fig. 3b) indicating it includes a contribution from the Zeeman spin Hall effect²⁴. With the help of magnetic exchange field and Zeeman field in graphene, a spin-polarized state with nonzero spin Hall conductivity is stabilized as a precursor of the $\nu = 0$ F-state. Figure 3c shows a fan chart of $V_{\text{TG}} - V_{\text{D}}$ as a function of B_{\perp} for Landau levels at filling factors $-14 \leq \nu \leq +14$. The dashed lines are calculated voltages at different Landau level filling factors. The calculated values of $V_{\text{TG}} - V_{\text{D}}$ agree with the experimental results indicating negligible orbital effects in hBN/graphene/YIG²⁴. Figures 3d-f show R_{xx} vs. $V_{\text{TG}} - V_{\text{D}}$ plots used for fan chart construction. B_{\perp} required to quantize the Landau levels is smaller than 1 T.

The energy of a Landau level N is $E_n = \pm \sqrt{2|N|\hbar v_{\text{F}}^2 e B_{\perp}}$, where e is the electron charge, \hbar is the Planck constant divided by 2π , v_{F} is the Fermi velocity, and $N = 0, \pm 1, \pm 2, \dots$. More quantum Hall plateaus $\sigma_{\text{xy}} = 4(N+1/2)e^2/h$ will appear at filling factors $\nu = 0, \pm 1, \dots$. The $\nu = 0$ at the centre of zeroth Landau level is different, as it does not exhibit the deep minimum in R_{xx} which is a characteristic of the quantum Hall effect for other filling factors.

Figure 4 shows evidence for a gapped $\nu = 0$ insulating state in hBN/graphene/YIG that appears in σ_{xy} vs. $V_{\text{TG}} - V_{\text{D}}$ for $B_{\perp} = 12$ T, while hints of the zeroth Landau level lifting appear in magnetic fields of only 4 T in σ_{xx} . Figures 4e,f show σ_{xy} vs. $V_{\text{TG}} - V_{\text{D}}$ where a standard integer family of plateaus is visible for $B_{\perp} < 6$ T, but for $B_{\perp} > 6$ T the $\nu = 0$ plateau initiates along with a splitting in σ_{xx} (Figs. 4c,d). A $\nu = 0$ plateau forms by $B_{\perp} = 12$ T (Fig. 4h). Equivalent measurements on hBN/graphene/SiO₂ and hBN/graphene/AlO_x/YIG Hall bars show a transition from $\nu = -2$ to 2 plateaus, but the $\nu = 0$ plateau and a splitting in σ_{xx} do not appear³⁰.

The onset of the $\nu = 0$ plateau in hBN/graphene/YIG coincides with a rapid rise in $R_{\text{xx,D}}$ vs. B_{\perp} (Fig. 5a), consistent with a transition to an insulating state. Control Hall bars do not show this behavior (fig. S9a) meaning that the presence of YIG promotes the low field formation of the $\nu = 0$ plateau. The $\nu = 0$ insulating state in hBN/graphene/YIG could arise due to various symmetry-broken states^{12-14,16-18}. However, the important role of YIG in stabilizing this state indicates that the magnetically-induced exchange field in graphene lowers the energy of the symmetry-broken state, and the CAF-state is the most plausible candidate for the insulating $\nu = 0$ quantum Hall state appearing with B_{\perp} .

The above interpretation is consistent with other observations - e.g. the $\nu = 0$ plateau develops at a similar values of B_{\perp} where a double-peak appears in $R_{\text{nl}}(V_{\text{TG}})$ (Figs. 5c,d) which is expected for the CAF-

state (Fig. 1c). By increasing B_{\perp} , $R_{\text{nl,D}}$ at the Dirac point approaches zero meaning that the magnitude of the edge gap is increasing, consistent with our theoretical calculations that show the angle between magnetic field and the direction of the spins in graphene increases with increasing B_{\perp} . The magnitude of B_{\perp} determines the Zeeman energy ($E_z = g\mu_B B_{\perp}$, where g is gyromagnetic ratio, μ_B is Bohr magneton) in graphene and the valley anisotropy energy related to electronic interactions which favor an AF-state, but the valley anisotropy energy increases faster with B_{\perp} . This leads to the phase diagram schematically illustrated in Fig. 5g, where B_{\perp} causes a phase transition from F- to CAF-state³⁰.

To test the above hypothesis, we investigate the effect of rotating the magnetic field (B) from B_{\parallel} to B_{\perp} (Figs. 5e,f). B_{\parallel} favors the F-state and will reduce the magnitude of the edge gap, which shows up as an increase of $R_{\text{nl,D}}$. A maxima in $R_{\text{nl,D}}$ will be reached at the phase transition from CAF- to F-state where the edge gap vanishes. As the magnitude of B is constant during magnetic field rotation, B_{\perp} decreases by rotating B in-plane and eventually the system is driven out of the quantum Hall regime with decreasing $R_{\text{nl,D}}$. Figures 5e,f confirm these predictions and they are well described by theory that focuses on a competition between CAF- and F-states assuming that YIG induces a 60 T magnetic exchange field in graphene³⁰. The magnitude of B controlling the magnetic order and the energy gap of the edge modes in graphene is of the order of 5-10 T, which is smaller than the 20-30 T field required in the absence of YIG⁹.

In conclusion, by placing graphene on YIG a magnetic exchange field in graphene of the order 60 T is induced which enables low field (8 T) tunability of the magnetic order and energy gap of the edge modes in graphene.

References

1. Zhang, Y. et al. Landau-level splitting in graphene in high magnetic fields. *Phys. Rev. Lett.* **96**, 136806 (2006).
2. Abanin, D. A. et al. Dissipative quantum Hall effect in graphene near the Dirac point. *Phys. Rev. Lett.* **98**, 196806 (2007).
3. Wei, D. S. et al. Electrical generation and detection of spin waves in a quantum Hall ferromagnet. *Science* **362**, 229–233 (2018).
4. Checkelsky, J. G. et al. Zero-energy state in graphene in a high magnetic field. *Phys. Rev. Lett.* **100**, 206801 (2008).
5. Giesbers, A. J. M. et al. Gap opening in the zeroth Landau level of graphene. *Phys. Rev. B* **80**, 201403 (2009).
6. Du, X. et al. Fractional quantum Hall effect and insulating phase of Dirac electrons in graphene. *Nature* **462**, 192–195 (2009).
7. Zhang, L. et al. Metal to insulator transition on the $N = 0$ Landau level in graphene. *Phys. Rev. Lett.* **105**, 046804 (2010).
8. Young, A. F. et al. Spin and valley quantum Hall ferromagnetism in graphene. *Nat. Phys.* **8**, 550–556 (2012).

9. Young, A. F. et al. Tunable symmetry breaking and helical edge transport in a graphene quantum spin Hall state. *Nature* **505**, 528–532 (2014).
10. Chiappini, F. et al. Lifting of the Landau level degeneracy in graphene devices in a tilted magnetic field. *Phys. Rev. B* **92**, 201412 (2015).
11. Stepanov, P. et al. Long-distance spin transport through a graphene quantum Hall antiferromagnet. *Nat. Phys.* **14**, 907–911 (2018).
12. Nomura, K. & MacDonald, A. H. Quantum Hall ferromagnetism in graphene. *Phys. Rev. Lett.* **96**, 256602 (2006).
13. Alicea, J. & Fisher, M. P. A. Graphene integer quantum Hall effect in the ferromagnetic and paramagnetic regimes. *Phys. Rev. B* **74**, 075422 (2006).
14. Yang, K., Das Sarma, S. & MacDonald, A. H. Collective modes and skyrmion excitations in graphene SU(4) quantum Hall ferromagnets. *Phys. Rev. B* **74**, 075423 (2006).
15. Abanin, D. A., Lee, P. A. & Levitov, L. S. Spin-filtered edge states and quantum Hall effect in graphene. *Phys. Rev. Lett.* **96**, 176803 (2006).
16. Kharitonov, M. Phase diagram for the $\nu = 0$ quantum Hall state in monolayer graphene. *Phys. Rev. B* **85**, 155439 (2012).
17. Kharitonov, M. Edge excitations of the canted antiferromagnetic phase of the $\nu = 0$ quantum Hall state in graphene: A simplified analysis. *Phys. Rev. B* **86**, 075450 (2012).
18. Feshami, B. & Fertig, H. A. Hartree-Fock study of the $\nu = 0$ quantum Hall state of monolayer graphene with short-range interactions. *Phys. Rev. B* **94**, 245435 (2016).
19. Roth, A. et al. Nonlocal transport in the quantum spin Hall state. *Science* **325**, 294–297 (2009).
20. Yang, H. X. et al. Proximity effects induced in graphene by magnetic insulators: first-principles calculations on spin filtering and exchange-splitting gaps. *Phys. Rev. Lett.* **110**, 046603 (2013).
21. Qiao, Z. et al. Quantum anomalous Hall effect in graphene proximity coupled to an antiferromagnetic insulator. *Phys. Rev. Lett.* **112**, 116404 (2014).
22. Hallal, A., Ibrahim, F., Yang, H., Roche, S. & Chshiev, M. Tailoring magnetic insulator proximity effects in graphene: first-principles calculations. *2D Mater.* **4**, 025074 (2017).
23. Lee, J. & Fabian, J. Magnetotransport signatures of the proximity exchange and spin-orbit couplings in graphene. *Phys. Rev. B* **94**, 195401 (2016).
24. Wei, P. et al. Strong interfacial exchange field in the graphene/EuS heterostructure. *Nat. Mater.* **15**, 711–716 (2016).
25. Hansen P., Röschmann P. & Tolksdorf W. Saturation magnetization of gallium-substituted yttrium iron garnet. *J. Appl. Phys.* **45**, 2728–2732 (1974).
26. Pietrobon, L. et al. Weak delocalization in graphene on a ferromagnetic insulating film. *Small* **11**, 6295–6301 (2015).
27. Leutenantsmeyer, J. C., Kaverzin, A. A., Wojtaszek, M. & van Wees, B. J. Proximity induced room temperature ferromagnetism in graphene probed with spin currents. *2D Mater.* **4**, 014001 (2016).
28. Evelt, M. et al. Chiral charge pumping in graphene deposited on a magnetic insulator. *Phys. Rev. B* **95**, 024408 (2017).
29. Phong, V. T., Walet, N. R. & Guinea, F. Effective interactions in a graphene layer induced by the proximity to a ferromagnet. *2D Mater.* **5**, 014004 (2017).
30. See supplementary materials.

Methods

Growth of YIG. (110)-oriented epitaxial YIG is grown from a stoichiometric target by pulse laser deposition (KrF laser, wavelength $\lambda = 248$ nm) at 750°C in flowing O₂ at 0.12 mbar with a pulse fluence of 2.2 J cm⁻² for 40 minutes and 4 Hz repetition rate onto lattice-matched 5 × 5 mm² (110) gadolinium gallium oxide. The films are annealed *in situ* at 850°C for 2 hours in 0.5 mbar of static O₂ and subsequently cooled at a rate of 5°C min⁻¹. Low angle reflectivity (Fig. 2a) confirms a typical roughness of ~0.14 nm and thickness 84 nm.

Device fabrication. Graphene is prepared by mechanical cleavage from high purity graphite and is transferred onto SiO₂/Si using pre-fabricated alignment markers. Few-layer hBN flakes (20-50 nm, confirmed by atomic force microscopy) are prepared by mechanical cleavage from hBN single crystal. An optical mask is prepared for the transfer process of graphene and hBN, which includes three layers: the first is a piece of thin transparent glass; the second, a transparent and flexible polydimethylsiloxane (PDMS) film, which has two adhesive sides; the third is a thin polycarbonate (PC) film. The selected hBN flake is picked up by a transfer system, which includes the optical mask, micromanipulator, hot plate (set to 50 °C) and optical microscope. The hBN flake on the optical mask is aligned to the selected graphene on SiO₂/Si and transfers graphene from SiO₂/Si to YIG. After the optical mask touches the YIG substrate, the hot plate is set to 180°C to melt the PC film and then the mask is lifted. hBN/graphene is released from the PDMS on the glass. Finally, the PC film on the hBN/graphene is dissolved by chloroform. The whole transfer process is illustrated in fig. S1.

Hall bars are fabricated by electron beam lithography (EBL) as shown in fig. S2. A 30-nm-thick Al mask layer is patterned by EBL and deposited by electron beam evaporator. The hBN/graphene stack is shaped into Hall bar using reactive ion etching with Al mask. Then the sample is rinsed with AZ 326 MIF developer to remove the Al mask. A double-layer PMMA resist (PMMA 495K A6 and 950K A2) is used to pattern the contacts on the hBN/graphene with EBL. 10-nm-thick Cr and 70-nm-thick Au films are deposited by electron beam evaporation to define contact layers. The dielectric layer for the top-gate is amorphous AlO_x (40-nm-thick) prepared by atomic layer deposition with trimethylaluminum (TMA) and H₂O as precursors at 120°C. The top-gate electrode (10 nm Cr/70 nm Au) is prepared by electron beam evaporator.

Transport measurement setup. Transport measurements are performed using lock-in amplifiers at low frequency (7 Hz) using an excitation current of 50 nA at 2.7 K and 100 nA at 9 K as a function of magnetic field (0-12 T) and top-gate voltage at varying temperatures ($T > 2.5$ K). A series resistance of 10 MΩ or

100 M Ω is introduced to maintain a constant current condition that is confirmed by the signal from the lock-in amplifier which measures the current fed through a 10 k Ω series resistor. For local measurements (ig. S4h), a current source (e.g. $I_{9,10} = V_{10k\Omega}/R_{10k\Omega}$) is applied between the electrodes (e.g. contacts 9 and 10), the measured voltage between the electrodes (1 and 2) is Hall voltage ($V_{1,2}$) and between the electrodes (2 and 4) is longitudinal voltage ($V_{2,4}$). The Hall resistance is calculated by $R_{xy} = V_{1,2}/I_{9,10}$, and longitudinal resistance $R_{xx} = V_{2,4}/I_{9,10}$. For the nonlocal measurement (fig. S4i), a current source ($I_{3,4} = V_{10k\Omega}/R_{10k\Omega}$) is applied between the electrodes (3 and 4), the measured voltage between the electrodes (1 and 2) is nonlocal voltage ($V_{1,2}$) and is often converted to nonlocal resistance (R_{nl}) by dividing the injection current ($R_{nl} = R_{34,12} = V_{1,2}/I_{3,4}$).

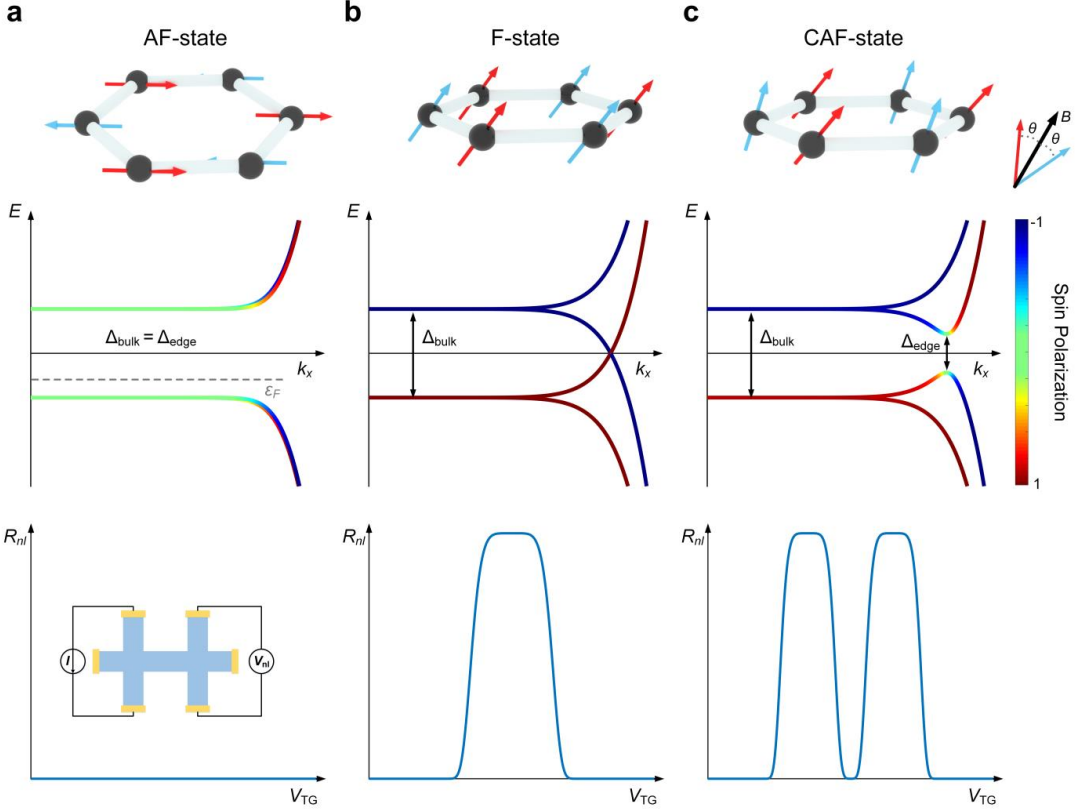


Figure 1 The AF-, F- and CAF-states in graphene. **(a)** The AF-state is spin-unpolarized and both the bulk and edge are gapped, $\Delta_{\text{edge}} = \Delta_{\text{bulk}}$. Due to degeneracy, the net spin polarization is zero at the edge. **(b)** In the F-state the bulk is fully spin-polarized and the system supports gapless helical edge modes. **(c)** The CAF-state continuously interpolates between the AF-state ($\theta = \pi/2$) and F-state ($\theta = 0$), where θ is the angle between the spins and magnetic field B . The bulk state is partially spin-polarized and $\Delta_{\text{edge}} < \Delta_{\text{bulk}}$. At the edges there appears a spin-texture. The edge gap depends continuously on θ , so that $\Delta_{\text{edge}} = \Delta_{\text{bulk}}$ for $\theta = \pi/2$ and $\Delta_{\text{edge}} = 0$ for $\theta = 0$. The middle panels show the edge state spectrum for the different states and the spin-polarization direction relative to B . Color bar shows the spin direction relative to B , scales from 1 to -1 mean that the spin direction is from along with to opposite to B . The lower panels illustrate how the edge spectrum can be probed by measuring $R_{nl}(V_{TG})$. The Fermi level (ϵ_F) can be controlled with V_{TG} and the appearance of the edge states at the given energy gives rise to nonlocal signal. This leads to a single-peak (double-peak) structure of R_{nl} in the case of F-state (CAF-state).

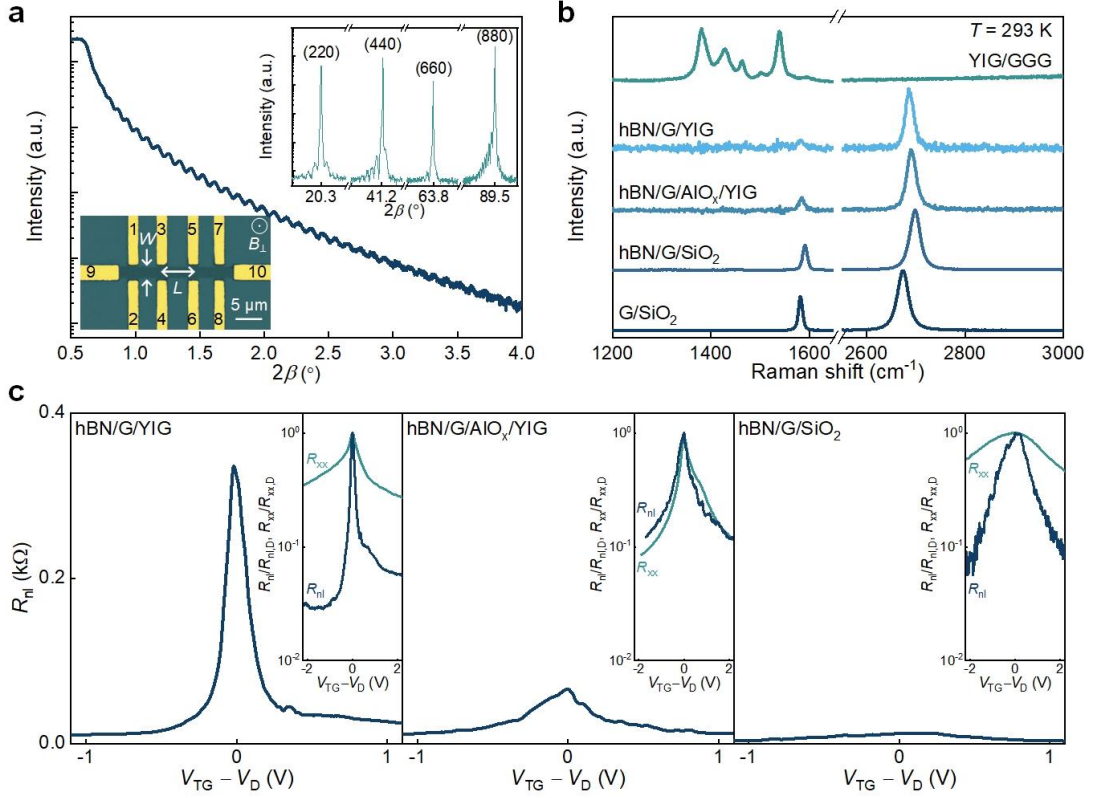


Figure 2 Device and transport properties in zero magnetic field. **(a)** Low angle X-ray reflectometry of (110) YIG confirming a thickness of 84 nm and roughness ~ 0.14 nm. (Upper inset) High angle X-ray diffraction demonstrating single phase (110) YIG. (Lower inset) Optical micrograph (false color) of a representative hBN/graphene/YIG Hall bar where B_{\perp} indicates an out-of-plane magnetic field. **(b)** Raman spectra at 293 K for different structures (labelled) where G stands for “graphene”. The background Raman spectra from hBN and YIG/GGG are subtracted where GGG stands for “gadolinium gallium oxide”. **(c)** R_{nl} vs. $V_{TG} - V_D$ at 9 K for hBN/graphene/YIG and control Hall bars (labelled) with insets showing $R_{xx}/R_{xx,D}$ and $R_{nl}/R_{nl,D}$ vs. $V_{TG} - V_D$ for the same Hall bar.

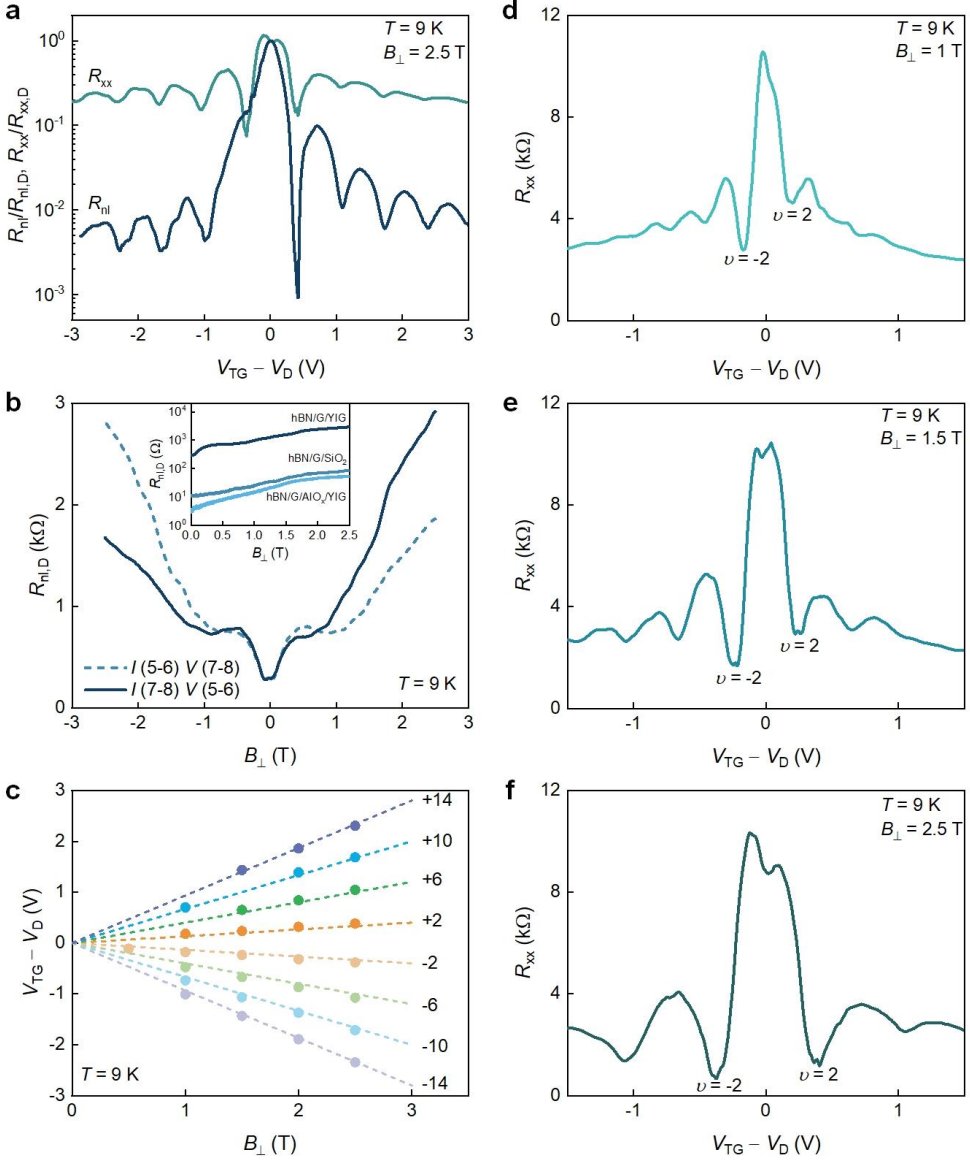


Figure 3 Nonlocal resistance R_{nl} and Landau levels in hBN/graphene/YIG for $B_{\perp} \leq 2.5$ T. **(a)** $R_{xx}/R_{xx,D}$ and $R_{nl}/R_{nl,D}$ vs. $V_{TG} - V_D$ at $B_{\perp} = 2.5$ T. **(b)** $R_{nl,D}$ vs. B_{\perp} for reverse nonlocal connections showing that the Onsager relation holds with the inset showing $R_{nl,D}$ vs. B_{\perp} for control Hall bars (labelled) where G stands for “graphene”. **(c)** $V_{TG} - V_D$ vs. B_{\perp} for different Landau level filling factors (numbered) with calculated fits (short dashed lines). **(d)-(f)** R_{xx} vs. $V_{TG} - V_D$ for B_{\perp} of 1 T, 1.5 T and 2.5 T (labelled).

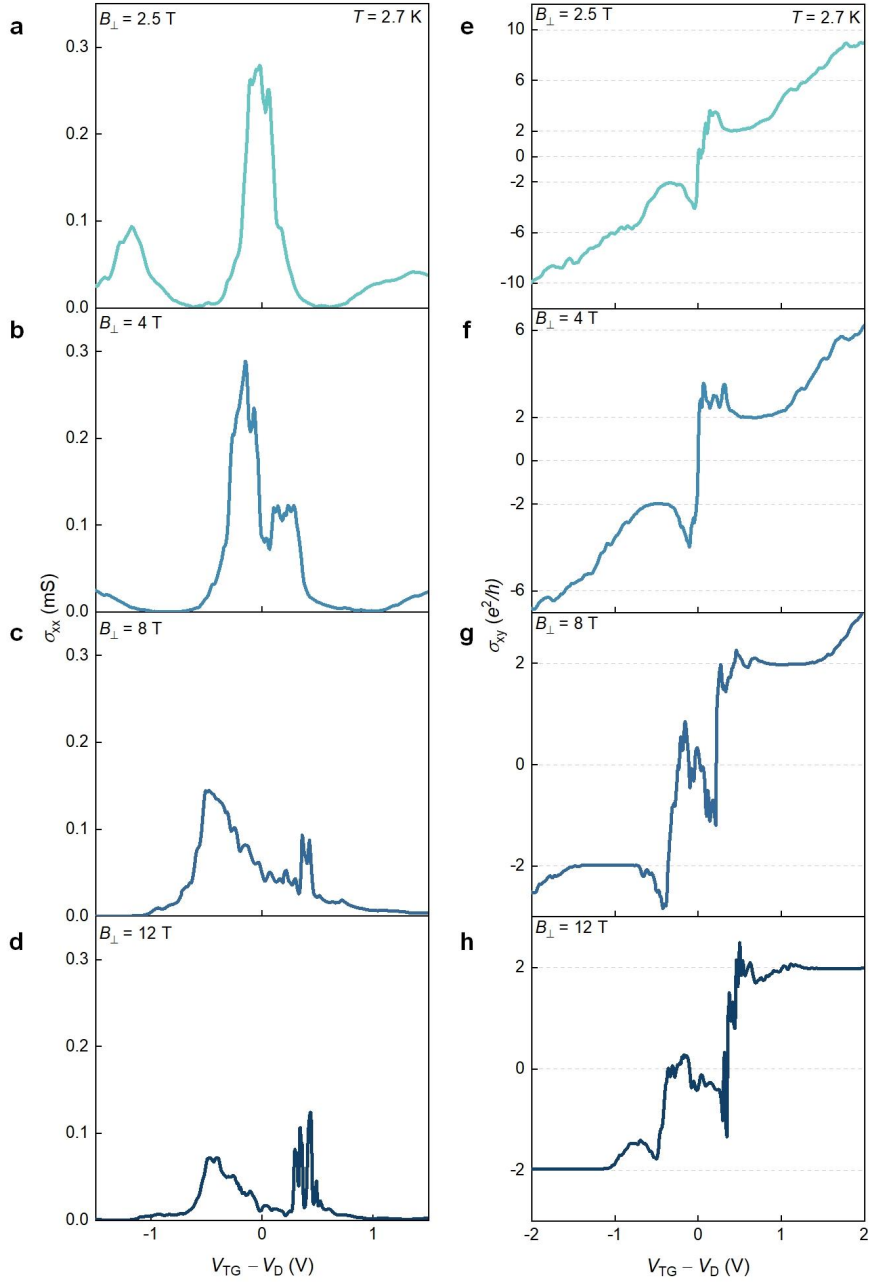


Figure 4 Lifting of the $\nu = 0$ plateau. **(a)-(d)** σ_{xx} vs. $V_{TG} - V_D$ for different values of B_{\perp} (labelled). **(e)-(h)** σ_{xy} vs. $V_{TG} - V_D$ for matching values of B_{\perp} in **(a)** to **(d)**.

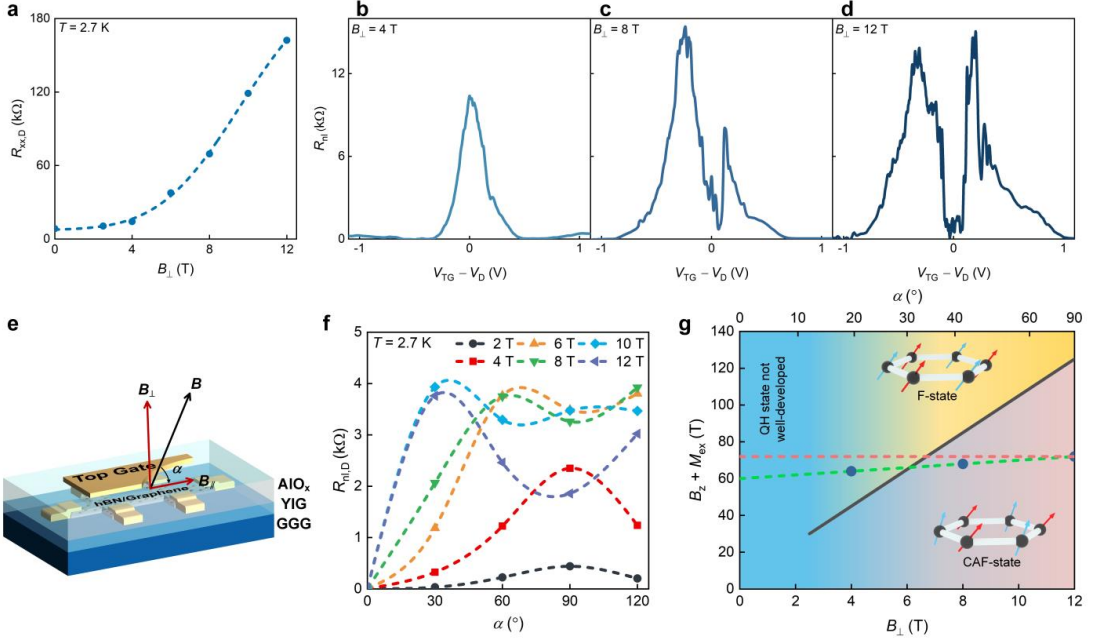


Figure 5 Phase transition versus the magnitude and direction of magnetic field B . **(a)** $R_{xx,D}$ vs. B_{\perp} showing a metal to insulator transition in hBN/graphene/YIG at 2.7 K. The dashed curve is a guide to the eye. **(b)-(d)** $R_{nl,D}$ vs. $V_{TG} - V_D$ for different values of B_{\perp} (labelled). **(e)** Schematic illustration of a device and the direction of B , where $B = \sqrt{B_{\perp}^2 + B_{\parallel}^2}$ and α is the angle between B and the graphene surface. **(f)** $R_{nl,D}$ vs. α for B spanning 2 to 12 T. **(g)** Phase diagram vs. B_{\perp} and the spin-splitting field ($B_z + M_{ex}$), where M_{ex} is the magnetic exchange field induced by YIG. For small B_{\perp} , the quantum Hall (QH) state is not well-developed. By increasing B_{\perp} there exists competition between the F- and CAF-states. For reasonably small B_{\perp} and large ($B_z + M_{ex}$), the F-state is realized, whereas for large B_{\perp} and small ($B_z + M_{ex}$), the CAF-state is energetically favoured. The phase transition line (solid black) is estimated by the experimental data reported in Ref. (9). The magnetic order and the energy gap of the edge modes can be controlled by the magnitude of B_{\perp} [green dotted line and blue circles relate to the states of Figs. 5(b)-(d)] and the direction of the B (red dotted line from $\alpha = 0$ to $\alpha = 90^\circ$ for $B = 12$ T). M_{ex} is estimated to be 60 T.

Supplementary Materials for

Competition between canted antiferromagnetic and spin-polarized quantum Hall states at $\nu = 0$ in graphene on a ferrimagnetic insulator

Y. Li,^{1,2†} M. Amado,^{1†} T. Hyart,³ G. P. Mazur,³ V. Risinggård,^{4,5} T. Wagner,^{1,6} L. McKenzie-Sell,^{1,7}
G. Kimbell,¹ J. Wunderlich,⁶ J. Linder,^{4,5} J. W. A. Robinson^{1*}

S1. Characterization of YIG and graphene/YIG

The magnetic properties of YIG are assessed through magnetization (M) vs. magnetic field (B) measurements (Fig. S3). The in-plane $M(B)$ loop is strongly anisotropic with an easy axis coercivity of ~ 0.3 mT and we estimate a volume magnetization at saturation of 144 emu cm^{-3} . The maximum in-plane (out-of-plane) field required to fully magnetize the YIG is 70 mT (300 mT).

To investigate structural and electronic homogeneity of the graphene on YIG, Raman spectroscopy maps are measured at 293 K (Figs. S4a,b). The positions of the 2D peaks [Pos(2D)] are in the 2680 and 2700 cm^{-1} range, and the full width at half maximum (FWHM) of the 2D peaks are typically 20 cm^{-1} to 30 cm^{-1} . From the Raman images, the homogeneous area [$2690 \text{ cm}^{-1} \leq \text{Pos}(2D) \leq 2700 \text{ cm}^{-1}$ and $20 \text{ cm}^{-1} \leq \text{FWHM} \leq 25 \text{ cm}^{-1}$] is selected and used to fabricate devices (Fig. S4c).

The quality of the Hall bars is characterized through Hall-effect and field-effect mobilities. The Hall-effect mobility of hBN/graphene/YIG Hall bars can be tuned via the top-gate voltage (from -5 V to 1 V with a leakage current of $\sim 2 \times 10^{-11}$ A) up to $\sim 50,000 \text{ cm}^2 \text{ V}^{-1} \text{ s}^{-1}$ with $5 \times 10^{10} \text{ cm}^{-2}$ carrier density at 9 K (Fig. S4d) and the field-effect mobility in the 3,000-12,000 $\text{cm}^2 \text{ V}^{-1} \text{ s}^{-1}$ range at 9 K (Figs. S4e,f) and 4,000 to 40,000 $\text{cm}^2 \text{ V}^{-1} \text{ s}^{-1}$ at 2.7 K (Fig. S4g) with carrier densities between 10^{11} and 10^{12} cm^{-2} .

S2. Ohmic contribution to R_{nl}

Several sources may induce nonlocal voltages in the absence of an external magnetic field. One source is the Ohmic contribution¹, which is given by

$$R_{\text{nl},\Omega} = \frac{W}{\pi L} R_{\text{xx}} \ln \left[\frac{\cosh(\pi L / W) + 1}{\cosh(\pi L / W) - 1} \right] \quad (\text{S1})$$

where L and W are the channel length and width as graphically defined in Fig. 2a of the main paper. In zero external magnetic field for the hBN/graphene/YIG, $L/W = 2.75$ and $R_{\text{xx}} = 9.8 \text{ k}\Omega$, and from Eq. (S1) we find $R_{\text{nl},\Omega} \sim 1 \Omega$, which is two orders of magnitude smaller than the measured R_{nl} (Fig. S5a). Furthermore, R_{nl} from hBN/graphene/YIG is sharper than R_{xx} when top-gate voltage approaches the Dirac point (V_{D}). We can therefore conclude that R_{nl} is not simply proportional to R_{xx} in zero magnetic field meaning that the nonlocal signal from hBN/graphene/YIG is dominated from other factors than the Ohmic contribution.

S3. Magnetoresistance at low magnetic fields

At low magnetic fields our device exhibits sharp negative magnetoresistance which is attributed to weak localization effect (Fig. S5b). The device shows high quality which is confirmed by Shubnikov-de Haas oscillations appearing at magnetic fields as low as 0.5 T. As Rashba spin-orbit coupling in graphene should give rise to weak antilocalization effect, in our device there is no strong spin-orbit coupling.

S4. Thermal contribution to R_{nl}

In all transport measurements we use an alternating-current excitation of $\sim 50 \text{ nA}$ at 2.7 K and $\sim 100 \text{ nA}$ at 9 K with a frequency $\sim 7 \text{ Hz}$. These low current amplitudes are chosen to minimize thermal contributions to the nonlocal transport due to Joule heating and Ettingshausen effects whilst simultaneously maximizing the signal-to-noise ratio of the measured voltages.

Joule heating can give rise to the second harmonic nonlocal signal $R_{\text{nl},J}^{2f}$, and Ettingshausen effect can lead to first harmonic nonlocal signal $R_{\text{nl},E}^f$ (Ref. 2, 3). For all the Hall bars, we measure both the first and second harmonic nonlocal signal using lock-in amplifiers. At 2.5 T, $R_{\text{nl},J}^{2f}$ is typically two orders of magnitude below the R_{nl} (Figs. S6a,b) and in the 8-10 Ω range when $I = 100 \text{ nA}$. Figures S6c,d show that $R_{\text{nl},J}^{2f}$ is directly proportional to the excitation current as expected and hence the excitation current is kept below 100 nA during the measurements to minimize the thermal contribution. In addition, when the

current and voltage probes are switched to reverse the current direction, $R_{nl,j}^{2f}$ changes sign due to heat flow reversal along the Hall bar (Figs. S6c,d). In zero magnetic field, $R_{nl,j}^{2f}$ is less than 1Ω , which is negligible (Fig. S6e).

Ettingshausen contributions to the first harmonic nonlocal signal are due to the heat flow generated by Ettingshausen effect, which can be described as $R_{nl,E}^f \propto S_{yx}^2 T$ (S_{yx} , transverse thermopower coefficient and T , temperature)³. The maximum $R_{nl,E}^f$ and S_{yx} both occur at $N = 0$ Landau level, but S_{yx} changes sign when the gate voltage locates between adjacent Landau levels or in the center of a Landau level², in which $R_{nl,E}^f$ should have peaks. Figure S6f compares the R_{nl} and R_{xx} as a function of top-gate voltage, but R_{nl} does not show other peaks except for at the Landau level positions, which suggests the Ettingshausen effect contribution is negligible.

S5. Nonlocal and local measurements on hBN/graphene/SiO₂ control Hall bars

We investigate R_{nl} and R_{xx} of hBN/graphene/SiO₂ control Hall bars in which the graphene is not coupled to ferrimagnetic insulator YIG. The field-effect mobility is in the $1,500$ to $3,500 \text{ cm}^2 \text{ V}^{-1} \text{ s}^{-1}$ range with a carrier density between 10^{11} and 10^{12} cm^{-2} . At $B_{\perp} = 12 \text{ T}$, both longitudinal conductivity (σ_{xx}) and R_{nl} show a single peak at the Dirac point (Fig. S7a), and the magnitude of the peak in the nonlocal signal is an order of magnitude smaller than in the presence of the coupling to YIG. The Hall conductivity σ_{xy} vs. top-gate voltage $V_{TG} - V_D$ only shows plateaus corresponding to $\nu = \pm 2$ (Fig. S7b). At 12 T and 0 T , $R_{nl,j}^{2f}$ is one order of magnitude below the R_{nl} (Figs. S7c,d). In zero external magnetic field for the hBN/graphene/SiO₂ Hall bar, $L/W = 2.6$ and $R_{xx} = 5.8 \text{ k}\Omega$, and from Eq. (S1) we find $R_{nl,\Omega} \sim 1 \Omega$, which is one order of magnitude smaller than the measured R_{nl} (Fig. S7e).

S6. Nonlocal and local measurements on hBN/graphene/AlO_x/YIG control Hall bars

We investigate R_{nl} and R_{xx} of hBN/graphene/AlO_x/YIG control Hall bars in which the graphene is decoupled from YIG by a thin layer of AlO_x ($\sim 6 \text{ nm}$). The Hall-effect mobility is $15,752 \text{ cm}^2 \text{ V}^{-1} \text{ s}^{-1}$ with $5 \times 10^{11} \text{ cm}^{-2}$ carrier density at 9 K , and the field-effect mobility is in the range of $12,000$ to $20,000 \text{ cm}^2 \text{ V}^{-1} \text{ s}^{-1}$ with a carrier density between 10^{11} and 10^{12} cm^{-2} . At $B_{\perp} = 12 \text{ T}$, both σ_{xx} and R_{nl} show a single peak at the Dirac point (Fig. S8a), and the Hall conductivity σ_{xy} vs. top-gate voltage only shows plateaus corresponding to $\nu = \pm 2$ (Fig. S8b). At 12 T and 0 T , $R_{nl,j}^{2f}$ is around two orders of magnitude below

R_{nl} (Figs. S8c,d). In zero external magnetic field for the hBN/graphene/ AlO_x /YIG Hall bar, $L/W = 2.3$ and $R_{xx} = 10 \text{ k}\Omega$, and from Eq. (S1) we find $R_{nl,\Omega} \sim 4 \Omega$, which is one order of magnitude smaller than the measured R_{nl} (Fig. S8e).

S7. Transition to an insulating quantum Hall state

In the presence of the magnetic exchange field induced by YIG, graphene undergoes a metal to insulator transition with increasing magnetic field indicated by a sharp rise in R_{xx} . Such a rise is not observed in hBN/graphene/ SiO_2 and hBN/graphene/ AlO_x /YIG Hall bars (Fig. S9a). Since no traces of broken degeneracies that might provoke the appearance of the insulating state have been observed in our control samples where graphene is decoupled from YIG, we conclude that the appearance of the plateau at $\nu = 0$ in our experiments is intimately related to the graphene/YIG coupling.

S8. Theoretical description of the competition between F- and CAF-states

We discuss the phase transition between the fully spin-polarized ferromagnetic (F-) state and the canted antiferromagnetic (CAF-) state in the light of the theory^{4,5} and the previous experiments⁶. The dependence of the tilting angle in the CAF-state on the magnetic field \mathbf{B} and the magnetic exchange field \mathbf{M}_{ex} induced by YIG is estimated.

In the non-interacting limit (when Zeeman field and spin-orbit interactions are neglected), graphene supports four zero-energy Landau levels and has spin degeneracy as well as valley (K, K') degeneracy. As in each valley the wave functions reside on one of the sublattices (A, B), the valley index is directly related to the degree of freedom of sublattice ($K \leftrightarrow A, K' \leftrightarrow B$). The electron-electron and electron-phonon interactions break the valley symmetry on the lattice scale and the generated valley anisotropy determines the ground state of the $\nu = 0$ quantum Hall state in graphene. In a systematic theoretical study of the possible anisotropies, there are a large number of different possible symmetry-broken states⁴, but from the experiments of Refs. (6-8) it indicates that the interactions favour antiferromagnetic (AF) insulating state (both bulk and edge excitations are gapped) with opposite spin polarizations on the two sublattices. On the other hand, the external magnetic field and the proximity of YIG lead to a breaking SU(4) symmetry,

$$H_{\vec{M}} = -\mu_B \vec{M} \cdot \vec{\sigma}, \vec{M} = \frac{g}{2} \vec{B} + \vec{M}_{ex} \quad (\text{S2})$$

favouring the spins to be parallel to the spin-splitting field \mathbf{M} which is the sum of the Zeeman field and \mathbf{M}_{ex} induced by the YIG. All fields \mathbf{M} , \mathbf{B} , and \mathbf{M}_{ex} are in units of Tesla. We have following assumptions: 1) $g = 2$; 2) \mathbf{M} is spatially constant, and \mathbf{M}_{ex} is considered as a spatial average of the magnetic exchange field induced by the YIG on graphene; 3) There is a disordered interface between graphene and YIG, so that the sublattice (valley) symmetry is not broken on average; 4)

$$\vec{M}_{ex} = M_{ex} \frac{\vec{B}}{|\vec{B}|} \quad (\text{S3})$$

In the absence of spin-orbit coupling effects, \mathbf{M}_{ex} is parallel or antiparallel to \mathbf{B} , but due to the ferrimagnetic nature of YIG, the magnitude of \mathbf{M}_{ex} could depend on the direction of \mathbf{B} . If the spatial locations of the oppositely polarized magnetic moments do not depend on the direction of \mathbf{B} , this dependence is not expected to be very strong. Therefore the magnitude of the \mathbf{M}_{ex} is independent of the direction of \mathbf{B} ; 5) The magnitude of the \mathbf{M}_{ex} does not depend on $|\mathbf{B}|$, when \mathbf{B} is sufficiently large so that the magnetization of YIG is saturated. In addition, in-plane and out-of-plane anisotropies of YIG are not important here.

The competition between the AF- and F-states leads to the CAF-state where the spins in the two different sublattices are tilted along the direction of the \mathbf{M} (as preferred by H_M), but also they have components perpendicular to \mathbf{M} which are pointing in opposite directions in the two sublattices (as preferred by the electron-electron interactions favouring AF-order). The spin directions in the two sublattices can be calculated by minimizing the energy^{4,5}

$$E(\theta) = E_0 + \frac{L^2}{\pi l_B^2} [-\mu_B M(B) \cos \theta + u(B_{\perp}) \cos^2 \theta] \quad (\text{S4})$$

where E_0 is a constant, L^2 is the area of the sample and l_B is the magnetic length. The anisotropy energy $u(B_{\perp})$ depends not only on the microscopic interactions that break the valley symmetry on the lattice scale, but also on the Landau level wavefunctions, so that it can be controlled with the help of B_{\perp} . Under the assumptions discussed above, $M(B) = |\mathbf{M}|$, which only depends on the magnitude of the total magnetic field $B = |\mathbf{B}|$. The spin directions are described by the polar angle θ of the spins relative to the direction of \mathbf{M} , and the azimuthal angles $\varphi, \varphi + \pi$ in the two sublattices. The energy does not depend on the azimuthal

angle, so φ describes spontaneously broken U(1)-symmetry in the CAF-state. The AF-state is reached when $\mathbf{M} = \mathbf{0}$ and in this case $\theta = \pi/2$, indicating that the spins in the two sublattices are pointing in opposite directions. As $\mathbf{M} = \mathbf{0}$, we can define θ relative to any axis and AF-state is described by spontaneously broken SU(2)-symmetry. In the F-state, the magnitude of \mathbf{M} is so large that spins are fully polarized along the direction of \mathbf{M} , then there is no spontaneously broken symmetry in this case (paramagnetic phase). The angle θ is determined by equation,

$$\cos\theta = \begin{cases} 1, & \mu_B M > 2u(B_\perp) \\ \mu_B M / 2u(B_\perp), & \mu_B M < 2u(B_\perp) \end{cases} \quad (\text{S5})$$

so that the transition from CAF- to F-state occurs at

$$\mu_B M_c = 2u(B_\perp) \quad (\text{S6})$$

The anisotropy energy $u(B_\perp)$ is not known very well theoretically, therefore we determine it by utilizing earlier experiment results⁶. From experiment, the edge mode conductance is measured as a function of B for various values of B_\perp . In the CAF-state, the edge is gapped giving a zero conductance. On the other hand, F-state supports counterpropagating helical edge modes. If they are ballistic (i.e. the length of the system is shorter than the mean free path), the conductance in a simple two-terminal geometry is given by $G = 2e^2/h$. Indeed, experimentally the conductance $G(B, B_\perp)$ shows a sharp crossover from $G = 0$ to $G \approx 2e^2/h$ as a function of B for different values of B_\perp . Then the critical value of the total magnetic field B_c can be well estimated by requiring

$$G(B_c, B_\perp) = e^2 / h \quad (\text{S7})$$

As in this experiment the magnetic exchange field is zero, we get $M_c = B_c$ and $u(B_\perp)$ can be determined from Eq. (S6). The phase transition lines in the (M, B_\perp) -plane for two different samples reported in Ref. (6) are shown in Fig. S9b. By averaging the two lines, we have

$$u(B_\perp) = 5\mu_B (B_\perp + 0.5) \quad (\text{S8})$$

It is a reasonable estimation in the light of Refs. (4, 5), but the shift of 0.5 T indicates that we are linearizing a nonlinear function. In the experiment of Ref. (9), the thermal activation gap increases approximately linearly with B_\perp up to magnetic field on the order of 30 T, so the assumption of linear dependence is reasonable. According to the estimation for $u(B_\perp)$, we find that $2\theta = 0.93\pi$ for large perpendicular magnetic fields. It means that the spins are practically pointing in the opposite directions,

leading to an AF-state, which is consistent with the experimental observations that $\nu = 0$ state in graphene is (approximately) spin unpolarized⁹, charged excitations are gapped both in the bulk and at the edge^{9,10} as well as with the observation of long-distance spin transport^{7,8}. In the case of tilted magnetic field, it leads to a CAF-state and θ decreases with increasing B when B_{\perp} is kept constant. To achieve a transition from CAF- to F-state, it needs a very large magnetic field⁶ ($\sim 10B_{\perp}$).

Our experiments indicate that the proximity from YIG does not lead to strong orbital effects in graphene, and therefore we expect that the estimation for the anisotropy energy [Eq. (S8)] is valid for our devices. In Fig. 5, the transition from CAF- to F-state occurs approximately at $B_{\perp} \approx 6$ T. So M_{ex} induced by YIG is estimated to be 60 T. Moreover we calculate how the angle θ depends on the magnitude of B_{\perp} . Interestingly, θ can be changed over a large range with relatively small external magnetic fields on the order of 5-10 T (Fig. S9c). Such kind of control of the magnetic order is not possible in the absence of magnetic exchange field.

The polar angle θ can be varied by rotating the direction of the magnetic field. Figures S10a,b plot the polar angle as a function of B and the α between magnetic field and sample surface (the perpendicular magnetic field $B_{\perp} = B \sin \alpha$ and the parallel magnetic field $B_{\parallel} = B \cos \alpha$) and the phase-diagram. In the presence of magnetic exchange field induced by YIG, it is possible to control θ with the direction and magnitude of \mathbf{B} and leading to a transition between CAF- and F-states. If B is kept constant, varying the angle α from $\pi/2$ to 0 first causes a transition from CAF- to F-state, and then by further decreasing α the system is driven away from the quantum Hall regime because B_{\perp} decreases. We expect that the quantum Hall state is not well-developed in our samples for magnetic fields below 3 T. In the absence of magnetic exchange field, it requires a very large value of B in order to access the regime where θ can be changed substantially. For external magnetic fields on the order of 5-10 T, the angle θ remains close to $\pi/2$ (approximately AF-state) until α is so small that the system is driven out of the quantum Hall regime.

It is worth pointing out that magnetic exchange field lowers the energy of both the CAF- and F-states. In the CAF-state, magnetic exchange field decreases the energy as $-\delta E \propto M^2/u(B_{\perp})$ and in the F-state as $-\delta E \propto M$. Therefore, magnetic exchange field can stabilize both CAF- and F-states in samples where the $\nu = 0$ quantum Hall state would not be realized in the absence of magnetic exchange field. This could explain why the quantum Hall state is only observed in the sample where the coupling to YIG is present and not in our control samples where this coupling is absent.

S9. Energy gap of the edge modes

The low-energy edge excitations in this type of quantum Hall systems are collective excitations¹¹⁻¹³. While the properties of these collective excitations are different from the single-particle excitations, for our purpose, an adequate estimation of the energy gap of the edge modes can still be obtained using a simplified mean-field single-particle approach developed in Ref. (5).

In the AF-state the charged bulk and edge excitations are gapped, whereas in the F-state the bulk excitations are gapped but gapless counterpropagating edge modes (protected by spin-rotation symmetry) appear at the edge. Because the CAF-state continuously interpolates between the AF ($\theta = \pi/2$) and F ($\theta = 0$) states, the edge gap has to gradually decrease when θ decreases from $\pi/2$ to 0. This behavior is captured by the mean-field Hamiltonian⁵

$$H = -\xi(k_x)\tau_x\sigma_0 - (\mu_B M + \Delta_z)\tau_0\sigma_z - \Delta_x\tau_z\sigma_x \quad (\text{S9})$$

where the Pauli matrices τ_i and σ_i operate on the valley and spin degrees of freedom, respectively, and the spin quantization axis (z -direction in the spin space) has been chosen to be along the direction of the external magnetic field. Here $M = |\mathbf{M}| = B + M_{ex}$, $\xi(k_x)$ describes the dispersion of the Landau levels and k_x is the momentum along the direction of the edge (x -direction), which is related to the position $y_{k_x} = k_x l_B^2$ perpendicular to the edge in Landau gauge. When y_{k_x} is deep inside the bulk, $\xi(k_x) = 0$, and when y_{k_x} approaches the edge, $\xi(k_x)$ increases. The exact functional form of $\xi(k_x)$ is not important here. Additionally, we have introduced the mean-field potentials obtained by performing decoupling of the interactions

$$\Delta_z = 2V_z(B_\perp)\cos\theta, \Delta_x = 2V_x(B_\perp)\sin\theta \quad (\text{S10})$$

The potential Δ_z arises due to the spin component of the electrons parallel to the spin-splitting field \mathbf{M} , and Δ_x is due to spin component perpendicular to \mathbf{M} pointing in opposite directions. We have neglected the spatial dependence of the mean-field potentials Δ_z and Δ_x . The effective interaction strengths $V_z(B_\perp)$ and $V_x(B_\perp)$ to increase with increasing B_\perp and the related anisotropy energy is

$$u(B_\perp) = V_x(B_\perp) - V_z(B_\perp) \quad (\text{S11})$$

Moreover, $V_x(B_\perp)$ is directly related to the bulk gap Δ_{bulk} in the AF- and CAF-states

$$\Delta_{\text{bulk}} = 4V_x(B_\perp) \quad (\text{S12})$$

Therefore $V_x(B_\perp)$ could be estimated using the thermal activation gap measured in the experiments, and $V_z(B_\perp)$ could be determined using Eqs. (S8) and (S11). In the experiment of Ref. (9), the thermal activation gap increases approximately linearly with B_\perp , so that all interaction strengths $V_x(B_\perp)$, $V_z(B_\perp)$ and $u(B_\perp)$ depend linearly on B_\perp in the range of magnetic fields we consider here. However, in the following we describe the edge gap Δ_{edge} in the units of Δ_{bulk} , so the exact values of the interaction strengths $V_x(B_\perp)$ and $V_z(B_\perp)$ are not essential.

According to the energy spectrum from the Hamiltonian [Eq. (S9)], the edge gap is given by

$$\Delta_{\text{edge}} = \begin{cases} 0, & \mu_B M > 2\mu(B_\perp) \text{ (F-state)} \\ \Delta_{\text{bulk}} \sin \theta, & \mu_B M < 2\mu(B_\perp) \text{ (CAF-state)} \end{cases} \quad (\text{S13})$$

and it immediately follows from this expression that $\Delta_{\text{edge}} = \Delta_{\text{bulk}}$ in the AF-state ($\theta = \pi/2$) and edge gap vanishes ($\Delta_{\text{edge}} \rightarrow 0$) when one approaches the F-state ($\theta \rightarrow 0$). Furthermore, Figures S10c,d show how the edge gap depends on \mathbf{B} . In the presence of magnetic exchange field, it is possible to tune Δ_{edge} efficiently using relatively small external magnetic fields. But in the absence of magnetic exchange field, the edge gap satisfies $\Delta_{\text{edge}} \approx \Delta_{\text{bulk}}$ unless very large magnetic fields are applied.

References

1. Abanin, D. A. et al. Giant nonlocality near the Dirac point in graphene. *Science* **332**, 328–330 (2011).
2. Wei, P. et al. Strong interfacial exchange field in the graphene/EuS heterostructure. *Nat. Mater.* **15**, 711–716 (2016).
3. Renard, J., Studer, M. & Folk, J. A. Origins of nonlocality near the neutrality point in graphene. *Phys. Rev. Lett.* **112**, 116601 (2014).
4. Kharitonov, M. Phase diagram for the $\nu = 0$ quantum Hall state in monolayer graphene. *Phys. Rev. B* **85**, 155439 (2012).
5. Kharitonov, M. Edge excitations of the canted antiferromagnetic phase of the $\nu = 0$ quantum Hall state in graphene: A simplified analysis. *Phys. Rev. B* **86**, 075450 (2012).
6. Young, A. F. et al. Tunable symmetry breaking and helical edge transport in a graphene quantum spin Hall state. *Nature* **505**, 528–532 (2014).
7. Wei, D. S. et al. Electrical generation and detection of spin waves in a quantum Hall ferromagnet. *Science* **362**, 229–233 (2018).
8. Stepanov, P. et al. Long-distance spin transport through a graphene quantum Hall antiferromagnet. *Nat. Phys.* **14**, 907–911 (2018).
9. Young, A. F. et al. Spin and valley quantum Hall ferromagnetism in graphene. *Nat. Phys.* **8**, 550–556 (2012).
10. Du, X. et al. Fractional quantum Hall effect and insulating phase of Dirac electrons in graphene. *Nature* **462**, 192–195 (2009).
11. Fertig, H. A. & Brey, L. Luttinger liquid at the edge of undoped graphene in a strong magnetic field. *Phys. Rev. Lett.* **97**, 116805 (2006).

12. Murthy, G., Shimshoni, E. & Fertig, H. A. Collective edge modes near the onset of a graphene quantum spin Hall state. *Phys. Rev. B* **90**, 241410 (2014).
13. Pikulin, D. I., Silvestrov, P. G. & Hyart, T. Confinement-deconfinement transition due to spontaneous symmetry breaking in quantum Hall bilayers. *Nat. Commun.* **7**, 10462 (2016).

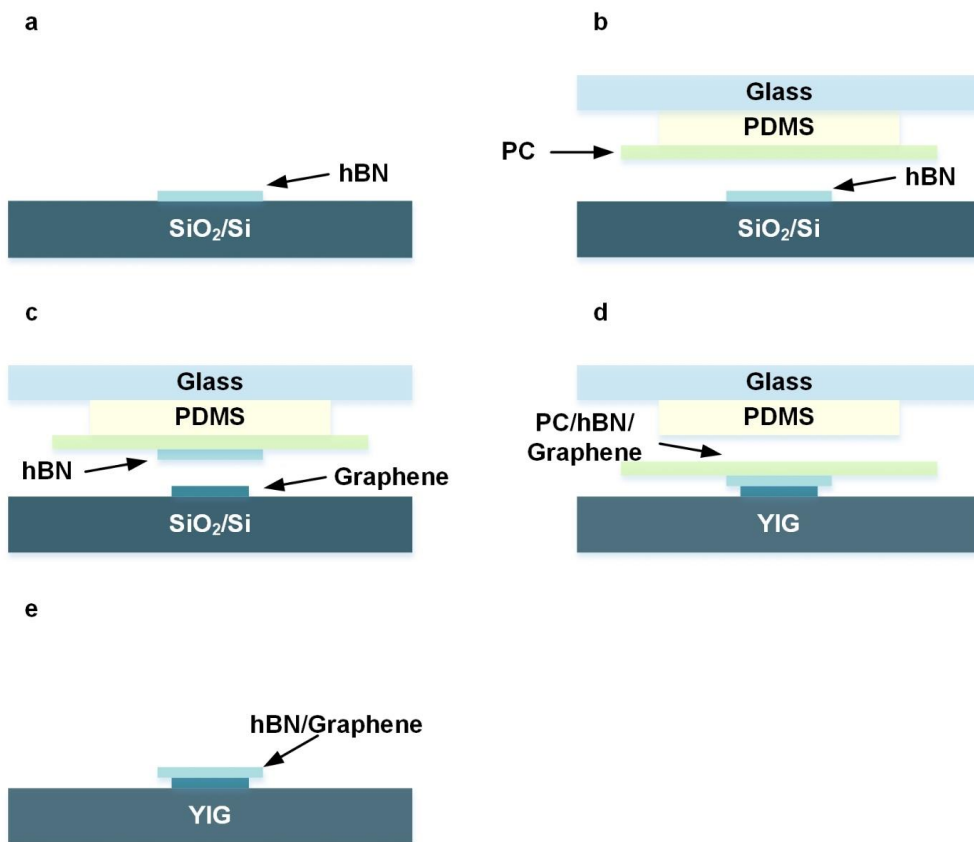


Figure S1 Transfer procedures for hBN/graphene/YIG. **(a)** Exfoliation of hBN flakes on SiO₂/Si. **(b)** Transfer hBN onto optical mask. **(c)** Transfer graphene onto hBN/optical mask. **(d)** Transfer PC/hBN/graphene onto YIG. **(e)** Remove PC film.

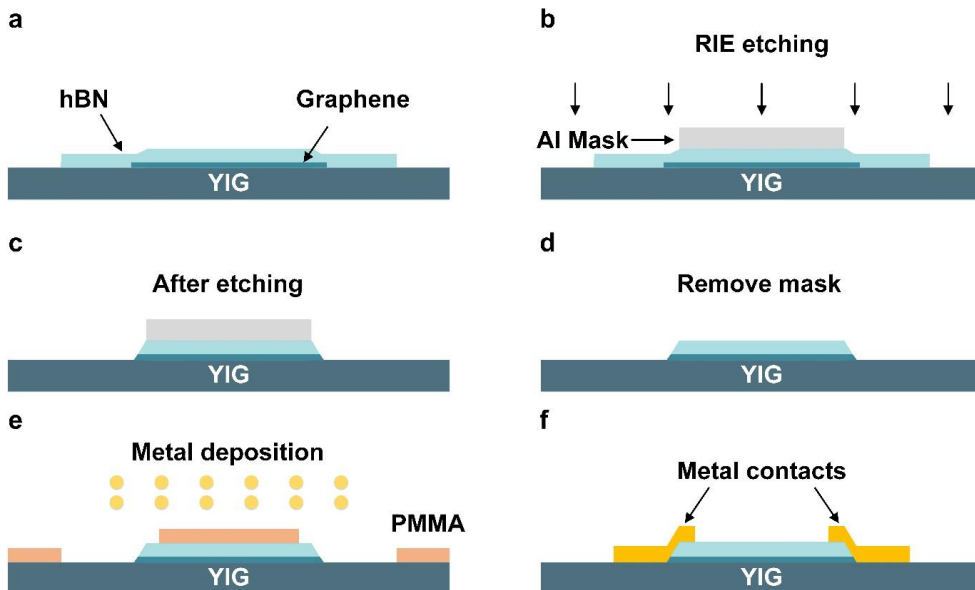


Figure S2 Contact fabrication procedures for hBN/graphene/YIG. (a) hBN/graphene/YIG structure. (b) Reactive ion etching of hBN/graphene on YIG with Al mask. (c) Al/hBN/graphene/YIG structure after etching. (d) hBN/graphene/YIG Hall bar structure. (e) Contacts deposition on hBN/graphene/YIG with PMMA mask. (f) hBN/graphene/YIG Hall bar device.

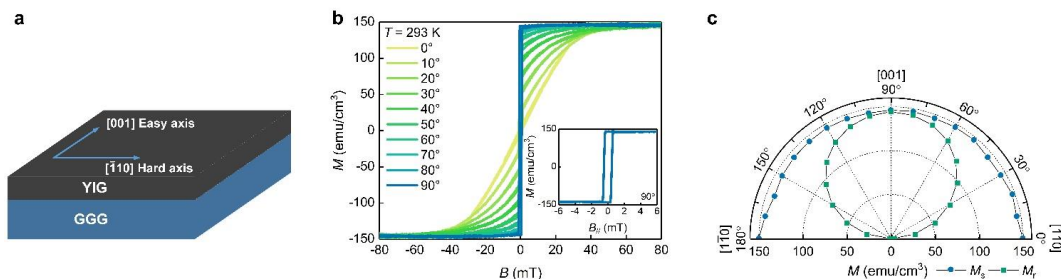


Figure S3 Magnetic properties of (110) YIG at 293 K. (a) Schematic illustration showing in-plane easy and hard axis directions on (110) YIG, where GGG stands for “gadolinium gallium oxide”. (b) Magnetization (M) vs. in-plane external magnetic field (B) hysteresis loops for different in-plane field directions. At 0°, B is parallel to the hard axis $[\bar{1}10]$, while for 90° along the easy axis $[001]$. The inset shows the low field $M(B_{||})$ along the in-plane easy axis. (c) Stoner plot shows constant saturation magnetization (M_s) and the variation of the remnant magnetization (M_r) on γ where $\gamma = 0^\circ$ is parallel to $[\bar{1}10]$.

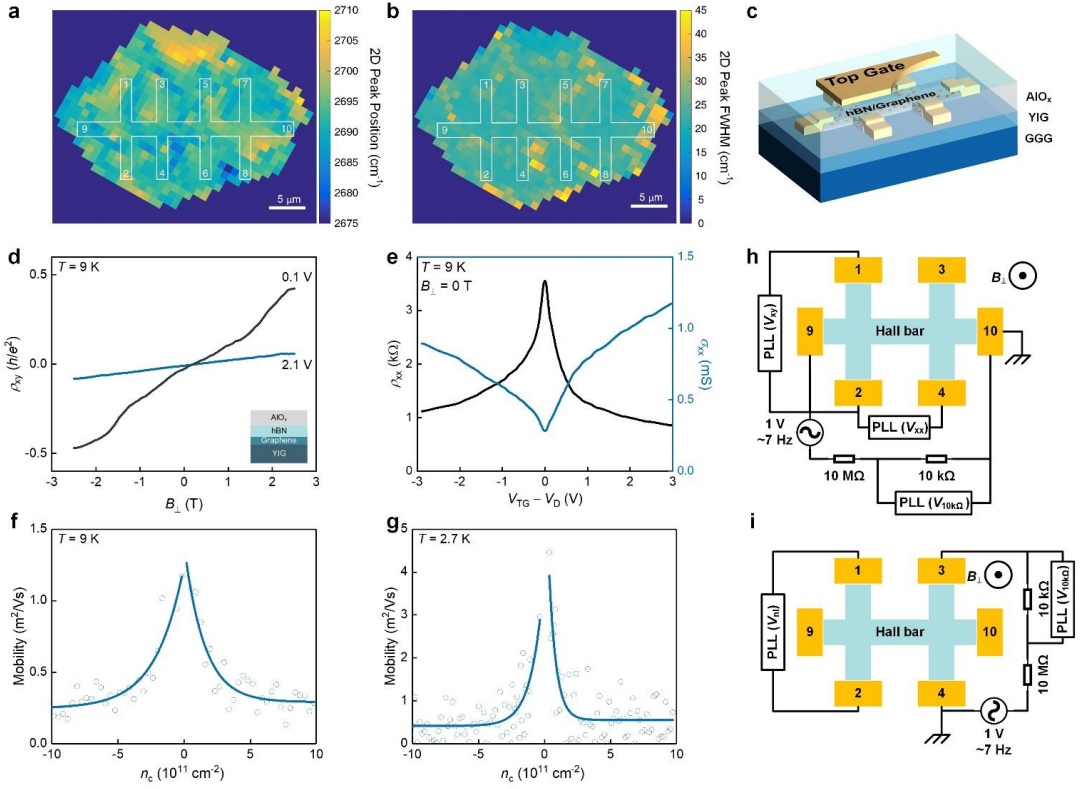


Figure S4 Raman and electrical properties of hBN/graphene/YIG device. Raman spectra maps of (a) positions (cm^{-1}) and (b) FWHM (cm^{-1}) of the 2D peaks at 293 K, where white solid lines show the position of the Hall bar. (c) Schematic illustration of the Hall bar device, where GGG stands for “gadolinium gallium oxide”. (d) Magnetic field (B_{\perp}) dependence of Hall resistivity (ρ_{xy}) at different top-gate voltage $V_{\text{TG}} - V_{\text{D}}$ at 9 K, inset shows the device structure of hBN/graphene/YIG. (e) $V_{\text{TG}} - V_{\text{D}}$ dependence of longitudinal resistivity (ρ_{xx}) and conductivity (σ_{xx}) at 0 T and 9 K. (f) and (g) Field-effect mobility vs. $V_{\text{TG}} - V_{\text{D}}$ at 9 K and 2.7 K. (h) R_{xx} and R_{xy} measurement setup. (i) R_{ni} measurement setup. PLL is the phase-locked loop system.

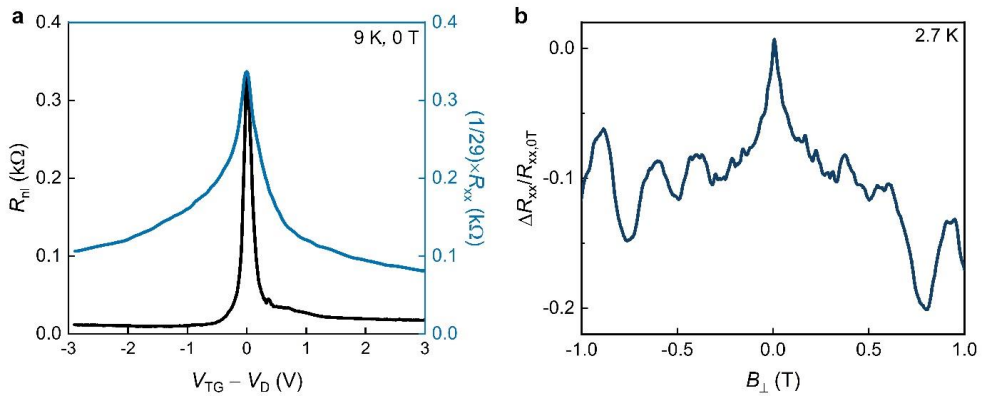


Figure S5 Ohmic contribution to R_{nl} and weak localization effect in hBN/graphene/YIG Hall bar. **(a)** Scaled R_{xx} and R_{nl} in zero external magnetic field at 9 K. **(b)** Low field normalized magnetoresistance $(R_{xx} - R_{xx,0T})/R_{xx,0T}$ vs. B_{\perp} at 2.7 K. It shows sharp and symmetric peak about zero magnetic field arising due to weak localization effect.

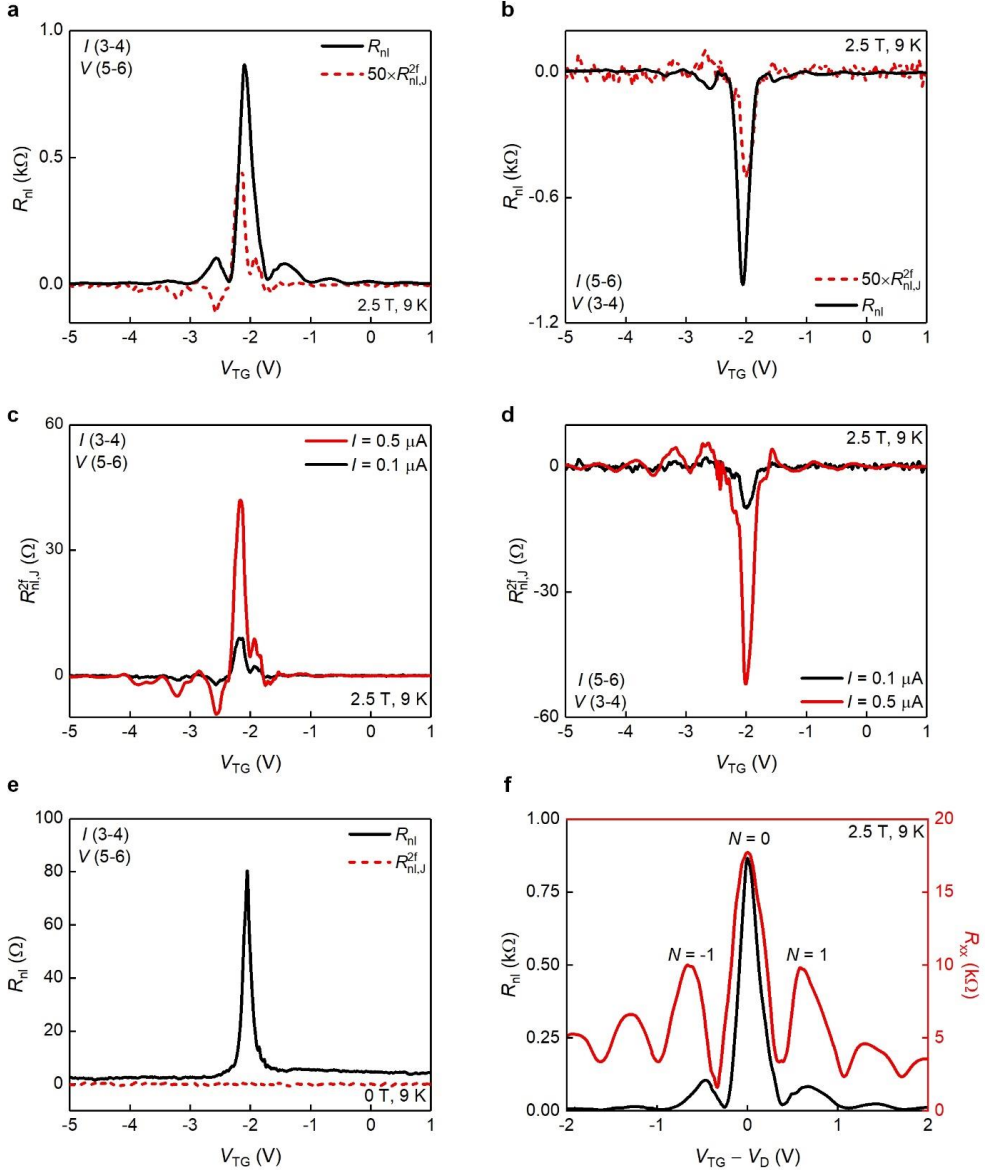


Figure S6 Comparison of first and second harmonic signal of R_{nl} and R_{xx} at 2.5 T and 0 T in hBN/graphene/YIG Hall bar. $R_{nl,J}^{2f}$ (multiplied by 50) (a) and R_{nl} (b) vs. V_{TG} at 2.5 T with reverse nonlocal connections. (c), (d) $R_{nl,J}^{2f}$ vs. V_{TG} when inject current $I = 0.1 \mu\text{A}$ and $0.5 \mu\text{A}$ with different reverse nonlocal connections. (e) Comparison of the $R_{nl,J}^{2f}$ and R_{nl} at 0 T, $R_{nl,J}^{2f}$ is less than 1Ω . (f) Comparison of R_{nl} and R_{xx} with no additional oscillations in R_{nl} at $N = \pm 1$ Landau levels, indicating that the Ettingshausen effect is negligible.

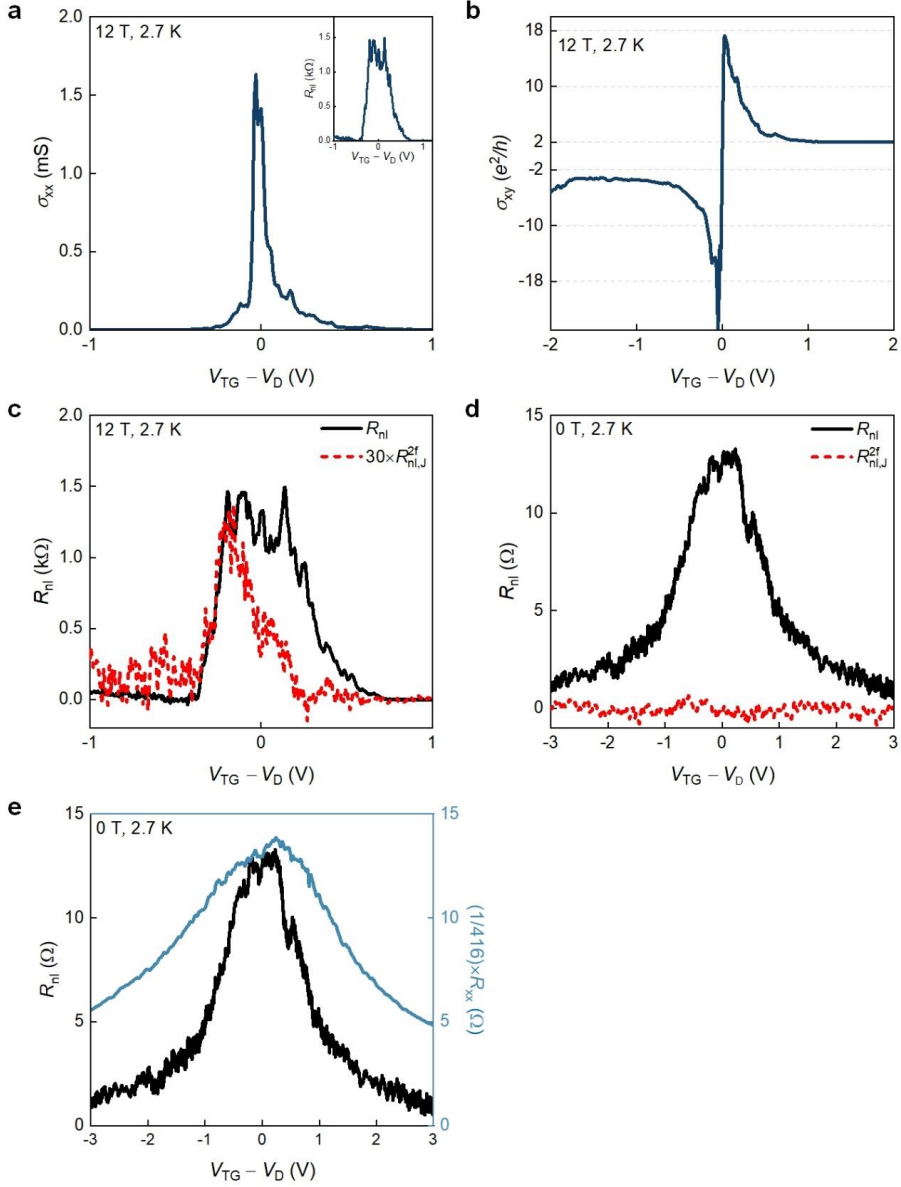


Figure S7 Nonlocal and local measurements in hBN/graphene/SiO₂ control Hall bar. **(a)** σ_{xx} vs. $V_{TG} - V_D$ at $B_{\perp} = 12$ T. The inset shows R_{nl} vs. $V_{TG} - V_D$. **(b)** σ_{xy} vs. $V_{TG} - V_D$ at $B_{\perp} = 12$ T, which only shows the plateaus of conductance corresponding to $\nu = \pm 2$. **(c)** Comparison between $R_{nl,J}^{2f}$ (multiplied by 30) and R_{nl} at $B_{\perp} = 12$ T. **(d)** Comparison between $R_{nl,J}^{2f}$ and R_{nl} at $B_{\perp} = 0$ T. **(e)** Comparison between the scaled R_{xx} and R_{nl} in zero external magnetic field at 2.7 K.

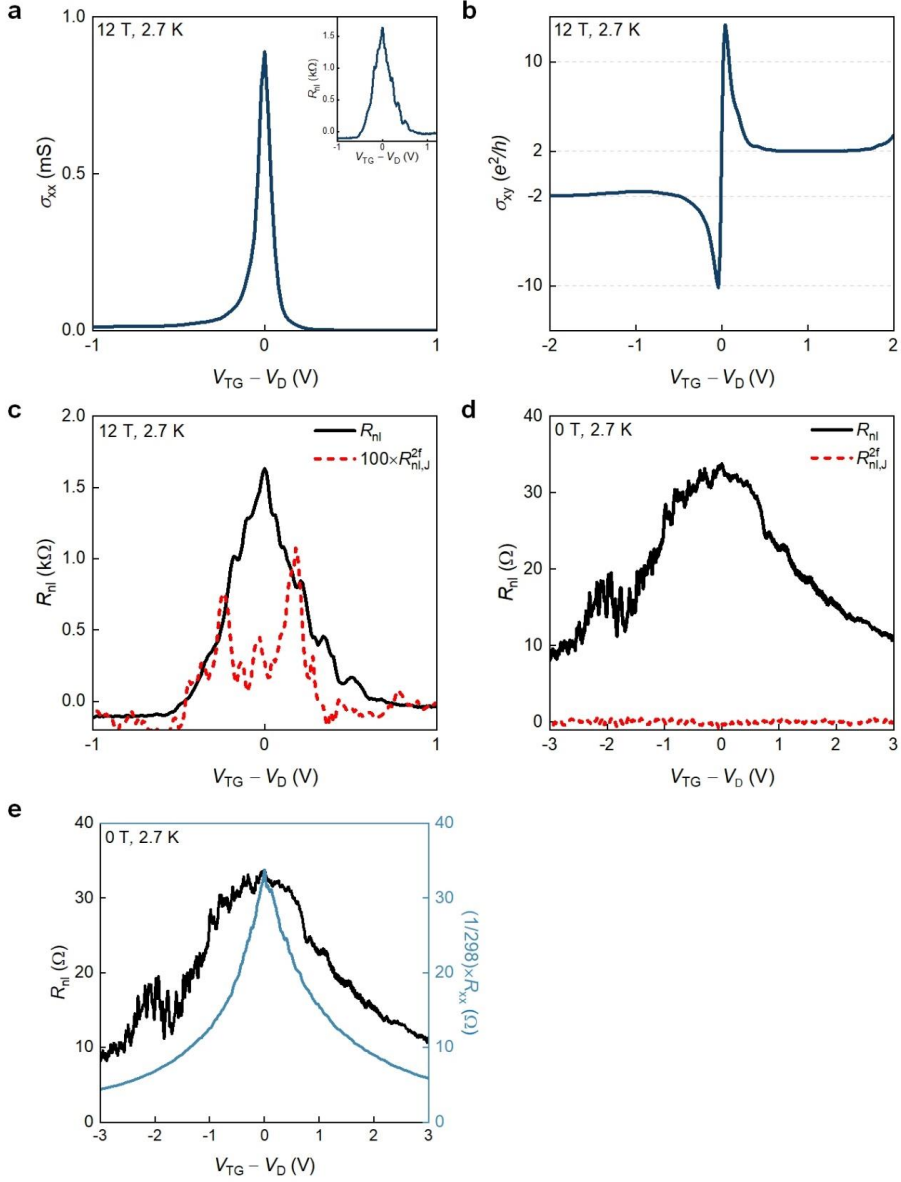


Figure S8 Nonlocal and local measurements in hBN/graphene/AlO_x/YIG Hall bar. (a) σ_{xx} vs. $V_{TG} - V_D$ at $B_{\perp} = 12$ T. The inset shows R_{nl} vs. $V_{TG} - V_D$. (b) σ_{xy} vs. $V_{TG} - V_D$ at $B_{\perp} = 12$ T, which only shows the plateaus of conductance corresponding to $\nu = \pm 2$. (c) Comparison between R_{nl} (multiplied by 100) and R_{nl}^{2f} at $B_{\perp} = 12$ T. (d) Comparison between R_{nl}^{2f} and R_{nl} at $B_{\perp} = 0$ T. (e) Comparison between the scaled R_{xx} and R_{nl} in zero external magnetic field at 2.7 K.

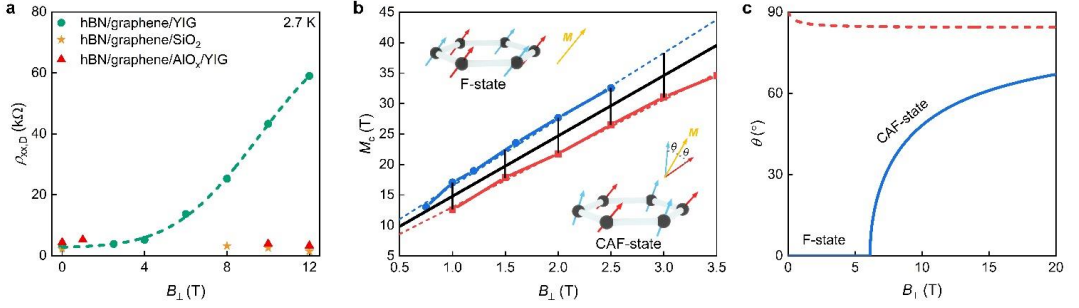


Figure S9 Phase transition diagrams. **(a)** $\rho_{xx,D}$ at Dirac point vs. B_{\perp} in hBN/graphene/YIG and control Hall bars (labelled) at 2.7 K. Green dashed curves are guides to the eye. **(b)** CAF- to F-state transition field M_c as a function of B_{\perp} , (blue line for $M_c = 10.9B_{\perp} + 5.6$, red line for $M_c = 8.8B_{\perp} + 4.2$ calculated from the previous experiment results⁶). The black line ($M_c = 9.9B_{\perp} + 4.9$) is an estimation for the phase transition, which is the average of the blue and red curves. **(c)** The polar angle θ of the spins relative to the direction of M as a function of B_{\perp} . The solid blue (dashed red) line corresponds to $M_{ex} = 60$ T ($M_{ex} = 0$). In the presence of proximity induced magnetic exchange field, it is possible to control θ with B_{\perp} . But in the absence of magnetic exchange field, $\theta \approx \pi/2$ for all values of B_{\perp} approximately corresponding to an AF-state.

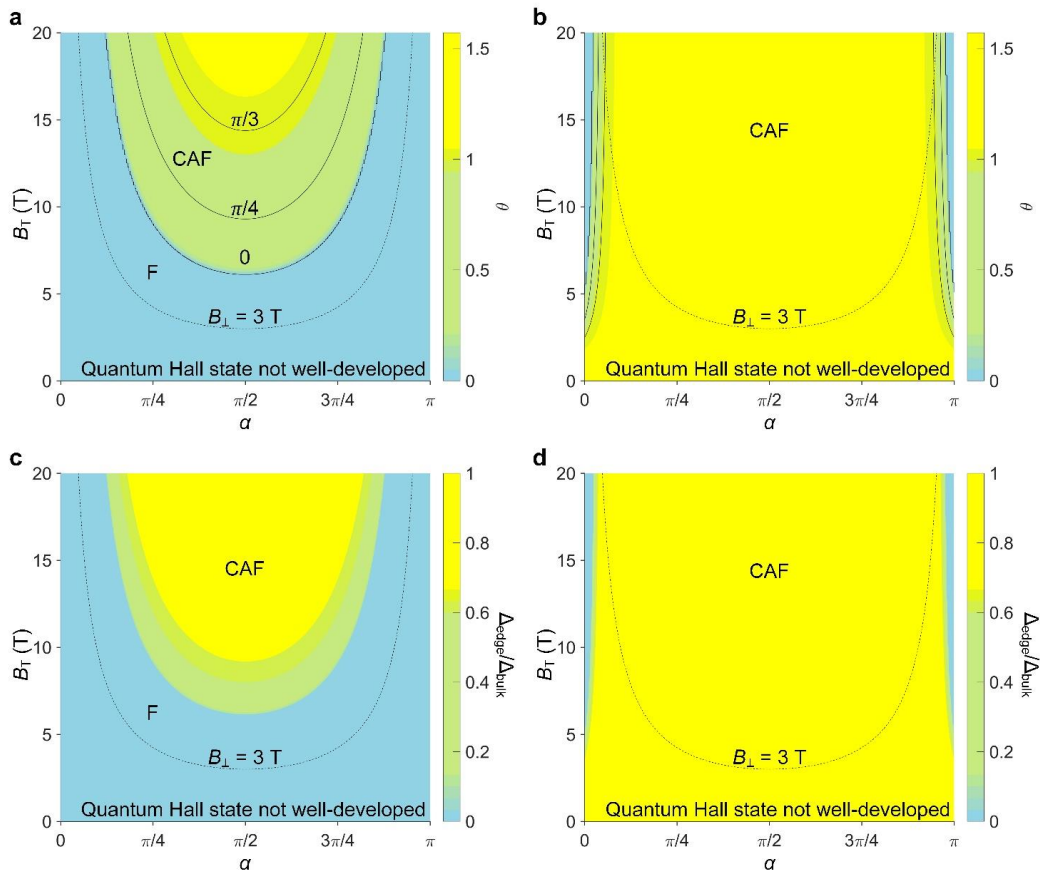


Figure S10 Phase transition versus the magnitude and direction of magnetic field B . **(a), (b)** The polar angle θ of the spins relative to the direction of M as a function of B and the angle α between magnetic field and sample surface for **(a)** $M_{\text{ex}} = 60$ T and **(b)** $M_{\text{ex}} = 0$. In the presence of magnetic exchange field, it is possible to control θ with the direction and magnitude of B and leading to a transition between CAF- and F-states. In the absence of magnetic exchange field, it needs a very large B in order to access the regime where θ can be changed substantially. The dashed line shows $B_{\perp} = 3$ T. Below this line, the quantum Hall state is not well-developed in our samples. **(c), (d)** The energy gap of the edge modes Δ_{edge} as a function of B and the angle α between magnetic field and sample surface for **(c)** $M_{\text{ex}} = 60$ T and **(d)** $M_{\text{ex}} = 0$. In the presence of magnetic exchange field, it is possible to control Δ_{edge} with the direction and magnitude of B . In the absence of magnetic exchange field, it needs very large values of B to tune Δ_{edge} substantially. The dashed line shows $B_{\perp} = 3$ T. Below this line the quantum Hall state is not well-developed in our samples.

VI

Reference

J. Linder, M. Amundsen, V. Risinggård.
Intrinsic superspin Hall current.
Physical Review B **96**, 094512 (2017).
10/gc5rrm

Contributions

JL initiated the project after discussions with MA. JL did the analytical and numerical work. VR and MA participated in the discussion of the results. JL conceived the physical mechanism responsible for the results after discussions with MA. VR compared and contrasted the superspin Hall effect with the ordinary spin Hall effect in terms of symmetry properties. JL drafted the manuscript. All authors contributed to the discussion of the physics and the revision of the final manuscript.

Comments

This work was presented at the 2016 workshop “Coherent superconducting hybrids and related materials” organized in the framework of COST action CA16218 (Les Arcs 1800, France).

Intrinsic superspin Hall current

Jacob Linder, Morten Amundsen, and Vetle Risinggård

Department of Physics, NTNU, Norwegian University of Science and Technology, N-7491 Trondheim, Norway and Center for Quantum Spintronics, Department of Physics, Norwegian University of Science and Technology, NO-7491 Trondheim, Norway

(Received 20 April 2017; revised manuscript received 16 August 2017; published 13 September 2017; corrected 3 May 2018)

We discover an intrinsic superspin Hall current: an injected charge supercurrent in a Josephson junction containing heavy normal metals and a ferromagnet generates a transverse spin supercurrent. There is no accompanying dissipation of energy, in contrast to the conventional spin Hall effect. The physical origin of the effect is an antisymmetric spin density induced among transverse modes k_y near the interface of the superconductor arising due to the coexistence of p -wave and conventional s -wave superconducting correlations with a belonging phase mismatch. Our predictions can be tested in hybrid structures including thin heavy metal layers combined with strong ferromagnets and ordinary s -wave superconductors.

DOI: [10.1103/PhysRevB.96.094512](https://doi.org/10.1103/PhysRevB.96.094512)

I. INTRODUCTION

By combining materials with different properties at the quantum-mechanical level into hybrid structures, new physics emerges that often cannot be found in pure materials. The field of superconducting spintronics [1] is a prime example of this, where the synthesis of superconducting and magnetic correlations has been shown [2–5] to yield physical effects that are interesting both from a fundamental viewpoint and from the viewpoint of potential cryogenic applications. One actively pursued direction in this field has been the prospect of producing dissipationless currents of spin carried by spin-polarized Cooper pairs [6,7]. The conversion of charge currents to spin currents is known to occur via the spin Hall effect [8–10] in conventional spintronics, but it is accompanied by the dissipation of energy due to the resistive nature of electric currents in nonsuperconducting structures. Here, we show that it is possible to achieve a dissipationless conversion from charge to spin supercurrents, using conventional superconducting materials. We discover that an injected charge supercurrent in a Josephson junction generates a pure transverse spin supercurrent that is thus time-reversal invariant. Due to the analogy with the conventional spin Hall current, we refer to this as a superspin Hall current. The microscopic origin of the superspin Hall current is a spin magnetization induced at the interface that is antisymmetric in transverse momentum k_y . This magnetization is in turn caused by the induction of p -wave superconductivity coexisting with conventional spin-singlet pairing. Our predictions can be verified using hybrid structures with thin heavy-metal layers combined with strong ferromagnets and ordinary s -wave superconductors (see Fig. 1) and open new vistas for making superconductors compatible with spintronics functionality.

II. THEORY

To describe physics occurring at atomic length scales and also incorporating strong spin-orbit coupling, we use the tight-binding Bogoliubov–de Gennes (BdG) framework, which is free from the limitations on length scales and self-energy magnitudes present in, e.g., quasiclassical theory [11]. Our

Hamiltonian reads

$$\begin{aligned}
 H = & -t \sum_{(i,j)\sigma} c_{i\sigma}^\dagger c_{j\sigma} - \frac{i}{2} \sum_{(i,j)\alpha\beta} \lambda_i c_{i\alpha}^\dagger \mathbf{n} \cdot (\boldsymbol{\sigma} \times \mathbf{d}_{ij})_{\alpha\beta} c_{j\beta} \\
 & - \sum_{i\sigma} \mu_i c_{i\sigma}^\dagger c_{i\sigma} - \sum_i U_i n_{i\uparrow} n_{i\downarrow} + \sum_{i\alpha\beta} c_{i\alpha}^\dagger (\mathbf{h}_i \cdot \boldsymbol{\sigma})_{\alpha\beta} c_{i\beta}.
 \end{aligned} \tag{1}$$

Here, t is the hopping integral, $\{c_{i\sigma}, c_{i\sigma}^\dagger\}$ are second-quantized fermion operators for site \mathbf{i} and spin σ , \mathbf{n} is a unit vector normal to the interface, λ_i is the site-dependent spin-orbit coupling magnitude, $\mathbf{d}_{ij} = -\mathbf{d}_{ji}$ is the nearest-neighbor vector from site \mathbf{i} to site \mathbf{j} , $n_{i\sigma} = c_{i\sigma}^\dagger c_{i\sigma}$, $\boldsymbol{\sigma}$ is the Pauli matrix vector, \mathbf{h}_i is the local magnetic exchange field, μ_i is the local chemical potential, and U_i is the on-site attractive interaction giving rise to superconductivity. For concreteness, we consider a square lattice of size $N_x \times N_y$ with lattice site indices $\mathbf{i} = (i_x, i_y)$. To demonstrate the superspin Hall current, we consider Fig. 1 which may be experimentally achieved by creating a stack of layers including one magnetic layer (e.g., Fe or Co) and two thin heavy-metal layers (e.g., Pt or Au) sandwiched between two conventional superconductors (e.g., Nb or Al). The various terms in Eq. (1) exist in their respective regions in Fig. 1. For instance, the spin-orbit coupling term λ_i is only finite for lattice points inside the heavy-metal regions. For brevity of notation, the lattice constant is set to $a = 1$ and all length scales are measured relative to a whereas all energies are measured relative to t . Since \mathbf{n} is the interface normal ($\mathbf{n} = \hat{\mathbf{x}}$), the Hamiltonian above is Hermitian without any requirement of symmetrization.

To simplify the calculations, we assume periodic boundary conditions in the $\hat{\mathbf{y}}$ direction, as is common practice [12–14]. While this represents an approximation to the geometry considered, it will still allow us to determine the presence of transverse currents. Equation (1) may now be diagonalized by Fourier transforming the fermion operators in the $\hat{\mathbf{y}}$ direction;

$$c_{i\sigma} = 1/\sqrt{N_y} \sum_{k_y} c_{i_x, k_y, \sigma} e^{ik_y i_y}. \tag{2}$$

Performing a standard mean-field ansatz $\Delta_i = -U_i \langle c_{i\downarrow} c_{i\uparrow} \rangle$, one arrives at the Hamiltonian

$$H = H_0 + \frac{1}{2} \sum_{ijk} B_{ik}^\dagger H_{ijk} B_{jk}, \quad (3)$$

where H_0 contains the superconducting condensation energy $N_y \sum_{i \in S} |\Delta_i|^2 / U_i$ (which must be retained when evaluating the free energy of the system). Let $i \equiv i_x$ and $j \equiv j_x$ from now on for brevity of notation. The superconducting regions are comprised of $N_{x,S}$ lattice points each, whereas the heavy metals generating interfacial Rashba spin-orbit coupling and strong ferromagnets have spatial extensions $N_{x,HM}$ and $N_{x,F}$, respectively. The total number of lattice sites is $N_x = N_y$. Setting $k \equiv k_y$, the basis above is

$$B_{ik}^\dagger = [c_{ik\uparrow}^\dagger, c_{ik\downarrow}^\dagger, c_{i,-k\uparrow}, c_{i,-k\downarrow}] \quad (4)$$

and we defined the 4×4 matrix:

$$H_{ijk} = \epsilon_{ijk} \hat{\sigma}_0 \hat{\tau}_3 + [h_i^y \hat{\sigma}_y + (\lambda \sin k/2) \hat{\sigma}_z] \hat{\tau}_0 + (h_i^x \hat{\sigma}_x + h_i^z \hat{\sigma}_z) \hat{\tau}_3 + \Delta_i i \hat{\sigma}_y \hat{\tau}^+ - \Delta_i^* i \hat{\sigma}_y \hat{\tau}^-, \quad (5)$$

where

$$\epsilon_{ijk} \equiv -t \cos(k) \delta_{ij} - t(\delta_{i,j+1} + \delta_{i,j-1})/2 - \mu_i \delta_{ij} \quad (6)$$

and $2\hat{\tau}^\pm \equiv \hat{\tau}_1 \pm i\hat{\tau}_2$. The matrices $\hat{\tau}_i$ that appear in Eq. (5) are the usual Pauli matrices ($i = 0, 1, 2, 3$, where $\hat{\tau}_0$ is the identity). By diagonalizing the above matrix, we end up with the Hamiltonian

$$H = H_0 + \frac{1}{2} \sum_{nk} E_{nk} \gamma_{nk}^\dagger \gamma_{nk}, \quad (7)$$

where the new (quasiparticle) fermion operators are related to the original ones via the relations

$$c_{ik\uparrow} = \sum_n u_{ink} \gamma_{nk}, \quad c_{ik\downarrow} = \sum_n v_{ink} \gamma_{nk}, \\ c_{i,-k,\uparrow}^\dagger = \sum_n w_{ink} \gamma_{nk}, \quad c_{i,-k,\downarrow}^\dagger = \sum_n x_{ink} \gamma_{nk}. \quad (8)$$

Here, $\{u, v, w, x\}$ are elements of the matrix that diagonalize the Hamiltonian and are numerically obtained. The diagonalized form of the Hamiltonian makes it trivial to evaluate expectation values of the type $\langle \gamma_{nk}^\dagger \gamma_{nk} \rangle = f(E_{nk}/2)$, where f is the Fermi-Dirac distribution function.

With the eigenvectors $\{u, v, w, x\}$ and eigenvalues $\{E_{nk}\}$ at hand, we can compute a number of physical quantities in the system under consideration. For instance, the order parameter takes the form

$$\Delta_i = -\frac{U_i}{L_y} \sum_{nk} v_{ink} w_{ink}^* [1 - f(E_{nk}/2)], \quad (9)$$

where the prime superscript on the sum indicates that only energy eigenvalues $|E_{nk}| < \omega_D$ should be included, and ω_D is the BCS Debye cutoff frequency. The free energy reads

$$F = H_0 - \frac{1}{\beta} \sum_{nk} \ln(1 + e^{-\beta E_{nk}/2}), \quad (10)$$

where $\beta = 1/T$ and T is temperature. The evaluation of charge and spin supercurrent \mathbf{j}_i and $\mathbf{j}_{i,S}$ operators requires a consid-

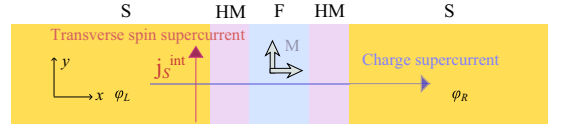


FIG. 1. Suggested experimental setup for demonstration of the superspin Hall current in a Josephson junction. The exchange field in the ferromagnetic region (gray arrows) is directed either along the \hat{x} or \hat{y} axis. In our calculations, we model the system as a 2D square lattice with periodic boundary conditions in the \hat{y} direction.

eration of the combined continuity and Heisenberg equation:

$$-\nabla \cdot \mathbf{j}_i = i[H, \rho_i], \quad -\nabla \cdot \mathbf{j}_i^S = i[H, \mathbf{S}_i]. \quad (11)$$

Here,

$$\rho_i = \sum_{\sigma} c_{i\sigma}^\dagger c_{i\sigma} \quad (12)$$

is the charge-density operator at site i , while

$$\mathbf{S}_i = \sum_{\alpha\beta} c_{i\alpha}^\dagger \boldsymbol{\sigma}_{\alpha\beta} c_{i\beta} \quad (13)$$

is the spin-density operator (we omitted constant prefactors such as the electronic charge $|e|$). After a Fourier transformation, the spin-density expectation value at site i reads

$$\mathbf{S}_i = \sum_{k\alpha\beta} \mathbf{S}_{ik}, \quad \mathbf{S}_{ik} = \langle c_{ik\alpha}^\dagger \boldsymbol{\sigma}_{\alpha\beta} c_{ik\beta} \rangle. \quad (14)$$

Here, \mathbf{S}_{ik} is the momentum-resolved spin-density expectation value at lattice point i , which will play a prominent role in the discussion later.

A spin supercurrent flowing along the interface has three polarization components and is most conveniently evaluated in the superconducting region:

$$\mathbf{j}_{i,S}^{\text{int}} = (\mathbf{j}_i^S \cdot \hat{y}) = -\frac{8t}{N_y} \sum_{k\alpha\beta} \sin(k) \boldsymbol{\sigma}_{\alpha\beta} \langle c_{ik\alpha}^\dagger c_{ik\beta} \rangle. \quad (15)$$

For instance, the spin supercurrent polarized in the \hat{x} and \hat{y} directions is

$$j_{i,S}^{\text{int},x} = -\frac{16t}{N_y} \sum_{nk} \sin(k) \text{Re}\{u_{ink} v_{ink}^*\} f(E_{nk}/2), \\ j_{i,S}^{\text{int},y} = \frac{16t}{N_y} \sum_{nk} \sin(k) \text{Im}\{u_{ink}^* v_{ink}\} f(E_{nk}/2). \quad (16)$$

III. RESULTS

A. Superspin Hall current

We first numerically diagonalize the Hamiltonian given by Eqs. (1) and (5) for the Josephson junction shown in Fig. 1 using the parameters $\mu_S = 0.9$, $\mu_N = 0.85$, $\mu_F = 0.8$, $\omega_D = 0.3$, $N_{x,S} = 35$, $N_{x,HM} = 4$, $N_{x,F} = 7$, $U = 2.1$, and $T = 0.01$. The order parameter phase is fixed at the last five lattice points in the S regions in order to model supercurrent injection via a phase difference, as is standard in the BdG lattice treatment. Fixing $\Delta\phi = 0.5\pi$ gives an effective

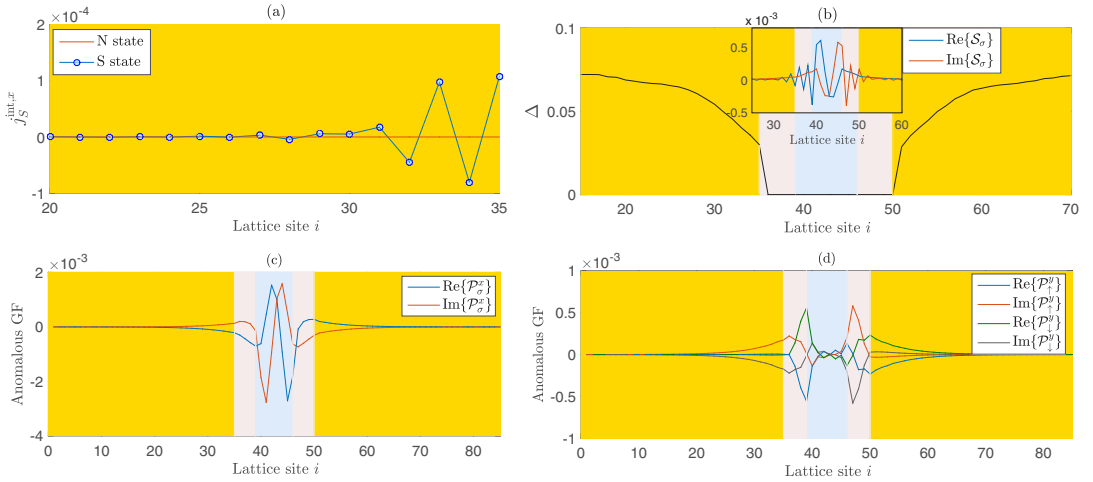


FIG. 2. (a) Superspin Hall current manifested via a transverse spin supercurrent $j_{i,S}^{\text{int},x}$ in the superconducting (S) state. It vanishes in the normal (N) state: $j_{i,S}^{\text{int},x} = 0$. (b) Spatial evolution of the superconducting order parameter. Inset: $S_{\sigma,i}(\tau)$ with relative time set to $\tau = 5$, (c) $\mathcal{P}_{\sigma,i}^x$, and (d) $\mathcal{P}_{\sigma,i}^y$. For the inset in panel (b) and in panel (c), the curves are identical for $\sigma = \uparrow$ and $\sigma = \downarrow$. We have used the parameter set specified in the main text, considered the system in Fig. 1, and set $h_y = 0.5$, $\lambda = 0.2$, and $\Delta\phi = 0.5\pi$.

phase difference between the superconducting interfaces of $\Delta\phi \simeq 0.47\pi$ due to the phase drop inside the superconductors. The following results are not qualitatively sensitive to the parameter choice above. For the above parameter set, and all other sets presented in the figures of this paper, we have checked that the superconducting state minimizes the free energy of the system.

When $\Delta\phi \neq 0$, a transverse spin supercurrent appears in the superconducting region as shown in Fig. 2(a). This demonstrates the intrinsic superspin Hall current. The effect occurs even if one removes one of the heavy-metal layers. The spin supercurrent predicted here does not exist in the absence of superconductivity, as also shown in Fig. 2(a). Reversing the phase difference, $\Delta\phi \rightarrow -\Delta\phi$, and thus the charge supercurrent, also reverses the transverse spin supercurrent. Before explaining the microscopic origin of the superspin Hall current, we note that there are both odd- and even-frequency triplet correlations in the system, denoted odd- ω and even- ω from now on. The on-site (s -wave) odd- ω anomalous triplet amplitudes \mathcal{S} are defined as

$$\begin{aligned} S_{0,i}(\tau) &= \langle c_{i\uparrow}(\tau)c_{i\downarrow}(0) \rangle + \langle c_{i\downarrow}(\tau)c_{i\uparrow}(0) \rangle, \\ S_{\sigma,i}(\tau) &= \langle c_{i\sigma}(\tau)c_{i\sigma}(0) \rangle, \end{aligned} \quad (17)$$

where τ is the relative time coordinate, and the subscripts 0 and $\sigma = \pm 1 = \uparrow, \downarrow$ denote the spin projection along the quantization axis. All \mathcal{S} vanish at $\tau = 0$. The p -wave even- ω anomalous triplet amplitudes \mathcal{P} have both a p_x - and p_y -wave component. They are defined as

$$\begin{aligned} \mathcal{P}_{0,i}^{x(y)} &= \sum_{\pm} \pm (\langle c_{i\uparrow}c_{i\pm\hat{x}(\hat{y}),\downarrow} \rangle + \langle c_{i\downarrow}c_{i\pm\hat{x}(\hat{y}),\uparrow} \rangle), \\ \mathcal{P}_{\sigma,i}^{x(y)} &= \sum_{\pm} \pm \langle c_{i\sigma}c_{i\pm\hat{x}(\hat{y}),\sigma} \rangle. \end{aligned} \quad (18)$$

The existence of these correlations and their spatial distribution throughout the system are shown in Figs. 2(b)–2(d), proving how they arise precisely near the interfaces between the superconductor and heavy metals where the transverse spin supercurrent flows. The triplet components of the Cooper pairs are generated from the broken spin rotational symmetry in our system, whereas the p -wave orbital symmetry emerges as a result of broken translational symmetry due to the presence of interfaces [16,17] and due to the presence of spin-orbit interactions. Note how the pairing amplitudes \mathcal{S} and \mathcal{P} are by definition \mathbf{k} -independent. The \mathbf{k} -resolved anomalous Green functions, which are odd under $\mathbf{k} \rightarrow (-\mathbf{k})$ for, e.g., p -wave pairing, will be examined in the following subsection as they play an important role in understanding the appearance of a transverse spin supercurrent.

The transverse spin-supercurrent in the present system exists when the exchange field contribution $\mathbf{h} \cdot \boldsymbol{\sigma}$ to the Hamiltonian does not commute with the spin-orbit contribution $\lambda \sin(k)\sigma_z$. In effect, the superspin Hall current arises when

$$[\mathbf{h} \cdot \boldsymbol{\sigma}, \lambda \sin(k)\sigma_z] \neq 0. \quad (19)$$

This means that the exchange field must be oriented in the xy plane of the system shown in Fig. 1. If the exchange field is oriented along the z axis, no superspin Hall current exists.

The polarization of the transverse spin-supercurrent is also dictated by the orientation of the exchange field \mathbf{h} . A comparison of Figs. 2(a) and 3(h) shows that the spin-supercurrent polarization is perpendicular to \mathbf{h} .

B. Microscopic origin

To explain the physical origin of the superspin Hall current in the system, we first note the close relation between the spin magnetization and the spin supercurrent in the system. From Eqs. (14) and (15), the only difference between them is a factor

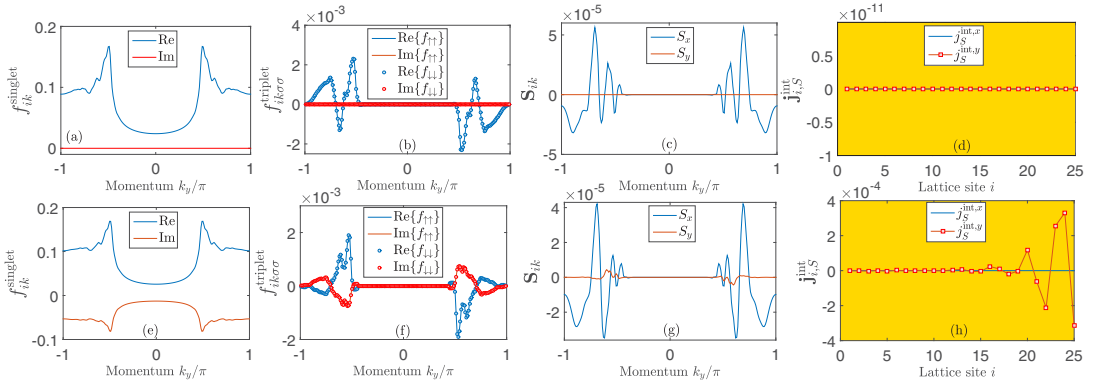


FIG. 3. Upper row: The panels show the induced singlet anomalous Green function f_{ik}^{singlet} , the triplet correlations $f_{ik\sigma\sigma}^{\text{triplet}}$ evaluated at lattice point $i_x = N_S - 1$ (right at the S/N interface), the induced spin-magnetization density S_{ik} evaluated at lattice point $i_x = N_S - 1$ (right at the S/N interface), and the superspin Hall current $j_{i,S}^{\text{int}}$, from left to right. Here, the phase difference has been set to $\Delta\phi = 0$, while $h = 0.3$, $\lambda = 0.3$, $T = 0.005$, $N_S = 25$, $N_{HM} = 4$, $N_F = 5$, $N_y = 200$, and $\mathbf{h} = h\hat{x}$. Lower row: Same as the upper row except that $\Delta\phi = \pi/2$. In this case, the coexistence of triplet and singlet correlations that are phase-mismatched produce an antisymmetric spin density S_{ik} , which in turn gives rise to a finite superspin Hall current. In the line labels of the second panels from the left, we have abbreviated $f_{ik\sigma\sigma}^{\text{triplet}} \equiv f_{\sigma\sigma}$. In this figure, the exchange field has been rotated to the \hat{x} direction to show that the superspin Hall current exists also in this case. In all other plots in this paper, the exchange field points in the \hat{y} direction.

$\sin(k_y)$ inside the summation. If the momentum-resolved spin magnetization S_{ik} is antisymmetric in momentum k_y , it will vanish when summed over the momentum index. However, due to the extra factor $\sin(k_y)$, an antisymmetric spin magnetization gives a symmetric spin supercurrent, which is thus finite upon summation over k_y . The factor $\sin(k_y)$ and the resulting difference in symmetry are physically reasonable. If a spin density is antisymmetric in momentum k_y , there will exist a net spin flow since the spin current requires an extra multiplication with the group velocity

$$\partial\epsilon_k/\partial k_y \propto \sin(k_y a) \quad (20)$$

for each transverse mode. On the other hand, a spin density that is symmetric in k_y does not induce any spin current.

An antisymmetric spin density in the momentum index k_y may emerge whenever conventional superconducting singlet pairing and triplet pairing (such as a p_y wave) coexist, for instance near interfaces, as we will explain below. A general superconducting order parameter F_{ik} accounting for both singlet and triplet pairing (considering here the even- ω symmetry contribution) can be written as

$$F_{ik} = (f_{i,s} + \mathbf{f}_{i,k} \cdot \boldsymbol{\sigma})i\sigma_2, \quad (21)$$

where $f_{i,s}$ is the singlet component and $\mathbf{f}_{i,k} = -\mathbf{f}_{i,-k}$ is a vector containing the triplet components according to

$$\mathbf{f} = \frac{1}{2}[f_{\downarrow\downarrow} - f_{\uparrow\uparrow}, -i(f_{\downarrow\downarrow} + f_{\uparrow\uparrow}), 2f_{\uparrow\downarrow}]. \quad (22)$$

Above, we suppressed the (i, \mathbf{k}) indices on the triplet anomalous Green functions $f_{ik\sigma\sigma'}$ for brevity of notation, and we also do so below when the index is not of importance for the argument. A nonunitary superconducting state, where the Cooper pairs have a finite spin expectation value, is defined by FF^\dagger not being proportional to the unit matrix.

A straightforward calculation shows that

$$FF^\dagger = |f_s|^2 + |\mathbf{f}_k|^2 + \boldsymbol{\sigma} \cdot [(f_s \mathbf{f}_k^* + f_s^* \mathbf{f}_k) + i(\mathbf{f}_k \times \mathbf{f}_k^*)]. \quad (23)$$

The term $i(\mathbf{f}_k \times \mathbf{f}_k^*)$ determines the spin expectation value of pure triplet Cooper pairs, whereas $(f_s \mathbf{f}_k^* + f_s^* \mathbf{f}_k)$ determines the spin magnetization of a given mode k_y resulting from the coexistence of singlet and triplet pairing. The spin magnetization arising due to the Cooper pairs in the system thus takes, in general, the following form for a given mode k_y :

$$S_k^{\text{Cooper}} \propto (f_s \mathbf{f}_k^* + f_s^* \mathbf{f}_k) + i(\mathbf{f}_k \times \mathbf{f}_k^*). \quad (24)$$

Performing a summation over modes k_y , one obtains the total spin density. Therefore, it is clear that if $(f_s \mathbf{f}_k^* + f_s^* \mathbf{f}_k) = 2\text{Re}\{f_s \mathbf{f}_k^*\}$ is nonzero, it will be antisymmetric in k_y due to the fundamental property of the triplet vector \mathbf{f}_k . It is crucial to note that the existence of p -wave triplet pairing alone is not sufficient to produce an antisymmetric spin density in k_y space. First of all, it has to coexist with singlet pairing. But even such a scenario is not sufficient, as it is only the real part of the product $f_s \mathbf{f}_k^*$ that contributes. Consider, for instance, the case in which singlet pairing coexists with $S_z = 0$ triplet pairing, such that $\mathbf{f}_k \parallel \hat{z}$. According to our above argumentation, this should produce a magnetization in the \hat{z} direction. It is not immediately obvious how a magnetization in the \hat{z} direction can arise from singlet pairs (which are spinless) and triplet pairs with zero spin projection along the \hat{z} axis. Therefore, we provide a detailed exposition of the physical mechanism behind this effect in the Appendix.

With this in mind, we can now explain why the superspin Hall current appears. As argued above, this current will exist when an antisymmetric spin density is induced near the interface. The spin density, in turn, is determined by the generation of p -wave superconducting correlations coexisting

with conventional singlet ones when these have an appropriate relative phase such that $\text{Re}\{f_s f_k^*\} \neq 0$ (as explained in the Appendix). The equal spin-pairing triplet anomalous Green functions may be obtained as

$$\begin{aligned} f_{ik\sigma\sigma}^{\text{triplet}} &= \langle c_{i,k,\sigma} c_{i,-k,\sigma} \rangle \\ &= \begin{cases} \sum_n u_{ink} w_{ink}^* [1 - f(E_{nk}/2)] & \text{for } \sigma = \uparrow, \\ \sum_n v_{ink} x_{ink}^* [1 - f(E_{nk}/2)] & \text{for } \sigma = \downarrow, \end{cases} \end{aligned} \quad (25)$$

where, as before, we have used the shorthand notation of $k_y \equiv k$. We now illustrate two instructive cases in Fig. 3. In the upper row (a)–(d), the phase difference is $\Delta\phi = 0$ (no current injected) while in the lower row (e)–(h), the phase difference is $\Delta\phi = \pi/2$ (finite current injected). In both cases, we have set $h = 0.3$, $\lambda = 0.3$, and $\mathbf{h} = h\hat{x}$. We also chose a different system size, exchange field orientation, and number of transverse modes from those in the previous figures in order to show that the effect does not depend on these details: $N_S = 25$, $N_{HM} = 4$, $N_F = 5$, and $N_y = 200$. As expected, a finite net magnetization S_x exists in the upper row, which comes from the inverse proximity effect caused by the magnetic region. However, there exists no net or k_y -resolved magnetization S_y despite the fact that the anomalous triplet correlations $f_{ik\sigma\sigma}^{\text{triplet}} \equiv f_{\sigma\sigma}$ are nonzero. The reason for this is that they are purely real, as seen in the figure. Consequently, $\text{Re}\{f_s f_k^*\} = 0$ since the singlet ones are purely real in the absence of a phase gradient. Note how the figure shows that $f_{\uparrow\uparrow} = f_{\downarrow\downarrow}$, such that no antisymmetric contribution is made to the x component according to Eq. (22). The finite magnetization induced along the x direction is instead caused by the odd- ω triplet component. In general, the triplet vector \mathbf{f} can have both a symmetric term in \mathbf{k} (the odd- ω component) and an antisymmetric term in \mathbf{k} (the even- ω component). Only the latter contributes to the spin supercurrent in the present context, as explained above.

Consider now instead the lower row, where a finite phase difference exists. The singlet and triplet correlations are now complex because of $\Delta\phi \neq 0$, and as a result the y component of the spin-magnetization (which exists since the term $\text{Re}\{f_s f_k^*\}$ is nonzero) is finite and antisymmetric in k_y . Although no net magnetization exists in the y direction, a net spin supercurrent now exists due to the relation between Eqs. (14) and (15) explained above. A phase gradient is thus physically required in order to render the singlet and triplet p_y -wave correlations complex: otherwise, no antisymmetric spin magnetization associated with a nonunitary superconducting state exists, and the spin supercurrent is zero. This explains the origin of the superspin Hall current predicted in this paper.

The above explanation is consistent irrespective of the direction of the in-plane exchange field. For instance, if we instead choose $\mathbf{h} = h\hat{y}$, one finds that the triplet anomalous function is purely imaginary at $\Delta\phi = 0$ and that $f_{\uparrow\uparrow} = -f_{\downarrow\downarrow}$. In this case, there is no contribution to the \hat{y} component according to Eq. (22), and although $\mathbf{f}_k \cdot \hat{x} \neq 0$ there is still no antisymmetric spin density since $\text{Re}\{f_s f_k^*\} = 0$. If $\Delta\phi \neq 0$, on the other hand, $\text{Re}\{f_s f_k^*\}$ is finite in the \hat{x} direction and a spin supercurrent polarized in this direction appears, as seen in the figure.

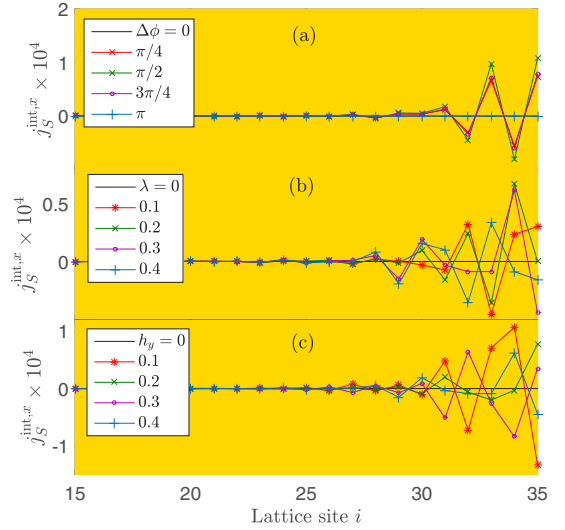


FIG. 4. The dependence of the superspin Hall current $j_{i,S}^{\text{int},x}$ on physical parameters in the system (Fig. 1). (a) $\lambda = 0.2$ and $h_y = 0.5$ for various values of the phase difference $\Delta\phi$. (b) $\Delta\phi = \pi/2$ and $h_y = 0.4$ for several spin-orbit magnitudes λ . (c) $\lambda = 0.3$ and $\Delta\phi = \pi/2$ for various values of the exchange field h_y . The values of the remaining parameters are the same as in Fig. 2. The background color indicates in which region the current has been evaluated (compare with the left part of Fig. 1).

The spatial dependence of the superspin Hall current on the phase difference, the Rashba spin-orbit interaction, and exchange field is shown in Fig. 4. The effect vanishes both in the absence of superconductivity ($\Delta\phi = 0$) and in the absence of a charge supercurrent ($\Delta\phi = 0$), as follows from the above explanation of the physical origin of the effect. We also find that the magnitude of the transverse current $j_{i,S}^{\text{int},x}$ evaluated at the superconducting interface ($i = N_S \equiv N_{x,S}$) oscillates with

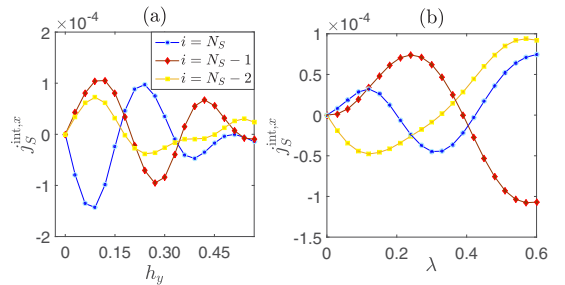


FIG. 5. The dependence of the superspin Hall current $j_{i,S}^{\text{int},x}$ on physical parameters in the system, evaluated at different lattice sites i . We have set $\Delta\phi = 0.5\pi$ and (a) $\lambda = 0.3$ and (b) $h_y = 0.4$. The values of the remaining parameters are the same as in Fig. 2. A scattering potential $V_{\text{int}} = 0.1$ at each of the interfaces was also added here to show that the effect is resilient toward interfacial scattering. The current oscillates with both h and λ and eventually decays with both as these quantities increase and suppress superconductivity.

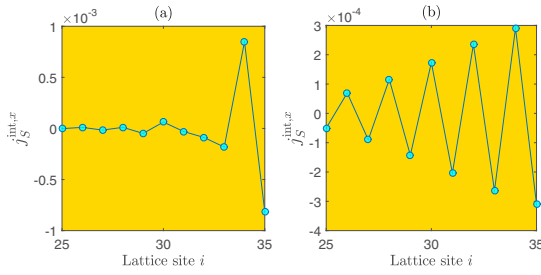


FIG. 6. Change in oscillation length of the superspin Hall current as the magnitude of the Rashba spin-orbit parameter is altered. The plots show the cases (a) $\lambda = 0.1$ and (b) $\lambda = 2.1$. The exchange field is $\mathbf{h} = h\hat{y}$ with $h = 0.3$, $T = 0.005$, and the other parameters are the same as in Fig. 2.

both the Rashba strength and the magnitude of the exchange field for the parameter regimes we have investigated, as shown in Fig. 5. The effect is also purely sinusoidal as a function of the superconducting phase difference $\Delta\phi$ (not shown). The oscillations could stem from the change in \mathbf{k} -space band structure due to the inverse proximity effect near the interface as one varies the magnitude of h and λ , as the detailed \mathbf{k} dependence of the spin magnetization (and thus in turn the magnitude of the spin supercurrent after summation over \mathbf{k}) will be affected by the details of the band structure.

The atomic-scale superimposed oscillations are characteristic for physical quantities in ballistic quantum-mechanical systems and are also present in, e.g., the proximity-induced magnetization in conventional superconductors [15] and helical edge-mode currents in triplet superconductors [14]. It should be noted, however, that the oscillation period of the spin supercurrent depends here on the system parameters. This is shown in Fig. 6, where it is clear that the oscillation period is altered by changing the magnitude of the Rashba parameter. The origin of the oscillations is likely to be similar to that described in Ref. [14], namely due to an interplay between the renormalized spectral weight in the superconductor due to the inverse proximity effect and how the p -wave superconducting correlations decay as a result.

IV. CONCLUDING REMARKS

Previous theoretical work has considered spin accumulation from spin Hall effects in superconducting structures [18–23], and a recent experimental work [24] demonstrated an enhancement of the inverse spin Hall signal [10] in a superconductor by three orders of magnitude. A similar edge spin magnetization might occur from the superspin Hall current predicted in this work. Although the interface between a superconductor and a ferromagnet breaks inversion symmetry on its own, the purpose of the HM layers is to enhance the magnitude of the resulting Rashba interaction. A transverse spin current induced by a charge supercurrent was also considered in Ref. [25], albeit in a different setup where spin-orbit coupling was present in the entirety of one superconducting region and where no magnetism was present. Reference [26] considered spin Hall effects in a Josephson setup both with and without an electric bias voltage applied to the system.

It is worth remarking that in comparison to the typical spin Hall phenomenology, where an injected current in the x direction is deflected in the y direction and polarized in the z direction, the spin supercurrent here is not polarized perpendicularly to the plane defined by its injection and deflection direction. However, similarly to the conventional spin Hall phenomenology, the spin supercurrent arises as a direct consequence of Cooper pairs that are polarized in the z direction. The details regarding how $S_z = \pm 1$ Cooper pairs give rise to a spin supercurrent polarized in the xy plane have been covered in detail in the main body of this paper.

Interesting future directions to explore include the precise circulation pattern of the superspin Hall current predicted herein in a finite-width sample, and the possible accompanying edge spin accumulation due to triplet Cooper pairs.

ACKNOWLEDGMENTS

J.L. thanks J. A. Ouassou for helpful discussions regarding the numerical analysis. The authors thank J. A. Ouassou, S. Jacobsen, A. Black-Schaffer, and H. Simensen for discussions. Funding via the Outstanding Academic Fellows program at NTNU, the NV-Faculty, and the Research Council of Norway Grants No. 216700 and No. 240806 and funding for the Center of Excellence QuSpin are gratefully acknowledged.

J.L. and M.A. contributed equally to this work.

APPENDIX: MAGNETIZATION ARISING OUT OF A NONUNITARY COEXISTENCE OF SINGLET AND TRIPLET PAIRING

Consider for simplicity a bulk system in which singlet pairing Δ_s coexists with $S_z = 0$ triplet pairing $\Delta_k = -\Delta_{-k}$. The Hamiltonian reads

$$H = \sum_{\mathbf{k}} \phi_{\mathbf{k}}^\dagger M_{\mathbf{k}} \phi_{\mathbf{k}}, \quad (\text{A1})$$

where we used a basis $\phi_{\mathbf{k}} = [c_{\mathbf{k}\uparrow} \ c_{\mathbf{k}\downarrow} \ c_{-\mathbf{k}\uparrow}^\dagger \ c_{-\mathbf{k}\downarrow}^\dagger]^\text{T}$ and defined

$$M_{\mathbf{k}} = \begin{pmatrix} \epsilon_{\mathbf{k}} & 0 & 0 & \Delta_{\mathbf{k}} + \Delta_s \\ 0 & \epsilon_{\mathbf{k}} & \Delta_{\mathbf{k}} - \Delta_s & 0 \\ 0 & \Delta_{\mathbf{k}}^* - \Delta_s^* & -\epsilon_{\mathbf{k}} & 0 \\ \Delta_{\mathbf{k}}^* + \Delta_s^* & 0 & 0 & -\epsilon_{\mathbf{k}} \end{pmatrix}. \quad (\text{A2})$$

The four eigenvalues are given as $\{E_+, E_-, -E_+, -E_-\}$, where

$$E_{\pm} = \sqrt{\epsilon_{\mathbf{k}}^2 + |\Delta_s \pm \Delta_{\mathbf{k}}|^2}. \quad (\text{A3})$$

Performing a standard diagonalization of the Hamiltonian by introducing a new quasiparticle basis

$$\gamma_{\mathbf{k}} = [\gamma_{1\mathbf{k}} \ \gamma_{2\mathbf{k}} \ \gamma_{3\mathbf{k}} \ \gamma_{4\mathbf{k}}]^\text{T}, \quad (\text{A4})$$

where $\gamma_{i\mathbf{k}}$ are second-quantized fermion operators, one arrives at

$$H = \sum_{\mathbf{k}} [E_{\mathbf{k}+} (\gamma_{1\mathbf{k}}^\dagger \gamma_{1\mathbf{k}} - \gamma_{2\mathbf{k}}^\dagger \gamma_{2\mathbf{k}}) + E_{\mathbf{k}-} (\gamma_{3\mathbf{k}}^\dagger \gamma_{3\mathbf{k}} - \gamma_{4\mathbf{k}}^\dagger \gamma_{4\mathbf{k}})]. \quad (\text{A5})$$

The relation between the original fermion operators c and the new ones γ is

$$\phi_k = P_k \gamma_k, \quad (\text{A6})$$

where P_k is the diagonalizing matrix containing the eigenvectors of the original Hamiltonian,

$$P_k = \begin{pmatrix} g_+(E_{k+}) & g_+(-E_{k+}) & 0 & 0 \\ 0 & 0 & g_-(E_{k-}) & g_+(-E_{k-}) \\ 0 & 0 & 1 & 1 \\ 1 & 1 & 0 & 0 \end{pmatrix}, \quad (\text{A7})$$

and we defined the auxiliary quantity

$$g_{\pm}(E) = \frac{\Delta_k \pm \Delta_s}{E - \epsilon_k}. \quad (\text{A8})$$

Now, the magnetization of the system in the \hat{z} direction is computed according to Eq. (14):

$$S_z = \sum_{k\sigma} \sigma \langle c_{k\sigma}^\dagger c_{k\sigma} \rangle. \quad (\text{A9})$$

To see how this magnetization is directly influenced by the coexistence of singlet and triplet pairs in the system, we replace the original fermion operators in Eq. (A9) with the new ones according to Eq. (A6). Considering for simplicity the $T = 0$ limit, one arrives at

$$S_z = \sum_k [|g_+(-E_{k+})|^2 - |g_-(-E_{k-})|^2]. \quad (\text{A10})$$

At this point, we distinguish between unitary and nonunitary states. In the *unitary case*, we have $\text{Re}\{\Delta_s \Delta_k^*\} = 0$ so that $E_{k+} = E_{k-}$: the magnitudes of both gaps $\Delta_{\pm} = \Delta_k \pm \Delta_s$ are equal. Moreover, it follows from Eq. (A8) that in the unitary case one has $|g_+(x)| = |g_-(x)|$. Combining these two facts, it follows that the term inside the summation \sum_k in Eq. (A10) is zero for any k value. In effect, there is no magnetization at any k point and obviously no net magnetization either.

Consider now instead a nonunitary state where $\text{Re}\{\Delta_s \Delta_k^*\} \neq 0$. In this case, the magnitudes of the gaps Δ_{\pm}

are *different*. Now, the term inside the summation of Eq. (A10) is no longer zero for a given k point. In effect, there exists a k -resolved magnetization. The *total magnetization*, obtained after a summation over k , is nevertheless zero even in the nonunitary case. This can be verified by splitting the sum in Eq. (A10) into $k > 0$ and $k < 0$ (the contribution from $k = 0$ vanishes) and using the general relation $E_{k,+} = E_{-k,-}$.

The above derivation establishes mathematically why a k -resolved, antisymmetric spin magnetization exists when singlet and p -wave triplet pairing coexists in a nonunitary state, precisely as in the system considered in the main body of this paper. The *physical picture* can be understood by going back to the fact that there exists two gaps with a different magnitude in the system. It is well known that the superconducting order parameter (gap) determines the condensation energy and binding energy between the electrons comprising the Cooper pairs. In particular, the Cooper pair density is proportional to the square of the magnitude of the gap. The point here is that Cooper pairing between two electron states $|k, \uparrow\rangle$ and $| -k, \downarrow\rangle$ is associated with a gap magnitude $|\Delta_k + \Delta_s| \equiv |\Delta_+|$, whereas pairing between two electron states $|k, \downarrow\rangle$ and $| -k, \uparrow\rangle$ is associated with a different gap magnitude $|\Delta_k - \Delta_s| \equiv |\Delta_-|$. This can be seen directly from the Hamiltonian that contains the terms $c_{k\uparrow}^\dagger c_{-k\downarrow}^\dagger \Delta_+$ and $c_{k\downarrow}^\dagger c_{-k\uparrow}^\dagger \Delta_-$. Now, if $|\Delta_+| > |\Delta_-|$ for a given k value, it is clear that the system will favor Cooper pairs where the \uparrow electron of the pair sits at k whereas the \downarrow electron sits at $-k$, since the Cooper pair state where the \uparrow electron sits at $-k$ and the \downarrow electron sits at k has a smaller binding energy. Therefore, a *net spin magnetization arises at k* since there exists a surplus of \uparrow spins there compared to \downarrow spins due to the difference in Cooper pair density stemming from the different gap magnitudes. Simultaneously, the opposite magnetization arises at $-k$ since at that momentum the situation is reversed: $|\Delta_-|$ is larger than $|\Delta_+|$ at $-k$.

In this way, the different magnitudes of the two gaps in a system where singlet pairing coexists with $S_z = 0$ triplet pairing in a nonunitary state cause the Cooper pairs to provide a k -resolved magnetization in the \hat{z} direction despite the fact that the net Cooper pair spin in the \hat{z} direction is zero.

-
- [1] J. Linder and J. W. A. Robinson, Superconducting spintronics, *Nat. Phys.* **11**, 307 (2015).
- [2] V. V. Ryazanov, V. A. Oboznov, A. Yu. Rusanov, A. V. Veretennikov, A. A. Golubov, and J. Aarts, Coupling of Two Superconductors Through a Ferromagnet: Evidence for a π -Junction, *Phys. Rev. Lett.* **86**, 2427 (2001).
- [3] M. G. Blamire and J. W. A. Robinson, The interface between superconductivity and magnetism: Understanding and device prospects, *J. Phys.: Condens. Matter* **26**, 453201 (2014).
- [4] M. Eschrig, Spin-polarized supercurrents for spintronics: A review of current progress, *Rep. Prog. Phys.* **78**, 104501 (2015).
- [5] D. Beckmann, Spin manipulation in nanoscale superconductors, *J. Phys.: Condens. Matter* **28**, 163001 (2016).
- [6] R. S. Keizer *et al.*, A spin triplet supercurrent through the half-metallic ferromagnet CrO₂, *Nature (London)* **439**, 825 (2006).
- [7] M. Eschrig and T. Löfwander, Triplet supercurrents in clean and disordered half-metallic ferromagnets, *Nat. Phys.* **4**, 138 (2008).
- [8] M. I. Dyakonov and V. I. Perel, Possibility of orientating electron spins with current, *JETP Lett.* **13**, 467 (1971).
- [9] M. I. Dyakonov and V. I. Perel, Current-induced spin orientation of electrons in semiconductors, *Phys. Lett. A* **35**, 459 (1971).
- [10] J. E. Hirsch, Spin Hall Effect, *Phys. Rev. Lett.* **83**, 1834 (1999).
- [11] V. Chandrasekhar, *Proximity-Coupled Systems: Quasiclassical Theory of Superconductivity in Superconductivity: Conventional and Unconventional Superconductors*, edited by K. H.

- Bennemann and J. B. Ketterson (Springer, Berlin, 2008), Chap. 8, pp. 279–313.
- [12] J.-X. Zhu and C. S. Ting, Proximity effect, quasiparticle transport, and local magnetic moment in ferromagnet d -wave-superconductor junctions, *Phys. Rev. B* **61**, 1456 (2000).
- [13] A. M. Black-Schaffer and S. Doniach, Self-consistent solution for proximity effect and Josephson current in ballistic graphene SNS Josephson junctions, *Phys. Rev. B* **78**, 024504 (2008).
- [14] D. Terrade, D. Manske, and M. Cuoco, Control of edge currents at a ferromagnet-triplet superconductor interface by multiple helical modes, *Phys. Rev. B* **93**, 104523 (2016).
- [15] K. Halterman, O. T. Valls, and P. H. Barsic, Induced triplet pairing in clean s -wave superconductor/ferromagnet layered structures, *Phys. Rev. B* **77**, 174511 (2008).
- [16] Y. Tanaka, A. A. Golubov, S. Kashiwaya, and M. Ueda, Anomalous Josephson Effect Between Even- and Odd-Frequency Superconductors, *Phys. Rev. Lett.* **99**, 037005 (2007).
- [17] M. Eschrig, T. Löfwander, T. Champel, J. C. Cuevas, J. Kopu, and G. Schön, Symmetries of pairing correlations in superconductor-ferromagnet nanostructures, *J. Low Temp. Phys.* **147**, 457 (2007).
- [18] S. Pandey, H. Kontani, D. S. Hirashima, R. Arita, and H. Aoki, Spin Hall effect in iron-based superconductors: A Dirac-point effect, *Phys. Rev. B* **86**, 060507(R) (2012).
- [19] H. Kontani, J. Goryo, and D. S. Hirashima, Intrinsic Spin Hall Effect in the s -Wave Superconducting State: Analysis of the Rashba Model, *Phys. Rev. Lett.* **102**, 086602 (2009).
- [20] K. Sengupta, R. Roy, and M. Maiti, Spin Hall effect in triplet chiral superconductors and graphene, *Phys. Rev. B* **74**, 094505 (2006).
- [21] F. S. Bergeret and I. V. Tokatly, Manifestation of extrinsic spin Hall effect in superconducting structures: Nondissipative magnetoelectric effects, *Phys. Rev. B* **94**, 180502(R) (2016).
- [22] A. G. Mal'shukov, S. Sadjina, and A. Brataas, Inverse spin Hall effect in superconductor/normal-metal/superconductor Josephson junctions, *Phys. Rev. B* **81**, 060502(R) (2010).
- [23] A. G. Mal'shukov, Supercurrent generation by spin injection in an s -wave superconductor–Rashba metal bilayer, *Phys. Rev. B* **95**, 064517 (2017).
- [24] T. Wakamura, H. Akaike, Y. Omori, Y. Niimi, S. Takahashi, A. Fujimaki, S. Maekawa, and Y. Otani, Quasiparticle-mediated spin Hall effect in a superconductor, *Nat. Mater.* **14**, 675 (2015).
- [25] Y. Zhi-Hong *et al.*, Interfacial spin Hall current in a Josephson junction with Rashba spin-orbit coupling, *Chin. Phys. B* **21**, 057402 (2012).
- [26] A. G. Mal'shukov and C. S. Chu, Spin Hall effect in a Josephson contact, *Phys. Rev. B* **78**, 104503 (2008); Spin-Hall current and spin polarization in an electrically biased SNS Josephson junction, *ibid.* **84**, 054520 (2011).

VII

Reference

V. Risinggård, J. Linder.

Direct and inverse superspin Hall effect in two-dimensional systems:

Electrical detection of spin supercurrents.

Physical Review B **99**, 174505 (2019).

10/c5qh

Contributions

VR and JL initiated the project. VR decided on a system geometry. VR did the analytical and numerical work, and drafted the manuscript. JL supervised the project. Both authors contributed to the discussion of the results and the revision of the final manuscript.

Direct and inverse superspin Hall effect in two-dimensional systems: Electrical detection of spin supercurrents

Vetle Risinggård* and Jacob Linder

Center for Quantum Spintronics, Department of Physics, NTNU, Norwegian University of Science and Technology, N-7491 Trondheim, Norway



(Received 22 November 2018; revised manuscript received 8 April 2019; published 8 May 2019)

A useful experimental signature of the ordinary spin Hall effect is the spin accumulation it produces at the sample edges. The superspin Hall current [Phys. Rev. B **96**, 094512 (2017)] is a transverse equilibrium spin current which is induced by a charge supercurrent. We study the superspin Hall current numerically, and find that it does not give rise to a similar edge magnetization. We also predict and numerically confirm the existence of the inverse superspin Hall effect, which produces a transverse charge supercurrent in response to an equilibrium spin current. We verify the existence of the inverse superspin Hall effect both for a spin-polarized charge supercurrent and an exchange spin current, and propose that a ϕ_0 junction produced by the inverse superspin Hall effect can be used to directly and electrically measure the spin polarization of a charge supercurrent. This provides a possible way to solve the long-standing problem of how to directly detect the spin polarization of supercurrents carried by triplet Cooper pairs.

DOI: [10.1103/PhysRevB.99.174505](https://doi.org/10.1103/PhysRevB.99.174505)

I. INTRODUCTION

Spin-polarized supercurrents are a central theme in superconducting spintronics [1]. Cooper pairs in conventional Bardeen–Cooper–Schrieffer superconductors are in the spin-singlet state [2–4]. Consequently, supercurrents in conventional superconductors are not spin polarized. To spin polarize such a supercurrent, the spin-singlet pairs must be converted to equal-spin triplet pairs. This can be accomplished by combining the processes known as spin mixing and spin rotation [1,5–7]. Because of the exchange splitting, proximity-induced Cooper pairs in a ferromagnet will oscillate between the spin-singlet and the spin-0 triplet state [8,9]. This is known as spin mixing. A magnetic inhomogeneity or spin-orbit coupling can rotate the resulting spin-0 triplets into equal-spin triplets [10–14]. This is known as spin rotation. So far, such a spin polarization of the supercurrent carried by triplet Cooper pairs has not been detected directly, but is only inferred from otherwise inexplicably long-ranged supercurrents in proximity structures [7].

Long-ranged spin-polarized supercurrents in phase-biased Josephson junctions are equilibrium currents. Various authors have suggested that spin supercurrents have observable consequences that can be detected via electrical [15–17] or mechanical [18] means, or through the magnetization dynamics they induce [19,20]. Nonetheless, experimental detection schemes based on these signatures have yet to be implemented. One particular difficulty with these suggestions is that an equilibrium spin current by definition cannot perform work without dissipating. Consequently, any attempt to extract useful work from, say, a voltage induced by an equilibrium spin current in order to detect that current will dissipate the spin current itself.

The spin Hall effect [21] and its Onsager reciprocal [22–24] have found many applications in nonsuperconducting spintronics. Among others, these include electrical detection of spin currents induced by spin pumping [25] or the spin Seebeck effect [26], spin Hall magnetoresistance [27,28], and spin Hall spin-transfer torques [29]. It is only natural to inquire whether a superconducting analog of the spin Hall effect can be used to detect the spin-polarization of a supercurrent.

Spin Hall effects in superconducting structures have been considered previously in several theoretical and experimental works. References [30–35] considered out-of-equilibrium situations, in which quasiparticle effects give rise to spin (charge) currents as a result of charge (spin) injection. In particular, Ref. [35] measured an enhancement of the inverse spin Hall signal by three orders of magnitude when the NbN is cooled below the superconducting transition temperature. References [36–40] considered equilibrium situations and it was shown that the combination of spin-orbit coupling and an exchange field could induce a phase difference between two superconductors to obtain a ϕ_0 junction [37,38].

In Ref. [41], we considered an equilibrium transverse spin current generated by a longitudinal charge supercurrent in a Josephson junction, which we will refer to here as the *superspin Hall current*. Whereas most studies of spin Hall effects in superconductors consider purely *s*-wave or quasiparticle effects [30–39], the superspin Hall current is the result of an interplay between the *s*-wave condensate of a conventional superconductor and a proximity-induced *p*-wave condensate. As opposed to the interfacial spin current considered in Ref. [40], the superspin Hall current considered in Ref. [41] arises in a magnetic Josephson junction. In Ref. [41], we also consider the ballistic limit, rather than the diffusive limit considered in Refs. [31,37–39].

An open question regarding the superspin Hall current is whether or not it induces an edge spin magnetization which

*vetle.k.risinggard@ntnu.no

could serve as an experimental signature of its existence. This question was not addressed in Ref. [41], which considered periodic boundary conditions and thus in practice a cylindrical geometry.

In this paper, we present two main results. The first result is a full two-dimensional analysis of the superspin Hall effect where we are able to address the issue of what happens to the spin supercurrent at the edges of the system. This issue is of interest with respect to possible experimental probes of the effect.

The second result is the prediction of a corresponding *inverse effect*, namely the inverse superspin Hall effect. In this case, an equilibrium spin current produces a transverse charge supercurrent, which gives rise to a ϕ_0 shift in the Josephson junction. The ϕ_0 shift is—as opposed to previous predictions of ϕ_0 junctions incorporating spin-orbit coupling and ferromagnets [19,37,38,42]—induced by a pure equilibrium spin current. We propose that the ϕ_0 shift can be used to detect the spin polarization of a supercurrent carried by Cooper pairs. Being an equilibrium property of the junction we consider, this detection scheme will not dissipate the equilibrium spin current. This offers a way to electrically and directly verify the spin polarization of previously detected long-ranged supercurrents [43–48].

The superspin Hall effect can not only be used to detect spin-polarized supercurrents, but also other equilibrium spin currents. To illustrate this we also calculate the ϕ_0 shift induced by the exchange spin current between two misaligned ferromagnets [49,50].

II. INTRODUCTION TO THE SUPERSPIN HALL EFFECT

The intrinsic superspin Hall effect, which we considered in Ref. [41], arises in a magnetic Josephson junction with Rashba spin-orbit interlayers, see Fig. 1. When a phase difference ϕ is applied over the junction, so that a longitudinal charge current flows between the two superconductors, a transverse spin current is induced near the superconductor–Rashba-metal interface. Being transverse, it flows parallel to the interface (y direction). Its spin polarization is perpendicular to the exchange field \mathbf{h} in the ferromagnet—along the y direction for $\mathbf{h} = h\mathbf{e}_x$, and along the x direction for $\mathbf{h} = h\mathbf{e}_y$.

As we explain in Ref. [41], this spin supercurrent is the result of a delicate interplay between the different condensates in the junction. Consider for instance $\mathbf{h} = h\mathbf{e}_y$ and, for the sake of the argument, even-frequency superconducting correlations. In addition to the s -wave spin-singlet condensate emanating from the proximitized superconductors, there are

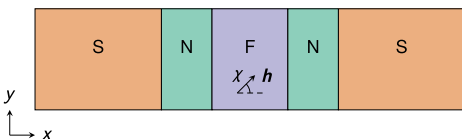


FIG. 1. Suggested experimental setup for the superspin Hall effect. A magnetic Josephson junction in the clean limit with Rashba spin-orbit interlayers. The in-plane exchange field \mathbf{h} in the ferromagnet makes an angle χ with the x axis.

also p -wave correlations in the junction due to the broken translation symmetry at the material interfaces [51,52] and due to the presence of spin-orbit coupling [53]. Due to the overall antisymmetry of the Cooper-pair wave function, the spin state of these even-frequency p -wave correlations must be one (or several) of the triplet states. The generation of both short- and long-range triplets is possible because of the simultaneous presence of both ferromagnetism and spin-orbit coupling [13,14]. As explained in Ref. [41], the interaction of the s - and p -wave condensates can be described via two different superconducting order parameters in the junction, which quantify the superconducting correlations present in the system. These are, respectively, the sum Δ_+ and the difference Δ_- of the original s -wave and p -wave order parameters, Δ_s and Δ_k , where k refers to the momentum in the y direction. The momentum index k is a good quantum number for a system with periodic boundary conditions in the y direction, as the one considered in Ref. [41]. The relative magnitude of these order parameters is determined by the relative phase of the original s -wave and p -wave order parameters,

$$|\Delta_{\pm}|^2 = |\Delta_s|^2 + |\Delta_k|^2 \pm 2 \text{Re}(\Delta_s \Delta_k^*). \quad (1)$$

When no phase difference is applied over the junction, the s -wave order parameter is purely real, whereas the p -wave order parameter is purely imaginary. Consequently, their sum and difference have equal magnitude, $|\Delta_+| = |\Delta_-|$, and as many Cooper pairs condense in the $|k \uparrow, -k \downarrow\rangle$ state as in the $|k \downarrow, -k \uparrow\rangle$ state. However, when a phase difference is applied, the s -wave order parameter acquires an imaginary component and the p -wave order parameter acquires a real component. In turn, their sum and difference are no longer equal, $|\Delta_+| \neq |\Delta_-|$, and Cooper pairs condense preferentially at either $|k \uparrow, -k \downarrow\rangle$ or $|k \downarrow, -k \uparrow\rangle$ because of the difference in condensation energies. Such a selective condensation gives rise to a nonzero k -resolved spin magnetization S_k that is antisymmetric in k . Subsequently, this antisymmetric momentum-resolved spin magnetization produces a spin current polarized along the spin magnetization direction. For an exchange field $\mathbf{h} = h\mathbf{e}_y$, the momentum-resolved spin magnetization points in the x direction; thus the application of a longitudinal phase difference (charge current) has given rise to a transverse spin current polarized along \mathbf{e}_x .

III. THEORY

We consider a superconducting heterostructure in two dimensions in the clean limit, incorporating strong spin-orbit coupling. For this, we use the tight-binding Bogoliubov–de Gennes framework [3]. Our heterostructure consists of superconductors, normal metals with Rashba spin-orbit coupling, and ferromagnets. Our Hamiltonian is

$$\begin{aligned} H = & -t \sum_{(i,j),\sigma} c_{i,\sigma}^\dagger c_{j,\sigma} - \sum_{i,\sigma} \mu_i c_{i,\sigma}^\dagger c_{i,\sigma} - \sum_i U_i n_{i,\uparrow} n_{i,\downarrow} \\ & - (i/2) \sum_{(i,j),\alpha,\beta} \lambda_{ij} [\mathbf{n} \cdot (\boldsymbol{\sigma} \times \mathbf{d}_{ij})]_{\alpha\beta} c_{i,\alpha}^\dagger c_{j,\beta} \\ & + \sum_{i,\alpha,\beta} (\mathbf{h}_i \cdot \boldsymbol{\sigma})_{\alpha\beta} c_{i,\alpha}^\dagger c_{i,\beta}, \end{aligned} \quad (2)$$

where i and j are position indices ($i, j = 1, \dots, N_x N_y$, where N_x and N_y are the dimensions of the lattice); $\langle i, j \rangle$ indicates that i and j are nearest neighbors; t is the hopping integral; $c_{i,\sigma}^\dagger$ and $c_{i,\sigma}$ are electron creation and annihilation operators at site i for spin σ ; μ_i is the local chemical potential; U_i is the local on-site attraction that gives rise to superconductivity ($U_i = 0$ outside the superconductors and $U_i = U > 0$ inside the superconductors); $n_{i,\sigma} = c_{i,\sigma}^\dagger c_{i,\sigma}$ is the number operator at site i for spin σ ; λ_i is the local Rashba parameter ($\lambda_i = 0$ outside the normal metals and $\lambda_i = \pm\lambda$ inside the normal metals); \mathbf{n} is the unit vector normal to the Rashba-metal/ferromagnet interface; $\boldsymbol{\sigma}$ is the vector of Pauli matrices; $\mathbf{d}_{ij} = -\mathbf{d}_{ji}$ is the vector pointing from site i to site j ; and \mathbf{h}_i is the local magnetic exchange field ($\mathbf{h}_i = 0$ outside the ferromagnet and $\mathbf{h}_i = \mathbf{h}$ inside the ferromagnet).

The two-particle Hubbard- U term can be recast as

$$-\sum_i U_i n_{i,\uparrow} n_{i,\downarrow} = \sum_i (\Delta_i c_{i,\downarrow}^\dagger c_{i,\downarrow}^\dagger + \Delta_i^\dagger c_{i,\downarrow} c_{i,\uparrow} + |\Delta_i|^2/U_i) \quad (3)$$

using the standard mean-field *ansatz* $\Delta_i = -U_i \langle c_{i,\downarrow} c_{i,\uparrow} \rangle$. We symmetrize the Hamiltonian using the fundamental fermionic anticommutator to write

$$\sum_{\lambda,\kappa} A_{\lambda,\kappa} c_\lambda^\dagger c_\kappa = \frac{1}{2} \sum_\lambda A_{\lambda,\lambda} + \frac{1}{2} \sum_{\lambda,\kappa} A_{\lambda,\kappa} (c_\lambda^\dagger c_\kappa - c_\kappa c_\lambda^\dagger). \quad (4)$$

Introducing the basis

$$B_i^\dagger = (c_{i,\uparrow}^\dagger, c_{i,\downarrow}^\dagger, c_{i,\uparrow}, c_{i,\downarrow}), \quad (5)$$

we may then write the Hamiltonian on the form

$$H = H_0 + \frac{1}{2} \sum_{i,j} B_i^\dagger H_{ij} B_j. \quad (6)$$

Here, we have identified the constant term H_0 ,

$$H_0 = \sum_i |\Delta_i|^2/U_i - \sum_i \mu_i, \quad (7)$$

where the first sum runs only over the superconductors, and the 4×4 matrix H_{ij} ,

$$H_{ij} = \frac{1}{2} t \tau_z \sigma_0 \delta_{j,i+\boldsymbol{\delta}} - \mu_i \tau_z \sigma_0 \delta_{i,j} + \frac{i}{2} \Delta_i \tau_x \sigma_y \delta_{i,j} - \frac{i}{2} \Delta_i^\dagger \tau_x \sigma_y \delta_{i,j} - \frac{i}{4} \lambda_i \tau_0 \sigma_z (\delta_{j,i+\boldsymbol{\delta}_y} - \delta_{j,i-\boldsymbol{\delta}_y}) + h_i^x \tau_z \sigma_x \delta_{i,j} + h_i^y \tau_0 \sigma_y \delta_{i,j} + h_i^z \tau_z \sigma_z \delta_{i,j}, \quad (8)$$

where $\delta_{i,j}$ is the Kronecker delta, we used $\mathbf{n} = \mathbf{e}_x$, we introduced the set of nearest-neighbor vectors $\boldsymbol{\delta} = (\delta_x, \delta_y)$, and τ_n and σ_n are the Pauli matrices for $n = x, y, z$ and $n = 0$ refers to the identity. Moreover, $\tau_\pm = \tau_x \pm i\tau_y$, and products of Pauli matrices are interpreted as Kronecker products. As is the usual definition, $\tau_z \sigma_0$, for instance, evaluates to $\tau_z \sigma_0 = \text{diag}(+1, +1, -1, -1)$ [54].

The index structure in Eq. (6) is that of a matrix product, in which the matrix M is multiplied from the left with the row vector B^\dagger , and the resulting row vector is multiplied with the column vector B . Each element in M is a 4×4 matrix H_{ij} , and each element in B (or B^\dagger) is a 4×1 (or 1×4) column (or row).

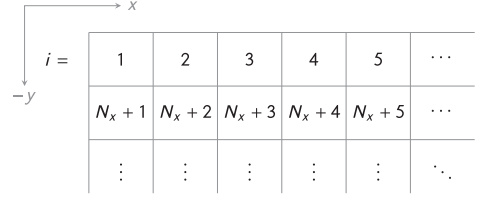


FIG. 2. Enumeration scheme for the $N_x \times N_y$ square lattice. The site index i is incremented site by site along the rows, starting in the upper left corner.

The structure of the matrix M is determined by how we combine the elements of B and B^\dagger into vectors. We consider a square lattice. The position indices i and j run over the entire system ($N_x \times N_y$ sites). Since each pair (i, j) corresponds to a 4×4 block H_{ij} , we expect M to be a $4N_x N_y \times 4N_x N_y$ matrix.

By choosing some enumeration scheme for the sites i (such as the one in Fig. 2), we can thus write

$$H = H_0 + \frac{1}{2} B^\dagger M B, \quad (9)$$

and diagonalize M by the techniques that are familiar from linear algebra. Since H is Hermitian, so is M , and M can thus be diagonalized as $M = PEP^{-1}$, where E is diagonal and real, and P is unitary, $P^{-1} = P^\dagger$ [55]. Substituting $M = PEP^{-1}$ into Eq. (9) we obtain

$$H = H_0 + \frac{1}{2} \sum_n E_n \gamma_n^\dagger \gamma_n, \quad (10)$$

where we defined the new quasiparticle operators $\gamma^\dagger = B^\dagger P$ and $\gamma = P^{-1} B$, γ_n is the n th element of γ , E_n is the n th eigenenergy, and $n = 1, \dots, 4N_x N_y$. The original electron operators can be related to the quasiparticle operators by

$$c_{i,\uparrow} = \sum_n u_{i,n} \gamma_n, \quad c_{i,\downarrow} = \sum_n v_{i,n} \gamma_n, \quad (11a)$$

$$c_{i,\uparrow}^\dagger = \sum_n w_{i,n} \gamma_n, \quad c_{i,\downarrow}^\dagger = \sum_n x_{i,n} \gamma_n, \quad (11b)$$

where $u_{i,n}$ with $i = 1, \dots, N_x N_y$ is, respectively, P_{ln} with $l = 1, 5, 9, \dots$. Likewise, $v_{i,n}$ with $i = 1, \dots, N_x N_y$ is P_{ln} with $l = 2, 6, 10, \dots$; $w_{i,n}$ with $i = 1, \dots, N_x N_y$ is P_{ln} with $l = 3, 7, 11, \dots$; and $x_{i,n}$ with $i = 1, \dots, N_x N_y$ is P_{ln} with $l = 4, 8, 12, \dots$.

We can now derive expressions for any of the observables in the system in terms of the eigenenergies E_n and the eigenvectors $u_{i,n}$, $v_{i,n}$, $w_{i,n}$, and $x_{i,n}$. For instance, the superconducting gap takes the form

$$\Delta_i = U_i \sum_n v_{i,n} w_{i,n}^* f(E_n/2), \quad (12)$$

and the spin magnetization takes the form

$$\langle S_i^x \rangle = 2 \sum_n \text{Re}(u_{i,n}^* v_{i,n}) f(E_n/2), \quad (13a)$$

$$\langle S_i^y \rangle = 2 \sum_n \text{Im}(u_{i,n}^* v_{i,n}) f(E_n/2), \quad (13b)$$

$$\langle S_i^z \rangle = \sum_n (|u_{i,n}|^2 - |v_{i,n}|^2) f(E_n/2). \quad (13c)$$

The free energy reads

$$F = H_0 - \frac{1}{\beta} \sum_n \ln[1 + \exp(-\beta E_n/2)], \quad (14)$$

where $1/\beta = T$ and T is temperature.

Expressions for the charge and spin currents can be obtained from their respective continuity equations,

$$\partial_t \rho_i = -\nabla \cdot \mathbf{j}_i \quad (15)$$

and

$$\partial_t \mathbf{s}_i = -\nabla \cdot \mathbf{J}_i, \quad (16)$$

where ρ_i is the charge density at i , \mathbf{j}_i is the current density at i , \mathbf{s}_i is the spin density at i , \mathbf{J}_i is the spin-current-density tensor at i , and the gradient of the spin-current-density tensor is taken with respect to the position variables. Note that the spin current defined by the spin continuity equation is only conserved in regions without ferromagnetism or spin-orbit coupling because these terms are spin nonconserving [56]. For each of the two continuity equations, we find expressions for the currents by integrating the equations over space to obtain (for the case of the charge current)

$$\partial_t Q_i = -\int_{\Omega} d\mathbf{r} (\nabla \cdot \mathbf{j}_i),$$

where $Q_i = \sum_{\sigma} c_{i,\sigma}^{\dagger} c_{i,\sigma}$ is the charge at i and Ω is the unit-cell volume. The integral on the right-hand side can be evaluated using Green's theorem,

$$\int_{\Omega} d\mathbf{r} (\nabla \cdot \mathbf{j}_i) = \int_{\partial\Omega} dS (\mathbf{j}_i \cdot \mathbf{e}_n) = \sum_l j_{i,l} a = \sum_l I_{i,l},$$

where $\partial\Omega$ is the unit-cell boundary, \mathbf{e}_n is the outward-pointing boundary normal, and a is the unit-cell side length. Since we consider a square lattice, $I_{i,l}$ is the current through the l th face of the square unit cell. The left-hand side of the continuity equation can be evaluated using Heisenberg's equation of motion. Thus the sum of currents out of the unit cell is

$$\sum_l I_{i,l} = -i[H, Q_i]. \quad (17)$$

Evaluating the commutator and taking a combined thermal and quantum-mechanical average gives the charge current in the x direction

$$\begin{aligned} \langle I_i^x \rangle &= t \sum_n \text{Im}(u_{i+1,n}^* u_{i,n} - u_{i-1,n}^* u_{i,n}) \\ &\quad + v_{i+1,n}^* v_{i,n} - v_{i-1,n}^* v_{i,n}) f(E_n/2) \end{aligned} \quad (18)$$

and in the y direction,

$$\begin{aligned} \langle I_i^y \rangle &= \sum_n \text{Im}(u_{i-N_x,n}^* u_{i,n} - u_{i+N_x,n}^* u_{i,n}) \\ &\quad + v_{i-N_x,n}^* v_{i,n} - v_{i+N_x,n}^* v_{i,n}) f(E_n/2) \\ &\quad - \frac{1}{2} \sum_n \lambda_i \text{Re}(u_{i-N_x,n}^* u_{i,n} + u_{i+N_x,n}^* u_{i,n}) \\ &\quad - v_{i-N_x,n}^* v_{i,n} - v_{i+N_x,n}^* v_{i,n}) f(E_n/2). \end{aligned} \quad (19)$$

A similar procedure for the spin currents gives the three spin components of the spin current in the x direction

$$\begin{aligned} \langle I_i^{xx} \rangle &= t \sum_n \text{Im}(u_{i+1,n}^* v_{i,n} + v_{i+1,n}^* u_{i,n}) \\ &\quad - u_{i-1,n}^* v_{i,n} - v_{i-1,n}^* u_{i,n}) f(E_n/2), \end{aligned} \quad (20)$$

$$\begin{aligned} \langle I_i^{xy} \rangle &= t \sum_n \text{Re}(u_{i+1,n}^* v_{i,n} - v_{i+1,n}^* u_{i,n}) \\ &\quad - u_{i-1,n}^* v_{i,n} + v_{i-1,n}^* u_{i,n}) f(E_n/2), \end{aligned} \quad (21)$$

$$\begin{aligned} \langle I_i^{xz} \rangle &= t \sum_n \text{Im}(u_{i+1,n}^* u_{i,n} - v_{i+1,n}^* v_{i,n}) \\ &\quad - u_{i-1,n}^* u_{i,n} + v_{i-1,n}^* v_{i,n}) f(E_n/2), \end{aligned} \quad (22)$$

and likewise the three spin components of the spin current in the y direction

$$\begin{aligned} \langle I_i^{yx} \rangle &= t \sum_n \text{Im}(u_{i-N_x,n}^* v_{i,n} + v_{i+N_x,n}^* u_{i,n}) \\ &\quad - u_{i+N_x,n}^* v_{i,n} - v_{i-N_x,n}^* u_{i,n}) f(E_n/2), \end{aligned} \quad (23)$$

$$\begin{aligned} \langle I_i^{yy} \rangle &= t \sum_n \text{Re}(u_{i-N_x,n}^* v_{i,n} - v_{i+N_x,n}^* u_{i,n}) \\ &\quad - u_{i+N_x,n}^* v_{i,n} + v_{i-N_x,n}^* u_{i,n}) f(E_n/2), \end{aligned} \quad (24)$$

$$\begin{aligned} \langle I_i^{yz} \rangle &= t \sum_n \text{Im}(u_{i-N_x,n}^* u_{i,n} - v_{i-N_x,n}^* v_{i,n}) \\ &\quad - u_{i+N_x,n}^* u_{i,n} + v_{i+N_x,n}^* v_{i,n}) f(E_n/2). \end{aligned} \quad (25)$$

A general superconducting order parameter F can be decomposed into a spin-singlet and a spin-triplet contribution [57],

$$F = (\psi + \mathbf{d} \cdot \boldsymbol{\sigma}) i\sigma_y, \quad (26)$$

where ψ is the singlet amplitude and the \mathbf{d} vector is the vector of triplet amplitudes along the x , y , and z axes,

$$\mathbf{d} = \frac{1}{2}[\Delta_{\downarrow\downarrow} - \Delta_{\uparrow\uparrow}, -i(\Delta_{\downarrow\downarrow} + \Delta_{\uparrow\uparrow}), 2\Delta_{\uparrow\downarrow}]. \quad (27)$$

The spin structure of the singlet amplitude is already familiar from Eq. (8), where the same factor $i\sigma_y$ appears. In a unitary superconducting state, the identity $F^{\dagger} = F^{-1}$ holds, and FF^{\dagger} is proportional to the identity. A general superconducting system is, however, not unitary, and straightforward calculation shows that

$$FF^{\dagger} = |\psi|^2 + |\mathbf{d}|^2 + \boldsymbol{\sigma} \cdot [(\psi \mathbf{d}^* + \psi^* \mathbf{d}) + i(\mathbf{d} \times \mathbf{d}^*)]. \quad (28)$$

The term $i(\mathbf{d} \times \mathbf{d}^*)$ is proportional to the spin expectation value of the pure triplet Cooper pairs [57], whereas the term $(\psi \mathbf{d}^* + \psi^* \mathbf{d})$ is proportional to the spin magnetization arising due to coexistence of singlet and triplet pairing [41],

$$\mathbf{S}_{\text{Cooper}} \propto (\psi \mathbf{d}^* + \psi^* \mathbf{d}) + i(\mathbf{d} \times \mathbf{d}^*). \quad (29)$$

In order to calculate the Cooper-pair spin magnetization, we need expressions for the superconducting amplitudes. The s -wave singlet amplitude $S_{i,0}$ at i is identical to the gap we

calculated in Eq. (12), except for the factor U_i ,

$$S_0 = \frac{1}{2}[\langle c_{i,\uparrow} c_{i,\downarrow} \rangle - \langle c_{i,\downarrow} c_{i,\uparrow} \rangle] = \sum_n v_{i,n} w_{i,n}^* f(E_n/2). \quad (30)$$

The direct and inverse superspin Hall effects depend on the existence of even-frequency, p_y -wave, spin-triplet amplitudes,

$$\begin{aligned} \mathcal{P}_{i,\uparrow\downarrow}^y &= \frac{1}{2} \sum_{\pm} \pm [\langle c_{i,\uparrow} c_{i\pm\delta_y,\downarrow} \rangle + \langle c_{i,\downarrow} c_{i\pm\delta_y,\uparrow} \rangle] \\ &= \frac{1}{2} \sum_{n,\pm} \pm (w_{i,n}^* v_{i\mp N_x,n} - v_{i,n} w_{i\mp N_x,n}^*) f(E_n/2), \end{aligned} \quad (31a)$$

$$\mathcal{P}_{i,\uparrow\uparrow}^y = \sum_{\pm} \pm \langle c_{i,\uparrow} c_{i\pm\delta_y,\uparrow} \rangle = \sum_{n,\pm} \pm w_{i,n}^* u_{i\mp N_x,n} f(E_n/2), \quad (31b)$$

$$\mathcal{P}_{i,\downarrow\downarrow}^y = \sum_{\pm} \pm \langle c_{i,\downarrow} c_{i\pm\delta_y,\downarrow} \rangle = \sum_{n,\pm} \pm x_{i,n}^* v_{i\mp N_x,n} f(E_n/2). \quad (31c)$$

In Sec. V, we will need the odd-frequency, s -wave, spin-triplet amplitudes,

$$\begin{aligned} S_{i,\uparrow\downarrow}(t) &= \frac{1}{2}[\langle c_{i,\uparrow}(t) c_{i,\downarrow}(0) \rangle + \langle c_{i,\downarrow}(t) c_{i,\uparrow}(0) \rangle] \\ &= \frac{1}{2} \sum_n (w_{i,n}^* v_{i,n} - x_{i,n}^* u_{i,n}) f(E_n/2) e^{iE_n t/2}, \end{aligned} \quad (32a)$$

$$S_{i,\uparrow\uparrow}(t) = \langle c_{i,\uparrow}(t) c_{i,\uparrow}(0) \rangle = \sum_n w_{i,n}^* u_{i,n} f(E_n/2) e^{iE_n t/2}, \quad (32b)$$

$$S_{i,\downarrow\downarrow}(t) = \langle c_{i,\downarrow}(t) c_{i,\downarrow}(0) \rangle = \sum_n x_{i,n}^* v_{i,n} f(E_n/2) e^{iE_n t/2}. \quad (32c)$$

IV. NUMERICAL CALCULATIONS

In this paper, we consider the three setups in Figs. 1, 7, and 9. In each case, we construct the matrix M from Eq. (9) and diagonalize it to find the eigenvalues and eigenvectors. Using these, we may calculate physical quantities such as the superconducting gap Δ_i or the spin magnetization $\langle S_i \rangle$. Because the matrix M depends on the superconducting gap, the equations must be solved self-consistently by substituting the gap calculated using Eq. (12) back into M and iterating.

For each of the systems we consider, we make sure that the superconducting state minimizes the free energy in Eq. (14). In all the systems, we take the exchange field \mathbf{h}_i of the ferromagnets to be an external parameter, that is, we do not calculate the exchange field self-consistently. This is consistent with an s - d -type model in which the localized d electrons are responsible for the magnetic behavior [58,59]. The spin magnetization $\langle S_i \rangle$ that we calculate is thus the spin polarization of the itinerant s electrons.

In the setup in Fig. 1, we consider the injection of a charge current into the junction by an applied phase difference. This is accomplished by fixing the phase of the superconducting gap Δ_i at the leftmost lattice points in the left superconductor and at the rightmost lattice points in the right superconductor. The applied phase difference between these points can be used as a proxy for the applied phase difference over the junction (N/F/N spacer) because the phase drop inside the

superconductors is typically small. (Fixing the phase difference at $\Delta\phi = 0.5\pi$ gives an effective phase difference over the N/F/N spacer of $\Delta\phi \approx 0.47$ – 0.48π .)

In the setup in Fig. 7, we consider the injection of a charge current across the injection junction by an applied phase difference. We fix the phase of the left superconductor in the detector at $\phi = 0$ (this choice is arbitrary—only phase differences matter). By varying the phase of the right superconductor from 0 to 2π we calculate the current-phase and free-energy-phase relations of the detector junction. We take the induced anomalous phase ϕ_0 to be the phase over the detector that minimizes the free energy and gives $\langle I^x \rangle = I(-\phi_0) = 0$.

In the setup in Fig. 9, we consider the injection of an exchange spin current from two misaligned ferromagnets. We fix the phase of both superconductors at $\phi = 0$ and calculate the anomalous charge current $I(0) = \langle I^x \rangle$. In its simplest form, a ϕ_0 junction [60–63] has the current-phase relation $I(\phi) = I_c \sin(\phi + \phi_0)$. For small ϕ_0 shifts, the anomalous phase ϕ_0 and the anomalous current $I(0) = I_c \sin \phi_0$ are proportional, $I(0) \approx I_c \phi_0$. Therefore, we can use the anomalous current as a proxy for the anomalous phase.

The advantage of tight-binding Bogoliubov–de Gennes framework [3] that we use is that it is not subject to the limitations on length and energy scales that are inherent to for instance quasiclassical theory [64]. However, using this tight-binding framework, only comparatively small lattice sizes are computationally manageable, especially in two-dimensional finite-size calculations. For superconducting structures, the relevant length scale is the superconducting coherence length $\xi = \hbar v_F / \pi \Delta$ [2,3]. If the coherence length is to be smaller than the thickness of the superconducting layers, this requires relatively large values of the superconducting gap and large critical temperatures. Nonetheless, the tight-binding framework can still be used to make qualitative and quantitative predictions for experimentally relevant systems. To do this requires that the spatial dimensions are scaled by the superconductive coherence length. One example of a successful application of this method is Ref. [65], whose predictions correspond very well to the experimental results of Ref. [66].

We take a similar approach. With the parameters chosen in Secs. V–VIII the thickness of the superconducting layers is about one coherence length, and the normal-metal and ferromagnetic layers vary from about $\xi/4$ to 2ξ . As long as the weak links are not orders of magnitude larger than the coherence length, the qualitative features of our results are robust towards variations of the system size. In particular, the ϕ_0 shift that we calculate in Sec. VII is nearly independent of the length of the detector junction.

V. SUPERSPIN HALL EFFECT IN TWO DIMENSIONS: SPIN CURRENT AND EDGE MAGNETIZATION

Our analysis of the superspin Hall effect in Ref. [41] was an effective one-dimensional analysis in the sense that we assumed periodic boundary conditions in the y direction and thus could get rid of the y coordinate by Fourier transformation. Whereas we were still able to calculate the transverse spin current, this left open the question of the

exact spin current circulation pattern and whether any spin magnetization arises at the edges of the sample. The latter would be a useful experimental signature of the superspin Hall effect, as it has been previously for the (nonequilibrium) spin Hall effect [67,68].

In the usual nonsuperconducting, nonequilibrium spin Hall effect, spin accumulates at the edges of the sample because the transverse spin current has nowhere to go upon reaching the sample boundary [21]. A steady state is achieved because the spin Hall effect is found in materials with strong spin-orbit coupling where spin is not conserved. The accumulated spin at the edge at any time is thus the result of a balance between influx of spin from the bulk and spin loss due to spin-orbit coupling.

We find that the superspin Hall current does not give rise to a spin magnetization at the sample edges by this familiar mechanism. The simple reason is that the superspin Hall current in our system does have somewhere to go—it can be drained from the superconductor, where in our model spin is conserved, into the Rashba-metal/ferromagnet spacer, where spin is not conserved. This circulation of the superspin Hall current from the spacer, into the superconductor, and back into the spacer, is shown in Fig. 3(a).

Note that, although the net flow of spin is from the bottom of the sample to the top, the direction of the spin current (up/down) oscillates as a function of the distance into the superconductor [Fig. 3(b)]. As explained in Ref. [41], the oscillation period is a function of the system parameters, such as the strength of the spin-orbit coupling in the normal layer and the strength of the exchange field in the ferromagnet. The period varies from atomic-scale oscillations to roughly a fourth of the coherence length. Such rapid oscillations are characteristic for physical quantities in ballistic quantum-mechanical systems. For instance, they can also be found in the proximity-induced magnetization in conventional superconductors [69] and helical edge-mode currents in triplet superconductors [70].

Although the superspin Hall current does not give rise to a spin magnetization at the edges of the sample, there is an x -polarized spin magnetization at the edges of the system [Fig. 4(a)]. However, contrary to what we would expect from a spin magnetization arising due to accumulation of spins deposited by the superspin Hall current, the spin magnetization sign pattern that we observe is $\pm\mp$, not $\pm\pm$, where the signs refer to the left upper/lower and right upper/lower edges, respectively. Furthermore, its amplitude varies as $\cos\phi$, where ϕ is the phase difference applied between the two superconductors [Fig. 5(a)]. We would expect a spin magnetization induced by the superspin Hall current—which is again induced by the longitudinal charge current—to have an amplitude that varied as $\sin\phi$ [compare with Figs. 5(c) and 5(d)].

The momentum-resolved spin magnetization that gives rise to the superspin Hall current is the result of the interaction of the s -wave spin-singlet and a p -wave spin-triplet condensate, both even in frequency. The edge spin magnetization we observe in Fig. 4, on the other hand, is the result of the interaction of the even-frequency, s -wave, spin singlet condensate and an odd-frequency, s -wave, spin-triplet condensate. In Fig. 4(a), we have plotted the x component of the total spin

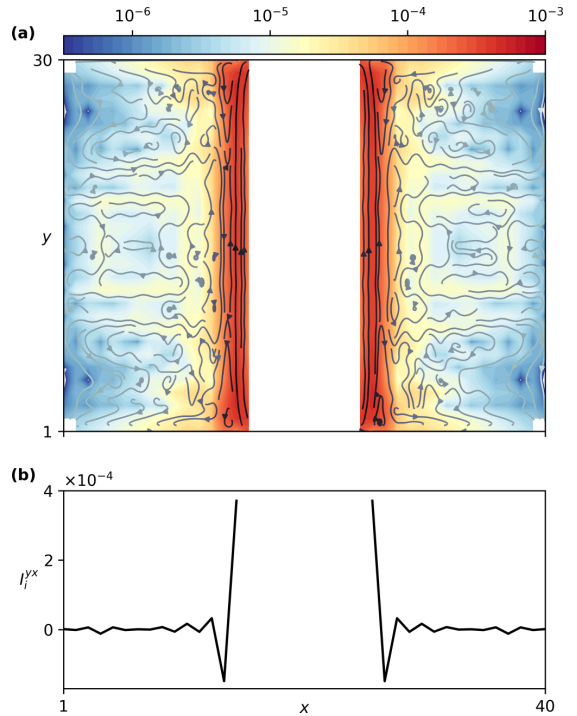


FIG. 3. Superspin Hall current in two dimensions at phase difference $\phi = \pi/2$. (a) Circulation pattern of the x component of the spin current. The spin current is only plotted in the superconductors, where spin is conserved. (b) Cut along the x direction at $y = 15$ inside the superconductors. The spin current oscillates as a function of the distance from the N/F/N weak link into the superconductors. We use the following parameter values: the system size is $N_x = 40$ times $N_y = 30$; the layer thicknesses are $N_S = 15$, $N_N = 3$, and $N_F = 4$; the chemical potentials are $\mu_S = 0.9$, $\mu_N = 0.85$, and $\mu_F = 0.8$; the Rashba spin-orbit coupling in the normal metal is $\lambda = 0.3$, the exchange field in the ferromagnet is $h_y = 0.15$ ($h_x = h_z = 0$), the on-site attraction in the superconductor is $U = 1.1$, and the temperature is $T = 0.01$. All energies are normalized with respect to the hopping parameter ($t = 1$).

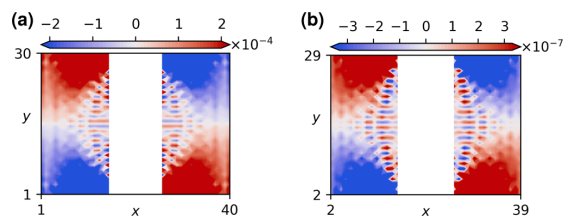


FIG. 4. x component of the spin magnetization at phase difference $\phi = 0$. (a) The total spin magnetization. (b) The spin magnetization induced by interaction of s -wave singlets and odd-frequency, s -wave triplets (arbitrary units). Except for the applied phase between the superconductors, all parameters are identical to Fig. 3.

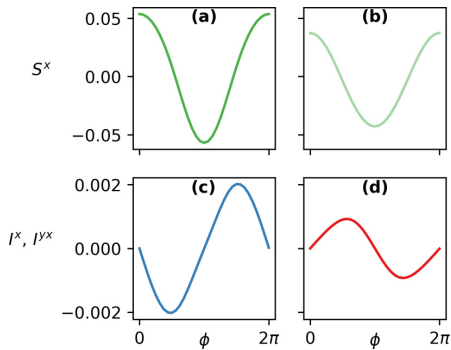


FIG. 5. Phase dependence of the superspin Hall effect. (a) Total spin magnetization (S^y) summed over the lower half of the right superconductor. (b) Cooper-pair spin magnetization S^y_{Cooper} summed over the lower half of the right superconductor (arbitrary units). (c) Longitudinal charge current (I^x) summed over the y cross section. (d) Transverse spin current (I^{yx}) summed over the x cross section. All parameters are identical to Fig. 3.

magnetization calculated using Eq. (13a). In Fig. 4(b), we have plotted the x component of the spin magnetization calculated using Eq. (29), where we have used the superconducting amplitudes in Eqs. (30) and (32). Apart from a constant prefactor, the plots are essentially identical. The spin magnetization due to the odd-frequency, s -wave spin triplets also reproduce the phase dependence of the total spin magnetization [compare Figs. 5(a) and 5(b)].

The fact that the edge spin magnetization is due to the odd-frequency triplets (s wave) whereas the superspin Hall effect is due to the even-frequency triplets (p wave) makes it clear that the spin magnetization is not a consequence of the superspin Hall current. Further evidence to this effect is that this particular spin magnetization is also predicted in the diffusive limit [71], where the superspin Hall effect is precluded because of the absence of p -wave correlations. Consequently, one can exist independently of the other—they are independent effects.

Nonetheless, the symmetries of the spin magnetization with respect to sign change of the Rashba spin-orbit coupling and the direction of the exchange field is the same as those of the superspin Hall current. In particular, rotating the exchange field by 90° from $\mathbf{h} = h\mathbf{e}_y$ to $\mathbf{h} = h\mathbf{e}_x$ also rotates the spin-triplet spin magnetization by 90° from x to y .

The temperature $T = 0.01$ (in units of t), which we chose for the simulations above, is well below the superconducting transition temperature, $T = 0.01 \lesssim T_c/2$. However, at still lower temperatures, Andreev bound states [72,73] with a more dispersive energy-phase relation appear in the junction. The appearance of such states is common in ballistic systems with high interface transparencies and low temperatures. Because these states bounce multiple times between the two superconductors, they produce higher-harmonic contributions to the current-phase relation. The higher harmonics will distort the pure sinusoidal shape of the current-phase relation and may even introduce discontinuities [74,75]. This,

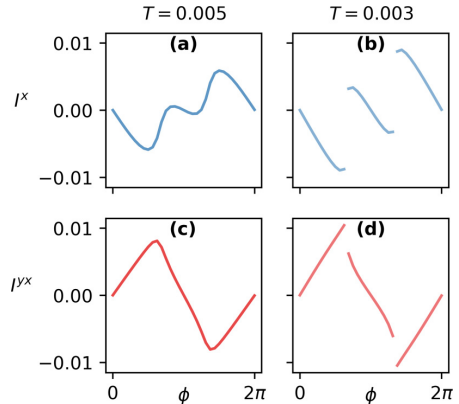


FIG. 6. Phase dependence of the superspin Hall effect at low temperatures. (a) Longitudinal charge current (I^x) summed over the y cross section. (b) Longitudinal charge current (I^x) at $T = 0.003$ summed over the y cross section. (c) Transverse spin current (I^{yx}) at $T = 0.005$ summed over the x cross section. (d) Transverse spin current (I^{yx}) at $T = 0.003$ summed over the x cross section. All parameters except the temperature are identical to Fig. 3.

of course, also affects the superspin Hall current, as shown in Fig. 6.

The presence of Andreev bound states in the junction also affects the spin magnetization, which deviates from a pure cosine as a function of the applied phase difference ϕ . Interestingly, there is also a discernible difference between the total spin magnetization and the Cooper-pair spin magnetization computed via Eq. (29) at low temperatures.

VI. INVERSE SUPERSPIN HALL EFFECT

The Onsager reciprocal of the usual nonsuperconducting, nonequilibrium spin Hall effect is the inverse spin Hall effect—that is, injection of a transverse spin current generates a longitudinal charge current. In a steady state, the charge current must either be drained into external leads or a voltage accumulates which exactly cancels the inverse spin Hall current. Analogously, one might expect that there should exist an inverse of the superspin Hall effect discussed in Sec. V—injecting an equilibrium transverse spin current should give rise to a longitudinal charge supercurrent.¹ However, in the absence of external leads, the steady state will be one with zero charge current. Instead, a phase difference ϕ_0 accumulates over the junction. This phase difference gives rise to a supercurrent that exactly cancels the one induced by the inverse superspin Hall effect. In this work, we confirm this expectation and find that the experimental signature of the inverse superspin Hall effect is a ϕ_0 junction.

¹Note that the term *inverse effect* cannot here be understood as the Onsager reciprocal proper, as our calculations are carried out in *equilibrium*.

VII. ELECTRICAL DETECTION OF THE SUPERCURRENT SPIN POLARIZATION

We propose to use the setup in Fig. 7 to detect the spin polarization of a supercurrent. This four-terminal setup consists of two perpendicular Josephson junctions. We will refer to the S/F(y)/F(x)/F(y)/S junction as the injection junction and the S/N/F(x)/N/S junction as the detector or detection junction.

By applying a phase bias over the injection junction, a spin-polarized supercurrent is produced by the combined processes of spin mixing in the S/F(y) bilayer and spin rotation [rotation of spin quantization axis between the F(y) and F(x) layers]. The current is spin-polarized in the x direction. The proximity to the F(y) layers provides the necessary conditions for the superspin Hall mechanism. Thus, the inverse superspin Hall effect converts this transverse spin current into a longitudinal charge supercurrent in the detector that flows from the left to the right superconductor. Consequently, in the steady state, the detection junction is a ϕ_0 junction. If the two terminals of the detection junction are connected to form a superconducting loop, the current-phase relation of the detector can be measured by threading a magnetic flux through the loop [76]. The anomalous current $I(0) = I_c \sin \phi_0$ can also be measured directly using a SQUID in zero applied flux.

Figures 8(a) and 8(b) show the current-phase and the free-energy-phase relations of the detector junction. At an applied phase difference of $\phi = 0$ over the injector junction [Fig. 8(a)], no spin current is injected across the detector. Consequently, the current-phase relation of the detector junction is that of an ordinary 0 junction. At an applied phase difference of $\phi = \pi/2$ over the injector junction [Fig. 8(b)], a large spin current is injected across the detector. Consequently, the current-phase relation is shifted by an amount $\phi_0 = -0.2\pi$.

Figure 8(c) shows the complete ϕ_0 -phase relation. The abscissa corresponds to the applied phase difference of the injection junction. On the right ordinate we have plotted the charge and spin currents injected across the detector, that is, $\langle I^y \rangle$ and $\langle I^{yx} \rangle$. The $\langle I^y \rangle$ -phase and the $\langle I^{yx} \rangle$ -phase relations are both almost sinusoidal, and we interpret the spin current as the spin polarization of the charge current. On the left ordinate we have plotted the induced ϕ_0 shift, i.e., the phase ϕ over the detector that corresponds to $\langle I^x \rangle = 0$ and $F = F_{\min}$. Clearly, the ϕ_0 shift is zero when the transverse spin current is zero. Moreover, the sign of the ϕ_0 shift is a good predictor for the sign of the spin current. We have not been able to find a simple

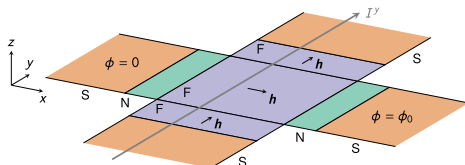


FIG. 7. Proposed experimental setup for detecting a spin-polarized supercurrent consisting of two crossed Josephson junctions. The charge supercurrent in the y direction injected into the S/F(y)/F(x)/F(y)/S junction is spin polarized in the x direction by the magnetic inhomogeneity provided by the F(y) layers. The transverse spin current thus injected into the S/N/F(x)/N/S junction induces a phase difference ϕ_0 between the left and right superconductors.

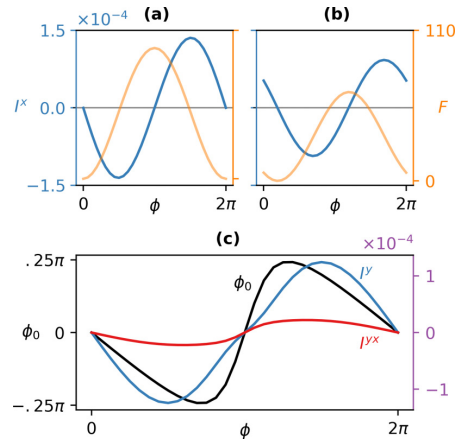


FIG. 8. ϕ_0 effect for the setup in Fig. 7. [(a) and (b)] Current-phase and free-energy-phase relations of the detector junction as a function of the phase difference applied over the detector junction at applied phase differences of (a) $\phi = 0$ (no injected charge current) and (b) $\phi = \pi/2$ (maximal injected charge current) over the injection junction. In (b), a ϕ_0 shift of $\phi_0 = -0.2\pi$ is clearly visible. (c) Right ordinate: the injected charge current and the resulting spin current through the injection junction as a function of the phase difference applied over the injection junction. Left ordinate: the induced ϕ_0 shift in the detection junction as a function of the phase difference applied over the injection junction. The system size is $N_x = 35$ times $N_y = 21$. The layer thicknesses of the detector are $N_S = 5$, $N_N = 10$, and $N_F = 5$, and the layer thicknesses of the injector are $N_S = 5$, $N_{F(x)} = 3$, and $N_{F(y)} = 5$. All material parameters are identical to Fig. 3.

explanation for the deviation of the ϕ_0 shift from a pure sine, but the fact that both the sign and zeros of the anomalous phase ϕ_0 follow the spin supercurrent is consistent with the latter being the origin of the anomalous phase shift.

In addition to serving as a measurement of the spin polarization of the supercurrent, the setup we propose in Fig. 7 can also serve as a current-controlled phase battery. Such functionality has recently been proposed for a voltage-controlled ϕ_0 junction [77], and recent experiments have made progress towards both magnetic and electric phase control [62,78].

VIII. ELECTRICAL DETECTION OF AN EXCHANGE SPIN CURRENT

The inverse superspin Hall effect is not only induced by a spin-polarized charge supercurrent, but also by other equilibrium spin currents. To demonstrate this, we consider the setup in Fig. 9. Here, the injection junction has been replaced by an F/N/F spin valve (no spin-orbit coupling in N). By misaligning the ferromagnets, we can inject an exchange spin current [49,50]. The spin current is proportional to the sine of the misalignment angle θ , $I_s \sim \sin \theta$.

In Fig. 10(a), we plot the resulting spin current $\langle I^{yx} \rangle$ in the central normal metal (where spin is conserved) and the anomalous current $I(0) = \langle I^x \rangle$ as a function of the misalignment angle θ . The spin current is sinusoidal as a function of θ , consistent with the prediction of Refs. [49,50]. The

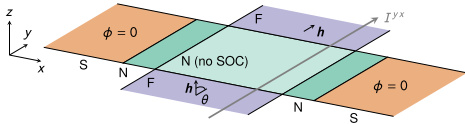


FIG. 9. Suggested experimental setup for the inverse superspin Hall effect. The misalignment of the two ferromagnets (misalignment angle θ) produces a transverse exchange spin current that gives rise to an anomalous current between the two superconductors.

sinusoidal response of the anomalous current is consistent with our interpretation that it is induced by the exchange spin current (and not directly induced by the transverse variation in the exchange field as in Ref. [37]).

In Figs. 10(b) and 10(c), we plot the current-phase relation at a misalignment angle $\theta = 0$ and $\pi/2$. The anomalous current $I(0)$ shows up as a ϕ_0 shift of the current-phase relation.

In Fig. 11, we have plotted the magnitude and phase of the resulting superconducting gap. The oscillations in the gap magnitude $|\Delta_i|$ at the sample edges are due to Fridel oscillations that create an oscillating charge density [79]. A ϕ_0 shift of $\phi_0 \approx -0.04\pi$ is clearly visible.

Figure 12 shows the dependence of the anomalous current $I(0)$ on the spin-orbit coupling strength λ in the Rashba metals and the exchange-field strength h in the ferromagnets. There is a pronounced peak (or dip) at $h \approx 0.8$ and $\lambda \approx 1.9$. This parameter dependence can be understood as follows: We expect the inverse superspin Hall effect to disappear when the exchange field vanishes because $h = 0$ means that no transverse

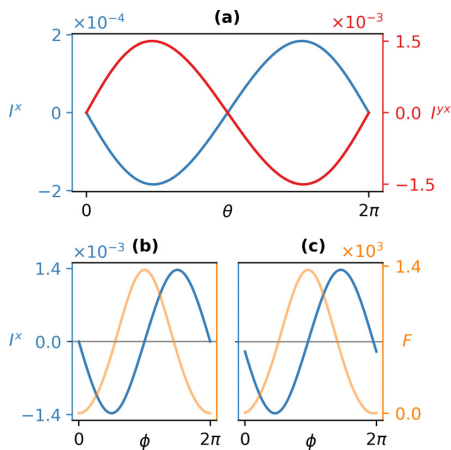


FIG. 10. (a) Injected spin current $\langle I^x \rangle$ in the central normal metal (no spin-orbit coupling) and anomalous current $I(0) = \langle I^x \rangle$ as a function of the misalignment angle θ . [(b) and (c)] Current-phase and free-energy-phase relations at a misalignment angle of, respectively, $\theta = 0$ (no injected spin current) and $\theta = \pi/2$ (maximal injected spin current). A ϕ_0 shift of $\phi_0 \approx -0.04\pi$ is clearly visible. We use the following parameter values: the system size is $N_x = 38$ times $N_y = 12$; the layer thicknesses of the detector are $N_S = 15$, $N_N = 2$, and $N_{N'} = 4$ and the layer thicknesses of the injector are $N_F = 1$ and $N_{N'} = 10$; the Rashba spin-orbit coupling is $\lambda = 1.87$; and the exchange field is $h = 0.8$. The remaining parameter values are identical to Fig. 3.

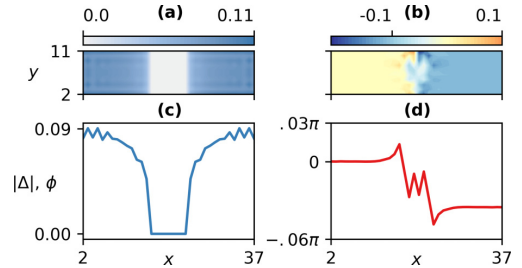


FIG. 11. ϕ_0 signature of the inverse superspin Hall effect. [(a) and (c)] Magnitude of the superconducting gap $|\Delta_i|$. The gap vanishes in the N/F/N spacer and the inverse proximity effect is clearly visible. The oscillations of the gap at the edges of the sample are due to Fridel oscillations. [(b) and (d)] Phase of the s -wave singlet amplitude $S_{i,0}$. A ϕ_0 shift of $\phi_0 \approx -0.04\pi$ is clearly visible. The plots in (c) and (d) are for $y = 5$. We use parameter values that are identical to Fig. 10.

spin current is injected. (Also, magnetism is a prerequisite for the superspin Hall effect.) For small values of h , we expect the anomalous current to increase with the exchange field because an increase in h leads to an increase in the transverse spin current. However, for large values of h , we expect the superspin Hall effect to disappear because the exchange field suppresses the superconducting proximity effect.

We also expect the anomalous current to vanish for vanishing spin-orbit coupling because spin-orbit coupling is a prerequisite for the superspin Hall effect. For finite λ , there is a finite anomalous current because of the superspin Hall effect, but we expect the superspin Hall effect to disappear for very large spin-orbit coupling because it suppresses the necessary p_y -wave spin-0 triplets [41] (d not parallel to \mathbf{g}_k in the notation of Ref. [80]).

IX. DISCUSSION

The superspin Hall effect and its inverse depend on the existence of p -wave correlations in the junction. These correlations are sensitive to disorder and will, in the face of too large amounts of disorder, be entirely suppressed.

The suppression of superconductivity by disorder has been studied in many systems, including heavy-fermion systems [81,82], iron pnictides [83,84], and Sr_2RuO_4 [85]. Strontium

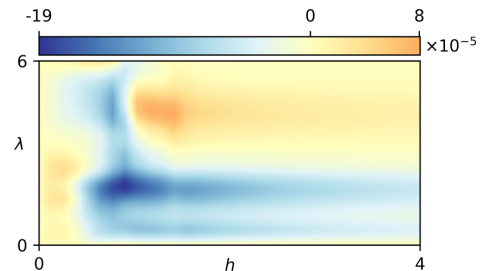


FIG. 12. Dependence of the anomalous current $I(0) = \langle I^x \rangle$ on the ferromagnet exchange field h and the Rashba metal spin-orbit coupling λ . Except for h and λ , the parameter values are identical to Fig. 10.

ruthenate is arguably the most relevant system for the p -wave correlations that the superspin Hall effect depends on. In strontium ruthenate, the disorder dependence of the critical temperature can be described using Abrikosov–Gor’kov pair-breaking theory [3,86]. Superconductivity vanishes in this compound when the mean free path ℓ is on the order of or smaller than the superconducting coherence length ξ of the p -wave order parameter. Experiments indicate that this corresponds to a residual resistivity of about $1\ \mu\Omega\text{cm}$ [85]. Results from the iron pnictides indicates that s_{\pm} -wave pairing is suppressed at a similar residual resistivity of about $10\ \mu\Omega\text{cm}$ [84], corresponding to an impurity concentration of only about 1% [83].

We expect that a similar strong suppression of the p -wave correlations will take place in the junctions we consider. To realize the effects we predict experimentally would thus require samples with good crystallinity and impurity concentrations below about 1%.

In the weakly disordered case—that is, for impurity concentrations below this level—we expect that the amount of p -wave correlations will be reduced, but not have vanished completely. This will lead to a reduction in the induced transverse spin current (superspin Hall effect) or the induced anomalous current (inverse superspin Hall effect) compared to the clean limit. For comparison, it is instructive to compare the behavior in this case to Fig. 12. Here, the p_y -wave spin-0 triplets are suppressed at large spin-orbit coupling, and the anomalous current vanishes. Similar behavior can be expected as a function of impurity concentration.

X. CONCLUSION

We have considered the superspin Hall and the inverse superspin Hall effects in a two-dimensional

S/N/F/N/S Josephson junction. We present two main results.

Firstly, the transverse spin supercurrent induced by the superspin Hall effect circulates from the N/F/N spacer, into the superconductors, and back into the N/F/N spacer. Consequently, it does not give rise to a spin magnetization at the sample edges, contrary to the usual spin Hall effect. The spin magnetization that *does* arise at the sample edges can be attributed to interaction between the proximity-induced even-frequency s -wave spin-singlet condensate and odd-frequency s -wave spin-triplet correlations.

Secondly, we predict and numerically confirm the existence of the inverse superspin Hall effect, which can be detected experimentally as a ϕ_0 shift in the Josephson junction. We have shown that both exchange spin currents and spin-polarized charge supercurrents produce a transverse charge supercurrent by the inverse superspin Hall effect. In particular, we propose that a ϕ_0 junction produced by the inverse superspin Hall effect can be used to—for the first time—measure directly the spin polarization of a charge supercurrent carried by triplet Cooper pairs.

ACKNOWLEDGMENTS

We would like to thank M. Amundsen and J. A. Ouassou for useful discussions. Funding via the “Outstanding Academic Fellows” program at NTNU, the NV Faculty, the Research Council of Norway Grant No. 240806, and the Research Council of Norway through its Centres of Excellence funding scheme, Project No. 262633, “QuSpin” is gratefully acknowledged. This research has benefited from the Notur high-performance computing facilities, Project No. NN9577K.

-
- [1] J. Linder and J. W. A. Robinson, Superconducting spintronics, *Nat. Phys.* **11**, 307 (2015).
 - [2] M. Tinkham, *Introduction to Superconductivity*, 2nd ed. (McGraw-Hill, New York, 1996).
 - [3] P. G. de Gennes, *Superconductivity of Metals and Alloys*, Advanced Book Classics (Westview Press, Boulder, CO, 1999).
 - [4] K. Fossheim and A. Sudbø, *Superconductivity: Physics and Applications* (Wiley, Chichester, 2004).
 - [5] M. Eschrig and T. Löfwander, Triplet supercurrents in clean and disordered half-metallic ferromagnets, *Nat. Phys.* **4**, 138 (2008).
 - [6] M. Eschrig, Spin-polarized supercurrents for spintronics, *Phys. Today* **64**(1), 43 (2011).
 - [7] M. Eschrig, Spin-polarized supercurrents for spintronics: A review of current progress, *Rep. Prog. Phys.* **78**, 104501 (2015).
 - [8] P. Fulde and R. A. Ferrell, Superconductivity in a strong spin-exchange field, *Phys. Rev.* **135**, A550 (1964).
 - [9] A. I. Larkin and Yu. N. Ovchinnikov, Inhomogeneous state of superconductors, *Sov. Phys. JETP* **20**, 762 (1965).
 - [10] F. S. Bergeret, A. F. Volkov, and K. B. Efetov, Long-Range Proximity Effects in Superconductor-Ferromagnet Structures, *Phys. Rev. Lett.* **86**, 4096 (2001).
 - [11] F. S. Bergeret, A. F. Volkov, and K. B. Efetov, Odd triplet superconductivity and related phenomena in superconductor-ferromagnet structures, *Rev. Mod. Phys.* **77**, 1321 (2005).
 - [12] A. I. Buzdin, Proximity effects in superconductor-ferromagnet heterostructures, *Rev. Mod. Phys.* **77**, 935 (2005).
 - [13] F. S. Bergeret and I. V. Tokatly, Singlet-triplet Conversion and the Long-range Proximity Effect in Superconductor-ferromagnet Structures with Generic Spin Dependent Fields, *Phys. Rev. Lett.* **110**, 117003 (2013).
 - [14] F. S. Bergeret and I. V. Tokatly, Spin-orbit coupling as a source of long-range triplet proximity effect in superconductor-ferromagnet hybrid structures, *Phys. Rev. B* **89**, 134517 (2014).
 - [15] V. P. Mineev and G. E. Volovik, Electric dipole moment and spin supercurrent in superfluid ^3He , *J. Low Temp. Phys.* **89**, 823 (1992).

- [16] F. Meier and D. Loss, Magnetization Transport and Quantized Spin Conductance, *Phys. Rev. Lett.* **90**, 167204 (2003).
- [17] E. B. Sonin, Spin currents and spin superfluidity, *Adv. Phys.* **59**, 181 (2010).
- [18] E. B. Sonin, Proposal for Measuring Mechanically Equilibrium Spin Currents in the Rashba Medium, *Phys. Rev. Lett.* **99**, 266602 (2007).
- [19] I. Kulagina and J. Linder, Spin supercurrent, magnetization dynamics, and φ -state in spin-textured Josephson junctions, *Phys. Rev. B* **90**, 054504 (2014).
- [20] I. V. Bobkova, A. M. Bobkov, and M. A. Silaev, Spin torques and magnetic texture dynamics driven by the supercurrent in superconductor/ferromagnet structures, *Phys. Rev. B* **98**, 014521 (2018).
- [21] J. Sinova, S. O. Valenzuela, J. Wunderlich, C. H. Back, and T. Jungwirth, Spin Hall effects, *Rev. Mod. Phys.* **87**, 1213 (2015).
- [22] L. Onsager, Reciprocal relations in irreversible processes. I, *Phys. Rev.* **37**, 405 (1931).
- [23] L. Onsager, Reciprocal relations in irreversible processes. II, *Phys. Rev.* **38**, 2265 (1931).
- [24] S. R. de Groot, *Thermodynamics of Irreversible Processes*, Selected Topics in Modern Physics Vol. 3 (North-Holland Publishing Company, Amsterdam, 1951).
- [25] E. Saitoh, M. Ueda, H. Miyajima, and G. Tatara, Conversion of spin current into charge current at room temperature: Inverse spin-Hall effect, *Appl. Phys. Lett.* **88**, 182509 (2006).
- [26] K. Uchida, S. Takahashi, K. Harii, J. Ieda, W. Koshibae, K. Ando, S. Maekawa, and E. Saitoh, Observation of the spin Seebeck effect, *Nature (London)* **455**, 778 (2008).
- [27] S. Y. Huang, X. Fan, D. Qu, Y. P. Chen, W. G. Wang, J. Wu, T. Y. Chen, J. Q. Xiao, and C. L. Chien, Transport Magnetic Proximity Effects in Platinum, *Phys. Rev. Lett.* **109**, 107204 (2012).
- [28] M. Weiler, M. Althammer, F. D. Czeschka, H. Huebl, M. S. Wagner, M. Opel, I.-M. Imort, G. Reiss, A. Thomas, R. Gross, and S. T. B. Goennenwein, Local Charge and Spin Currents in Magnetothermal Landscapes, *Phys. Rev. Lett.* **108**, 106602 (2012).
- [29] K. Ando, S. Takahashi, K. Harii, K. Sasage, J. Ieda, S. Maekawa, and E. Saitoh, Electric Manipulation of Spin Relaxation Using the Spin Hall Effect, *Phys. Rev. Lett.* **101**, 036601 (2008).
- [30] H. Kontani, J. Goryo, and D. S. Hirashima, Intrinsic Spin Hall Effect in the s -wave Superconducting State: Analysis of the Rashba Model, *Phys. Rev. Lett.* **102**, 086602 (2009).
- [31] A. G. Mal'shukov and C. S. Chu, Spin-Hall current and spin polarization in an electrically biased SNS Josephson junction, *Phys. Rev. B* **84**, 054520 (2011).
- [32] S. Pandey, H. Kontani, D. S. Hirashima, R. Arita, and H. Aoki, Spin Hall effect in iron-based superconductors: A Dirac-point effect, *Phys. Rev. B* **86**, 060507(R) (2012).
- [33] A. G. Mal'shukov, Supercurrent generation by spin injection in an s -wave superconductor-Rashba metal bilayer, *Phys. Rev. B* **95**, 064517 (2017).
- [34] C. Espedal, P. Lange, S. Sadjina, A. G. Mal'shukov, and A. Brataas, Spin Hall effect and spin swapping in diffusive superconductors, *Phys. Rev. B* **95**, 054509 (2017).
- [35] T. Wakamura, H. Akaike, Y. Omori, Y. Niimi, S. Takahashi, A. Fujimaki, S. Maekawa, and Y. Otani, Quasiparticle-mediated spin Hall effect in a superconductor, *Nat. Mater.* **14**, 675 (2015).
- [36] K. Sengupta, R. Roy, and M. Maiti, Spin Hall effect in triplet chiral superconductors and graphene, *Phys. Rev. B* **74**, 094505 (2006).
- [37] A. G. Mal'shukov, S. Sadjina, and A. Brataas, Inverse spin Hall effect in superconductor/normal-metal/superconductor Josephson junctions, *Phys. Rev. B* **81**, 060502(R) (2010).
- [38] F. S. Bergeret and I. V. Tokatly, Manifestation of extrinsic spin hall effect in superconducting structures: Nondissipative magnetoelectric effects, *Phys. Rev. B* **94**, 180502(R) (2016).
- [39] A. G. Mal'shukov and C. S. Chu, Spin Hall effect in a Josephson contact, *Phys. Rev. B* **78**, 104503 (2008).
- [40] Z.-H. Yang, Y.-H. Yang, and J. Wang, Interfacial spin Hall current in a Josephson junction with Rashba spin-orbit coupling, *Chin. Phys. B* **21**, 057402 (2012).
- [41] J. Linder, M. Amundsen, and V. Rasinggård, Intrinsic superspin Hall current, *Phys. Rev. B* **96**, 094512 (2017).
- [42] F. Konschelle, I. V. Tokatly, and F. S. Bergeret, Theory of the spin-galvanic effect and the anomalous phase shift φ_0 in superconductors and Josephson junctions with intrinsic spin-orbit coupling, *Phys. Rev. B* **92**, 125443 (2015).
- [43] R. S. Keizer, S. T. B. Goennenwein, T. M. Klapwijk, G. Miao, G. Xiao, and A. Gupta, A spin triplet supercurrent through the half-metallic ferromagnet CrO₂, *Nature (London)* **439**, 825 (2006).
- [44] T. S. Khaire, M. A. Khasawneh, W. P. Pratt, and N. O. Birge, Observation of Spin-triplet Superconductivity in Co-based Josephson Junctions, *Phys. Rev. Lett.* **104**, 137002 (2010).
- [45] J. W. A. Robinson, J. D. S. Witt, and M. G. Blamire, Controlled injection of spin-triplet supercurrents into a strong ferromagnet, *Science* **329**, 59 (2010).
- [46] M. S. Anwar, M. Veldhorst, A. Brinkman, and J. Aarts, Long range supercurrents in ferromagnetic CrO₂ using a multilayer contact structure, *Appl. Phys. Lett.* **100**, 052602 (2012).
- [47] W. M. Martinez, W. P. Pratt, and N. O. Birge, Amplitude Control of the Spin-triplet Supercurrent in S/F/S Josephson Junctions, *Phys. Rev. Lett.* **116**, 077001 (2016).
- [48] A. Singh, C. Jansen, K. Lahabi, and J. Aarts, High-Quality CrO₂ Nanowires for Dissipation-Less Spintronics, *Phys. Rev. X* **6**, 041012 (2016).
- [49] J. C. Slonczewski, Conductance and exchange coupling of two ferromagnets separated by a tunneling barrier, *Phys. Rev. B* **39**, 6995 (1989).
- [50] W. Chen, P. Horsch, and D. Manske, Dissipationless spin current between two coupled ferromagnets, *Phys. Rev. B* **89**, 064427 (2014).
- [51] Y. Tanaka, A. A. Golubov, S. Kashiwaya, and M. Ueda, Anomalous Josephson Effect Between Even- and Odd-Frequency Superconductors, *Phys. Rev. Lett.* **99**, 037005 (2007).
- [52] M. Eschrig, T. Löfwander, T. Champel, J. C. Cuevas, J. Kopu, and G. Schön, Symmetries of pairing correlations in superconductor-ferromagnet nanostructures, *J. Low Temp. Phys.* **147**, 457 (2007).
- [53] M. Sigrist and K. Ueda, Phenomenological theory of unconventional superconductivity, *Rev. Mod. Phys.* **63**, 239 (1991).
- [54] D. S. Dummit and R. M. Foote, *Abstract Algebra*, 3rd ed. (Wiley, Hoboken, NJ, 2004).

- [55] F. R. Gantmacher, *The Theory of Matrices* (American Mathematical Society, Providence, RI, 2000), Vol. 1.
- [56] J. A. Ouassou, S. H. Jacobsen, and J. Linder, Conservation of spin supercurrents in superconductors, *Phys. Rev. B* **96**, 094505 (2017).
- [57] A. J. Leggett, A theoretical description of the new phases of liquid ^3He , *Rev. Mod. Phys.* **47**, 331 (1975).
- [58] J. M. D. Coey, *Magnetism and Magnetic Materials* (Cambridge University Press, Cambridge, England, 2010).
- [59] R. C. O’Handley, *Modern Magnetic Materials: Principles and Applications* (Wiley, Hoboken, NJ, 2000).
- [60] J.-F. Liu and K. S. Chan, Relation between symmetry breaking and the anomalous Josephson effect, *Phys. Rev. B* **82**, 125305 (2010).
- [61] J.-F. Liu and K. S. Chan, Anomalous Josephson current through a ferromagnetic trilayer junction, *Phys. Rev. B* **82**, 184533 (2010).
- [62] D. B. Szombati, S. Nadj-Perge, D. Car, S. R. Plissard, E. P. A. M. Bakkers, and L. P. Kouwenhoven, Josephson φ_0 -junction in nanowire quantum dots, *Nat. Phys.* **12**, 568 (2016).
- [63] A. Rasmussen, J. Danon, H. Suominen, F. Nichele, M. Kjaergaard, and K. Flensberg, Effects of spin-orbit coupling and spatial symmetries on the Josephson current in SNS junctions, *Phys. Rev. B* **93**, 155406 (2016).
- [64] V. Chandrasekhar, Proximity-coupled systems: quasiclassical theory of superconductivity, in *Superconductivity*, edited by K. H. Bennemann and J. B. Ketterson (Springer, Berlin, 2008), p. 279.
- [65] A. M. Black-Schaffer and J. Linder, Strongly anharmonic current-phase relation in ballistic graphene Josephson junctions, *Phys. Rev. B* **82**, 184522 (2010).
- [66] C. D. English, D. R. Hamilton, C. Chialvo, I. C. Moraru, N. Mason, and D. J. Van Harlingen, Observation of nonsinusoidal current-phase relation in graphene Josephson junctions, *Phys. Rev. B* **94**, 115435 (2016).
- [67] Y. K. Kato, R. C. Myers, A. C. Gossard, and D. D. Awschalom, Observation of the spin Hall effect in semiconductors, *Science* **306**, 1910 (2004).
- [68] J. Wunderlich, B. Kaestner, J. Sinova, and T. Jungwirth, Experimental Observation of the Spin-Hall Effect in a Two-Dimensional Spin-Orbit Coupled Semiconductor System, *Phys. Rev. Lett.* **94**, 047204 (2005).
- [69] K. Halterman, O. T. Valls, and P. H. Barsic, Induced triplet pairing in clean s -wave superconductor/ferromagnet layered structures, *Phys. Rev. B* **77**, 174511 (2008).
- [70] D. Terrade, D. Manske, and M. Cuoco, Control of edge currents at a ferromagnet–triplet superconductor interface by multiple helical modes, *Phys. Rev. B* **93**, 104523 (2016).
- [71] Shin-ichi Hikino, Magnetization reversal by tuning Rashba spin–orbit interaction and Josephson phase in a ferromagnetic Josephson junction, *J. Phys. Soc. Jpn.* **87**, 074707 (2018).
- [72] A. F. Andreev, The thermal conductivity of the intermediate state in superconductors, *Sov. Phys. JETP* **19**, 1228 (1964).
- [73] J. A. Sauls, Andreev bound states and their signatures, *Philos. Trans. R. Soc., A* **376**, 20180140 (2018).
- [74] I. Kulik and A. Omel’yanchuk, Properties of superconducting microbridges in the pure limit, *Sov. J. Low Temp. Phys.* **3**, 459 (1977).
- [75] J. Linder, T. Yokoyama, D. Huertas-Hernando, and A. Sudbø, Supercurrent Switch in Graphene π Junctions, *Phys. Rev. Lett.* **100**, 187004 (2008).
- [76] A. A. Golubov, M. Yu. Kupriyanov, and E. Il’ichev, The current-phase relation in Josephson junctions, *Rev. Mod. Phys.* **76**, 411 (2004).
- [77] J. A. Ouassou and J. Linder, Voltage control of superconducting exchange interaction and anomalous Josephson effect, [arXiv:1810.02820](https://arxiv.org/abs/1810.02820).
- [78] J. A. Glick, V. Aguilar, A. B. Gougam, B. M. Niedzielski, E. C. Gingrich, R. Loloee, W. P. Pratt, and N. O. Birge, Phase control in a spin-triplet SQUID, *Sci. Adv.* **4**, eaat9457 (2018).
- [79] N. W. Ashcroft and N. D. Mermin, *Solid State Physics*, 1st ed. (Harcourt College Publishers, Orlando, FL, 1976).
- [80] P. A. Frigeri, D. F. Agterberg, A. Koga, and M. Sigrist, Superconductivity Without Inversion Symmetry: MnSi Versus CePt₃Si, *Phys. Rev. Lett.* **92**, 097001 (2004).
- [81] Y. Dalichaouch, M. C. de Andrade, D. A. Gajewski, R. Chau, P. Visani, and M. B. Maple, Impurity Scattering and Triplet Superconductivity in UPt₃, *Phys. Rev. Lett.* **75**, 3938 (1995).
- [82] C. Geibel, C. Schank, F. Jährling, B. Buschinger, A. Grauel, T. Lühmann, P. Gegenwart, R. Helfrich, P.H.P. Reinders, and F. Steglich, Doping effects on UPd₂Al₃, *Physica B* **199–200**, 128 (1994).
- [83] S. Onari and H. Kontani, Violation of Anderson’s Theorem for the Sign-Reversing s -wave State of Iron-pnictide Superconductors, *Phys. Rev. Lett.* **103**, 177001 (2009).
- [84] Y. Wang, A. Kreisel, P. J. Hirschfeld, and V. Mishra, Using controlled disorder to distinguish s_{\pm} and s_{++} gap structure in Fe-based superconductors, *Phys. Rev. B* **87**, 094504 (2013).
- [85] A. P. Mackenzie, R. K. W. Haselwimmer, A. W. Tyler, G. G. Lonzarich, Y. Mori, S. Nishizaki, and Y. Maeno, Extremely Strong Dependence of Superconductivity on Disorder in Sr₂RuO₄, *Phys. Rev. Lett.* **80**, 161 (1998).
- [86] A. A. Abrikosov and L. P. Gor’kov, Contribution to the theory of superconducting alloys with paramagnetic impurities, *Sov. Phys. JETP* **12**, 1243 (1961).

This thesis is set in Arno Pro (serif), Cronos Pro (sans serif), AMS Euler (math), and Fira Mono (monospace) using Lua \LaTeX .

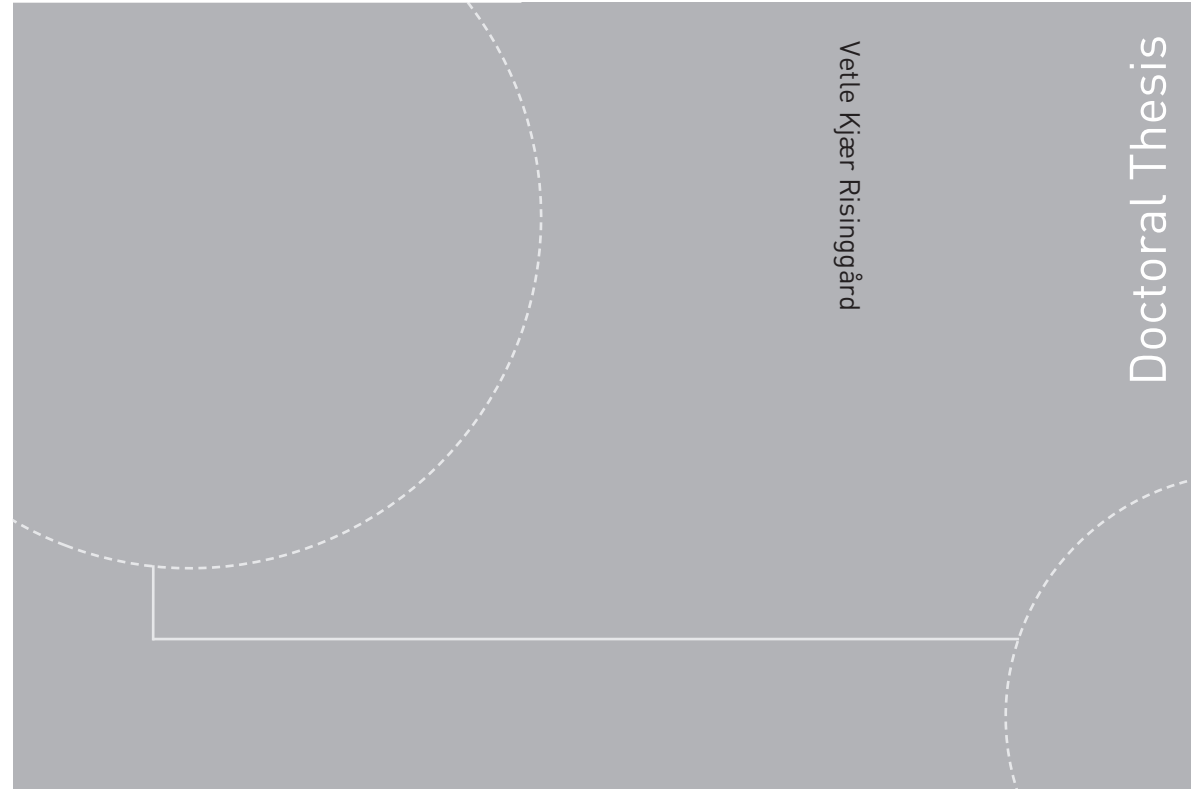
Arno Pro and Cronos Pro are designed by Robert Slimbach and were issued by Adobe Systems in 2007 and 1996, respectively. Arno is a humanist roman inspired by the Venetian and Aldine typefaces and named after the river that runs through Florence. Cronos is a humanist sans serif, and is inspired by the calligraphy of the Italian Renaissance.

Euler was designed by Hermann Zapf and Donald E. Knuth, on commission for the American Mathematical Society in 1985. Euler is a humanist script inspired by handwritten mathematics and named after Leonhard Euler.

\TeX is a typesetting system designed and implemented by Donald E. Knuth and released in 1978. \LaTeX is a \TeX format first introduced by Leslie Lamport in 1983.

Lua \LaTeX is \LaTeX based on the Lua \TeX engine, first released in 2007. The original authors of Lua \TeX are Taco Hoekwater, Hartmut Henkel, and Hans Hagen.

ISBN 978-82-326-4044-7 (printed version)
ISBN 978-82-326-4045-4 (electronic version)
ISSN 1503-8181



Doctoral theses at NTNU, 2019:224

Vetle Kjær Risinggård
**Spin currents and torques
via magnons, electrons,
and Cooper pairs**

Doctoral theses at NTNU, 2019:224

NTNU
Norwegian University of
Science and Technology
Faculty of Natural Sciences
Department of Physics

 **NTNU**
Norwegian University of
Science and Technology

 **NTNU**

 **NTNU**
Norwegian University of
Science and Technology